# Probabilistic Imaging and Dynamic Modeling of Earthquake Source Processes

Thesis by

Junle Jiang

In Partial Fulfillment of the Requirements

for the Degree of

Doctor of Philosophy


California Institute of Technology

Pasadena, California

2016

(Defended December 9, 2015)

# Acknowledgements

Pursuing a Ph.D. at Caltech has been a special journey for me which not only rewarded me with intellectual development, but also personal growth and a sense of cultural identity. I am truely grateful that Nadia and Mark have been the most significant people of my time at Caltech, as they were friends who imparted life experiences as well as mentors who guided my academic trainings. Nadia was the first person I turned to as a physics major, intrigued and yet perplexed by the complex geophysical world, and I always enjoyed critical thinking and discussions with her. Mark is the mastermind who provided me with first-hand and teamwork experiences of working on megathrust earthquakes over the years whenever they culpably generate tsunamis, and I appreciate that he always challenged me to think outside the box. I feel fortunate to have been involved with both of their groups and to have been introduced to unique perspectives on some geophysical problems. Indeed, the work I present in my thesis could not have been accomplished without their encouragement, support, and trust as well as patience over the years. I want to especially express my appreciation for their support in face of the adversities of my personal life; their words of advice and comfort at the time were just as precious as those of my family.

I'd like to thank the rest of my thesis committee – Pablo, Jean-Philippe, and Tom – for engaging discussions on a variety of topics over the years and valuable suggestions on improving my thesis. I thank Tom for teaching my first seismology class, Pablo for

Computational Geophysics, and Jean-Philippe for the most inspiring series of Ge277 Active Tectonics seminar classes, which I still benefit from reviewing time after time.

I thank other professors at Seismo Lab, including Rob, Don, Victor, Joann, Jennifer, Hiroo, Mike, Egill, and Zhongwen for classes, field trip opportunities, discussions, and everything else. Outside the Seismo Lab, I am particularly grateful to Joe for introducing me to the Palau project, several Ge136 excursions to the Grand Canyon, Baja California etc., and leading the division enrichment trip to Japan, together with Paul and Atsuko.

I have heartfelt gratitude for many postdocs and senior members in the group who provided support and inspirations for me, in particular, Hiro, Sylvain, Anthony, Sarah, Francisco, and Zacharie, because I think parts of my thesis directly benefit from their guidance and foundational work. I want to thank all the group members over the years who offered great company and enjoyable exchanges: Ting, Ahmed, Surendra, Hasha, Vahe, Nina, Ravi, Marion, Brent, Semechah, Stephen, Bryan, Vito, Hilary, Romain, Jessica, Marcello, Srivatsan, Nadaya, Jeff, Han, and Chris; my officemates Laura, Thomas, Dunzhu, Xiaolin, Vish, Minyan, and Jack; those with whom I share lots of interesting conversations and activities, Yiran, Dongzhou, and Yingdi; and everyone else in the Seismo Lab. I thank all the admins for their wonderful support and always pleasant interactions: Donna, Rosemary, Viola, Julia, Sarah, Evelina, Kim, Maria, Liz, Leticia, Priscilla, and Carolina.

I'm thankful for Michael and Hailiang for their guidance on computation and support in developing AlTar as a teamwork.

I want to thank several groups of people on the campus: Laura and Daniel at the International Student Office, Portia and Taso at the Center for Diversity, and the group of fellow board members during my time at the Graduate Student Council, and, last but not the least, the group of aspiring friends in Chinese Student and Scholar Association.

I thank Yihe and Zhihong for the most memorable times at Caltech.

I'm also thankful for my undergraduate university, Peking University, which has cast deep influence on me in ways that I appreciate greatly.

Finally, my most genuine gratitude goes to my family, especially my grandmother and mother, for unconditional love, for love that sometimes does not come without misunderstanding, and for always looking out for me. Additionally, I owe a thank-you to my 13-year-old brother Leo for being there with the family, when I cannot always be.

# Abstract

Investigation of large, destructive earthquakes is challenged by their infrequent occurrence and the remote nature of geophysical observations. This thesis sheds light on the source processes of large earthquakes from two perspectives: robust and quantitative observational constraints through Bayesian inference for earthquake source models, and physical insights on the interconnections of seismic and aseismic fault behavior from elastodynamic modeling of earthquake ruptures and aseismic processes.

To constrain the shallow deformation during megathrust events, we develop semi-analytical and numerical Bayesian approaches to explore the maximum resolution of the tsunami data, with a focus on incorporating the uncertainty in the forward modeling. These methodologies are then applied to invert for the coseismic seafloor displacement field in the 2011 $M_{\mathrm{w}}$ 9.0 Tohoku-Oki earthquake using near-field tsunami waveforms and for the coseismic fault slip models in the 2010 $M_{\mathrm{w}}$ 8.8 Maule earthquake with complementary tsunami and geodetic observations. From posterior estimates of model parameters and their uncertainties, we are able to quantitatively constrain the near-trench profiles of seafloor displacement and fault slip. Similar characteristic patterns emerge during both events, featuring the peak of uplift near the edge of the accretionary wedge with a decay toward the trench axis, with implications for fault failure and tsunamigenic mechanisms of megathrust earthquakes.

To understand the behavior of earthquakes at the base of the seismogenic zone on

continental strike-slip faults, we simulate the interactions of dynamic earthquake rupture, aseismic slip, and heterogeneity in rate-and-state fault models coupled with shear heating. Our study explains the long-standing enigma of seismic quiescence on major fault segments known to have hosted large earthquakes by deeper penetration of large earthquakes below the seismogenic zone, where mature faults have well-localized creeping extensions. This conclusion is supported by the simulated relationship between seismicity and large earthquakes as well as by observations from recent large events. We also use the modeling to connect the geodetic observables of fault locking with the behavior of seismicity in numerical models, investigating how a combination of interseismic geodetic and seismological estimates could constrain the locked-creeping transition of faults and potentially their co- and post-seismic behavior.

# Contents

**Acknowledgements** **iv**

**Abstract** **vii**

**1 Introduction** **11**

**2 Bayesian Inference of Coseismic Seafloor Deformation During the 2011 Tohoku-Oki Earthquake with Near-field Tsunami Waveforms** **15**

**Abstract** **16**

2.1 Introduction . . . . . 18

2.2 Tsunami observations and modeling . . . . . 21

2.2.1 Observations of the 2011 Tohoku-Oki earthquake induced tsunami . 21

2.2.2 Model parameterization of seafloor deformation and tsunami excitation 23

2.2.3 Forward modeling of the tsunami propagation . . . . . 26

2.3 Bayesian inference of seafloor deformation model . . . . . 29

2.3.1 Bayesian formulation of the inverse problem . . . . . 29

2.3.2 Semi-analytical approach for the quasi-static problem . . . . . 30

2.3.3 Sampling approach for the kinematic problem . . . . . 31

2.3.4 Design of the model prediction error $\mathbf{C}_{\mathrm{p}}$ . . . . . 32

2.3.5 Posterior uncertainty and resolution analysis . . . . . 34

2.4 Synthetic scenarios . . . . . 36

2.5 Applications to the 2011 Tohoku-Oki earthquake . . . . . 42

2.5.1 Quasi-static seafloor deformation models . . . . . 42

2.5.2 Kinematic seafloor deformation models . . . . . 43

2.6 Discussion . . . . . 50

2.6.1 The resolution of tsunami data . . . . . 50

2.6.2 Assumptions and advantages of our methodology . . . . . 51

2.6.3 Seafloor deformation and fault slip near the trench . . . . . 52

2.7 Conclusion . . . . . 60

**Appendices** **62**

2.A Frequency dispersion in tsunami propagation . . . . . 62

2.B Different formulations of $\mathbf{C}_{\mathrm{p}}$ for tsunami waveforms . . . . . 64

**3 A Bayesian Perspective on the Complementarity of Tsunami and Geodetic Observations for the 2010 $M_{\mathbf{w}}$ 8.8 Maule, Chile Earthquake** **71**

**Abstract** **72**

3.1 Introduction . . . . . 74

3.2 Data and methods . . . . . 75

3.2.1 Fault geometry and model parameterization . . . . . 75

3.2.2 Geodetic observations and modeling . . . . . 76

3.2.3 Tsunami observations and modeling . . . . . 76

3.2.4 Semi-analytical Bayesian approach to fault slip models . . . . . 79

3.2.5 Error models for geodetic and tsunami modeling . . . . . 81

3.3 Results and discussions . . . . . 83

3.3.1 Fault slip models from tsunami, geodetic, and joint inversions . . . . 83

3.3.2 Effects of dispersion, elastic structure, and error models . . . . . 89

3.3.3 Updip and downdip resolution of fault slip . . . . . 97

3.4 Conclusion . . . . . 99

**4 Deeper Penetration of Large Earthquake Ruptures on Seismically Quiescent Faults 103**

**Abstract 104**

4.1 Main Text . . . . . 105

**Appendices 116**

4.A Materials and Methods . . . . . 116

4.A.1 Earthquake catalogues and coseismic slip models . . . . . 116

4.A.2 Microseismicity vs. depth extent of earthquakes from slip models . . 117

4.A.3 Paleoseismic Records for the San Andreas and San Jacinto Faults . . 123

4.A.4 Numerical methods and model setup . . . . . 132

4.B Supplementary Text . . . . . 137

4.B.1 Physical mechanisms favoring or discouraging deeper coseismic slip . 137

4.B.2 Long-term fault behavior in numerical simulations . . . . . 138

4.B.3 Estimating the migration of stress concentration front . . . . . 140

**5 Connecting Seismicity, Fault Locking and Large Earthquake Rupture at Depth 154**

**Abstract 155**

5.1 Introduction . . . . . 157

5.2 Model setup . . . . . 159

5.3 Seismic and aseismic behavior in long-term fault models . . . . . 160

5.3.1 Large earthquake rupture and seismicity . . . . . 160

5.3.2 Fault coupling and geodetically-estimated fault locking depth . . . . 164

5.3.3 Spatial relations and temporal evolutions of different depths . . . . . 168

5.4 Inferring the geodetic locking depths on major faults . . . . . 170

5.5 Seismicity and fault heterogeneity at the transitional depth . . . . . 175

5.6 Conclusion . . . . . 179

**6 Conclusion and Perspective** **181**

# List of Figures


2.1 Source region and tsunami records for the 2011 Tohoku-Oki earthquake . . . 22

2.2 Parameterization of the seafloor deformation and forward modeling of tsunami excitation and propagation. . . . . 25

2.3 Design of the variance-covariance matrix for the model prediction error $\mathbf{C}_{\mathrm{p}}$ . 35

2.4 Inversions of a synthetic scenario with maximum seafloor uplift away from the trench . . . . . 40

2.5 Inversions of a synthetic scenario with maximum seafloor uplift at the trench 41

2.6 Spatial averaging of posterior solutions and model uncertainties . . . . . 42

2.7 Spatial averaging and uncertainty analysis of the posterior solutions. . . . . 44

2.8 Posterior mean models for the quasi-static problem with different $\mathbf{C}_{\mathrm{p}}$ . . . . 45

2.9 Posterior data fit and prediction of later waveforms for the quasi-static solutions. 46

2.10 The uncertainty, averaging scale, and original posterior mean models for the kinematic problem. . . . . 48

2.11 The uncertainty, averaging scale, and 1R-averaged posterior mean models for the kinematic problem. . . . . 49

2.12 Posterior data fit and prediction of later waveforms for the kinematic solutions. 50

2.13 Seafloor deformation near the trench in the kinematic model and comparisons with seafloor geodetic observations . . . . . 55

2.14 Probabilistic characterization of the near-trench seafloor tilt . . . . . 56

2.15 Seafloor deformation near the trench in the quasi-static model . . . . . 57

2.16 2D subduction zone models with different elastic structure and bathymetry . 59

2.17 Seafloor uplift and subsurface fault slip in 2D elastic models . . . . . 60

2.18 The original and filtered tsunami waveforms . . . . . 67

2.19 Frequency dispersion relations for tsunami propagation . . . . . 68

2.20 The effect of water layer attenuation and wave dispersion on tsunami GF . . 68

2.21 Different formulations of $\mathbf{C}_{\mathrm{p}}$ for tsunami forward modeling . . . . . 69

2.22 Great-circle path and ray path approximations in tsunami propagation . . . 70

3.1 Fault geometry and station distribution for the 2010 $M_{\mathrm{w}}$ 8.8 Maule earthquake 77

3.2 The reference velocity model and perturbed models . . . . . 83

3.3 $\mathbf{C}_{\chi}$ for the geodetic (GPS & InSAR) and tsunami modeling . . . . . 84

3.4 Coseismic fault slip models from tsunami, geodetic, and joint inversions with $\mathbf{C}_{\chi}$ . . . . . 87

3.5 Predicted surface displacement from tsunami, geodetic, and joint models with $\mathbf{C}_{\chi}$ . . . . . 88

3.6 Observed and predicted InSAR measurements using the favored joint models 90

3.7 Observed and predicted GPS displacements using the favored joint models . 92

3.8 Observed and predicted DART waveforms using the favored joint models . . 93

3.9 The effect of elastic structure and error models on geodetic inversions . . . . 94

3.10 The effect of dispersion and error models on tsunami inversions . . . . . 95

3.11 Coseismic fault slip models from tsunami, geodetic, and joint inversions with $\mathbf{C}_{\mathrm{d}}$ . . . . . 96

3.12 The trench-normal profile of surface displacements predicted from the favored joint models . . . . . 100
3.13 Along-strike integrated seismic potency . . . . . 101
3.14 Comparisons between co- and post-seismic fault slip models and aftershocks . 102

4.1 Schematic illustration of our fault model and the locked-creeping transition . 106
4.2 Observations of large earthquakes and microseismicity patterns on major strike-slip faults . . . . . 107
4.3 Microseismicity and the potential for deeper ruptures on the San Andreas Fault (SAF) and the San Jacinto Fault (SJF) in Southern California . . . . . 108
4.4 The relation between the depth extent of large earthquakes and microseismicity in simulated earthquake sequences . . . . . 112
4.5 2004 $M_{\mathrm{w}}$ 6.0 Parkfield and 1984 $M_{\mathrm{w}}$ 6.3 Morgan Hill earthquakes . . . . . 124
4.6 1979 $M_{\mathrm{w}}$ 6.4 Imperial Valley and 1987 $M_{\mathrm{w}}$ 6.7 Superstition Hills earthquakes 125
4.7 1989 $M_{\mathrm{w}}$ 7.1 Loma Prieta earthquake . . . . . 125
4.8 1999 $M_{\mathrm{w}}$ 7.6 Izmit earthquake . . . . . 126
4.9 2002 $M_{\mathrm{w}}$ 7.9 Denali earthquake . . . . . 127
4.10 2001 $M_{\mathrm{w}}$ 7.9 Kokoxili earthquake . . . . . 128
4.11 1906 $M_{\mathrm{w}}$ 7.9 San Francisco earthquake . . . . . 129
4.12 Uncertainty of earthquake locations . . . . . 130
4.13 Depth dependence of rate-and-state frictional properties and normal stress . 135
4.14 Illustration of the locations of the along-depth profiles and observation points 139
4.15 Accumulated fault slip along depth over several large earthquakes . . . . . 141
4.16 Long-term evolution of stress and slip rate of the points on the fault . . . . . 142
4.17 Long-term evolution of stress and slip rate of the points within VW patches . 143

4.18 Time evolution of the along-depth shear stress and slip rate profiles in model M1 . . . . . 144
4.19 Time evolution of the along-depth shear stress and slip rate profiles in model M2 . . . . . 145
4.20 Post- and inter-seismic migration of the SCF after a deeper-penetrating event. 147
4.21 Post- and inter-seismic response of faults with different frictional properties at depth . . . . . 151
4.22 Post- and inter-seismic fault slip and the migration of SCF . . . . . 152
4.23 Dependence of migration distance $D_{\rm prop}$ of the SCF on $\Delta\tau_{\rm eq}$ and $a\sigma$ . . . . . 153

5.1 Seismicity and geodetic locking depths on the San Andreas and San Jacinto faults . . . . . 158
5.2 Conventional elastic dislocation model for earthquake cycles . . . . . 159
5.3 Fault models with different frictional properties at the seismic-aseismic transition 161
5.4 Distribution of large earthquake slip and seismicity in the long-term fault models 162
5.5 The depth distributions of stress, stressing, fault slip tand seismicity . . . . . 165
5.6 Time evolution of fault coupling in the interseismic periods . . . . . 166
5.7 Time-dependent fault slip rates at depth and surface velocity . . . . . 168
5.8 Inversion of the locking depth $D_{\rm geod}$ and fault slip rate $V_{\rm cr}$ . . . . . 169
5.9 Time dependence of $D_{\rm lock}$, $D_{\rm geod}$, and $D_{0.5C}$ in the interseismic period . . . . 171
5.10 The effect of layered elastic structure on the inference of $D_{\rm geod}$ and $V_{\rm cr}$ . . . 173
5.11 Illustration of slip partition and $D_{\rm geod}$, $D_{\rm seis}$ $D_{\rm lock}$, and $D_{\rm rupt}$ in a seismic cycle 175
5.12 Conceptual and physical models for faults with other heterogeneity . . . . . 177
5.13 Complex fault behavior and variation of fault coupling in model M5 . . . . . 178
5.14 Shallower locking depth and deeper seismicity in model M5 . . . . . 179

6.1 Variability in earthquake slip and arresting depths in models with depth-dependent permeability and shear-zone width . . . . . 185

# List of Tables

2.1 Summary on the characteristics of different $\mathbf{C}_\mathrm{p}$ . . . . . 67

4.1 Coseismic slip models and catalogues for events that satisfy our selection criteria. 118

4.2 Calendar years for historical and prehistorical earthquakes (after A.D. 1000) on the SAF and SJF. . . . . 131

4.3 Parameters for the fault models . . . . . 136

# Chapter 1

# Introduction

Since the elastic rebound theory was first put forth by Harry Fielding Reid in 1910, shortly after the devastating 1906 San Francisco earthquake in Northern California, the phenomena of earthquakes in the shallow crust have been well recognized as a major behavior of tectonic faults to release strain energy, which is stored during long-term stasis, through rapid displacements across the fault. The nature of recurrence and virtual unpredictability of earthquakes makes them a formidable natural hazard.

Modern geophysical observations, including seismological instruments and geodetic techniques that measure crustal deformation over a wide range of spatial and temporal scales, have been enriching our experiences and understandings of earthquakes and fault behavior. Among all, large earthquakes are rare occurrences and often are more challenging to observe due to their remoteness. In major subduction zones, fault slip during megathrust events occurs offshore, but the induced tsunami still bears a significant impact on the coast. Large continental earthquakes usually initiate deep in the seismogenic zone of faults, under the extreme conditions that are still beyond the reach of the most advanced drilling techniques and borehole observations.

Over the recent decade we have witnessed a number of large earthquakes that have occurred worldwide, many of them in the subduction zones, such as Sumatra, Chile, and

Japan. Some of them came with surprising features, with the 2011 $M_{\rm w}$ 9.0 Tohoku-Oki earthquake as a notable example, which occurred in unanticipated locations with much underestimated impact from the induced tsunami (*Simons et al.*, 2011). The event serves as a constant reminder for us that predicting the behavior of earthquakes is a challenging task. How these rare earthquakes behave provides us with valuable and vital information for solving their mystery, thus motivating quests into understanding the detailed coseismic physical processes, and also leading to studies of other closely related phenomenon – aftershocks, postseismic afterslip, viscoelastic and poroelastic bulk relaxations, etc. (*Segall*, 2010) – which have now been routinely carried out after major earthquakes.

For another type of major fault systems – continental strike-slip faults – we still have limited experiences of large earthquakes in heavily-populated modern urban regions. As one of the most prominent faults of this type in a well-instrumented and well-studied region, the San Andreas Fault in California has not had an event of $M_{\rm w} > 7$ since the 1906 temblor in Northern California, and not since the 1857 $M_{\rm w}$ 7.9 Fort Tejon earthquake in Southern California, with an even more overdue Coachella segment at the southernmost end, which sits in peace since $\sim$ 1690 (*WGCEP*, 1995). Paleoseismic studies continue to reveal more information about these past events (e.g., *Sieh*, 1978a; *Zielke et al.*, 2010), which complements our current observations which are limited to only several decades of seismic monitoring and over a decade of quality geodetic measurements for the late interseismic period of faults.

Along with the observational endeavor for understanding earthquakes are the developments of laboratory and theoretical studies that shed light on the conditions of crustal faulting and processes of earthquake slip. Insights from these experiments and theories suggest that fault behavior can be understood as a frictional phenomenon governed by the

so-called rate-and-state friction laws, in which earthquakes occur as slip instability that develops under loading (*Dieterich*, 2007). Such a framework gains acceptance and validation through many successful applications for understanding the recurrence of earthquakes, depth variation of fault slip, etc. (*Scholz*, 2002). Among many important implications, it is suggested that aseismic processes can influence the initiation, i.e. nucleation, of earthquakes. Recent experiments under high velocity conditions further reveal a variety of mechanisms through which enhanced dynamic weakening could occur (*Tullis*, 2015), alluding to the further complexity in the earthquake process that their nucleation and rupture are potentially governed by different mechanisms. On tectonic faults, they might be interconnected through aseismic processes. Understanding how these laboratory findings connect with large-scale earthquake phenomena and how their combinations with theories can guide us in the real world requires comparing model predictions with different lines of observations.

This thesis consists of two main parts in which we develop new observational and physical approaches to understand the earthquake source processes. Our studies focus on two typical tectonic settings where large earthquakes occur: the megathrust faults in subduction zones (Chapter 1 and 2), and continental mature strike-slip faults (Chapter 3 and 4).

In Chapter 1, we study, for the 2011 $M_{\mathrm{w}}$ 9.0 Tohoku-Oki earthquake, whether the shallow fault slip process can be resolved by the tsunami observations and contribute to understanding the extent of fault failure and deformation at the accretionary wedge during this event. In the process, we sharpen our imaging ability through Bayesian inference, and make our inference more robust with an improved understanding of the uncertainty in our problem. Our probabilistic source models provide robust constraints on the coseismic process, and hence important foundations for studing post-earthquake phenomena, e.g., postseismic afterslip, bulk relaxation, stress calculations, and aftershock analysis, which all

depend on robust and well-characterized source models.

In Chapter 2, we explore the complexity in the finite-fault slip inversions for the 2010 $M_{\mathrm{w}}$ 8.8 Maule, Chile earthquake with joint use of geodetic and tsunami observations. Previously published models based on different types of datasets feature large discrepancies in the locations of the peak slip and slip near the trench, even though, in this case, the trench-to-coast distance is evidently shorter than in Japan. Using the Bayesian formulation, we aim to understand the complementarity and respective roles of tsunami and geodetic data in inferring the final joint models and the significance of model prediction uncertainty associated with each of them, and to eventually better understand the shallow slip process during this event and compare it with the Tohoku-Oki earthquake.

In Chapter 3, we focus on the long-standing enigma of seismic quiescence on several fault segments of the San Andreas Fault in California, and on other mature faults. We resort to dynamic modeling of the interactions between large earthquake rupture, microseismicity, and aseismic slip in fault models with laboratory-derived friction laws, and combine physical insights with observational clues to understand the phenomena of deeper penetration of large earthquakes below the seismogenic zones on these mature faults, with implications for fault rheology and earthquake scaling.

In Chapter 4, we further analyze and explore the connections between geodetic observables of fault locking and the behavior of seismicity at the base of the seismogenic zone. We study how the combinations of geodetic and seismological observations can help constrain the state of the locked-creeping transition on faults and provide insights on the interconnections between inter- and co-seismic fault behavior, which are potentially applicable to the San Andreas and San Jacinto Faults in Southern California.

# Chapter 2

# Bayesian Inference of Coseismic Seafloor Deformation During the 2011 Tohoku-Oki Earthquake with Near-field Tsunami Waveforms

# Abstract

To improve our understanding of the source process during the 2011 $M_{\mathrm{w}}$ 9.0 Tohoku-Oki earthquake, we develop an approach to invert for seafloor deformation using only tsunami waveforms recorded by a variety of near-field instruments. Our Bayesian formulation allows us to explore the maximum resolution of the tsunami data, and to investigate still unresolved questions such as the extent of near-trench seafloor displacement and inferred shallow fault slip. In this analysis, we place special focus on the error structure used in the inverse problem. By focusing purely on seafloor displacements and not on subsurface fault slip, we avoid the need to address common sources of uncertainties, such as fault geometry and spatial variations in elastic structure encountered in conventional fault slip inversions. For the quasi-static problem, we adopt a semi-analytical Bayesian approach to derive closed-form expressions for the posterior solutions of seafloor displacement with minimal *a priori* assumptions; for the kinematic problem, we use an efficient parallel algorithm for sampling the full posterior ensemble of plausible models. Uncertainty and resolution analysis of the posterior enables us to derive representative solutions at appropriate spatial scales. While the semi-analytical approach allows fast source characterization using the first arrivals of tsunami waveforms, the sampling approach on kinematic models provides more robust constraints on the coseismic seafloor deformation field at the inherent resolution of the data. For the 2011 Tohoku earthquake, our models are characterized by large seafloor uplift of

about 2 m at the trench, but even greater seafloor uplift of about 5 m occurring about 50 km landwards of the trench, all consistent with seafloor geodetic measurements within uncertainties. Given the representative structure and fault geometry in the region, simple elastic modeling suggests that the peak of the associated subsurface fault slip coincides with the maximum surface uplift and decreases towards the trench.

## 2.1 Introduction

The 2011 $M_w$ 9.0 Tohoku-Oki earthquake is one of the most destructive and best documented megathrust events. Its location, extent of rupture, and induced tsunamis provide us a unique opportunity to study the mechanisms of a great earthquake.

There are many models addressing the spatio-temporal characteristics of the 2011 Tohoku-Oki earthquake. Static models based solely on dense on-land GPS (Global Positioning System) measurements are best resolved on the landward part of the source (*Iinuma et al.*, 2011; *Ozawa et al.*, 2011; *Miyazaki*, 2011). Kinematic observations, e.g., teleseismic waves and near-field strong motion and high-rate GPS records, provide additional constraints on the temporal evolution of the fault-slip (*Hayes*, 2011; *Ide et al.*, 2011; *Lay*, 2011; *Shao et al.*, 2011; *Yoshida et al.*, 2011; *Wei et al.*, 2012; *Yue and Lay*, 2013). Discrepancies in the distribution of slip between these static and kinematic models, e.g., the location of large slip relative to the hypocenter, partially reflect the difference in the resolution of these datasets, and perhaps to a greater extent the interaction of their inherent resolution with different choices in detailed fault parameterization and approach to regularization or smoothing in the inverse problem. Observations of tsunami waveforms are particularly sensitive to shallow process near the trench, and have been used to directly infer the near-trench fault slip in static (*Maeda et al.*, 2011; *Saito et al.*, 2011) or kinematic models (*Satake et al.*, 2013) with relatively coarse model parameterization. In addition, the emerging marine geodetic techniques which directly measure the deformation of the seafloor have also been used to constrain estimates of fault slip on the shallow part of the fault (*Ito et al.*, 2011; *Kido et al.*, 2011; *Sato et al.*, 2011; *Iinuma et al.*, 2012). The complementary resolutions of different data types motivate studies based on joint inversions of multiple datasets, including the

static and/or kinematic data (*Ammon et al.*, 2011; *Hayes*, 2011; *Koketsu et al.*, 2011; *Simons et al.*, 2011; *Yokota et al.*, 2011; *Romano et al.*, 2012, 2014; *Wei et al.*, 2012; *Yue and Lay*, 2013; *Bletery et al.*, 2014; *Minson et al.*, 2014).

The joint inversions produce several consistent large-scale features, including large-amplitude fault slip updip of the hypocenter that reaches the trench. However, these models still disagree in ways that have important implications for fault mechanics and source physics. For example, they differ in the inferred location and thus the depth of peak fault slip and the profile of near-trench seafloor deformation. Here, we are particularly concerned with the range of source models that can be resolved by the tsunami data within the uncertainty of seafloor geodetic measurements. These questions remain unresolved, with important implications for hazard analyses as well as on follow-up studies such as calculations of stress interactions, postseismic afterslip, and bulk relaxation near the trench.

Common challenges impact most finite-fault slip inversions. Assumed fault geometry and elastic structure directly affect the parameterization of the source model and the prediction of surface deformation due to subsurface fault slip. In practice, the fault is often simplified as a surface discretized by rectangular patches with poor representation of the trench geometry, and the structure is approximated as an elastic half space or layered elastic medium. Even when a more realistic 3D model can be constructed (e.g., *Romano et al.*, 2014), it is still difficult to assess how the uncertainties in the assumed geometry and structure propagate into characterizations of the source model. In order to mitigate these issues, we invert only for seafloor deformation field using tsunami waveforms, with a parameterization of the seafloor that honors the curved trench geometry and regional bathymetry. We simulate the nonlinear dispersive tsunami propagation to capture essential physics and to reduce errors in the forward modeling. We still face the challenge that the error structure

adopted in the inversion critically influences our inference. Here, we explicitly consider the model prediction error due to uncertainties in the physics of tsunami propagation, in addition to the relatively insignificant observational error due to imprecise measurements. We adopt a Bayesian formulation of the inverse problem to derive the posterior solutions, from which uncertainty and resolution are readily assessed. Since this approach does not explicitly involve fault slip, the impact of other processes, e.g., submarine landslides, are in principle included. Our efforts to decouple the tsunami excitation problem from the finite-fault slip inversions and to explore the error structure and resolution of tsunami waveforms are the first step toward a more complete and consistent integration with other types of datasets and other sources of uncertainty (e.g., elastic properties).

In the following sections, we begin with the tsunami observations for the 2011 Tohoku-Oki earthquake, our parameterization of the seafloor deformation field, and forward modeling of tsunami excitation and propagation. We then derive posterior estimates for the seafloor deformation model through a Bayesian formulation of the least-square inverse problem using both semi-analytical and sampling approaches for the quasi-static and kinematic problems, respectively. We also propose different approaches to accounting for model prediction error through a variance-covariance matrix ($\mathbf{C}_\mathrm{p}$) and ways to apply posterior averaging and analyze posterior uncertainty and resolution. Following this discussion, we consider synthetic scenarios to assess the resolution of data and to gain intuitive understanding of the effect of source kinematics, error models, and inaccuracy in the Green's function (GF) on posterior solutions. Following the discussion of the synthetics, we use the observed tsunami waveforms during the 2011 Tohoku-Oki earthquake to derive representative solutions with associated uncertainty and spatial resolution. Finally, we discuss the inherent resolution of the observed tsunami data, the advantages of our approach and the validity of its assump-

tions, implications for coseismic seafloor deformation and fault slip near the trench, and the value of a probabilistic view for source models.

## 2.2 Tsunami observations and modeling

### 2.2.1 Observations of the 2011 Tohoku-Oki earthquake induced tsunami

The tsunami generated by the 2011 Tohoku-Oki earthquake was observed by a variety of modern seafloor and ocean surface instruments, making the event unique for the diverse, comprehensive, and high-quality available tsunami records. Near the source region, ocean bottom pressure gauges, e.g., TM1 and TM2 in *Maeda et al.* (2011), recorded the earliest arrivals and the largest amplitude of the traveling tsunami waves. Closer to the coast, these waves were also recorded by cable pressure gauges (e.g, `www.jamstec.go.jp/scdc/top_e.html`) on the seafloor and GPS gauges (NOWPHAS, `nowphas.mlit.go.jp/index_eng.html`), which are tethered to the seafloor and record the water height. Coastal water gauges and tide gauges record these incoming tsunami waves and interactions of the tsunami with local features. In the open ocean, the long-wave tsunamis are recorded by the DART® (Deep-ocean Assessment and Reporting of Tsunamis) tsunameters in the Pacific. The distribution of these near-field stations is shown in Fig. 2.1A.

For our inversions, we select waveform data from two ocean bottom pressure gauges (TM1 and TM2), six GPS gauges (GB802, GB804, GB803, GB801, GB806, and GB807), two cable pressure gauges (KPG1 and KPG2) and three DART tsunameters (D21418, D21401, and D21413), based on their azimuthal distribution and data quality, and avoid stations with shallow water depth and/or waveform complexity due to coastal reflections. While DART tsunameters have time-averaged measurements every minute, other recordings

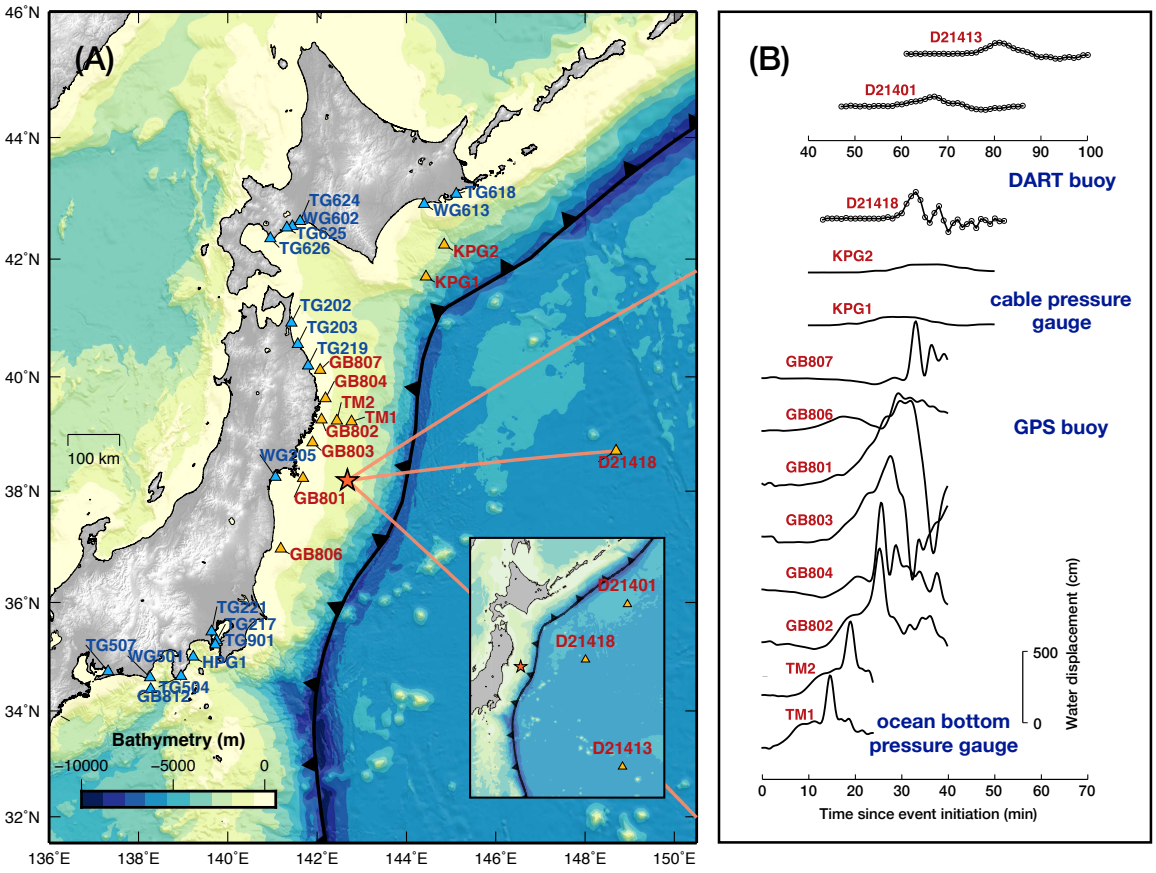


Figure 2.1: *Source region and tsunami records for the 2011 Tohoku-Oki earthquake.* (A) The distribution of stations that recorded the tsunami generated by the earthquake. Tsunami waveforms from stations in red are used in the inversion, as shown in (B), and those from stations in blue are not. Event hypocenter is indicated by the red star. (B) Tsunami waveforms recorded by different types of instruments, including cable pressure gauges, GPS gauges, ocean bottom pressure gauges, and open-ocean DART. Waveforms at the DART stations have a sampling rate of 1 min, and other waveforms are low-pass-filtered at 15 seconds.

have higher sampling rates at 5 seconds. DART records, lowpass-filtered at 2 minutes, and other waveforms at 60 seconds, are shown in Fig. 2.1B (the original and filtered waveforms in Fig 2.18). All waveforms are offset to start at zero displacement at the initiation time of the earthquake. We use the 30-40 minutes of each waveform that include only the first arrivals, thereby avoiding complex wave interactions with coastal reflections in later waveforms. These recordings form a unique dataset in the near field of the source with good azimuthal coverage.

### 2.2.2 Model parameterization of seafloor deformation and tsunami excitation

We parameterize our model of the seafloor deformation field (positive values for effective uplift and negative for effective subsidence) without explicit consideration of the underlying causal physical process, as illustrated in Fig. 2.2A. We consider an area of the seafloor which spans from the coastline to a limited distance seaward of the trench. We then discretize each side of the trench into a triangulated surface with an unstructured grid, using split nodes on the trench where the two meshes meet. From the triangulated meshes we construct overlapping piece-wise linear (tent) functions centered on each node, including full-tents for the interior nodes ($S_i$) and half-tents for boundary nodes, including those on the trench ($S_j$). Following *Geist and Dmowska* (1999), we then apply a spatial filter $1/\tanh(kh)$ to the source to reduce short-wavelength features that would normally be attenuated by the water layer (*Kajiura*, 1981) (the effect of such attenuation on the resultant waveform GFs is shown in Fig. 2.20), and then renormalize all the smoothed sources to unit peak uplift for use in the forward modeling.

On the coastal boundary, GPS measurements of vertical offset are interpolated and im-

posed on the nodes (*Simons et al.*, 2011). Offshore nodes on the boundary of the mesh are set to zero and are thus assumed to be beyond the region of significant seafloor deformation. We do not impose values on nodes at the trench, so that nonzero uplift at the trench is allowed. Such a parameterization has several advantages relative to a conventional quadrilateral based parameterization: (1) The triangulated surface honors the curved shape of the trench line; (2) When compared to a piece-wise constant parameterization, the smoothed tent function is a physically realistic representation of the source of tsunami excitation with the advantage of being numerically stable in the wave propagation model; (3) The smoothed half-tent function still allows relatively sharp deformation features at the trench.

Seafloor uplift or subsidence during the earthquake occurs mainly as a result of slip on the fault. In some cases, local triggered submarine landslides can also act as tsunami sources (e.g., *Tappin et al.*, 2014). Due to the shallow water depth and relative incompressibility of water, tsunami excitation occurs almost instantaneously relative to the timing of seafloor deformation. Furthermore, if we only consider larger-scale process of the earthquake rupture, the process from fault slip to seafloor deformation and tsunami excitation could also be assumed as instantaneous due to the fast propagation of seismic waves through the overriding plate to the seafloor. The last argument and perhaps the foremost assumption for treating tsunami excitation as a quasi-static process (instantaneous occurrence with rupture velocity $V_r = \infty$) is that the earthquake rupture speed ($\sim$ 2 km/s) is much faster than the propagation speed of gravity waves as the tsunami ($\sim$200 m/s for water of 4 km depth). The quasi-static assumption is adopted in most studies of megathrust earthquake inversions incorporating tsunami data (e.g., *Lorito et al.*, 2010, 2011, for the 2004 Sumatra-Andaman and 2010 Maule earthquake, respectively), but is challenged in the presence of high-quality near-field data for the Tohoku-Oki earthquake (*Satake et al.*, 2013; *Hossen et al.*, 2015), in

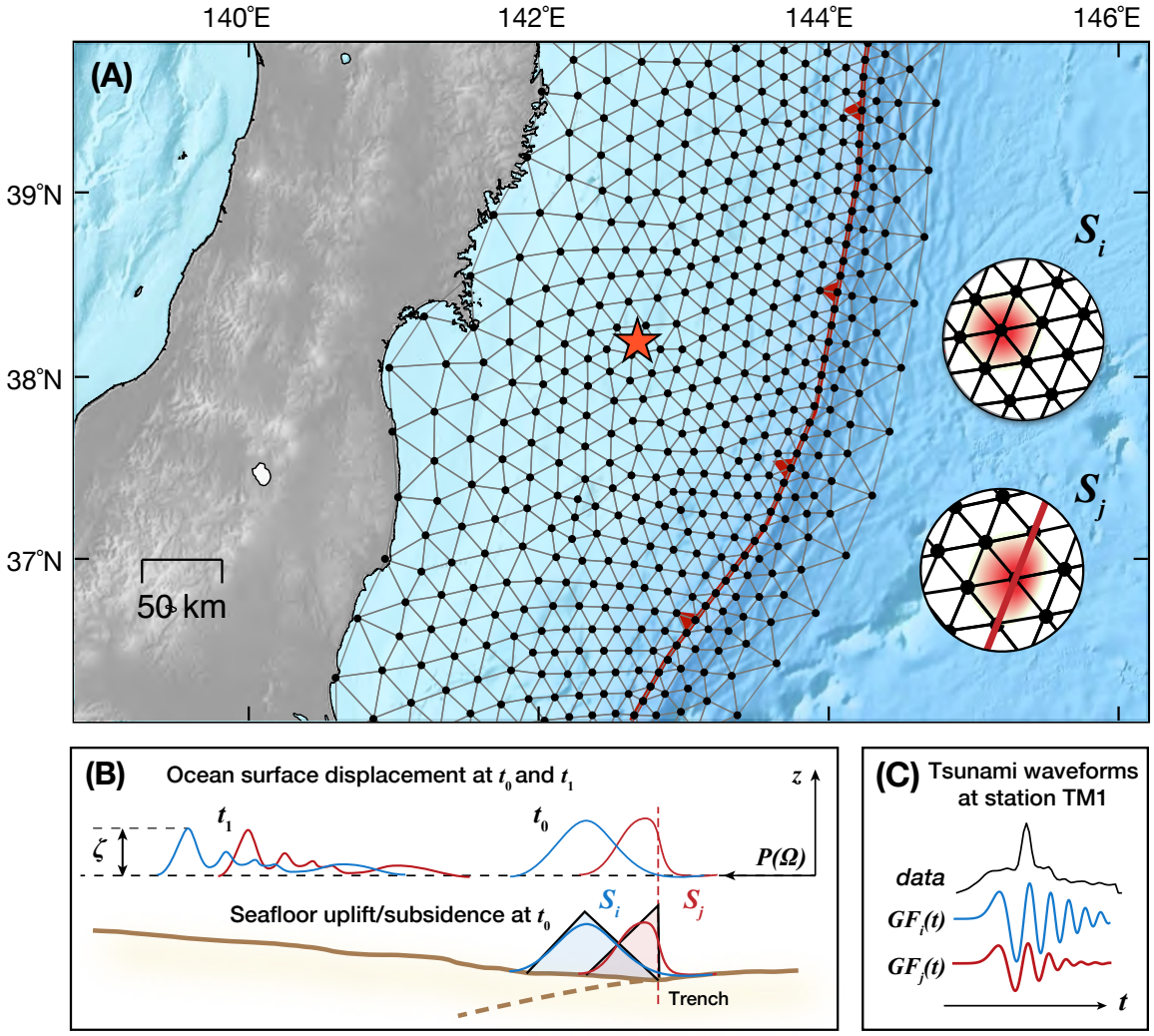


Figure 2.2: *Parameterization of the seafloor deformation and forward modeling of tsunami excitation and propagation.* (A) Spatially smooth unit seafloor displacement (positive for uplift and negative for subsidence) derived from piece-wise linear tent ($S_i$) or half-tent ($S_j$) functions. (B) Ocean surface is disturbed with water height $\zeta$ at time $t_0$ as a result of seafloor deformation, which is typically, but not exclusively, due to slip on the fault. The disturbed ocean water volume propagates to a distance away from the source with frequency dispersion at time $t_1$. The wave propagation is governed by non-linear non-hydrostatic water equations. (C) Tsunami waveforms due to the unit source, i.e., the Green's function $G_i(t)$, recorded at station TM1.

spite of the short duration and compact size of the event, which is usually used to justify the quasi-static treatment. Here we consider both the quasi-static and kinematic formulations.

### 2.2.3 Forward modeling of the tsunami propagation

Numerical methods based on linear or nonlinear shallow water wave equations (e.g., COMCOT, *Liu et al.*, 1995) are generally effective and computationally efficient in simulating tsunami waveforms in the open ocean, as are recorded at DART stations. However, it is more challenging to simulate tsunami propagation in the near-source and coastal regions with shallower water depth. Nonlinear effects become increasingly important, and we can no longer neglect finite wave amplitude, ocean stratification, Coriolis forces, and bottom friction. The assumption of long waves in the shallow water equation can break down, requiring a more appropriate Boussinesq type formulation (*Peregrine*, 1967) or even fully hydrodynamic simulations. Frequency dispersion is also an important characteristic of the tsunami propagation process. Even in the long-wave (long period) limit in the open ocean, far-field tsunami dispersion has been recognized to play an important role in delayed travel times and responsible for the initial reversed polarity in many waveforms observed during recent large earthquakes, including the 2011 Tohoku-Oki event (*Tsai et al.*, 2013; *Watada*, 2013; *Watada et al.*, 2014). These dispersion effects can be included numerically (*Allgeyer and Cummins*, 2014) or empirically (*Yue et al.*, 2014). Dispersion also occurs in the short wave (short period) limit and can produce features not captured in simplified waveform modeling.

To model the tsunami propagation, we use NEOWAVE (Non-hydrostatic Evolution of Ocean WAVE, *Yamazaki et al.*, 2009, 2011), a methodology capable of simulating nonlinear dispersive tsunami propagation. For the simulation, we use the J-EGG500 500-

meter bathymetry (`http://www.jodc.go.jp/data_set/jodc/jegg_intro.html`) for near-field stations and ETOPO1 bathymetry (*Amante and Eakins*, 2009) for DART. In both cases, we use a grid spacing of 500 m. We also consider the uncertainty in the modeling of tsunami propagation associated with different assumptions with respect to dispersion. In Appendix A, we summarize the variability of frequency dispersion relations for different tsunami problems, as they will be useful when we consider modeling uncertainties (Section 2.3.4).

For the quasi-static problem, we assume that seafloor deformation and tsunami excitation occur instantaneously over the entire source region, with no time delay beween sources. For the kinematic problem, we consider time-dependent seafloor displacement by assuming a spatially variable local propagation velocity governed by an Eikonal equation:

$$|\nabla t_0(x,y)| = 1/v_{\mathrm{r}}(x,y), \tag{2.1}$$

where $t_0$ is the initiation time of seafloor deformation at location $(x,y)$ and equals 0 at the epicenter location, and $v_{\mathrm{r}}$ is the velocity of the deformation front corresponding to the apparent rupture velocity of the earthquake, which we call the displacement propagation velocity for simplicity. We assume a triangular function with a half-width of 30 sec for the displacement rate at each source, and divide the entire event duration into 8 time windows of 30 sec each. For a given distribution of non-uniform $v_{\mathrm{r}}$, we solve for $t_0$ in Eq. 2.1 on the triangular mesh using the Fast Iterative Method on GPU (Graphics Processing Unit) (*Fu et al.*, 2011), and the initiation time of each source of displacement is assigned to be the beginning of the corresponding time window for $t_0$.

We simulate tsunami waveforms due to each unit uplift source, as recorded at a given

station. Synthetic waveforms are generated as a linear combinations of these Green's functions without or with a time shift for quasi-static and kinematic problems, respectively (Fig. 2.2B-C). Both observed and simulated waveforms are offset to zero at the origin time. The linearity of the forward problem is commonly assumed in source inversions of tsunami waveforms (*Satake and Tanioka*, 1999), and is generally valid for recordings some distance away from the coast. Thus in matrix form we have:

$$\mathbf{d} = [H_1(t_1^{\mathrm{s}}), ..., H_1(t_1^{\mathrm{e}}), ..., H_N(t_N^{\mathrm{s}}), ..., H_N(t_N^{\mathrm{e}})]^T$$

$$\mathbf{m} = \left[U_1, U_2, ..., U_M\right]$$

$$\mathbf{G} = \begin{bmatrix} G_{1,1}(t_1^{\mathrm{s}}+T_1) & \cdots & G_{1,2}(t_1^{\mathrm{s}}+T_2) & \cdots & G_{1,M}(t_1^{\mathrm{e}}+T_M) \\ \vdots & \ddots & \vdots & & \vdots \\ G_{1,1}(t_1^{\mathrm{e}}+T_1) & \cdots & G_{1,2}(t_1^{\mathrm{e}}+T_2) & \cdots & G_{1,M}(t_1^{\mathrm{e}}+T_M) \\ \vdots & & \vdots & \ddots & \vdots \\ G_{N,1}(t_N^{\mathrm{e}}+T_1) & \cdots & G_{N,2}(t_N^{\mathrm{e}}+T_2) & \cdots & G_{N,M}(t_N^{\mathrm{e}}+T_M) \end{bmatrix},$$

where the data vector $\mathbf{d}$ consists of concatenated records from $N$ stations with $H_i(t)$ for respective time windows $[t_i^{\mathrm{s}}, t_i^{\mathrm{e}}]$ $(i = 1, ..., N)$ (superscripts $s$ and $e$ indicate the start and the end of the time series, respectively), with time shift $T_j$ $(j = 1, .., M)$ corresponding to different sources, the vector $\mathbf{m}$ consists of $M$ seafloor uplift/subsidence sources $U_k$ $(k = 1, ..., M)$, and $\mathbf{G}$ is the Green's function matrix, containing Green's function $G_{i,j}(t)$ between station $i$ and source $j$. The quasi-static problem with $T_i = 0$ is linear with respect to the total model parameter vector $\boldsymbol{\theta}$ $(\boldsymbol{\theta} = \mathbf{m})$. Even though the kinematic problem is nonlinear with respect to the model $\boldsymbol{\theta} = [\mathbf{m}, \mathbf{v_r}]$ which includes displacement propagation velocity as additional parameters, it can be reformulated as a linear problem of $\mathbf{m}$ for a given set

of time shifts, which has computational advantages. For both quasi-static and kinematic problems, the predicted data is $\mathbf{d}_{\text{pred}} = \mathbf{G}(\boldsymbol{\theta}) = \mathbf{G} \cdot \mathbf{m}$.

## 2.3 Bayesian inference of seafloor deformation model

### 2.3.1 Bayesian formulation of the inverse problem

We adopt the Bayesian formulation of the inverse problem to explore the parameter space of the model constrained by the data and our prior knowledge, as expressed in Bayes theorem (*Bayes and Price*, 1763):

$$P(\boldsymbol{\theta}|\mathbf{d}) \propto P(\mathbf{d}|\boldsymbol{\theta})P(\boldsymbol{\theta}), \tag{2.2}$$

where the posterior probability distribution, $P(\boldsymbol{\theta}|\mathbf{d})$, is proportional to the product of the data likelihood $P(\mathbf{d}|\boldsymbol{\theta})$, a measure of how well the model $\boldsymbol{\theta}$ predicts the observed data $\mathbf{d}$, and the prior probability distribution $P(\boldsymbol{\theta})$ that reflects *a priori* information on model parameters.

Assuming normal (Gaussian) distributions for all uncertainties in the problem, which is justifiable by the principle of maximum entropy (e.g., *Jaynes*, 2003; *Beck*, 2010), the data likelihood is expressed as:

$$P(\mathbf{d}|\boldsymbol{\theta}) \propto \exp\big[-(\mathbf{G}(\boldsymbol{\theta}) - \mathbf{d})^T \mathbf{C}_{\boldsymbol{\chi}}^{-1} (\mathbf{G}(\boldsymbol{\theta}) - \mathbf{d})\big], \tag{2.3}$$

where the total error variance-covariance matrix $\mathbf{C}_{\boldsymbol{\chi}}$ is simply a sum $\mathbf{C}_{\text{d}} + \mathbf{C}_{\text{p}}$, where $\mathbf{C}_{\text{d}}$ is associated with the observational error due to imprecise measurements, and $\mathbf{C}_{\text{p}}$ is associated with the model prediction error due to imperfect forward modeling (*Tarantola*, 2005; *Minson et al.*, 2014; *Duputel et al.*, 2014). While $\mathbf{C}_{\text{d}}$ is often well-known and accounted for, $\mathbf{C}_{\text{p}}$

is usually ignored or underestimated. For large-scale problems, the variances of $\mathbf{C}_\mathrm{p}$ can overwhelm those of $\mathbf{C}_\mathrm{d}$ and may contain significant spatial and/or temporal correlations.

### 2.3.2 Semi-analytical approach for the quasi-static problem

For the seafloor deformation problem, uplift (positive values) and subsidence (negative values) are both possible and equally likely. Therefore it is reasonable to assume a normal prior:

$$P(\mathbf{m}) \propto \exp\big[-(\mathbf{m}-\mathbf{m}_0)^T\mathbf{C}_\mathbf{m}^{-1}(\mathbf{m}-\mathbf{m}_0)\big], \tag{2.4}$$

where $\mathbf{m}_0$ is a prior mean model, chosen as $\mathbf{0}$, suggesting a preference toward no deformation in the absence of data, and $\mathbf{C_m}$ is the prior model covariance matrix, and could be a diagonal matrix with uniform variance if we assume constant and uncorrelated uncertainty for and no correlation between all model parameters. Increasing the variance in $\mathbf{C_m}$ results in a less informative prior.

Combining Eq. 2.4 with Eq. 2.3, the posterior distribution is given as:

$$P(\mathbf{m}|\mathbf{d}) \propto \exp\big[-(\mathbf{G}(\mathbf{m})-\mathbf{d})^T{\mathbf{C}_\chi}^{-1}(\mathbf{G}(\mathbf{m})-\mathbf{d})-(\mathbf{m}-\mathbf{m}_0)^T\mathbf{C}_\mathbf{m}^{-1}(\mathbf{m}-\mathbf{m}_0)\big] \tag{2.5}$$

$$\propto \exp\big[-(\mathbf{m}-\tilde{\mathbf{m}})^T\tilde{\mathbf{C}}_\mathbf{m}^{-1}(\mathbf{m}-\tilde{\mathbf{m}})\big], \tag{2.6}$$

where $\tilde{\mathbf{m}}$ is the posterior mean model, equivalent to the maximum *a posteriori* (MAP) model in this case, and $\tilde{\mathbf{C}}_\mathbf{m}$ is the posterior model covariance matrix, with the following expressions (*Tarantola*, 2005, Chapter 3):

$$\tilde{\mathbf{m}} = (\mathbf{G}^T\mathbf{C}_\chi^{-1}\mathbf{G}+{\mathbf{C}_\mathbf{m}}^{-1})^{-1}(\mathbf{G}^T\mathbf{C}_\chi^{-1}\mathbf{d}+\mathbf{C}_\mathbf{m}^{-1}\mathbf{m}_0) \tag{2.7}$$

$$\tilde{\mathbf{C}}_\mathbf{m} = (\mathbf{G}^T\mathbf{C}_\chi^{-1}\mathbf{G}+{\mathbf{C}_\mathbf{m}}^{-1})^{-1}. \tag{2.8}$$

Compared with the traditional optimization approach, the expression for the Bayesian posterior mean model (Eq. 2.8) is equivalent to the maximum likelihood estimate (MLE) in the (weighted) damped least-square problem, with a regularization term that reduces the model size (*Aster et al.*, 2013, Chapter 4). In the least-square case, the conventional least-square optimization approach is a special case of the Bayesian approach.

### 2.3.3 Sampling approach for the kinematic problem

In the case of a non-linear forward model, we do not have an analytic solution and must rely on sampling approaches to estimate solutions to the inverse problem. Sampling of the Bayesian posterior in high dimensional space is computationally demanding. Here we adopt the CATMIP (Cascading Adaptive Tempered Metropolis In Parallel) algorithm (*Minson et al.*, 2013), based on the Transitional Markov chain Monte Carlo, which makes it possible to sample hundreds of model parameters efficiently with reasonable computational resources. We use the AlTar software suite, which is a reimplementation of CATMIP for hybrid CPU-GPU platforms. The CATMIP algorithm and AlTar software have previously been successfully applied to problems of finite-fault earthquake slip (*Simons et al.*, 2011; *Minson et al.*, 2013, 2014; *Duputel et al.*, 2015), interseismic fault creep (*Jolivet et al.*, 2015), and problems in oceanography (*Miller et al.*, 2015).

In our kinematic seafloor problem, the computationally expensive parts of the forward modeling, including Eikonal equation solver on the triangular mesh and the calculations as discussed earlier (Section 2.2.3) are done mostly on GPUs. CATMIP takes a series of tempering steps to sample intermediate PDFs starting from the initial prior distribution toward the final posterior distribution (*Minson et al.*, 2013). For each tempering step, we sample Markov chains on the order of $10^4$ with chain lengths of approximately $10^3$, thus a

total of approximately $10^7$ models to explore in the parameter space.

### 2.3.4 Design of the model prediction error $\mathbf{C_p}$

The error structure of the problem, characterized by the total variance-covariance matrix $\mathbf{C}_\chi$, plays a significant role in determining the data likelihood function and the eventual posterior distribution (Eq. 2.3). $\mathbf{C}_\mathrm{d}$ is usually well known, and is independent of the source. In contrast, $\mathbf{C}_\mathrm{p}$ is generally expected to scale with the source, and is more difficult to characterize and quantify (*Duputel et al.*, 2014). For a large event, such as the Tohoku-Oki earthquake, the nominal observational errors for these tsunami recordings are on the order of several cm, while the model prediction error could be much larger, given that the maximum waveform amplitudes reach several meters. Ignoring, under-estimating, or drastically mischaracterizing $\mathbf{C}_\mathrm{p}$ can lead to over-fitting of data as well as biases in solutions and uncertainty estimates (see Section 2.4). The appropriate formulation of $\mathbf{C}_\mathrm{p}$ is essential and thus designing $\mathbf{C}_\mathrm{p}$ is a major component of this study.

Without regard to the specific forward models, there are several empirical ways to account for modeling errors. An over-simplified approach adopts a diagonal $\mathbf{C}_\mathrm{p}$ with inflated variances but then ignores important temporal correlations of the tsunami waveforms contained in the off-diagonal terms. A more reasonable approach assumes an auto-regressive error model for the time series of tsunami waveforms, resulting in a banded-Toeplitz $\mathbf{C}_\mathrm{p}$ with a characteristic correlation length based on the auto-correlation function of waveform residuals.

We can also consider the unmodeled effects directly from a physical perspective, i.e., consider random perturbations to the physical model. We characterize the predominant uncertainties in the tsunami propagation modeling as deviations in the frequency dispersion

relations. In Fig. 2.3, we illustrate our procedure to devise a physics-based formulation of $\mathbf{C}_\mathrm{p}$ and its comparison with an empirical formulation. The simulated tsunami waveforms based on a reasonable reference model are perturbed based on deviations in the dispersion relations that influence the tsunami propagation between different source-station pairs (Fig. 2.3A, B). Random realizations of perturbations from the reference dispersion relation (based on a linearized analysis for NEOWAVE) follow a log-normal distribution for each period (Fig. 2.3B). We choose the variation for the distribution of these dispersion curves to be 30% around the reference curve, so that these perturbed dispersion relations cover the range of variability in theoretical dispersion curves. The deviation of these perturbed waveforms from the unperturbed ones are used to calculate a variance-covariance matrix. We call this formulation the raypath $\mathbf{C}_\mathrm{p}$ ($\mathbf{C}_\mathrm{p}^\mathrm{RP}$) (Fig. 2.3D), which has the largest variance and covariance near peak waveform amplitudes, and smaller variance associated with the beginning part of the waveforms which the model can generally reproduce well. For comparison, we empirically calculate an alternative estimate for $\mathbf{C}_\mathrm{p}$ from the auto-correlation function of the waveform misfit, which we call the autocorrelation $\mathbf{C}_\mathrm{p}$ ($\mathbf{C}_\mathrm{p}^\mathrm{AC}$) (Fig. 2.3C, F). We assign the variance in $\mathbf{C}_\mathrm{p}^\mathrm{AC}$ for each station as corresponding to 15% of the maximum waveform amplitude based on empirical estimates of the uncertainties. While the correlation length in $\mathbf{C}_\mathrm{p}^\mathrm{AC}$ is generally larger than the $\mathbf{C}_\mathrm{p}^\mathrm{RP}$, and less sensitive to the details of the reference model, the relative uncertainties between data points within given time series and between different stations are unknown. An alternative form of $\mathbf{C}_\mathrm{p}$, which we call the hybrid $\mathbf{C}_\mathrm{p}$ ($\mathbf{C}_\mathrm{p}^\mathrm{HB}$) (Fig. 2.3E), combines the advantages of both formulations: correlation lengths from the empirical approach and relative variance between data points within a given time series and stations from the physics-based approach. We have only considered the intra-station variance and covariance in these $\boldsymbol{C}_\mathrm{p}$, since they should capture the first order features in

the error models. We include a more comprehensive discussion about various formulations of $\mathbf{C}_\mathrm{p}$ in Appendix B, with comparisons shown in Table 2.1 and Fig. 2.21.

### 2.3.5 Posterior uncertainty and resolution analysis

The Bayesian formulation explicitly provides the uncertainty and correlation of model parameters in the posterior solutions. Intuitively, we expect that uncertainties increase as we reduce the assumed patch size in the model, as would anti-correlation between nearby patches. However, we can always explore the PDF of local averages of the posterior solutions to learn the resolution scales inherent to the problem.

For the quasi-static problem, the posterior mean model $\tilde{\mathbf{m}}$ and the posterior model covariance matrix $\tilde{\mathbf{C}}_\mathbf{m}$ are obtained in closed-form expressions, and hence the posterior solutions with *ad hoc* spatial averaging can be derived semi-analytically:

$$\tilde{\mathbf{m}}^{1\mathrm{R}} = \mathbf{S}^{1\mathrm{R}}\tilde{\mathbf{m}} \tag{2.9}$$

$$\tilde{\mathbf{C}}_\mathbf{m}^{1\mathrm{R}} = \mathbf{S}^{1\mathrm{R}}\tilde{\mathbf{C}}_\mathbf{m}(\mathbf{S}^{1\mathrm{R}})^T, \tag{2.10}$$

where $\mathbf{S}^{1\mathrm{R}}$ is a spatial averaging operator that averages each node value with all its nearest "one-ring" (1R) neighboring nodes (defined as nodes connected through only one edge line), and $\tilde{\mathbf{m}}^{1\mathrm{R}}$ and $\tilde{\mathbf{C}}_\mathbf{m}^{1\mathrm{R}}$ are the corresponding posterior mean and covariance matrix in solutions with 1R spatial averaging. Since nodes in the mesh have different effective tent areas (about 1/3 of the total area the tent covers), we choose to weight node values by their effective areas during the spatial averaging, which is incorporated into $\mathbf{S}^{1\mathrm{R}}$ once the parameterization is known. Besides spatially uniform 1R averaging, we can also apply spatial averaging over two-ring (2R) neighboring nodes (defined as nodes connected through two edge lines),

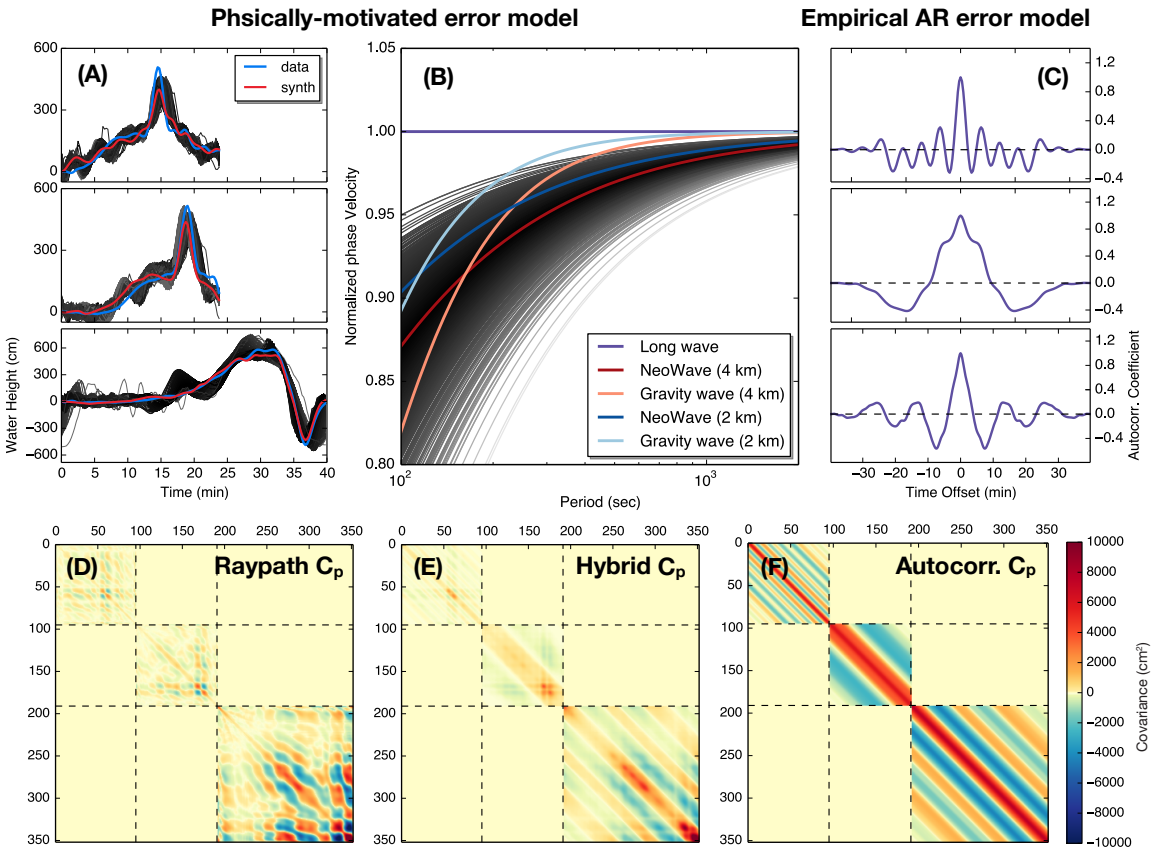


Figure 2.3: *Design of the variance-covariance matrix for the model prediction error* $\mathbf{C}_\mathrm{p}$. (A) Data (blue) and synthetic waveforms (red) predicted from a reference model (red line in panel B), and realizations of perturbed waveforms (black) based on perturbed dispersion curves in (black lines in panel B). (B) Random realizations of frequency dispersion curves (normalized phase velocity as a function of period). (C) Autocorrelation functions for the data misfit shown in (A). (D-F) Three forms of $\mathbf{C}_\mathrm{p}$: (D) $\mathbf{C}_\mathrm{p}^\mathrm{RP}$ based on covariances of the residuals between the perturbed and synthetic waveforms, (E) $\mathbf{C}_\mathrm{p}^\mathrm{HB}$ with empirical correlation lengths in (C) and relative variances obtained in (D), and (F) $\mathbf{C}_\mathrm{p}^\mathrm{AC}$ with empirical correlation lengths and uniform variances.

further reducing model uncertainties at the expense of reduced spatial resolution. For the kinematic problem, we have a posterior ensemble of models, from which $\tilde{\mathbf{m}}$ and $\tilde{\mathbf{C}}_{\mathbf{m}}$ can be computed, and we can either use Eq. 2.9 and 2.10, or apply spatial averaging directly on the sample set of the model ensemble.

For the Gaussian posterior in our case, the uncertainty $E_i$ of model parameter $m_i$ is obtained from the posterior variance-covariance matrix:

$$E_i = \sqrt{(\tilde{\mathbf{C}}_{\mathbf{m}})_{i,i}}. \tag{2.11}$$

The spatial averaging operator (e.g., $\mathbf{S}^{1\mathrm{R}}$) imposes a minimum length scale $D_i^{\mathrm{s}}$, which we choose as an effective circular diameter for the area of spatial averaging:

$$D_i^{\mathrm{s}} = 2\sqrt{(\sum_j A_j + A_i)/\pi}, \tag{2.12}$$

where the summation is over all the neighboring nodes of parameter $m_i$ (based on 1R, 2R or other spatial averaging criteria), and $A_j$ is the effective tent area for node $j$. The impact of averaging $\tilde{\mathbf{m}}$ and $\tilde{\mathbf{C}}_{\mathbf{m}}$ wil be illustrated first using synthetic scenarios.

## 2.4 Synthetic scenarios

Before applying our approach to the real problem, we first explore here how well the tsunami data can resolve different source models in synthetic cases. A popular choice in synthetic source inversion is the checker-board test, as an evaluation of the resolution limit of the problem. However, *Lévěque and Rivera* (1993) demonstrate that checker-board tests do not provide a reliable estimate of resolution, because in some cases, it is possible for small-scale

features to be well-resolved while large-scale features may not be when the latter solution is in the null space. Therefore, we use some potentially realistic scenarios in these synthetic tests, and simply aim to obtain a qualitative assessment of the data resolution and an intuitive understanding of how different assumptions of source kinematics and error models might influence the results.

We consider two synthetic source models both of which are kinematic. The two scenarios differ in the proximity of maximum uplift to the trench (Figs. 2.4A and 2.5A). In both scenarios, we generate synthetic data with dispersive GF, and consider alternatively quasi-static and kinematic inversions with different combinations of $\mathbf{C}_\mathrm{d}$ and $\mathbf{C}_\mathrm{p}$, and dispersive (DSP) and non-dispersive (NDSP) GF, i.e., a total of eight synthetics. Using non-dispersive GF for a dispersive propagation scenario is motivated by the fact that in real cases, we anticipate inaccuracy and limitations of our GF, which makes it necessary to use $\mathbf{C}_\chi$ instead of just $\mathbf{C}_\mathrm{d}$ in large problems. Here we use a $\mathbf{C}_\chi$ that includes $\mathbf{C}_\mathrm{p}^\mathrm{RP}$ based on the perturbation of waveforms using the known reference true model, while for $\mathbf{C}_\mathrm{d}$ we assume 10 cm uncorrelated Gaussian error. We use the entire mesh for the quasi-static problem, while adopting a near-source subset of the seafloor mesh for the kinematic problem, to reduce the number of free parameters and computational demand. We choose a Gaussian prior on the uplift $P(\mathbf{m}) = \mathcal{N}(\mathbf{0}, (10\,\mathrm{m})^2\mathbf{I})$, since we believe that the real seafloor uplift is unlikely to much exceed 10 m based on experience with marine terrace and sea surface uplift during large earthquakes (e.g., *Plafker and Rubin*, 1978; *Meltzner et al.*, 2006), and a uniform prior $P(\mathbf{v}_\mathrm{r}) = \mathcal{U}(0.5\,\mathrm{km/s}, 2.5\,\mathrm{km/s})$ for the additional parameter displacement propagation velocity $\mathbf{v}_\mathrm{r}$ in the kinematic problem. Although previous studies (*Satake et al.*, 2013) suggest that tsunami data are not sensitive to different $\mathbf{v}_\mathrm{r}$ in this range, we allow $\mathbf{v}_\mathrm{r}$ to vary. All kinematic inversions are done with a fixed initiation point, which we assume to be the

hypocenter location of the Tohoku-oki earthquake (*Chu et al.*, 2011).

In Fig. 2.6, we first demonstrate the effect of spatial averaging on the posterior solutions, including the mean value and uncertainty, using the posterior of a synthetic scenario in which a compact source of uplift occurs near the trench. The posterior mean model becomes smoother with the increase in the range of spatial averaging, accompanied by the reduction of error ellipses associated with the parameters highlighted. In principle, we can apply spatially nonuniform adaptive averaging based on desired resolution or criterion on the absolute or relative uncertainty, in order to eliminate null solutions where the model is less constrained and produce representative models useful for geophysical interpretations. In most of our models, we find that 1R spatial averaging is sufficient to reduce uncertainty to acceptable values and produce appropriate resolution for the source region of our interest, so we adopt the uniform 1R spatial averaging in this study. In Figs. 2.4 and 2.5, all posterior solutions are shown after 1R averaging.

From the results of synthetic tests, we find that inversions of quasi-static models with only $\mathbf{C}_\mathrm{d}$ tend to bias the solutions toward more localized and larger uplift with peak value offset in space from the input model (Figs. 2.4B,E and 2.5B,E). Spurious features of subsidence to the south are also observed in these models, and are particularly bad in Fig. 2.5B,E, because source kinematics and the dispersive nature of tsunami both introduce waveform complexity, and ignoring finite displacement propagation velocity would force these additional features into the model in order to fit the waveform, as is also reported by *Hossen et al.* (2015). Such a bias is amplified for the case of a more dispersive tsunami wave excited at the trench (see Fig. 2.20). However, we observe that with the incorporation of more realistic $\mathbf{C}_\chi$ (Figs. 2.4C,F and 2.5C,F), the bias due to the quasi-static assumption is reduced, and the model uncertainties are reasonably increased, so that the resulting model

is more compatible with the true model within uncertainty. In the quasi-static problem, we notice that by using NDSP GFs (Fig. 2.4E,F and 2.5E,F), not only are spurious features worse, but uncertainties are also underestimated more than their counterparts with DSP GF (Fig. 2.4B,C and 2.5B,C), suggesting that an inaccurate GF without an appropriate $\mathbf{C}_\mathrm{p}$ can lead to a biased mean solution and underestimated uncertainties.

Inversions of kinematic models recover the first synthetic scenario well (Fig. 2.4D,G,H,I), due to the spatially non-uniform $\mathbf{v}_\mathrm{r}$. These extra degrees of freedom lead to improved fits to the waveforms, even in cases where non-dispersive GF are used (Fig. 2.4H,I). Uncertainties of model parameters in the kinematic models is smaller than those in quasi-static counterparts, partly because the causality constraint imposed by the deformation front requires that distant regions do not experience deformation and thus reduces the plausible parameter space for the problem. The use of $\mathbf{C}_\mathrm{p}$ yields more realistic estimate of model uncertainties when incorrect GF is used. For the second synthetic scenario, the combinations of $\boldsymbol{C}_\mathrm{d}$ and NDSP GF (Fig. 2.5H) produce a solution with a similar uplift pattern as the one with correct DSP GF (Fig. 2.5D) and yet significant deviations in the inferred deformation fronts. In the cases with $\mathbf{C}_\mathrm{p}$ (Fig. 2.5G,I), short-wavelength uplift (about 20 km) at the trench can not be fully resolved, but the overall long-wavelength pattern could still be retrieved with well-recovered deformation fronts and more realsitic error estimates. Generally, these results show that the tsunami data can indeed resolve features of offshore sources over the length scale of tens of kilometers.

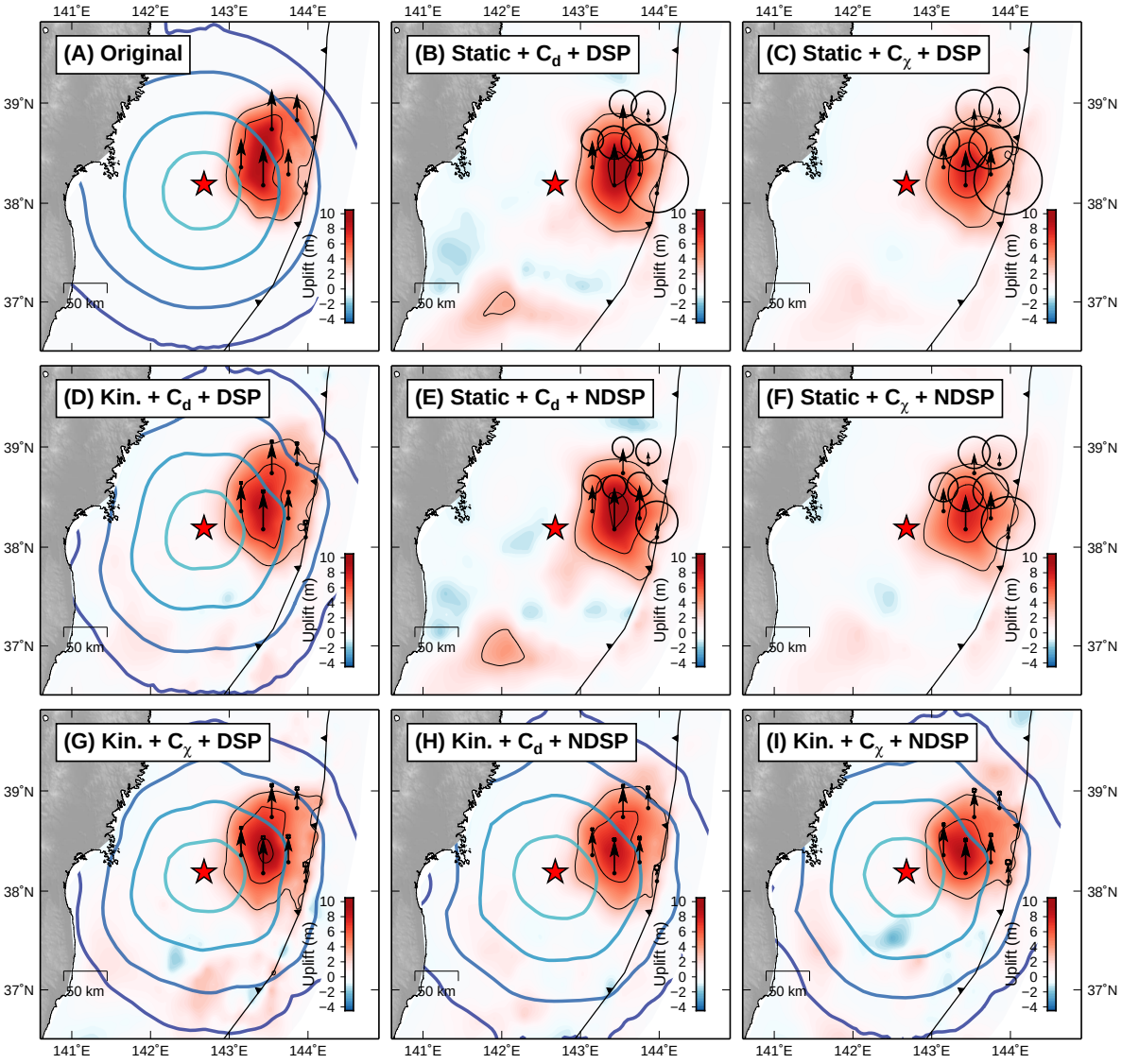


Figure 2.4: *The effect of source kinematics, error structure and inaccuracy in GF on the inversion of a synthetic scenario with maximum uplift away from the trench.* The synthetic data is produced from (A) a kinematic scenario with maximum uplift landward of the trench and dispersive GF. Eight inversions (B-I) are conducted for quasi-static and kinematic scenarios with the combinations of $\mathbf{C}_\mathrm{d}$ or $\mathbf{C}_\chi$, and dispersive (DSP) or non-dispersive (NDSP) GFs. The contours represent inferred kinematic deformation fronts with intervals of 30 sec.

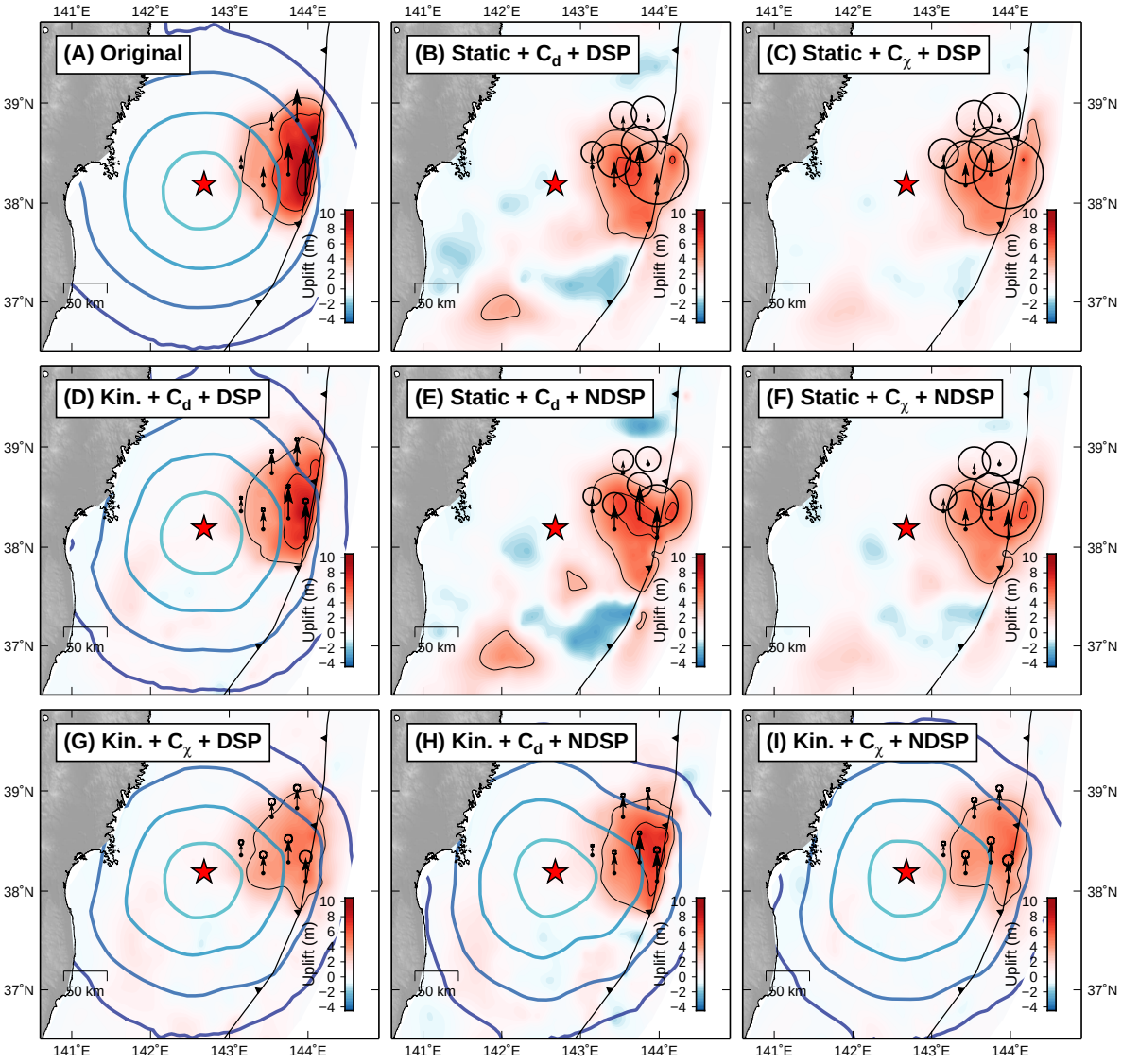


Figure 2.5: *The effect of source kinematics, error structure, and inaccuracy in GF on the inversion of a synthetic scenario with maximum uplift at the trench.* The synthetic data is produced from (A) a kinematic scenario with maximum uplift at the trench and dispersive GF. Eight inversions (B-I) are conducted for quasi-static and kinematic scenarios with the combinations of $\mathbf{C}_\mathrm{d}$ or $\mathbf{C}_\chi$, and dispersive (DSP) or non-dispersive (NDSP) GFs. The contours represent kinematic deformation fronts with intervals of 30 sec.

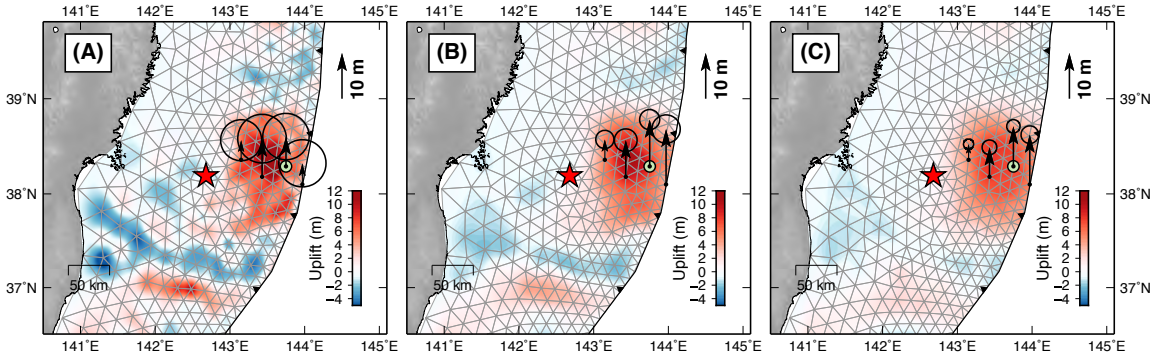


Figure 2.6: *Spatial averaging of posterior solutions and model uncertainties.* Posterior mean models are shown with (A) no spatial averaging and (B) "one-ring" (1R) and (C) "two-ring" (2R) spatial averaging for a synthetic example. The mean values and uncertainties of uplift are plotted as vertical arrows and circles, respectively, for several near-source nodes. The red star indicates the assumed hypocenter of the scenario event.

## 2.5 Applications to the 2011 Tohoku-Oki earthquake

### 2.5.1 Quasi-static seafloor deformation models

We first apply our approach to the quasi-static problem. In Fig. 2.7, we show the uncertainty (Eq. 2.11) and averaging scale (Eq. 2.12) of the quasi-static models inverted from real tsunami waveforms using $\mathbf{C}_{\mathrm{p}}^{\mathrm{HB}}$ as an example. In the case without spatial averaging (Fig. 2.7A), we show the posterior mean model, which is characterized by heterogeneous uplift patterns and mostly large uncertainties beyond 4 m, while the slightly over-parameterized model attempts to resolve length scales less than 20 km. The interpretation of the resultant rough model would be difficult and not meaningful given the uncertainties. With 1R posterior averaging (Fig. 2.7B), the source region in the posterior solutions are now associated with reasonable levels of uncertainty (1-3 m) and resolution scale (30-60 km). Further averaging over 2R nodes (Fig. 2.7C) leads to smaller uncertainty at the expense of increased scale that the data can resolve, which would limit our inference.

We compare the impact of adopting the three different forms of $\mathbf{C}_{\mathrm{p}}$ (discussed in Section 2.3.4) on the inversions of the real observations. In Fig. 2.8, posterior mean models

without *ad hoc* averaging for all three $\mathbf{C}_\mathrm{p}$ are highly heterogeneous with large uncertainties. After 1R averaging, posterior mean models appear smoother, and the difference between $\mathbf{C}_\mathrm{p}^\mathrm{AC}$ and $\mathbf{C}_\mathrm{p}^\mathrm{HB}$ is reduced, while $\mathbf{C}_\mathrm{p}^\mathrm{RP}$ produces larger peak uplift in the mean model. These models are still similar to each other within uncertainties, and they all resolve similar features – the length scale of the uplift and the location of its peak value.

As *a posteriori* validation of our models, we evaluate the posterior data fit as well as prediction to the later part of the tsunami waveforms which are not included in the inversion in Fig. 2.9. We only show results derived with $\mathbf{C}_\mathrm{p}^\mathrm{HB}$. For models without spatial averaging, fit to the data is excellent, and predictions of later waveforms are consistent with the observed ones within the large uncertainty, because regions far from the source are unconstrained by the early part of the waveforms and therefore can produce large variability in late-coming signals. It should be noted that there is likely additional complexity in the later waveforms due to stronger nonlinear effects and coastal reflections unaccounted for in our forward modeling and error models. For models with spatial averaging, the discrepancy between observations and mean of the data fit is increased, but it is still within the uncertainty.

### 2.5.2 Kinematic seafloor deformation models

We obtain the kinematic models of seafloor deformation using CATMIP as discussed in Section 2.3.3. We sample $\sim 10^7$ kinematic models $\boldsymbol{\theta} = [\mathbf{m}, \mathbf{v}_\mathrm{r}]$ per tempering steps with the prior $P(\mathbf{m}) = \mathcal{N}(\mathbf{0}, (10\,\mathrm{m})^2\mathbf{I})$ and $P(\mathbf{v}_\mathrm{r}) = \mathcal{U}(0.5\,\mathrm{km/s}, 2.5\,\mathrm{km/s})$. Since updating $\mathbf{C}_\mathrm{p}$ based on kinematic solutions for each transitional tempering step of CATMIP is computationally too expensive, we only consider the form of hybrid $\mathbf{C}_\mathrm{p}$ for the kinematic problem, which combines the relative variance of raypath $\mathbf{C}_\mathrm{p}$ in the quasi-static model and the empirical

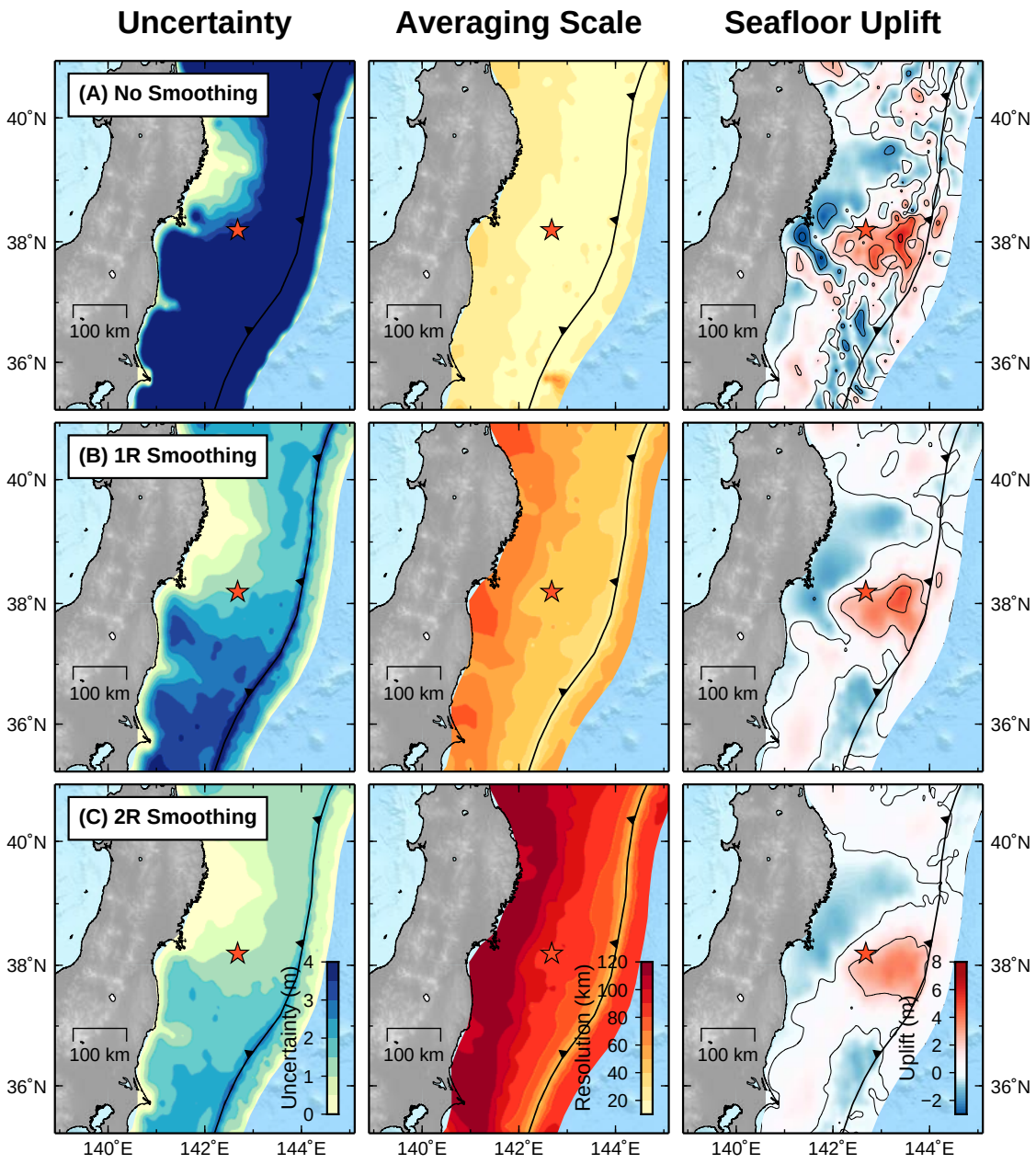


Figure 2.7: *Spatial averaging and uncertainty analysis of the posterior solutions.* The distributions of uncertainty, averaging length, and the associated model are shown in the columns. Posterior solutions are shown in the rows with (A) no spatial averaging, (B) 1R averaging, and (C) 2R averaging.

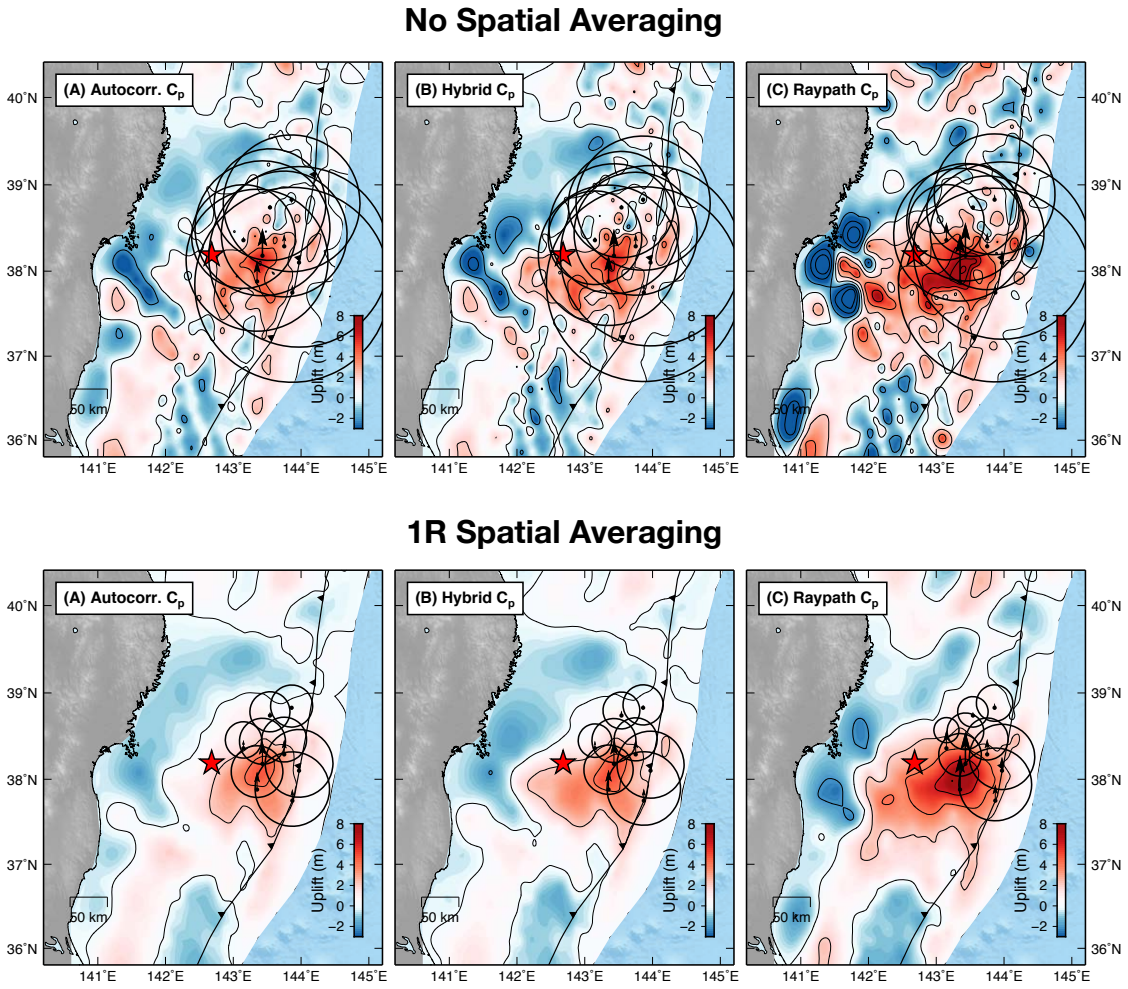


Figure 2.8: *Posterior mean models for the quasi-static problem with different* $\mathbf{C}_\mathrm{p}$. (A) $\mathbf{C}_\mathrm{p}^\mathrm{AC}$, (B) $\mathbf{C}_\mathrm{p}^\mathrm{HB}$, and (C) $\mathbf{C}_\mathrm{p}^\mathrm{RP}$ are used to derive solutions without spatial averaging (top row) and with 1R spatial averaging (bottom row). Mean values and uncertainties of representative model parameters near the source are shown as vertical arrows and circles, respectively. Note that in this case the posterior mean model without averaging is equivalent to the maximum *a posteriori* (MAP) and maximum-likelihood estimate (MLE) models.

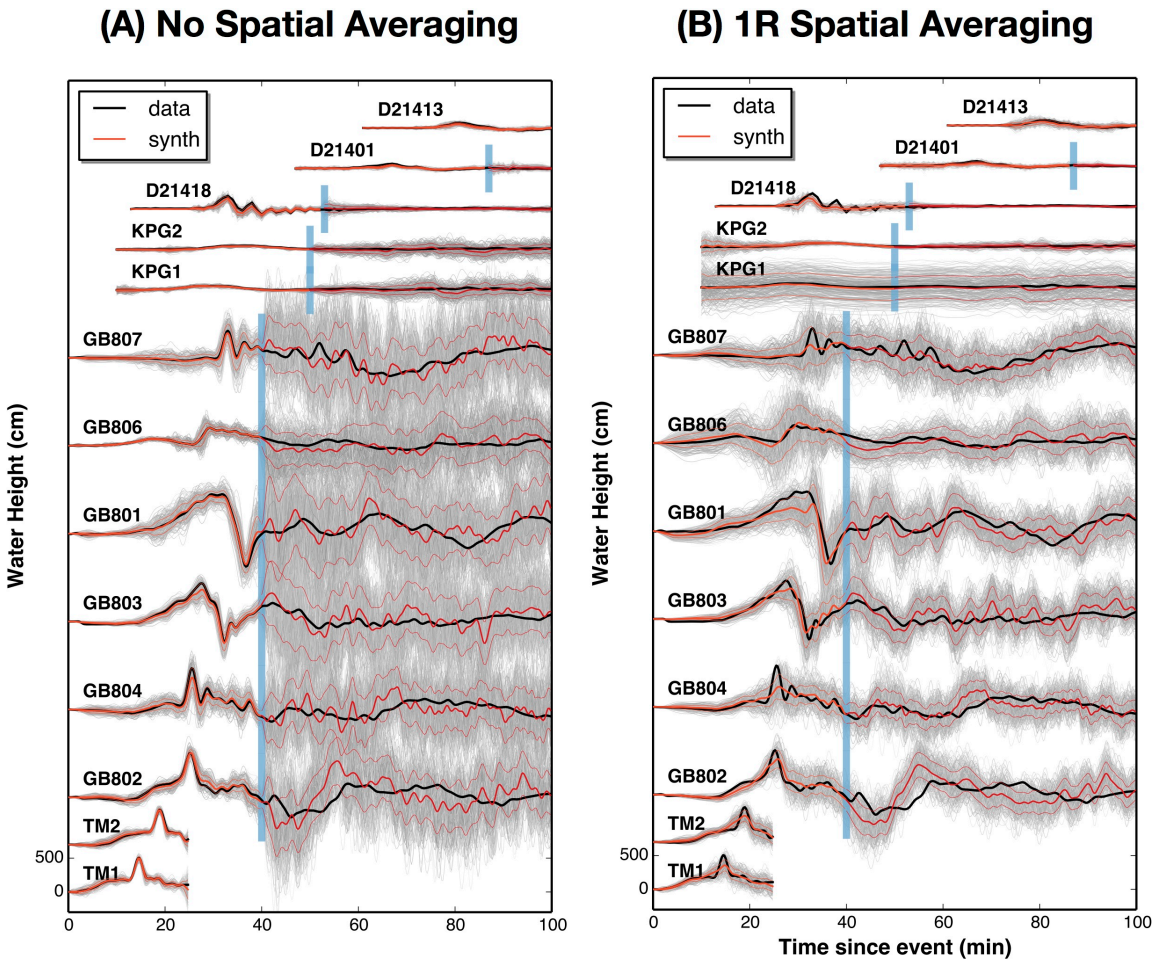


Figure 2.9: *Posterior data fit and prediction of later waveforms for the quasi-static solutions.* Posterior solutions that include $\mathbf{C}_{\mathrm{p}}^{\mathrm{HB}}$ (A) without spatial averaging and (B) with 1R spatial averaging are used for the data fit and prediction. The data is represented by thick black curves, and the waveforms predicted by random models from the posterior solutions are represented by thin gray curves, with their mean values in red. Only waveforms to the left of the blue vertical bars are used in the inversion, while those to the right are only used for *a posteriori* validation.

correlation length in $\mathbf{C}_{\mathrm{p}}^{\mathrm{AC}}$.

The kinematic posterior solutions without spatial averaging and with 1R averaging are shown in Fig. 2.10 and 2.11, respectively. In addition to absolute uncertainty, averaging scale and the posterior mean model, we also show the relative uncertainty, which is defined as the ratio between the absolute uncertainty and the absolute values of the mean model and indicates confidence in the inferred parameter. We note that the most confident model parameter values lie in 1R averaged posterior solutions (Fig. 2.11), which is expected due to the increased averaging scales. In the near-source region, the averaging scale is about 40 km with the uncertainty around 0.6 m. The displacement propagation velocity has a mean value near 1.5 km/s and uncertainty of nearly 0.5 km/s, suggesting that the tsunami data is not very sensitive to the variation of $\mathbf{v}_{\mathrm{r}}$ in this range. Peak seafloor uplift in the representative model occurs near the trench, at similar locations as the quasi-static models (Fig. 2.8), but with slightly reduced amplitude. Further, the spatial pattern of the uplift source is broadened, with uplift to the north between 38.5° and 39.0° N (resolvable given the smaller uncertainty), generally consistent with the findings of *Satake et al.* (2013) that kinematic modeling allows fault slip to extend to the north. This northerly extension is postulated to be responsible for the large run-up events in the Tohoku region. In Fig. 2.12, posterior solutions of the kinematic seafloor models produce reasonable data fit and predictions of later arrivals within uncertainty. In comparison with the static model, uncertainty for the later waveform predictions are reduced due to the incorporation of source kinematics and thus the restricted model space.

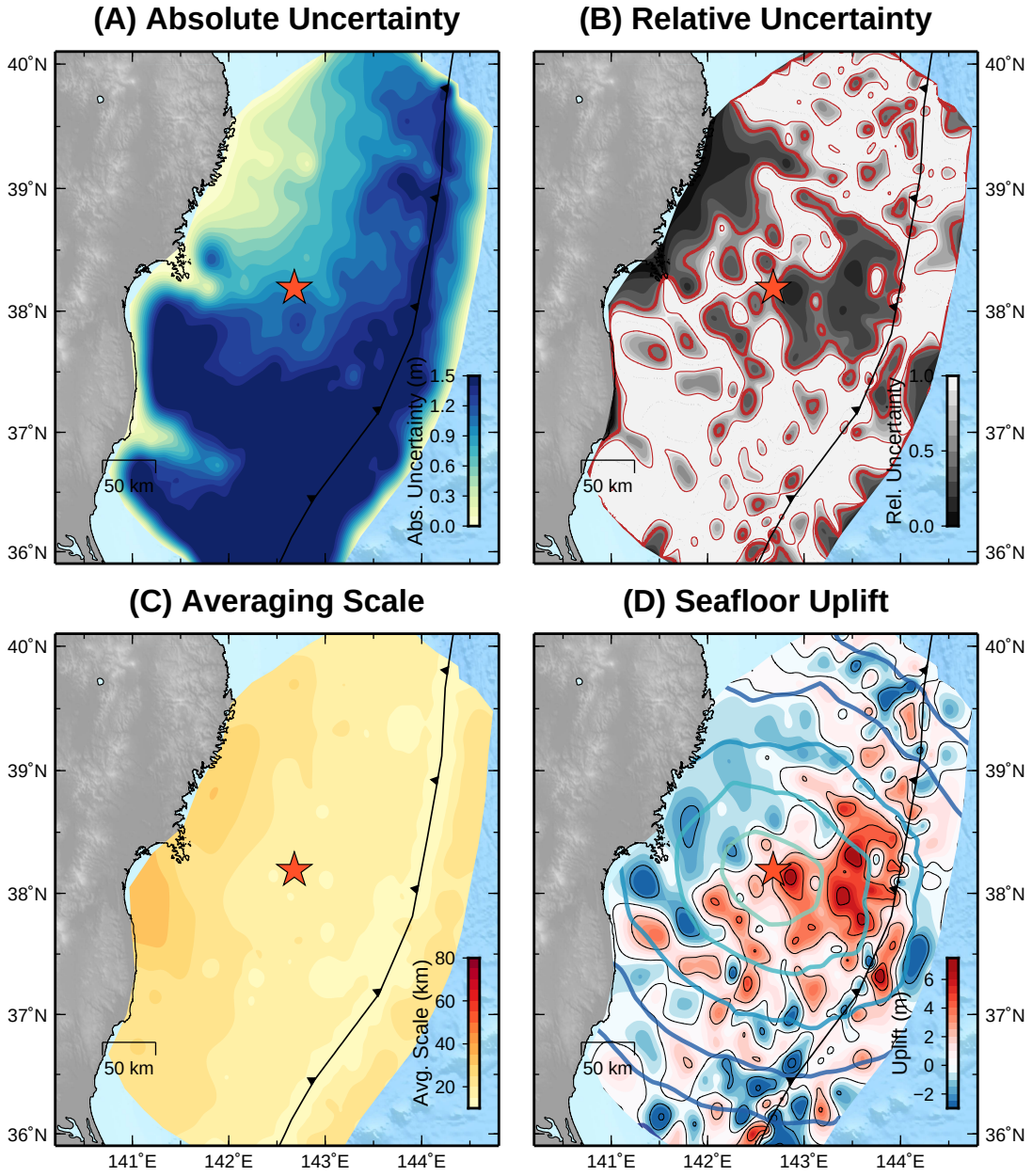


Figure 2.10: *The uncertainty, averaging scale, and original posterior mean models for the kinematic problem.* Absolute uncertainty, relative uncertainty, averaging scale, and 1R-averaged posterior mean models are shown in (A)-(D), respectively. Solutions are derived with $\mathbf{C}_{\mathrm{p}}^{\mathrm{HB}}$. Thick and thin red contour lines in (B) represent relative uncertainty of 0.5 and 1.0. Contours in (D) represent kinematic deformation fronts with intervals of 30 sec.

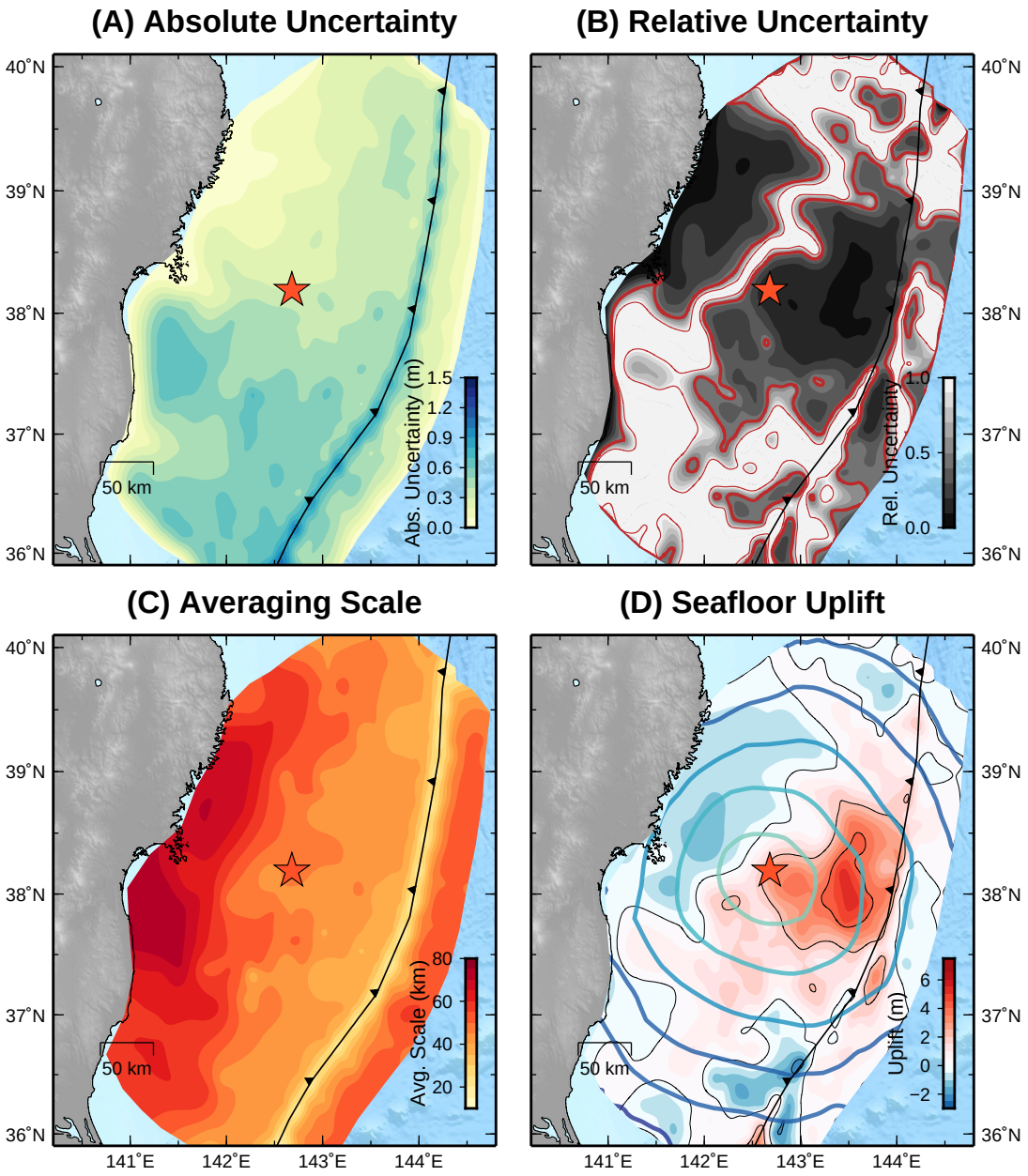


Figure 2.11: *The uncertainty, averaging scale, and 1R-averaged posterior mean models for the kinematic problem.* Plotting conventions follow 2.10.

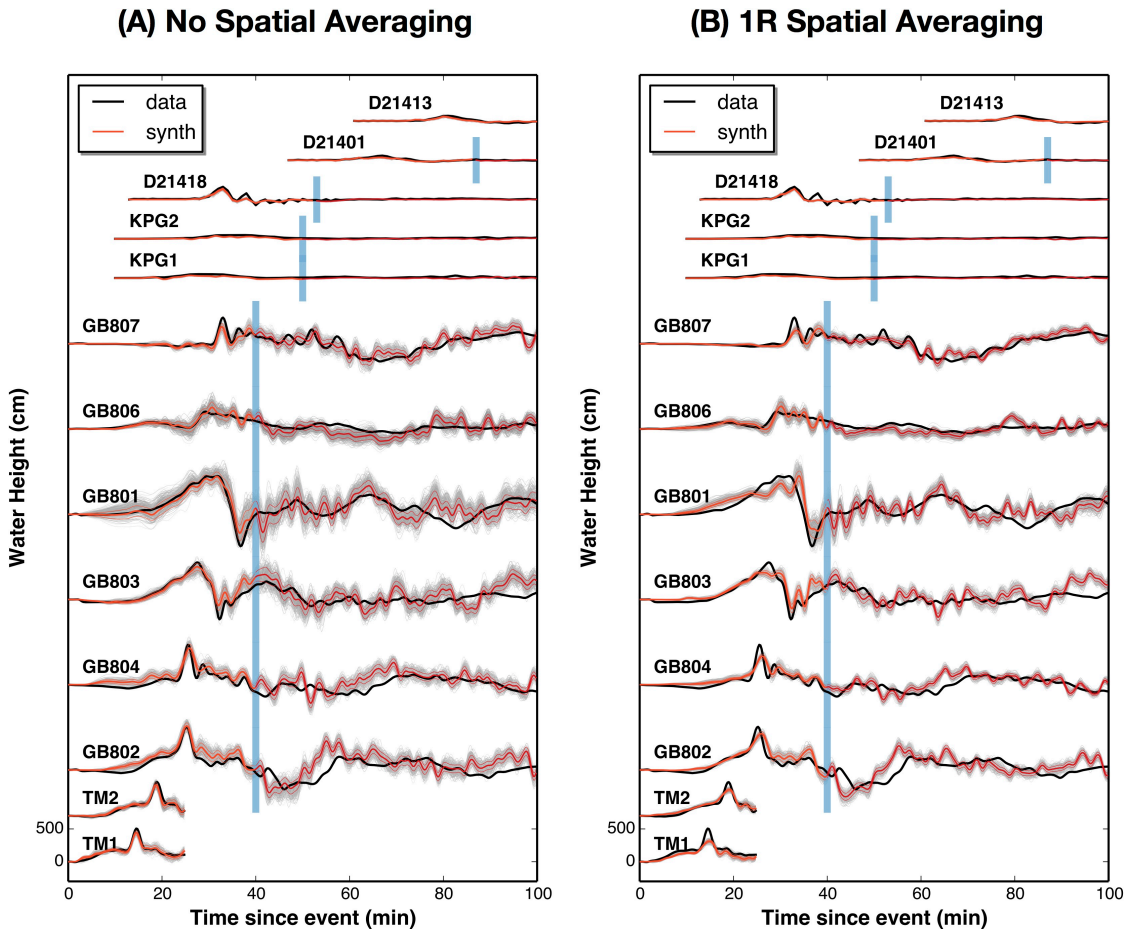


Figure 2.12: *Posterior data fit and prediction of later waveforms for the kinematic solutions.* Posterior solutions that include $\mathbf{C}_{\mathrm{p}}^{\mathrm{HB}}$ (A) without spatial averaging and (B) with 1R spatial averaging are used for the data fit and prediction. Other conventions are the same as Fig. 2.9.

## 2.6 Discussion

### 2.6.1 The resolution of tsunami data

Compared with conventional geodetic or seismological observations, tsunami waveform data provide unique resolving power for deformation near the trench and hence shallow slip on the fault. Understanding the resolution limit is critical for the interpretation of the source process. Attenuation through the water layer (*Kajiura*, 1981) effectively limits the resolution power depending on water depth. As a rule of thumb, the minimum resolution

scale is about three times the water depth (*Geist and Dmowska*, 1999). Furthermore, 2D depth-integrated tsunami modeling methods are less accurate in simulating source features at scales comparable to the water depth. Given the water depth of 7 km at the Japan trench, our parameterization and resolution is limited to a minimum of about 20 km. Because of this limit, smaller-scale features, e.g., due to edge discontinuity in the parameterization, or numerical artifacts, should be filtered when we try to predict tsunami waveforms.

### 2.6.2 Assumptions and advantages of our methodology

Our method to directly parameterize and model seafloor uplift allows us to explicitly consider the error structure of tsunami data alone, avoiding complications from other sources of uncertainties typically associated with finite-fault slip inversions. By focusing on effective seafloor uplift, we implicitly include the additional effective uplift due to the horizontal movement of the steep bathymetric slope (*Tanioka and Satake*, 1996) but ignore the possible effect of the additional horizontal momentum during tsunami excitation, as argued for in some studies (*Song et al.*, 2008b). For the quasi-static problem, the closed-form expression for the Bayesian posterior is computationally very efficient. Given that all parameterizations and Green's functions can be pre-computed for any subduction zone seafloor, this approach can be suitable for rapid characterization of the source.

Both quasi-static and kinematic problems are based on the assumption of a linear forward model. For the Tohoku-Oki earthquake, this assumption generally works well for records taken far offshore, and has been validated in previous studies (e.g., *Melgar and Bock*, 2013; *Satake et al.*, 2013). For the quasi-static problem, the assumptions of instantaneous uplift and infinite rupture velocity might not be ideal in the presence of high-quality data, as suggested by (*Satake et al.*, 2013; *Hossen et al.*, 2015). Indeed, our synthetic tests

in Fig. 2.4B,E and 2.5B,E show bias in quasi-static solutions (without $\mathbf{C}_\mathrm{p}$), with spurious uplift features to the south, similar to the narrow "finger" features described in *Hossen et al.* (2015). However, except for the slightly broader uplift pattern, our kinematic model is not significantly different from the quasi-static models, in particular when we consider the uncertainties of the two models. Both models reveal similar main features including the location and approximate peak value of maximum uplift. We attribute their similarity to the more realistic error models we have adopted, which reduces potential bias in the solution with the quasi-static assumption. Therefore, for events with a compact source like the Tohoku-Oki earthquake, we conclude that the semi-analytical quasi-static approach is generally sufficient for constraining the tsunami source. However, a full kinematic treatment is possibly necessary for events with longer along-strike dimensions. Whether or not explicit consideration of source kinematics strongly influence predictions of coastal inundation and run-up remains to be explored.

### 2.6.3 Seafloor deformation and fault slip near the trench

The extent and style of deformation near the trench and in the accretionary wedge is a critical problem in tsunamigenesis and together with the associated slip on the fault has strong implication for our understanding of fault mechanics and earthquake physics in subduction zones (e.g., *Wang and Hu*, 2006; *Wang and He*, 2008). Prior to the 2011 Tohoku-Oki earthquake, the shallow part was considered to be aseismic, because (1) seismicity is usually at low levels in shallow parts of the fault and (2) the shallow faults are considered to have velocity-strengthening frictional property, which discourages earthquake nucleation (*Scholz*, 2002). In contrast, the 2011 Tohoku-Oki earthquake produced significant slip near the trench, as supported by observations of changes in bathymetry (*Fujiwara et al.*, 2011)

and seismic reflection profiles (*Kodaira et al.*, 2012), as well as inferred in even the earliest slip models (*Simons et al.*, 2011; *Lay*, 2011).

Numerical models can explain the possibility of shallow and large slip by either favorable fault weakening conditions at seismic slip rates (*Noda and Lapusta*, 2013; *Cubas et al.*, 2015), or dynamic inertial effects that enable rupture penetration into the velocity-strengthening regions (*Kozdon and Dunham*, 2013). *Scholz* (2014) proposes that a wrinkle pulse rupture mode on the bi-material interface enables the shallow surge to propagate all the way to the trench. Friction experiments suggest low dynamic friction for fault materials sampled from the fault core, which could facilitate fault failure and earthquake rupture (*Ujiie et al.*, 2013). Furthermore, based on structural studies of common subduction zone megathrusts and shallow thrust faults, *Hubbard et al.* (2015) suggest that coseismic failure of the shallow acretionary wedge could be common.

While coseismic slip undoubtedly reaches the trench, the profiles of seafloor deformation and fault slip near the trench remains unresolved. Numerical models of *Kozdon and Dunham* (2013) find that the profile of displacement depends on the frictional properties of the shallow par to the fault, and could either increase or decrease near the trench. *Ma* (2012) models the elasto-plastic failure of accretionary prism as a critical wedge, and argues that vertical coseismic seafloor displacement should taper down toward the trench in the presence of inelastic bulk deformation.

Our kinematic model, shown in Fig. 2.13A, includes a broad region of uplift far offshore and subsidence near the coast. In Fig. 2.13B, the cross-sectional profile through the maximum uplift and normal to the trench axis shows that approximately 2 m of uplift is required at the trench, while the maximum uplift of 5 m occurs 50 km landward from the trench. Our seafloor deformation model only constrains the total effective uplift, and thus

to compare with seafloor geodetic measurements (*Ito et al.*, 2011; *Kido et al.*, 2011; *Sato et al.*, 2011) we must account for the effect of the horizontal displacements in regions of steep bathymetric slope (*Tanioka and Satake*, 1996). Measurements from *Ito et al.* (2011) only record horizontal displacement for the two stations closest to the trench, and therefore we only compute the contribution to the uplift due to the horizontal components, thereby potentially underestimating the total effective uplift. A direct comparison between the model and these seafloor measurements at coinciding locations is shown in Fig. 2.13C. We note that the resolution could be quite different for the model and the local observations, with the possibility that the seafloor measurements might be capturing smaller-scale processes that tsunami waveforms cannot resolve. Regardless, our model is generally consistent with these measurements within uncertainty.

We further analyze the plausible range of gradients in seafloor uplift, i.e., the tilt, as constrained by our kinematic solutions as shown in Fig. 2.14. We calculate the least-squares best-fitting tilt for 500 random realizations of seafloor uplift profiles generated from the kinematic solutions and conclude that the most plausible seafloor tilt is approximately 0.1 m/km, which leads to an uplift increase of about 5 m over a landward distance of 50 km from the trench.

Our quasi-static models also capture the similar location of maximum uplift and the general trend of the deformation profile, and is consistent with seafloor geodetic measurements, albeit with larger overall uncertainties (Fig. 2.15). These results are in agreement with some previous finite-fault studies based on joint datasets and with the quasi-static assumption of tsunami, such as *Romano et al.* (2012) and *Minson et al.* (2014).

Relating seafloor uplift to fault slip is subject to uncertainties in the fault geometry and elastic structure. In Fig. 2.16 and 2.17, we explore simple 2D elastic models using a

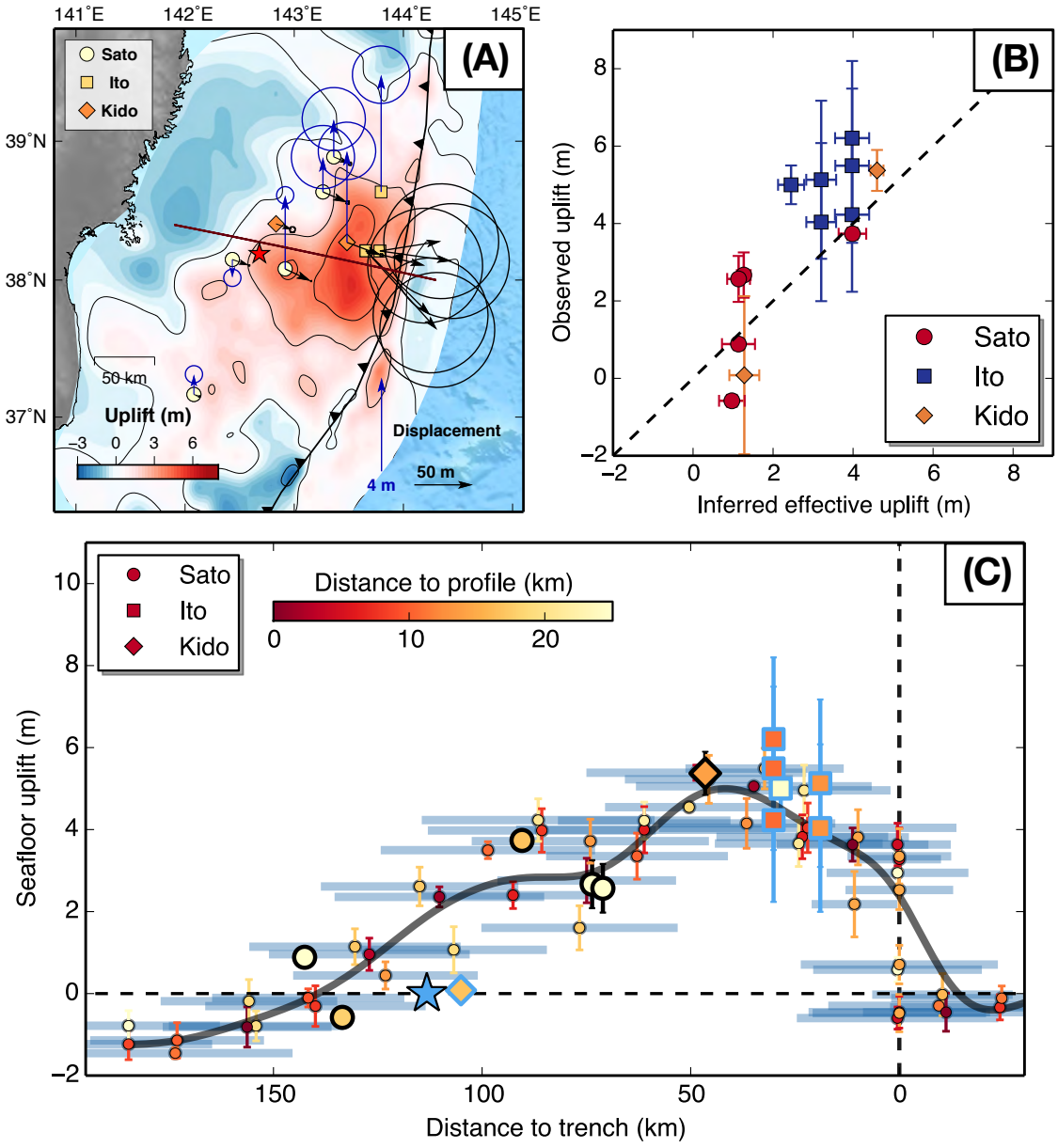


Figure 2.13: *Seafloor deformation near the trench in the kinematic model and comparisons with seafloor geodetic observations.* (A) Our seafloor uplift model and available seafloor geodetic measurements. (B) Comparisons between inverted and observed uplift at coinciding locations and uncertainties associated with both. The dashed line marks where two uplift values match exactly. (C) A cross-section profile of the effective seafloor uplift in the model and available seafloor measurements. The uncertainty of the uplift are shown as vertical error bars, and the effective averaging scale as horizontal error bars. The uplift in both models and seafloor geodetic measurements are colored (red-yellow) by the distance of nodes to the profile. Seafloor measurements (with symbols outlined in black) comprise the vertical displacement and the additional uplift from the horizontal displacement of the steep bathymetric slope. Symbols outlined in blue represent measurements with only horizontal components. The solid black line represents the mean stacked trench-normal profiles of the inverted uplift within 25 km to the profile shown. The black line is filtered with a minimum wavelength of 50 km, the approximate averaging scale of the model.

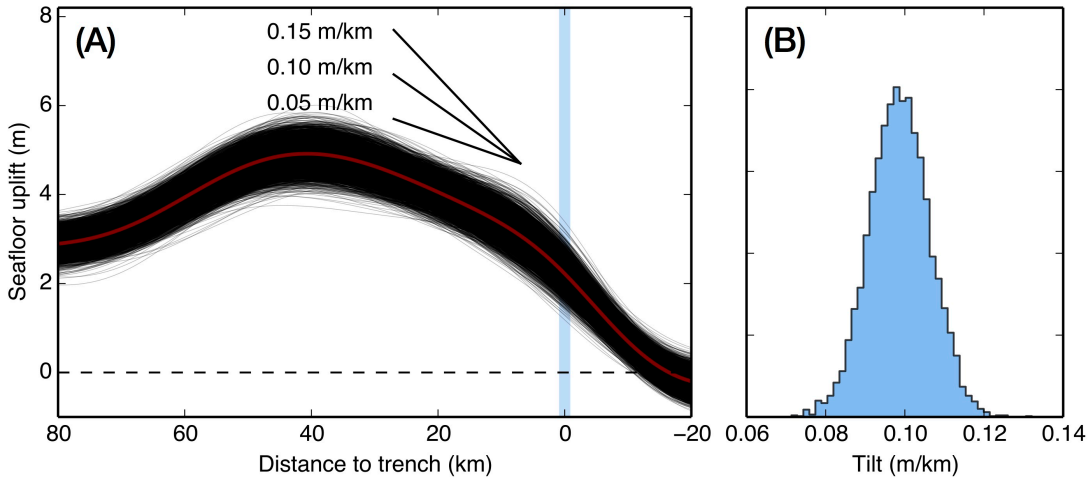


Figure 2.14: *Probabilistic characterization of the near-trench seafloor tilt.* (A) Smoothed near-trench uplift profiles (black lines, lowpass-filtered at 25 km) for 5000 random realizations of models from the posterior kinematic solutions shown in Fig. 2.11. Each profile represents the mean of stacked trench-normal profiles over a swath for a random uplift model, as is similarly done for the uplift profile (black line) in Fig. 2.13C. Vertical blue line indicates the location of the trench. (B) The histogram distribution for the plausible seafloor tilt.

finite element method (PyLith, *Aagaard et al.*, 2013) as qualitative examples of the relation between subsurface fault slip and seafloor uplift, with simplified and yet representative fault geometry and elastic structure. The three models we considered consist of a homogeneous elastic model with flat bathymetry (M1), a homogeneous elastic model with realistic bathymetry (M2), and a 2D elastic model with realistic bathymetry (M3) (Fig. 2.16). All three models include a curved fault as used in *Minson et al.* (2014). We consider three fault slip profiles that have peak slip of 40 m about 50 km away from the trench, with the slip magnitude either increasing, remaining constant, or decreasing as one approaches the trench. The comparisons of seafloor uplift and slip profiles from the three fault models (Fig. 2.16) shows that (1) incorporating real bathymetry affects the overall shape of the surface deformation, highlighting the need to adopt more realistic 3D models (Fig. 2.17B); (2) 2D elastic structure mostly influences near trench deformation, including the maximum uplift (Fig. 2.17C); (3) horizontal displacement coupled with steep bathymetry contributes

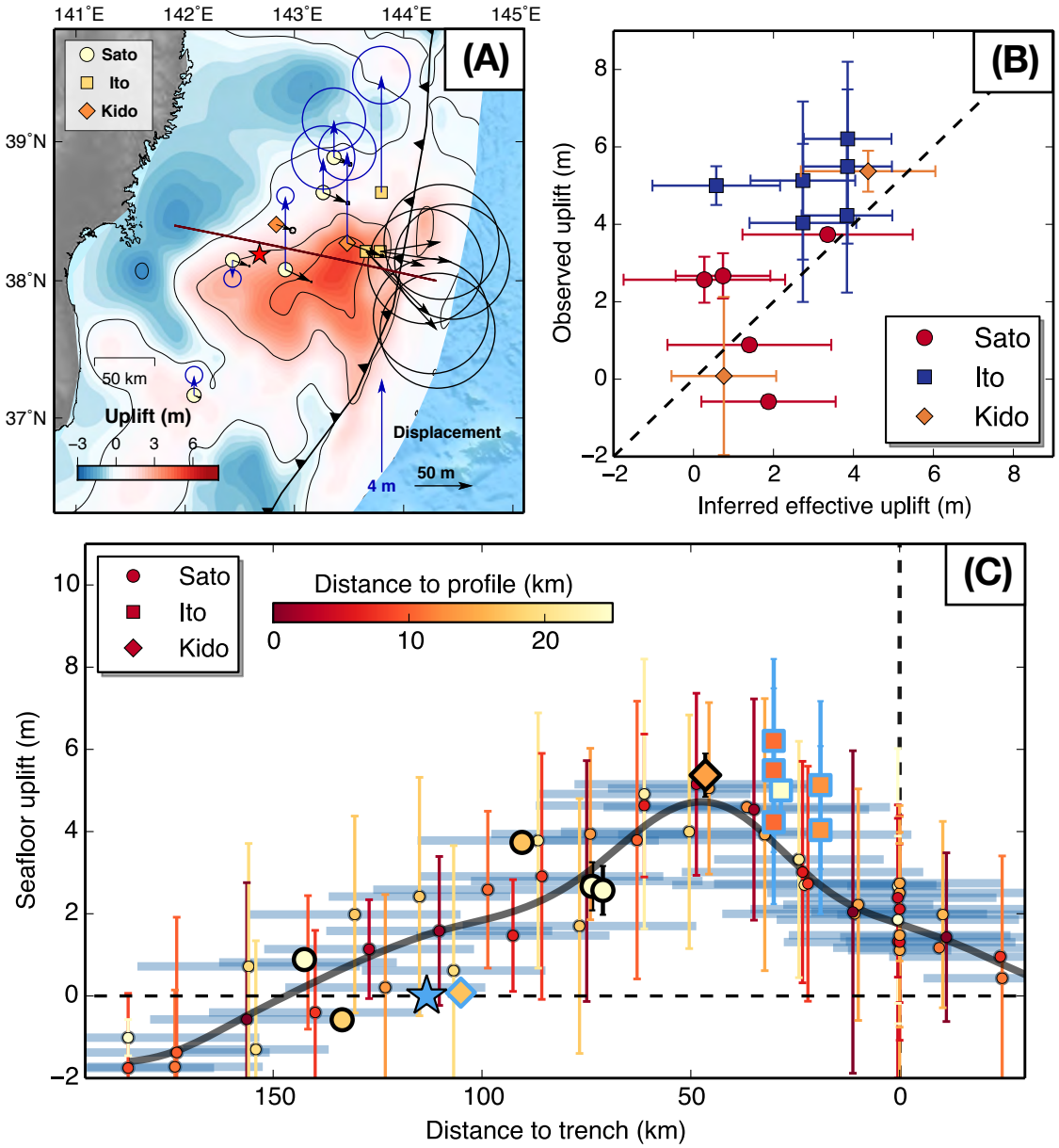


Figure 2.15: *Seafloor deformation near the trench in the quasi-static model and comparisons with seafloor geodetic observations.* All the plotting conventions follow Fig. 2.13.

to a significant fraction of total effective uplift (Fig. 2.17D); (4) The profiles of fault slip and seafloor uplift toward the trench are similar in shape for all three models (comparing Fig. 2.17A and D). Therefore, if elastic modeling is valid for this region as most studies assumed, we conclude from the profile of seafloor uplift that fault slip profile also decreases towards the trench from the peak slip about 50 km landward of the trench. In this interpretation, coseismic slip of 20-30 m could occur at the trench, and such estimate of slip is within the uncertainty range of differential bathymetry measurements (*Fujiwara et al.*, 2011; *Kodaira et al.*, 2012). A recent reinterpretation of these bathymetry measurements in the context of elastic models also reaches a similar conclusion regarding the location of maximum fault slip (*Wang et al.*, 2015).

Overall, our results clearly suggest that a broad coseismic uplift region near the trench, with peak uplift 50 km landward from the trench, is responsible for the excitation of the damaging tsunami. In the context of previously proposed physical models, our findings are consistent with suggestions of velocity-strengthening properties near the trench(*Kozdon and Dunham*, 2013), decreased efficiency of enhanced dynamic weakening, if it occurs (*Noda and Lapusta*, 2013; *Cubas et al.*, 2015), or inelastic deformation (*Ma*, 2012). Future studies are needed to illuminate the roles of these physical mechanisms, and the relation between the source process and the geometry, structure, and properties of the fault.

*Tappin et al.* (2014) suggested the possibility of a submarine landslide near the trench at the northern end of the earthquake rupture, and argued that this additional tsunami source contributes to the damaging impact of tsunami in the Tohoku region. Their proposed source is a $\pm \sim$100 m uplift dipole over 20 km across the trench, and therefore is a feature of very short wavelength and large amplitude that would generate a very dispersive tsunami. The effective averaging scale of our model in the source region is about 40 km, and hence the

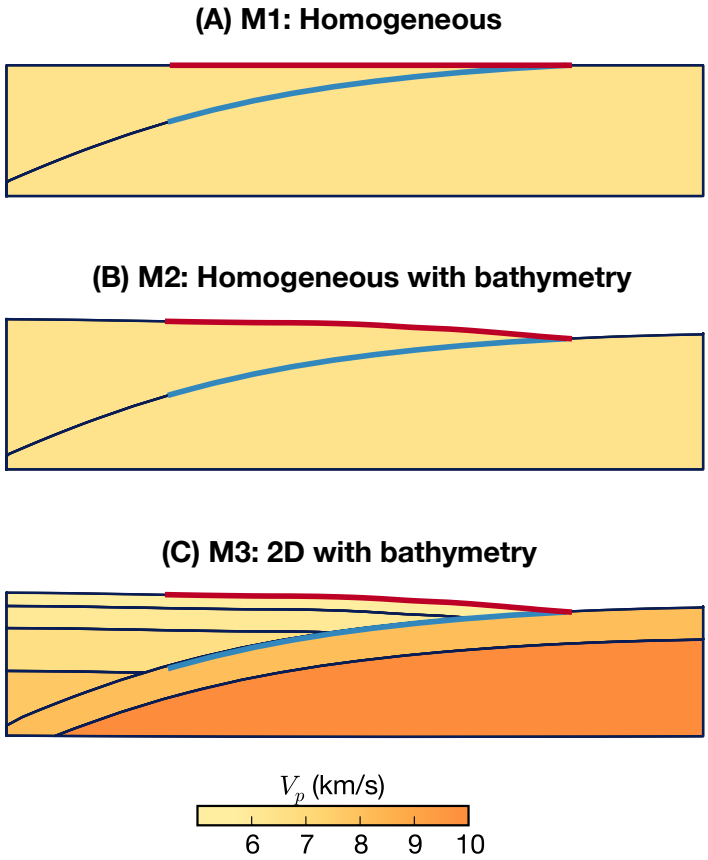


Figure 2.16: *2D subduction zone models with different elastic structure and bathymetry.* (A) Homogeneous model M1 with a flat surface and curved fault geometry. (B) Homogeneous model M2 with realistic bathymetry and curved fault geometry. (C) Model M3 with 2D elastic properties, realistic bathymetry, and curved fault geometry.

source cannot be fully resolved even in the ideal case. In our model, to the north of the largest uplift, a subsidence source of about 1 $\pm$ 0.5 m on the scale of $\sim$40 km does exist in the targeted source region (Fig. 2.11). If the proposed submarine landslide or some other similar processes occurred, it is possible that such sources, after being spatially and temporally filtered, could exist within our solutions, but they do not contribute significantly to the portions of the waveforms we considered.

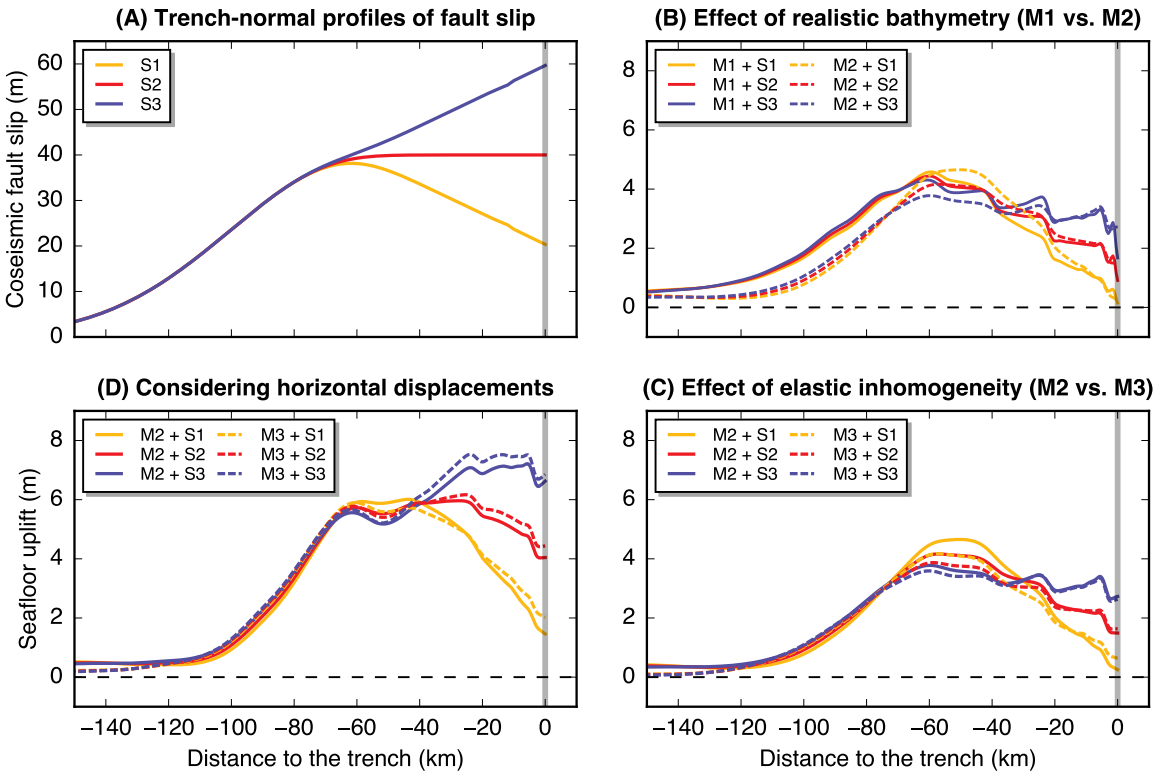


Figure 2.17: *Seafloor uplift and subsurface fault slip in 2D elastic models.* (A) Different trench-normal fault slip profiles represented by S1, S2, and S3. (B) Comparisons of seafloor uplift profiles between models M1 and M2 for different slip profiles. (C) Comparisons of seafloor uplift profiles between M2 and M3 for different slip profiles. (D) The uplift profiles in (C) after accounting for the bathymetry effect.

## 2.7 Conclusion

To resolve robust and detailed source processes during the 2011 Tohoku-Oki earthquake and avoid common issues associated with fault slip inversions, we present a methodology to directly invert for the coseismic seafloor deformation field using near-field tsunami waveform recordings. Using a semi-analytical Bayesian approach, we obtain a closed-form expression for the posterior distribution for quasi-static seafloor deformation. Similarly, we explore kinematic models using a numerical approach to directly sample for the posterior ensemble of all plausible models, which are subject to minimal *a priori* assumptions. A critical ingredient in these Bayesian approaches is the inclusion of realistic model prediction error

($\mathbf{C}_\mathrm{p}$) for the tsunami forward modeling, in addition to the observational error ($\mathbf{C}_\mathrm{d}$). We explore formulations of $\mathbf{C}_\mathrm{p}$ based on empirical models and physical considerations that errors in tsunami modeling could be characterized as stochastic deviations in the frequency dispersion relations. The incorporation of $\mathbf{C}_\mathrm{p}$ helps reduce both bias in the model and overfit tendencies to data. From the posterior, we derive representative solutions with reasonable uncertainty and averaging scales. The semi-analytical approach provides fast source characterization using the first arrivals of tsunami waveforms, while the numerical approach on the full kinematic models provide more robust constraints on the seafloor deformation profiles.

This study reveals that extensive uplift over a broad region contributes to the tsunami hazard during the 2011 Tohoku-oki earthquake, with large uplift of about 2 m at the trench and maximum seafloor uplift of about 5 m occurring about 50 km from the trench. 2D elastic modeling with representative fault geometry and structure suggests that fault slip decreases towards the trench, in a similar manner as the seafloor deformation profile. Future studies on other megathrust earthquakes should provide further insights into the physical process of coseismic fault failure and tsunamigenesis, and an improved assessment of earthquake and tsunami hazard.

# Appendix

## 2.A Frequency dispersion in tsunami propagation

Different approximations for the tsunami propagation model lead to different frequency dispersion characteristics. Based on analysis of the linear wave (Airy wave) theory, a typical frequency dispersion relation can be derived (e.g., *Kundu et al.*, 2012). We express such relation in terms of the phase speed $c$ as a function of the wavenumber $k$:

$$c = \sqrt{\frac{g \tanh(kh)}{k}}, \tag{2.13}$$

where the wavenumber $k = 2\pi/\lambda$ with $\lambda$ as the wavelength, $g$ is the acceleration of gravity and $h$ is the water depth.

The shallow water approximation can be adopted when $h/\lambda \gg 1$, which is applicable for open-ocean propagation of tsunamis. Shallow-water waves have a constant phase speed with a given water depth and are hence non-dispersive:

$$c = \sqrt{hg}. \tag{2.14}$$

The deep water approximation is valid when $h\lambda \ll 1$. Deep-water waves are dispersive with

the following dispersion relation:

$$c = \sqrt{\frac{g}{k}}. \tag{2.15}$$

In the long-wave (long-period) limit, an additional mechanism modifies the dispersion relation due to the interaction between waves and the elastic substrate (e.g., *Watada*, 2013; *Tsai et al.*, 2013):

$$c = \sqrt{\frac{g \tanh(kh)}{k}} \sqrt{1 - \frac{(1-\nu)\rho g}{\mu k}}, \tag{2.16}$$

where $\nu$ is the Poisson's ratio, and $\mu$ is the shear modulus. This effect can be ignored for small-scale problems. In the short-wave (short-period) limit, numerical approaches commonly adopt the Boussinesq approximation, in which the depth-dependence of horizontal velocities is accounted for, and weakly dispersive waves are produced.

Here, we use NEOWAVE (*Yamazaki et al.*, 2009, 2011) which achieves the wave dispersion through non-hydrostatic terms, effectively reproducing dispersion relations that are closer to the theoretical predictions (Eq. 2.13) than the classical Boussinesq-type equations. Based on analysis of the linearized equations, the dispersion characteristics in NEOWAVE can be expressed as:

$$c = \sqrt{\frac{gh}{1 + \frac{1}{4}(kh)^2}}. \tag{2.17}$$

Several dispersion relations above (Eq. 2.13, 2.16, and 2.17) clearly depend on the local water depth $h$. Following the treatment of *Watada et al.* (2014), we normalize these relations by the long-wave phase speed $\sqrt{Hg}$ with reference water depths $H = 4$ km and $H = 2$ km in Fig. 2.19. In reality, the "true" (normalized) dispersion curve could be complicated by nonlinear effects, and also be site- and path-dependent due to waves traveling through variable water depths.

## 2.B Different formulations of $\mathbf{C_p}$ for tsunami waveforms

Uncertainties in forward modeling are expected to increase with the size of the source and will overwhelm the observational errors typically determined by the instrumental precisions. In Fig. 2.21 and Table 2.1, we present seven formulations of $\mathbf{C}_\mathrm{p}$ based on different considerations and techniques. The first three methods are based on empirical estimates. In Fig. 2.21A, we design a $\mathbf{C}_\mathrm{p}^\mathrm{DG}$ with only diagonal elements, whose variance represents a pre-assumed ratio ($\alpha$=15%) of the peak data amplitude $\mathbf{d}_\mathrm{max}$ for each record, as has been done in *Minson et al.* (2014). This approach obviously misses the inherent correlation between neighboring data points in the waveforms. In Fig. 2.21B, as well as Fig. 2.3F, we design a $\mathbf{C}_\mathrm{p}^\mathrm{AC}$ based on the correlation revealed in the auto-correlation functions of waveform misfits for each station. While keeping the correlation between data points, we scale the maximum variance for each station to be $\alpha\mathbf{d}_\mathrm{max}$. This banded-Toeplitz $\mathbf{C}_\mathrm{p}$ captures some correlation in the off-diagonal terms, but has constant variance within a single record, which likely overestimates model prediction errors at some data points. In Fig. 2.21C, we design a third $\mathbf{C}_\mathrm{p}^\mathrm{WV}$ based on the considerations of error structure in the wavelet domain. It could be speculated that the errors in physical modeling would be associated with wavelet components of certain scales and time offsets and that small correlation, i.e., little physical coupling, exists between these different wavelets. Therefore, we first convert the data into wavelet domain with 1D discrete orthogonal Meyer wavelet transform, construct a $\tilde{\mathbf{C}}_\mathrm{p}$ in the wavelet domain with variance of $\alpha\tilde{\mathbf{d}}_\mathrm{max}$ ($\tilde{\mathbf{d}}_\mathrm{max}$ is the peak amplitude of each wavelet), and transform $\mathbf{C}_\mathrm{p}$ back to the time domain through 2D inverse wavelet transform. This $\mathbf{C}_\mathrm{p}$ has off-diagonal terms which indicate correlation in the time domain, with the variances varying over the record and scaling approximately with the size of the data. For all three

cases, a scaling parameter $\alpha_{data}$ needs to be chosen *a priori* to represent our belief on the size of the model prediction errors compared to the data.

The next three methods are based on physical considerations. For tsunami modeling, deviation from the "true" dispersion curve is an inevitable source of error for the waveform prediction, so we propose to explore the structure of $\mathbf{C}_\mathrm{p}$ for waveform misfits due to such kind of deviations. The empirical corrections of tsunami waveforms can be done with given dispersion curve in the deterministic sense (e.g., *Yue et al.*, 2014). Here, we carry out such waveforms corrections in the stochastic sense based on a perturbation approach. As shown in Fig. 2.21, we generate random realizations of the (normalized) dispersion curves with small deviations that follow a log-normal distribution centered on the curve associated with NEOWAVE (Eq. 2.17) and are bounded by the long-wave curve (Eq. 2.14). The synthetic waveforms generated from a reference model could be perturbed based on the deviation in dispersion characteristics for each random realization. We consider three ways to make such perturbations/corrections. For each frequency $\omega$, the time delay $\Delta t(\omega)$ and phase delay $\phi(\omega)$ along the tsunami travel paths are:

$$\Delta t(\omega) = t_0(\omega) - t_\mathrm{p}(\omega) = \sum_i \big(\frac{p_i}{c_0(\omega, h_i)} - \frac{p_i}{c_\mathrm{p}(\omega, h_i)}\big), \tag{2.18}$$

$$\phi(\omega) = -2\pi i\omega\Delta t(\omega), \tag{2.19}$$

where $c_0$ and $c_\mathrm{p}$ are the reference and perturbed phase speed, respectively, both as a function of $\omega$ and local water depth $h_i$, and $p_i$ is the discretized tsunami travel path.

First, if we assume that the effects of variable water depth and variable travel path are

negligible, meaning that the dispersion curve is path-independent, then

$$\Delta t(\omega) = \sum_i p_i \big(\frac{1}{c_0(\omega)} - \frac{1}{c_{\rm p}(\omega)}\big), \tag{2.20}$$

$$\Delta t(\omega)/t_0(\omega) = \frac{1}{c_0(\omega)} / \big(\frac{1}{c_0(\omega)} - \frac{1}{c_{\rm p}(\omega)}\big) = \frac{c_{\rm p}(\omega) - c_0(\omega)}{c_{\rm p}(\omega)}. \tag{2.21}$$

The ratio of travel time delay and total travel time is hence path-independent. The phase correction could be applied for each bandpass-filtered reference waveforms (or the real data without the need for a reference model) by scaling the arrival time using Eq. 2.21. From the random realizations of the perturbed waveforms, we calculate the covariance matrix $\mathbf{C}_{\rm p}^{\rm BP}$, shown in Fig. 2.21D. The assumptions in this approach might be more valid for far-field open-ocean propagation, where variation in water depth and travel path are small.

Adopting Eq. 2.18, we make corrections for each source-station pair at each frequency in the synthetic GFs, and use the reference model to construct the final perturbed waveforms. We can choose the great-circle path for the travel path between each source-station pair, leading to the $\mathbf{C}_{\rm p}^{\rm GC}$ shown in Fig. 2.21E. More realistically, we should use ray paths that better describe the travel path of tsunamis (*Satake*, 1988). We calculate the ray paths using a fast sweeping method based on an Eikonal equation with long-wave speed dependent on local bathymetry (*Zhao*, 2005). As we can see in Fig. 2.22, the great-circle paths and ray paths differ significantly for many source-station pairs due to the presence of deep trench bathymetry which guides the propagation of tsunami. This approach gives us the formulation of $\mathbf{C}_{\rm p}^{\rm RP}$, shown in Fig. 2.3D and 2.21E.

In Fig. 2.3E, we consider another formulation, $C_{\rm p}^{\rm HB}$, by combining features of empirical estimates and physical considerations. $C_{\rm p}^{\rm HB}$ is characterized by the inter-station correlation structure estimated empirically from $C_{\rm p}^{\rm AC}$, and relative misfit variances (weighting) within

the waveform for each station determined from $C_{\mathrm{p}}^{\mathrm{RP}}$.

| $\mathbf{C}_{\mathrm{p}}$ | $\mathbf{C}_{\mathrm{p}}^{\mathrm{DG}}$ | $\mathbf{C}_{\mathrm{p}}^{\mathrm{AC}}$ | $\mathbf{C}_{\mathrm{p}}^{\mathrm{WV}}$ | $\mathbf{C}_{\mathrm{p}}^{\mathrm{BP}}$ | $\mathbf{C}_{\mathrm{p}}^{\mathrm{GC}}$ | $\mathbf{C}_{\mathrm{p}}^{\mathrm{RP}}$ | $\mathbf{C}_{\mathrm{p}}^{\mathrm{HB}}$ |
|---|---|---|---|---|---|---|---|
| off-diagonal terms | No | Yes | Yes | Yes | Yes | Yes | Yes |
| relative weighting | No | No | No | Yes | Yes | Yes | Yes |
| correlation | No | No | No | Yes | Yes | Yes | Yes |
| reference model needed | No | Yes | No | No | Yes | Yes | Yes |

Table 2.1: *Summary on the characteristics of different* $\mathbf{C}_{\mathrm{p}}$. DG: diagonal; AC: autocorrelation; WV: wavelet; BP: bandpass; GC: great-circle path; RP: ray path; HB: hybrid.

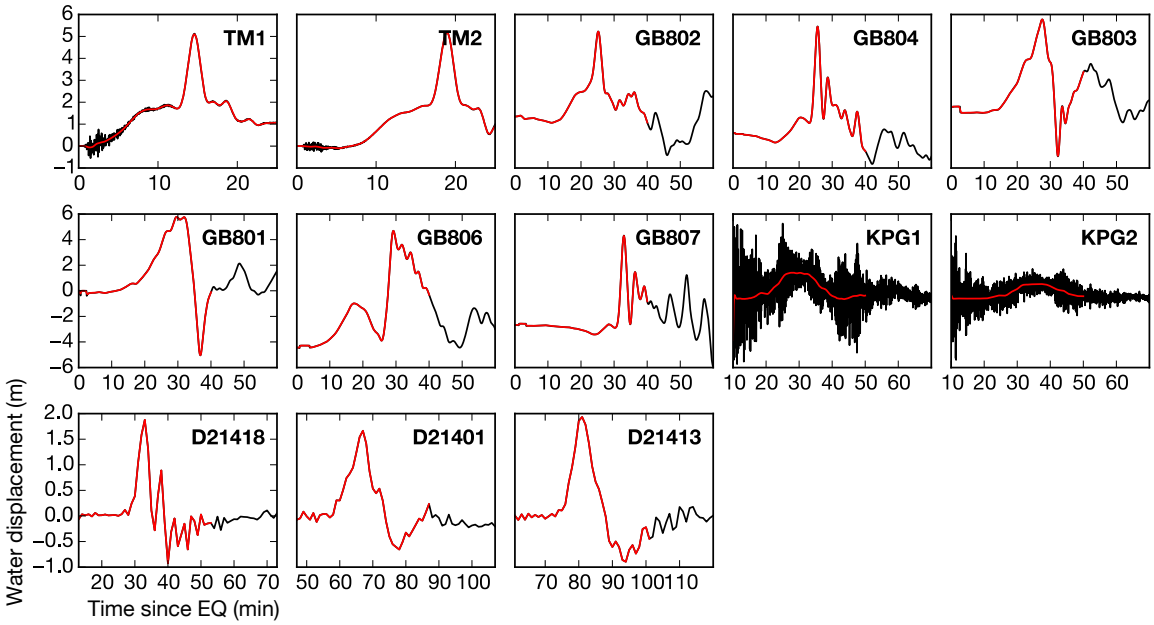


Figure 2.18: *The original and filtered waveforms.* Tsunami waveforms at 13 stations used in the study are lowpass-filtered at 2 mins for DARTs and 60 seconds for others.

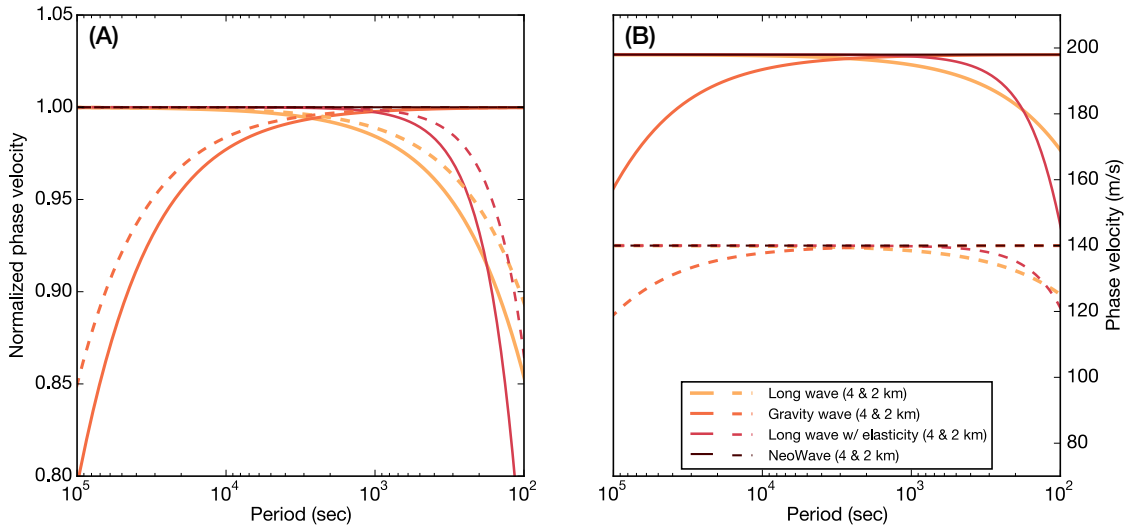


Figure 2.19: *Frequency dispersion relations for tsunami propagation.* (A) Phase speed normalized by the non-dispersive long-wave phase speed. (B) Absolute phase speed for cases with a water depth of 4 km (solid lines) and 2 km (dashed lines).

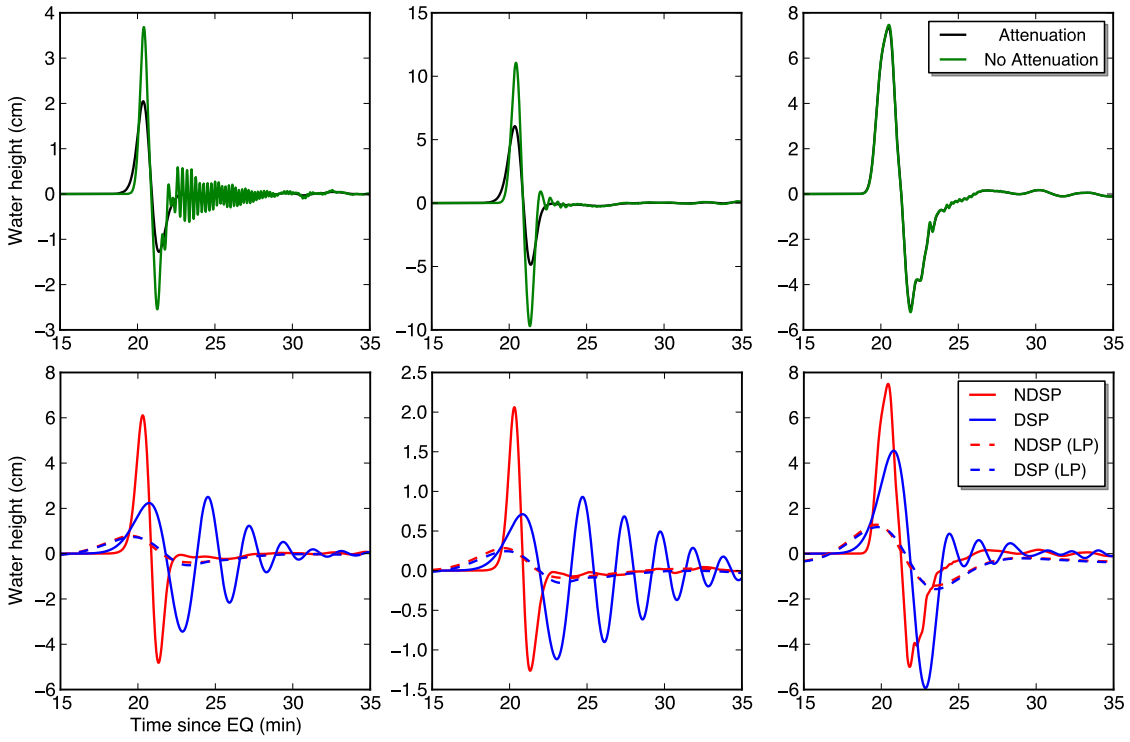


Figure 2.20: *The effect of water layer attenuation and wave dispersion on tsunami Green's functions (GFs).* Tsunami GFs at station TM1 for (A, D) on-trench, (B, E) near-trench, and (C, F) far-from-trench deformation sources. (A-C) Cases with (black) and without (green) consideration of the elastic attenuation of water layer. (D-F) Dispersive (DSP, blue) and non-dispersive (NDSP, red) tsunami GFs are shown in solid lines, with their lowpass-filtered (LP, at 2 min) counterparts shown as dashed lines.

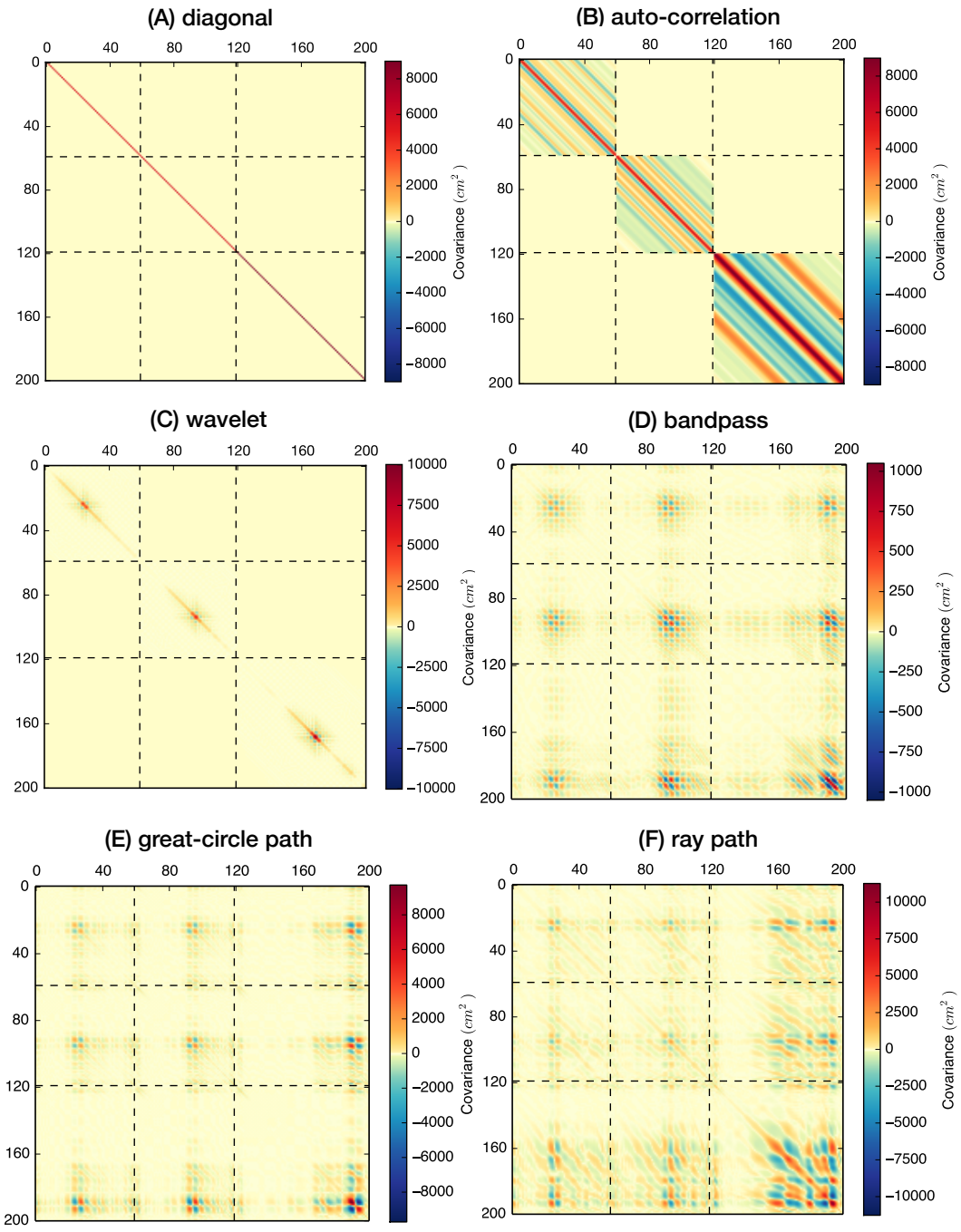


Figure 2.21: *Different formulations of* $\mathbf{C}_p$. (A) $\mathbf{C}_{\mathrm{p}}^{\mathrm{DG}}$ with inter-station uniform variances. (B) $\mathbf{C}_p^{\mathrm{AC}}$ based on the autocorrelation function of waveform misfits for each station. (C) $\mathbf{C}_{\mathrm{p}}^{\mathrm{WV}}$ based on uniform variances in the discrete (Meyer) wavelet domain. (D-F) correspond to physics-motivated approaches that consider the deviations in dispersion relations. (D) $\mathbf{C}_{\mathrm{p}}^{\mathrm{BP}}$ based on a bandpass approach that corrects travel time for each frequency band with no need for tsunami travel paths. (E) $\mathbf{C}_{\mathrm{p}}^{\mathrm{GC}}$ based on perturbing tsunami waveforms along a great-circle path from source to station. (F) $\mathbf{C}_{\mathrm{p}}^{\mathrm{RP}}$ based on perturbing tsunami waveforms along a ray path from source to station.

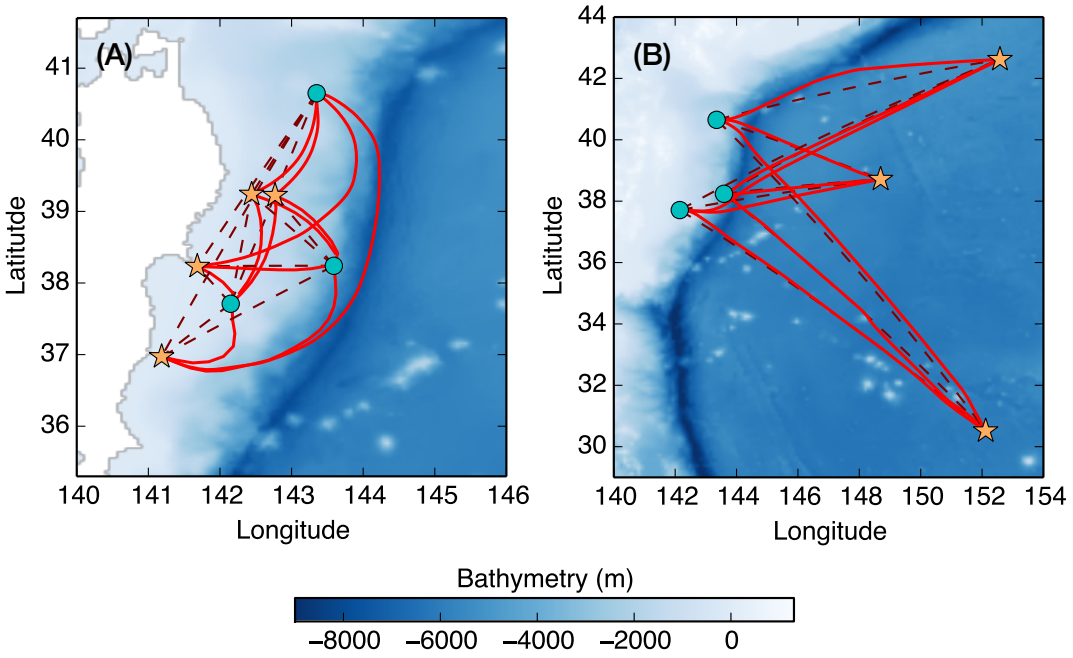


Figure 2.22: *Great-circle path and raypath approximations in tsunami propagation.* (A) Near-field stations and (B) DART stations are represented by orange stars. Deformation sources are represented by blue circles. The great-circle path and ray path for each source-station pair are indicated by dashed and solid lines, respectively.

# Chapter 3

# A Bayesian Perspective on the Complementarity of Tsunami and Geodetic Observations for the 2010 $M_{\mathbf{w}}$ 8.8 Maule, Chile Earthquake

# Abstract

Both geodetic and tsunami observations are commonly used to study the distribution of fault slip in large megathrust earthquakes. While on-land geodetic data has better resolution on the down-dip fault slip close to the coast, tsunami data is considered to provide better constraints on fault slip at the shallower parts of the megathrust. For the 2010 $M_{\mathrm{w}}$ 8.8 Maule, Chile earthquake, studies that considered tsunami and geodetic observations separately produced significantly different source models. Even in models with joint datasets, variability in the inferred extent of updip fault slip is significant for understanding the failure process of the shallow subduction zone.

To understand the complementary roles of tsunami and geodetic data in these joint inversions, we use a semi-analytical Bayesian approach to derive the posterior solutions of coseismic slip models for the Maule earthquake based on dense on-shore geodetic measurements and open ocean tsunami waveforms. We adopt minimal *a priori* assumptions of fault slip, which allows us to explore the inherent resolution of each dataset. We find that far-field tsunami data for the Maule earthquake, when used alone, is associated with a large null space, and can only resolve shallow fault slip when used with additional geodetic constraints. For joint inversions, improvements in forward modeling, including tsunami dispersion and more realistic elastic structure, together with incorporation of consistent model prediction errors, are crucial for obtaining posterior solutions in which the two datasets

fully complement each other and reduce model uncertainties optimally compared to their separate uses. Our fault slip model is characterized by a peak slip of 21 m offshore to the north of the hypocenter, generally consistent with most previous studies, and small slip at the trench. This model predicts a maximum seafloor uplift of about 4 m just 50 km from the trench, coinciding with the edge of the accretionary wedge, and an insignificant uplift of 1 m or less at the trench.

## 3.1 Introduction

The 2010 $M_w$ 8.8 Maule, Chile earthquake has been studied using a wide range of observations, including tsunami and geodetic data, which are expected to provide spatial resolution on up-dip and down-dip fault slip, respectively. Source models of static coseismic slip distribution have been inverted from tsunami waveforms (*Fujii and Satake*, 2012), geodetic measurements (*Tong et al.*, 2010; *Vigny et al.*, 2011; *Lin et al.*, 2013), and joint tsunami and geodetic data (*Lorito et al.*, 2011). Kinematic source models are also developed based on inversions of teleseismic waves (*Lay et al.*, 2010; *Moreno et al.*, 2012), teleseismic and geodetic data (*Delouis et al.*, 2010; *Lin et al.*, 2013), and a full integration of tsunami, geodetic, and seismic observations (*Yue et al.*, 2014). Significant differences exist between models that consider tsunami and geodetic separately, e.g., maximum slip below the coast in *Fujii and Satake* (2012) and much closer to the trench in *Vigny et al.* (2011). Such discrepancies in the location of peak slip are reduced in joint models that incorporate both geodetic and tsunami data (*Lorito et al.*, 2011; *Yue et al.*, 2014), but the shallower part remains inconsistent between models, with near-trench slip of 20 m in *Yue et al.* (2014), but virtually none in *Lorito et al.* (2011). This difference is significant for our understanding of the mechanics and tsunamigenesis of the shallow subduction zone.

In Chapter 2, we demonstrated that tsunami observations alone can be used to infer for the coseismic seafloor deformation during the 2011 Tohoku-Oki earthquake. However, most major earthquakes that occurred earlier or in other regions do not have as comprehensive tsunami records as the Tohoku-Oki event, and therefore additional constraints from other observations are desirable in order to reach firm conclusions on the extent of shallow fault slip. Here, we incorporate tsunami data into finite-fault slip inversions with a focus on

understanding the complementary resolution provided by tsunami and geodetic data, and investigate their respective roles in joint inversions. We adopt a semi-analytical Bayesian approach to the fault slip problem, similar to the approach developed in Chapter 2, explicitly incorporating model prediction errors in tsunami modeling and elastic structure. In particular, we study the significance of tsunami dispersion and elastic structure on inversions, as well as the importance of accounting for these sources of uncertainty. With improved Green's functions and consistent error models, we aim to constrain the slip distribution of the Maule earthquake, in particular the updip profile of fault slip and the predicted seafloor displacement.

## 3.2 Data and methods

### 3.2.1 Fault geometry and model parameterization

We adopt a nonplanar fault geometry for the 2010 Maule earthquake on the Nazca-South American plate interface (Fig. 3.1). The 3D plate interface model is built by *Ortega Culaciati* (2013) with constraints from relocated global earthquake catalogues (*Engdahl et al.*, 1998; *Engdahl and Villaseñor*, 2002), regional catalogues (*Comte et al.*, 2004), seismic reflection profiles (*Krabbenhöft et al.*, 2004; *Hampel et al.*, 2004; *Oncken et al.*, 1999), and a previous Nazca plate geometry (*Tassara et al.*, 2006). We mesh the fault geometry with Delaunay triangulation and obtain near-uniform triangles (close to equilaterals) with an edge length of about 22 km. The nonplanar fault geometry honors the curved trench, which is important for resolving fault slip close to the trench.

We parameterize the dip-slip and strike-slip components on the fault as unit sources represented by piece-wise linear tent functions centered on each node of the triangulated

geometry. The boundary nodes on the trench are treated as half-tents which allow nonzero fault slip at the trench. Nodes on other boundaries are assigned with zero slip and not included in the inversion, thereby assuming that they are significantly away from the source region.

### 3.2.2 Geodetic observations and modeling

We use InSAR (interferometric synthetic aperture radar) and GPS (Global Positioning System) measurements based on a compiled dataset used in previous studies of coseismic slip models (*Vigny et al.*, 2011; *Lin et al.*, 2013). The GPS observations consist of 110 three-component coseismic GPS displacements, about 40 of which are close to the source region. The station distribution is shown in Fig. 3.1. The InSAR measurements are based on image acquisitions from the Japanese L-band Advanced Land Observation Satellite (ALOS), including 6 descending tracks (420 and wideswath 422) and 10 ascending tracks (110 through 119), which are processed and downsampled in *Lin et al.* (2013). In the inversion, we solve for a three-parameter linear ramp for each scene to absorb potential orbital errors.

The surface deformation due to slip on the fault is computed with a 1D layered structure that is extracted from 2D models by spatial averaging over the near-source region (*Tassara et al.*, 2006; *Haberland et al.*, 2009). For the calculation of seafloor displacements used for tsunami excitation, the shallowest layer of 2 km is removed from both the velocity model and fault geometry, in order to account for the water layer over the source.

### 3.2.3 Tsunami observations and modeling

We use tsunami waveforms recorded at far-field open-ocean NOAA DART (Deep-ocean Assessment and Reporting of Tsunamis) stations 32412, 32411, 51406, and 43412. Stations

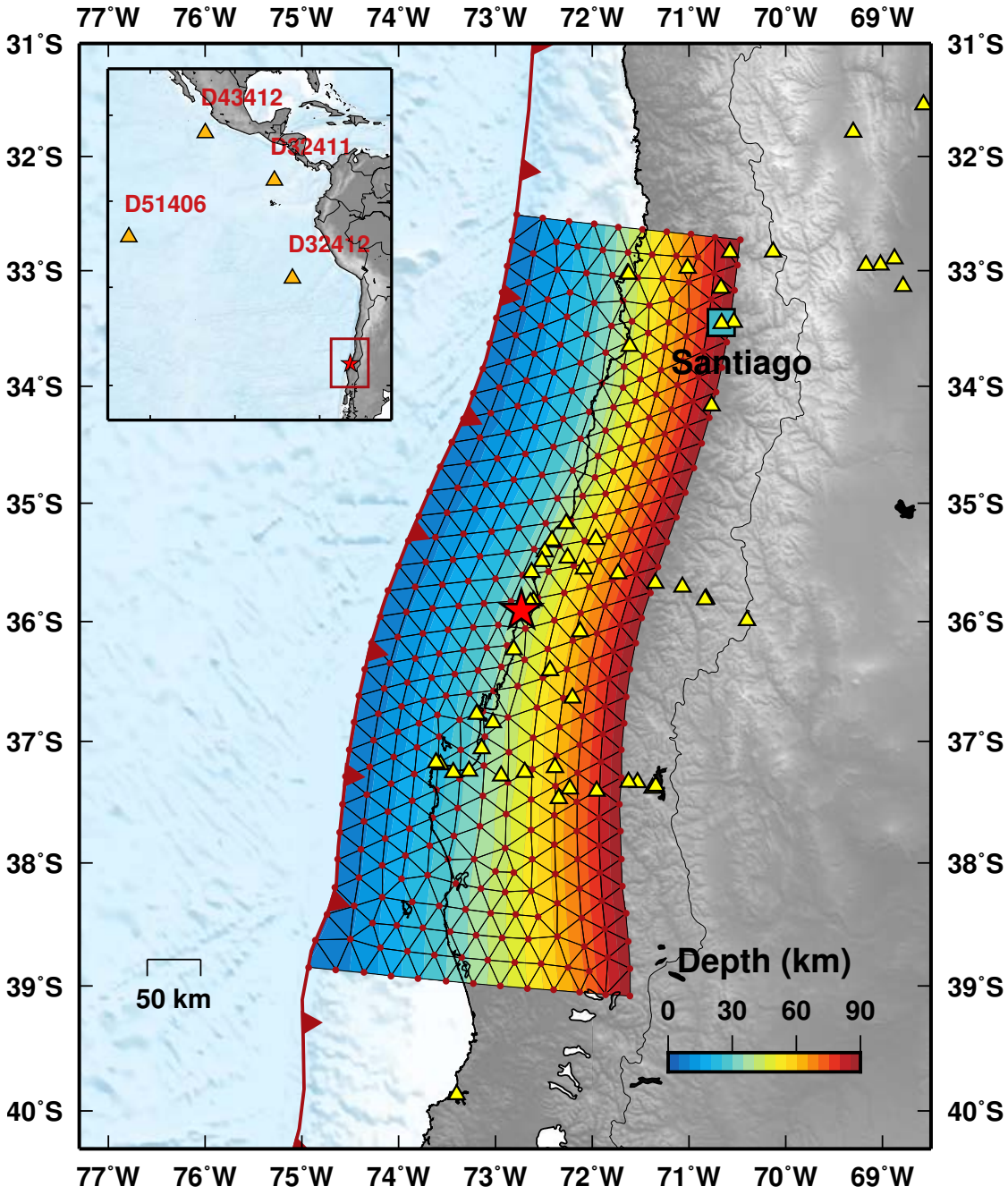


Figure 3.1: *Fault geometry and station distribution for the 2010 $M_w$ 8.8 Maule earthquake.* The triangulated fault geometry matches the 3D megathrust fault interface, with its depth in color. GPS stations are represented by yellow triangles. Far-field DART stations are shown in the map inset as orange triangles next to the corresponding station names. Event hypocenter location from the NEIC/USGS solution is indicated by the red star.

32411 and 51406 have higher sampling rates, with a time-averaged measurement every 15 seconds, and Stations 32411 and 51406 have a measurement every minute. We remove tidal signals by fitting high-order polynomials to a two-day time window spanning the event, and then lowpass filtering the data at 30 sec for stations 32411 and 51406, and 60 sec for stations 32411 and 51406. For use in the inversions, we select a 40-min time window around the main arrivals of the tsunami waveforms, since the later arrivals contain less information about the source and are more sensitive to wavefront interactions with coastal bathymetry which is difficult to simulate accurately. Nonetheless, we will use the later waveforms as *a posteriori* validation of our probabilistic source models.

We calculate the effective vertical seafloor displacement, including the additonal contributions from the horizontal displacement of the steep bathymetric slope, which is important for tsunami excitation near the trench (*Tanioka and Satake*, 1996). We assume that tsunami excitation, as well as the induced seafloor displacement, occurs instantaneously with respect to the earthquake centroid time (60 sec after the earthquake initiation time). The quasi-static assumption is valid since we only consider the far-field tsunami data with low sampling rates.

We simulate tsunami waveforms with nonlinear shallow water equation implemented in COMCOT (*Liu et al.*, 1995) to be used as Green's functions (GF) for the tsunami data. The methodology does not incorporate physical dispersion that has been observed for far-field tsunami propagation during recent large earthquakes (e.g., *Tsai et al.*, 2013; *Watada*, 2013; *Watada et al.*, 2014), attributed primarily to the interaction of water layer with the elastic earth and the ocean density stratification. Such physical processes could be incorporated into numerical simulations (e.g., *Allgeyer and Cummins*, 2014) at the expense of increased computational expense, which is not suitable for our calculations of GFs for hundreds of

sources. We adopt the empirical approach to correct the simulated waveforms based on the dispersion relation predicted by theoretical models (*Tsai et al.*, 2013), following a similar approach used in *Yue et al.* (2014).

### 3.2.4 Semi-analytical Bayesian approach to fault slip models

Combining the parameterized coseismic fault slip model (Section. 3.2.1) and the Green's functions (Sections 3.2.2 and 3.2.3), we have the following linear forward problem for our joint datasets:

$$\mathbf{G}\cdot\boldsymbol{\theta} = \begin{bmatrix} \mathbf{G}_{\mathrm{s}}^{\mathrm{i}} & \mathbf{G}_{\mathrm{d}}^{\mathrm{i}} & \mathbf{R} \\ \mathbf{G}_{\mathrm{s}}^{\mathrm{g}} & \mathbf{G}_{\mathrm{d}}^{\mathrm{g}} & \mathbf{0} \\ \mathbf{G}_{\mathrm{s}}^{\mathrm{t}} & \mathbf{G}_{\mathrm{d}}^{\mathrm{t}} & \mathbf{0} \end{bmatrix} \begin{bmatrix} \mathbf{s}_{\mathrm{s}} \\ \mathbf{s}_{\mathrm{d}} \\ \mathbf{n}_{\mathrm{r}} \end{bmatrix} = \begin{bmatrix} \mathbf{p}^{\mathrm{i}} \\ \mathbf{p}^{\mathrm{g}} \\ \mathbf{p}^{\mathrm{t}} \end{bmatrix}, \tag{3.1}$$

where $\mathbf{G}$, $\boldsymbol{\theta}$, $\mathbf{s}$, and $\mathbf{p}$ correspond to the GF matrix, total model vector, slip vector, and data vector. $\mathbf{R}$ and $\mathbf{n}_{\mathrm{r}}$ are the ramp construction matrix and ramp parameter vector (nuisance parameters) for InSAR. The superscript i, g and t correspond to InSAR, GPS, and tsunami data, respectively. The subscript s and d correspond to the strike-slip and dip-slip components, respectively. For cases that involve only geodetic or tsunami data, the corresponding rows of $\mathbf{G}$ and $\mathbf{p}$ are removed from the equation above.

Estimating parameters in the fault slip model $\boldsymbol{\theta}$ given the observed data $\mathbf{d}$ is thus a linear inverse problem. We adopt the Bayesian formulation of this inverse problem to derive the posterior solutions $P(\boldsymbol{\theta}|\mathbf{d})$ (*Bayes and Price*, 1763). Assuming Gaussian distributions for all uncertainties, data likelihood $P(\mathbf{d}|\boldsymbol{\theta})$ follows the same expression as Eq. 2.3 in Chapter 2. We choose uncorrelated Gaussian priors on both strike-slip and dip-slip components: $P(\boldsymbol{\theta}) = P(\mathbf{s}_{\mathrm{s}})P(\mathbf{s}_{\mathrm{d}})P(\mathbf{s}_{\mathrm{r}})$, in which $P(\mathbf{s}_{\mathrm{s}}) = \mathcal{N}(\mathbf{0}, (25\ \mathrm{m})^2\mathbf{I})$, $P(\mathbf{s}_{\mathrm{d}}) = \mathcal{N}(\mathbf{0}, (8\ \mathrm{m})^2\mathbf{I})$, and

$P(\mathbf{s}_\mathrm{r})$ is arbitrarily chosen to be a wide distribution. The chosen priors cover a wider range of slip amplitudes and rake angles than expected for such an event and are hence not significantly informative, so we consider these as minimal *a priori* constraints.

More informative priors could be used but need to be physically justified. For example, imposing spatial correlations between nearby fault slip could produce smoother posterior solutions, but it is difficult to choose *a priori* the appropriate form of spatial correlation given the parameterization and to assess the effect of these assumptions on the final solutions. As another common choice, the positivity constraint of slip in the preferred rake direction is a physically reasonable assumption in the fault slip problem. However, we still prefer the uninformative Gaussian priors here because: (1) Gaussian priors, combined with Gaussian data likelihood, allow for closed-form expressions of the posterior solutions, uncertainty estimates, and predictions; (2) With minimally informative priors, we can validate our models *a posteriori* against other physical constraints. For example, significant backward slip in our models would indicate an inconsistency between error models, GFs, and the data. Therefore, the use of uninformative priors provides a direct test on the compatibility between our error models and GFs, and serves as the first step toward adopting stronger prior constraints to reduce the parameter space.

Following the same procedure developed in Section 2.3.5, we estimate the uncertainty of model parameters from the posterior model covariance matrix $\tilde{\mathbf{C}}_\mathbf{m}$. With uninformative priors, our over-parameterized models are characterized by large uncertainties and anti-correlations between nearby fault slip, making physical interpretations difficult. For all the fault slip models shown in Section 3.3, we apply *ad hoc* spatial averaging on the posterior solutions by averaging each node value with their "one-ring" (1R) neighbors. Such averaging helps eliminate solutions that have shorter-wavelength variations in slip, thereby reducing

the overall uncertainties of model parameters.

### 3.2.5 Error models for geodetic and tsunami modeling

As discussed in Chapter 2, the total uncertainties of the inverse problem, represented by the error covariance matrix $\mathbf{C}_\chi$, is expressed as the sum of two parts in the least-squares case:

$$\mathbf{C}_\chi = \mathbf{C}_\mathrm{d} + \mathbf{C}_\mathrm{p}, \tag{3.2}$$

where the model prediction error $\mathbf{C}_\mathrm{p}$ due to imperfection in the forward modeling depends on the size of the source, while the observational error ($\mathbf{C}_\mathrm{d}$) depends only on the accuracy of the observations. For earthquakes of large sizes, $\mathbf{C}_\mathrm{p}$ usually overwhelms $\mathbf{C}_\mathrm{d}$, and ignoring or underestimating $\mathbf{C}_\mathrm{p}$ can directly bias the posterior estimates. In our problems, the main sources of model prediction uncertainty come from the elastic structure used to predict on-land and seafloor displacements and the tsunami propagation modeling. The inaccuracy of the GF could usually be mitigated by adopting more sophisticated forward modeling approaches, and yet cannot be fully accounted for realistically. Therefore, more consistent error models are necessary.

For InSAR and GPS observations, we design $\mathbf{C}_\mathrm{p}$ by considering the uncertainty in the elastic structure, following a stochastic perturbational approach (*Duputel et al.*, 2014). We characterize the uncertainty in elastic parameters $\mathbf{\Omega}$ ($V_\mathrm{p}$, $V_\mathrm{s}$, and $\rho$) of a layered structure as log-normal deviations from their reference values $\tilde{\mathbf{\Omega}}$, i.e., $P(\ln \mathbf{\Omega}) = \mathcal{N}(\ln \tilde{\mathbf{\Omega}}, \mathbf{C}_\Omega)$, where $\mathbf{C}_\Omega$ is the covariance matrix for elastic parameters. The log-normal distribution of uncertainties is preferred, because $\mathbf{\Omega}$ are Jefferey's parameters that have positive supports (*Tarantola*, 2005). We pre-calculate the sensitivity kernels $\mathbf{K}_\Omega^G$ of the Green's functions $\mathbf{G}$ with respect

to the deviations in $\mathbf{\Omega}$ as linearized perturbations:

$$(\mathbf{K}_{\Omega}^{G})_{i,j,k} = \frac{\partial G_{i,j}}{\partial \ln \Omega_k}. \tag{3.3}$$

Given a reference model $< \mathbf{m} >$, which we obtain through previous iterations, we can relate the covariance matrix $\mathbf{C}_{\Omega}$ for elastic parameters to $\mathbf{C}_{\mathrm{p}}$

$$\mathbf{K}_{\Omega} = \mathbf{K}_{\Omega}^{G} \cdot < \mathbf{m} > \tag{3.4}$$

$$\mathbf{C}_{\mathrm{p}} = \mathbf{K}_{\Omega} \cdot \mathbf{C}_{\Omega} \cdot \mathbf{K}_{\Omega}^{T}. \tag{3.5}$$

We choose $\mathbf{C}_{\Omega} = \mathcal{N}(\mathbf{0}, 0.1^2\mathbf{I})$ for our problem, so that there is 10% uncorrelated uncertainty in $\ln \mathbf{\Omega}$ for elastic parameters $\mathbf{\Omega}$. In Fig. 3.2, we show the random realizations of such perturbations from the reference elastic structure. The observational error $\mathbf{C}_{\mathrm{d}}$ has an uncertainty of about 1 cm or less for GPS measurements and several cm for InSAR, and does not contain off-diagonal terms. The corresponding $\mathbf{C}_{\boldsymbol{\chi}}$ is shown in Fig. 3.3A, suggesting strong spatial covariances between data points within the InSAR tracks and for near-field GPS measurements, and less covariances for far-field GPS measurements.

For tsunami waveforms, $\mathbf{C}_{\mathrm{p}}$ contains both uncertainties from predicting the seafloor displacements with the assumed elastic structure and from numerical modeling of tsunami propagation. Given the low resolution of tsunami data, we adopt an empirical approach of $\mathbf{C}_{\mathrm{p}}^{\mathrm{AC}}$ that uses autocorrelation functions of waveform misfits to determine the correlation lengths (see Section 2.3.4 of Chapter 2). To be comparable to the model prediction error for the geodetic data, we assign the uncertainty in $\mathbf{C}_{\mathrm{p}}$ for tsunami waveforms as 10% of the maximum waveform amplitude for each station. The uncertainty in $\mathbf{C}_{\mathrm{d}}$ for tsunami waveforms is a constant of 1 cm based on a conservative estimate of the instrumental

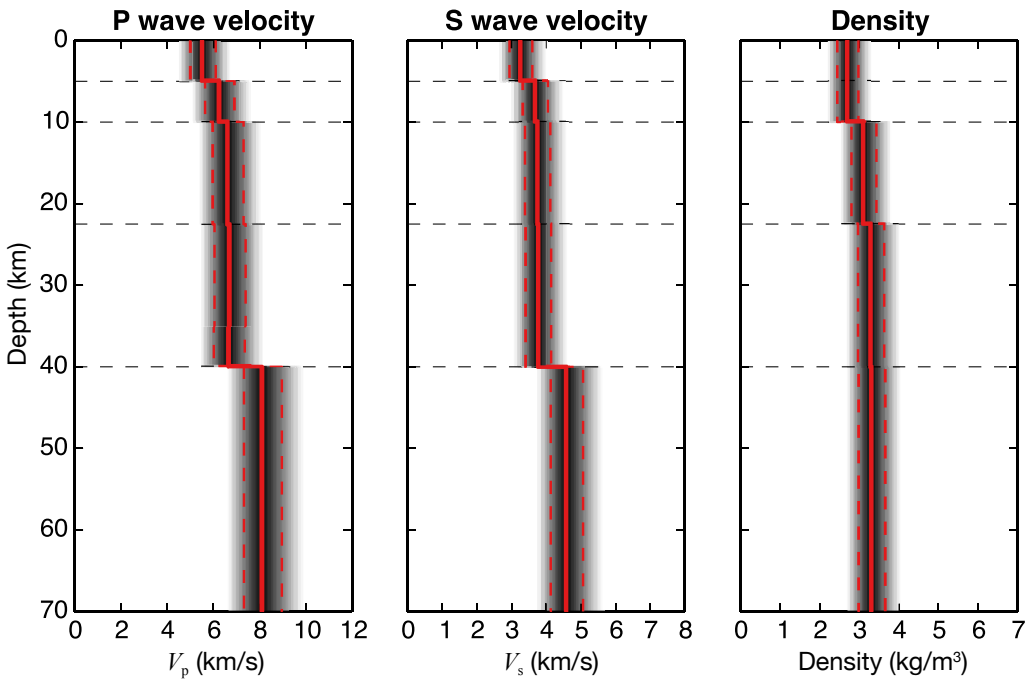


Figure 3.2: *The reference velocity model and perturbed models.* The 1D velocity model (solid red lines) is extracted from *Tassara et al.* (2006) and *Haberland et al.* (2009). The region in gray indicates the approximate range of perturbation from the reference model, with $1\sigma$ deviation shown as the dashed red lines.

accuracy. The resultant $\mathbf{C}_\chi$ are shown in Fig. 3.3B.

There are other forms of modeling uncertainties that we do not consider here, e.g., the uncertainty in the fault geometry. However, by designing a curved fault geometry from a 3D plate interface model with multiple constraints (Sec. 3.2.1), we have made our best efforts to mitigate such inaccuracy in the GF.

## 3.3 Results and discussions

### 3.3.1 Fault slip models from tsunami, geodetic, and joint inversions

In Fig. 3.4, we show the posterior mean models of fault slip distribution derived from tsunami, geodetic, and joint inversions that incorporate $\mathbf{C}_\mathrm{p}$, together with their uncertainties. We apply posterior spatial averaging over the nearest "one-ring" (1R) neighbors for

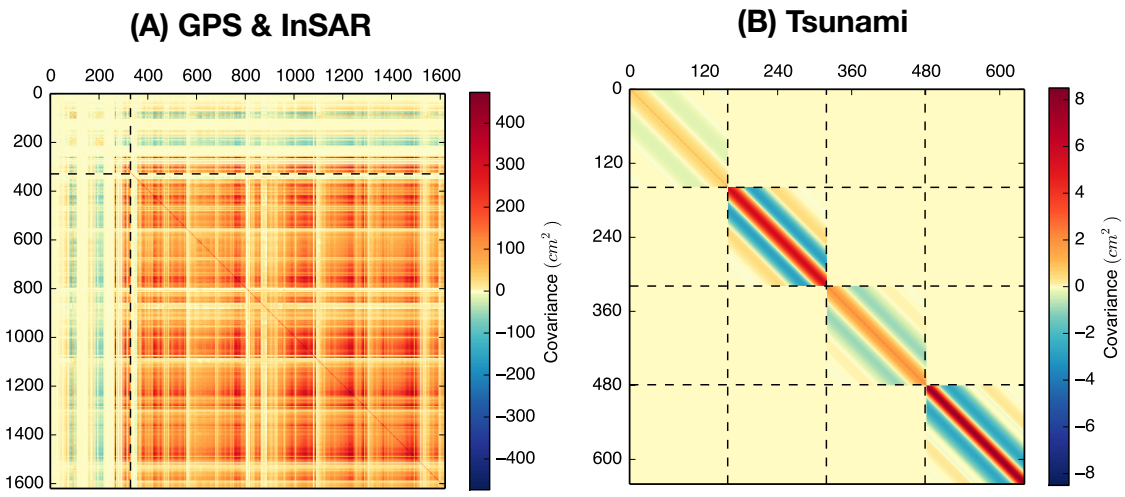


Figure 3.3: $\mathbf{C}_\chi$ *for the geodetic (GPS and InSAR) and tsunami modeling.* $\mathbf{C}_\chi$ are shown for (A) GPS and InSAR observations, and (B) tsunami waveforms. Both horizontal and vertical axes correspond to the dimension of the data vector. The dashed lines mark the divisions between submatrices associated with the GPS and InSAR data in (A), and different DART stations in (B).

each model parameter (Section 2.3.5), so these models appear smooth over the length scales of our tent functions. For the slip models derived from only tsunami data (Fig. 3.4A), fault patches that do not underlie water produce negligible tsunami, and hence their estimates are not affected by the data, with error ellipses of the slip vectors reflecting only the prior constraints. Even in the near-source region, non-zero slip is only resolved over large spatial scales, suggesting that the far-field tsunami waveforms for this event only provide relatively low resolution on the estimated distribution of fault slip. In contrast, the geodetic-only models (Fig. 3.4B) resolve downdip fault slip and peak slip offshore. In this case, the dense coverage of geodetic measurements and the relatively short distance between the coast and the trench allow some resolution in the updip regions, as indicated by the decreased size of error ellipses for those near-trench nodes, albeit with the general trend of decreasing resolution toward the trench. The models based on joint inversions of tsunami and geodetic observations (Fig. 3.4C) have slip better constrained almost everywhere compared to

separate inversions. While tsunami data has overall low resolution on the slip model, it still contributes to reducing the parameter space when quality geodetic constraints are included. To the south, the shallow slip in the geodetic model is discouraged by the inclusion of the tsunami data. To the north, small slip at the trench is observed up dip to the region of maximum slip. Although the amplitudes for the near-trench slip found in the geodetic model are not significantly altered in the final joint solutions, their uncertainties are further reduced with the constraints from the tsunami data. Therefore, the tsunami observation is still important for constraining the shallow fault slip process. We note some backward slip to the southernmost end of the geodetic and joint models, mostly within the error ellipses. This feature suggests that there might be incompatibility between error models, GFs, and/or data to some extent.

We also show the distributions of earthquake moment magnitudes for the posterior models in Fig. 3.4, using depth-dependent rigidity values calculated from the reference velocity model (Fig. 3.2). The solutions constrained by only tsunami observation feature a wide range of magnitudes with a mean value of 8.82, while magnitudes of geodetic and joint models are more tightly constrained, with the same mean magnitude of 8.94. Since static observations only constrain the potency of the event, rather than the magnitude, these estimates can be altered with different assumptions of the elastic structure, and therefore may still be reconciled with the estimate from seismic studies ($M_{\mathrm{w}} = 8.8$; *Lay et al.*, 2010). The overall discrepancy between tsunami-only and geodetic-inclusive models could be attributed to the very early postseismic deformation, which is potentially recorded by only the InSAR and GPS measurements.

In Fig. 3.5, the predictions of the surface displacement field using posterior solutions show similar features as the fault slip models in terms of the locations of the peak value, as

well as the complementarity of geodetic and tsunami data in reducing the uncertainties for the prediction.

In Figs. 3.6-3.8, we evaluate the performance of 1R smoothed posterior solutions (see Chapter 2) of our favored joint models in reproducing InSAR and GPS measurements, and tsunami waveforms within the assumed uncertainties. In Fig. 3.6, InSAR measurements show excellent match between the data and prediction from the mean model, with no systematic misfit. While uncertainty of data and variability of model predictions are difficult to visualize for dense InSAR measurements, we do so for the GPS measurements in Fig. 3.7. We show three types of error ellipses that correspond to $\mathbf{C}_\mathrm{d}$ (black), $\mathbf{C}_\mathrm{p}$ (blue), and $\tilde{\mathbf{C}}_\mathrm{d}$ (red), where $\tilde{\mathbf{C}}_\mathrm{d}$ is the posterior data covariance matrix and is obtained through $\tilde{\mathbf{C}}_\mathrm{d} = \mathbf{G} \cdot \tilde{\mathbf{C}}_\mathbf{m} \cdot \mathbf{G}^T$. The observational errors represented by $\mathbf{C}_\mathrm{d}$ is usually much smaller than the model prediction errors represented by $\mathbf{C}_\mathrm{p}$, which corresponds to about 10% log-normal uncertainties in the elastic parameters. In particular, the error ellipses for the vertical GPS components are greatly increased, suggesting that the vertical components are more sensitive to the elastic structure. Indeed, considering $\mathbf{C}_\mathrm{p}$ avoids overfitting of the vertical components while still reproduces the large-scale features well, e.g., the transition from uplift to subsidence. The residuals of the GPS displacements (Fig. 3.7C, D) are well within the uncertainty, and thus not significant. In Fig. 3.8, we show the fit for the tsunami waveforms using the posterior solutions and predictions of later waveforms which are not included in the inversion. In general, the range of synthetic waveforms matches the observed waveforms well, even for the general trend in later arrivals, which are usually more susceptible to the complexity in wavefront interactions and more difficult to simulate accurately.

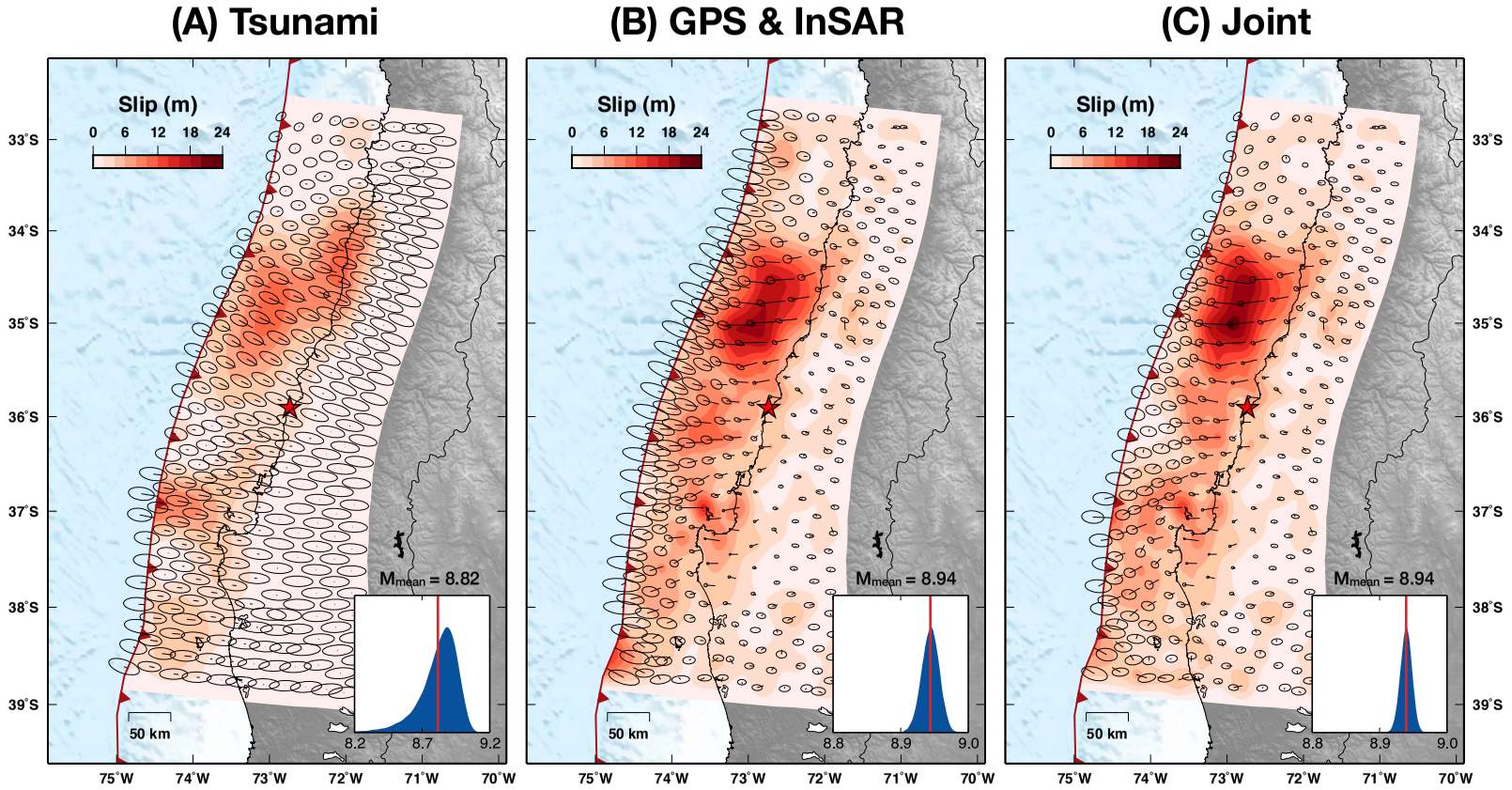


Figure 3.4: *Coseismic fault slip models from tsunami, geodetic, and joint inversions with* $\mathbf{C}_\chi$. Tsunami dispersion is considered for (A) and (C). A 1D elastic layered structure is used in computing both seafloor and land deformation for (A-C). The posterior mean models are shown with the slip amplitude in color and slip directions represented by the vectors outward from the nodes. Error ellipses represent the uncertainty of and correlation between the dip-slip and strike-slip components at each node. Event hypocenter is indicated by the red star. The posterior distribution of the corresponding earthquake moment magnitudes (blue histogram), together with the mean value $M_{\text{mean}}$ (red line), is shown for each model ensemble in the bottom right corner. (C) is our favored joint model.

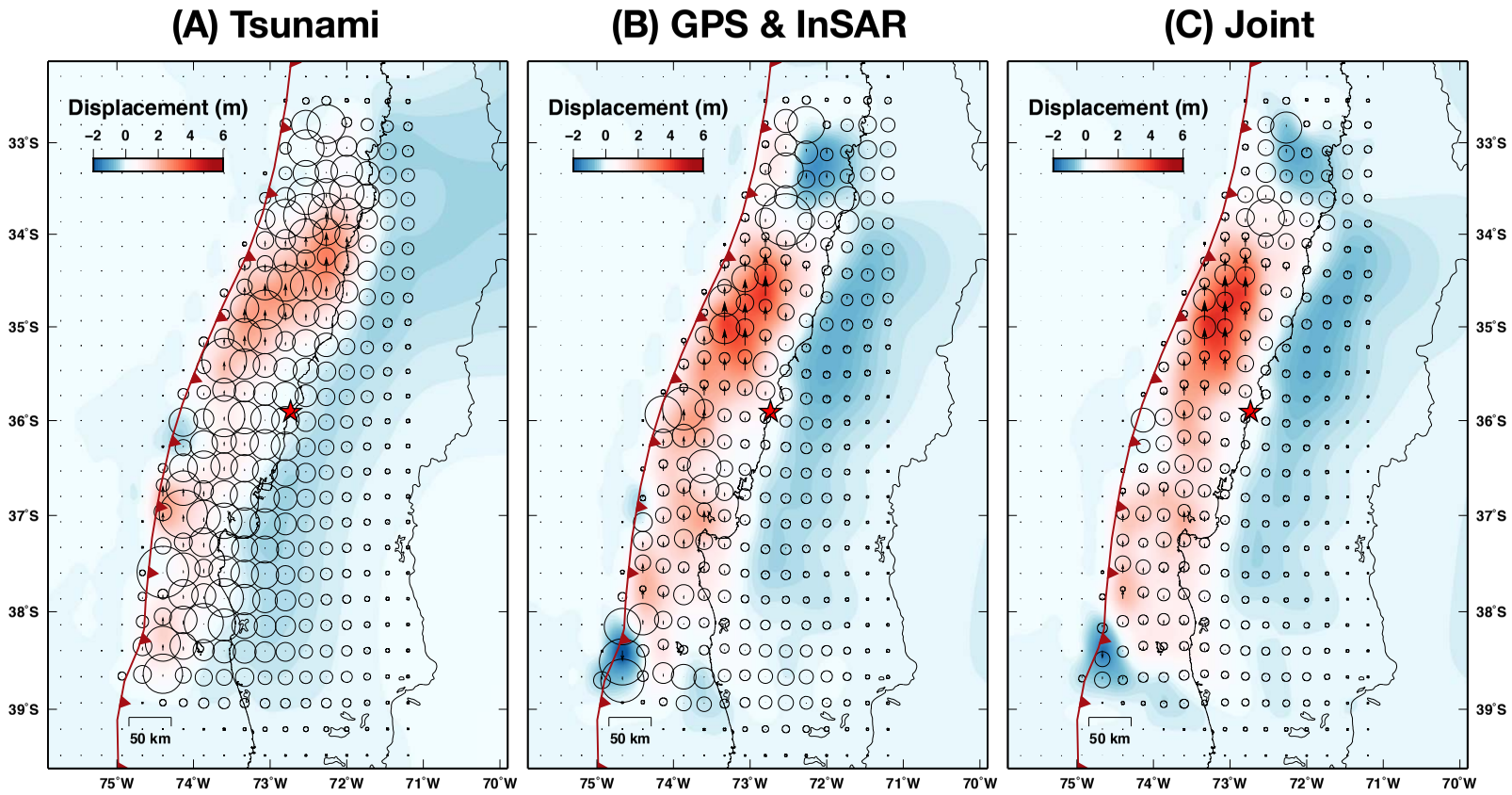


Figure 3.5: *Predicted surface displacement from tsunami, geodetic, and joint models with* $\mathbf{C}_\chi$. Surface displacement field is shown in color based on the posterior prediction and interpolation on a dense grid, with uplift vectors and associated error ellipses shown for representative points.

### 3.3.2 Effects of dispersion, elastic structure, and error models

The elastic structure and tsunami propagation model are essential elements in our GF calculations for the geodetic and tsunami data, and also the largest sources of uncertainties in our problem. For typical choices of the elastic structure, a homogeneous half-space or a layered structure could make a difference in the calculated GF for surface displacements and the inferred models. In principle, 3D models would be more realistic (e.g., *Masterlark et al.*, 2001; *Masterlark*, 2003; *Hsu et al.*, 2011), but such models are not very well constrained. For tsunami propagation, using dispersive or non-dispersive wave equations can also affect the timing and waveforms in the GFs (e.g., *Allgeyer and Cummins*, 2014). Therefore, adopting more accurate GFs, together with consistent error models $\mathbf{C}_\mathrm{p}$, is important for deriving more robust posterior solutions.

In Fig. 3.9, we show different slip models based on inversions of geodetic data with a homogeneous half-space or a layered structure, combined with either $\mathbf{C}_\mathrm{d}$ or $\mathbf{C}_{\boldsymbol{\chi}}$. The half-space solutions with $\mathbf{C}_\mathrm{d}$ (Fig. 3.9A) produce more shallow slip away from the coast, with significant artifacts in the form of backward slip away from the source region, suggesting that the observational error $\mathbf{C}_\mathrm{d}$ is not compatible with the GFs used in this case. Slip models based on the layered structure (Fig. 3.9B,C) have much smoother solutions, and artifacts are mitigated in particular when we consider $\mathbf{C}_{\boldsymbol{\chi}}$ in Fig. 3.9C. *Lin et al.* (2013) found similar pattens of slip that extends closer to the trench in half-space models compared to those with a layered structure, but their solutions are still further downdip compared to Fig. 3.9C, perhaps in part due to ignoring $\mathbf{C}_\mathrm{p}$.

In Fig. 3.10, we demonstrate the effect of tsunami dispersion on the inversions of fault slip models using tsunami data alone. We use the same layered structure for computing seafloor displacements in these models. Slip models based on non-dispersive tsunami GF

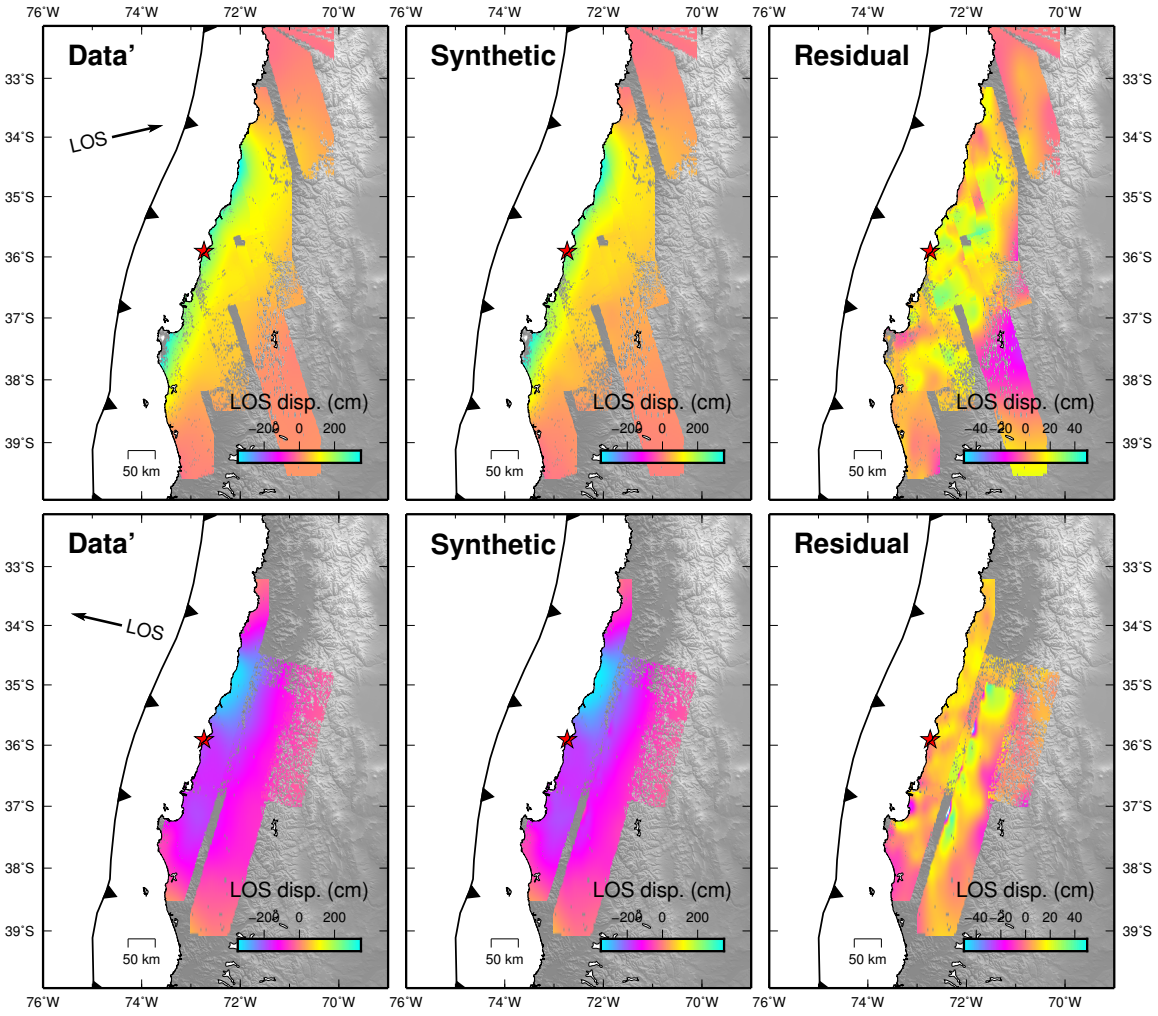


Figure 3.6: *Observed and predicted InSAR measurements using the favored joint models.* Observations, synthetics and residuals are shown for ascending (top) and descending (bottom) tracks. Orbital ramps are derived from the inversion and removed from the data and synthetics shown. Residuals are calculated by subtracting the synthetics from the data and are plotted with a different color scale. The satellite-to-ground line-of-sight (LOS) vector is shown.

(Fig. 3.10A) tend to place more coseismic slip below the coast, in order to compensate for the faster propagation speed of non-dispersive waves than those in reality. Models with $\mathbf{C}_\chi$ are devoid of noticeable backward slip in most regions. However, the location of maximum slip is away from the trench compared to cases considering dispersion, as also observed by *Yue et al.* (2014).

We also consider joint models with only $\mathbf{C}_\mathrm{d}$ in order to assess the effect of error models on the posterior solutions, even when more accurate GFs (considering tsunami dispersion and/or a layered elastic structure) are used. We find that models inverted from single datasets have the maximum slip at different locations due to the tendency of overfitting, and the final joint models feature larger amplitudes of peak slip, greater slip heterogeneity, and more significant backward slip in the solutions, suggesting incompatibility between error models and GFs, compared to cases including $\mathbf{C}_\mathrm{p}$ (Fig. 3.4).

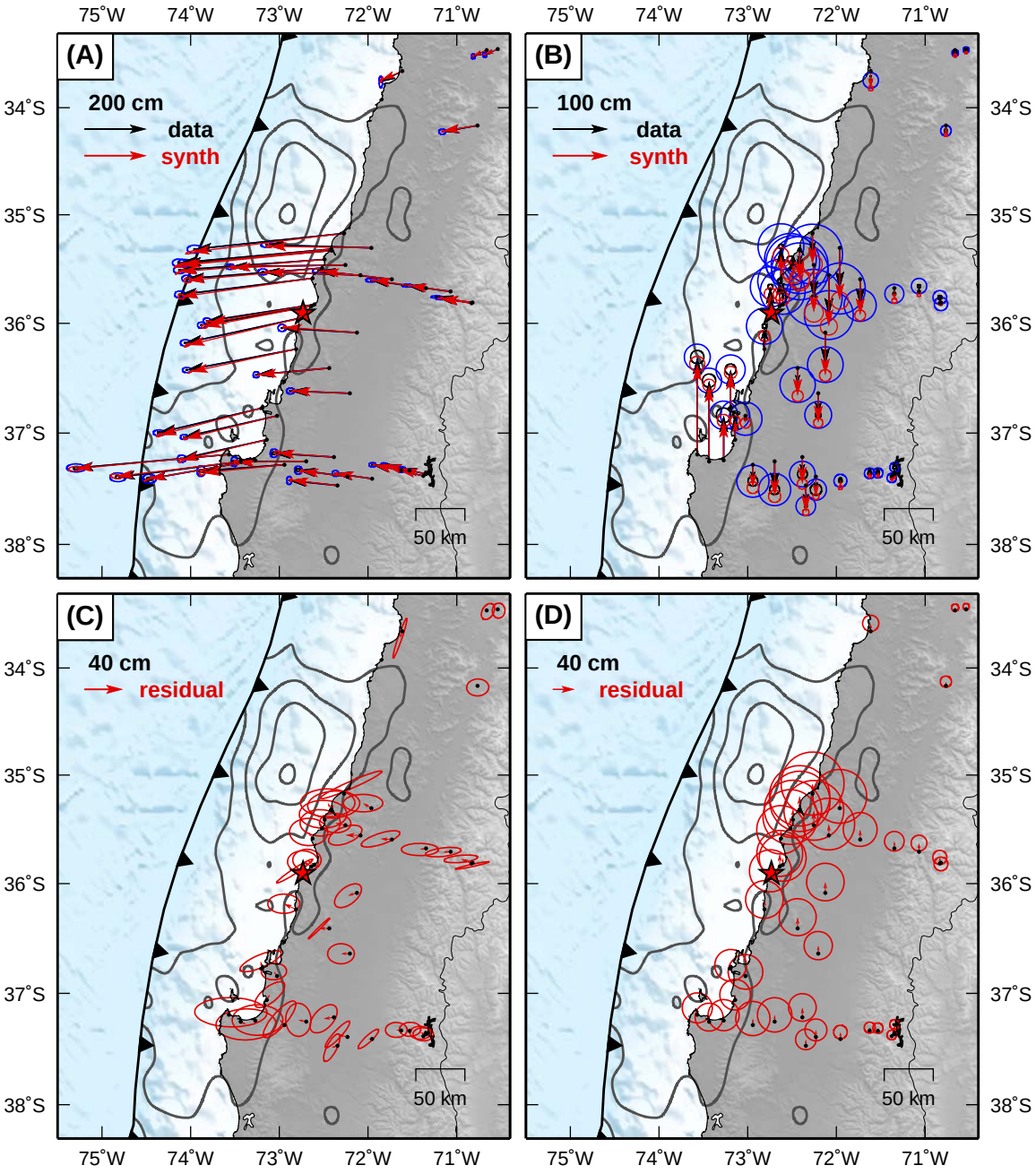


Figure 3.7: *Observed and predicted GPS displacements using the favored joint models.* (A, B) Observations (black) and predictions (red) for the (A) horizontal and (B) vertical components of GPS displacements. Error ellipses represent the uncertainty and correlation in $\mathbf{C}_\mathrm{d}$ (black), $\mathbf{C}_\mathrm{p}$ (blue), and $\tilde{\mathbf{C}}_\mathrm{d}$ (red). (C, D) Residuals (data minus synthetics) for the (C) horizontal and (D) vertical components. Correlations between east and north components are considered in (A, C) and no correlation is considered in (B, D). The slip contours for our favored mean model are shown in black with intervals of 5 m starting at 5 m.

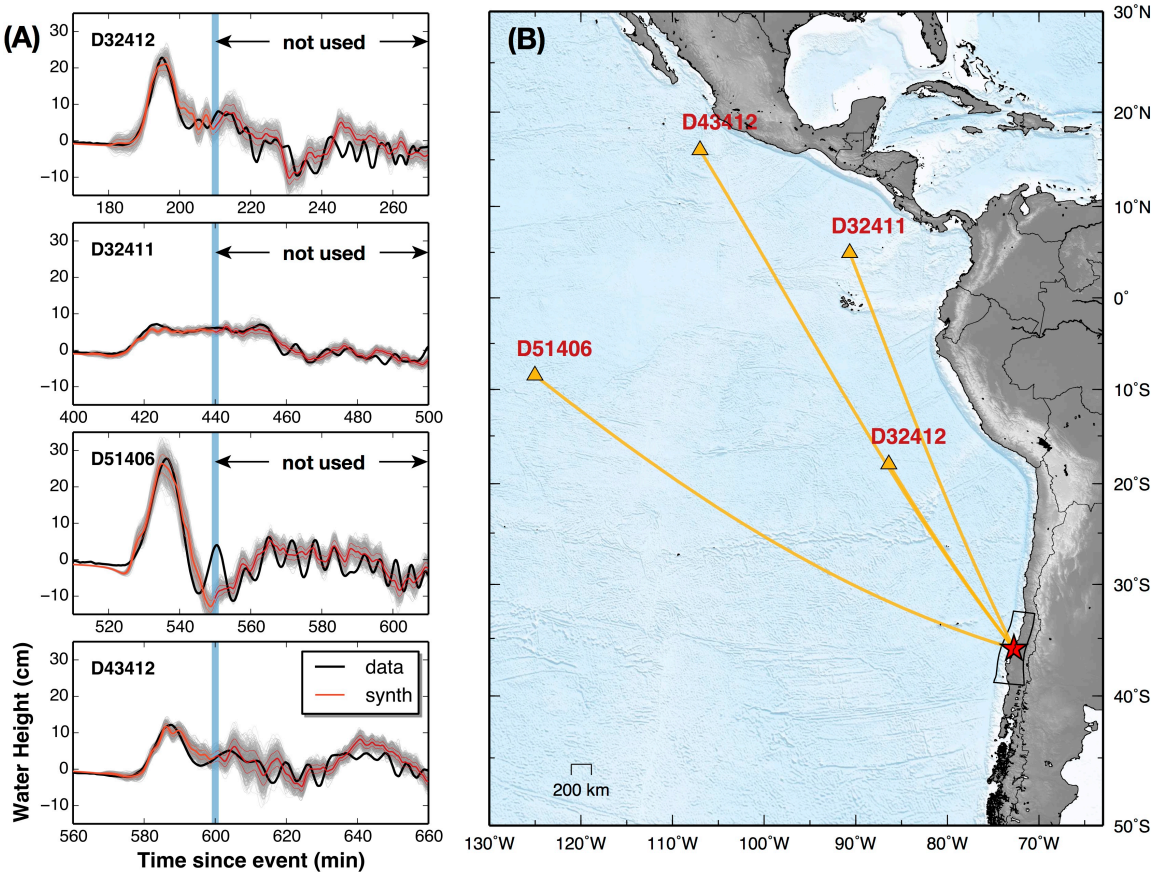


Figure 3.8: *Observed and predicted DART waveforms using the favored joint models.* (A) The observed tsunami waveforms at DART stations are represented by thick black line. The predicted waveforms from an ensemble of joint models are in gray, with their mean values and $1\sigma$ uncertainty indicated by the thick and thin red lines, respectively. Only the first 40 min of the waveforms (to the left of the blue lines) are used in the inversions. (B) Station distribution and the approximate great-circle paths between the source and stations.

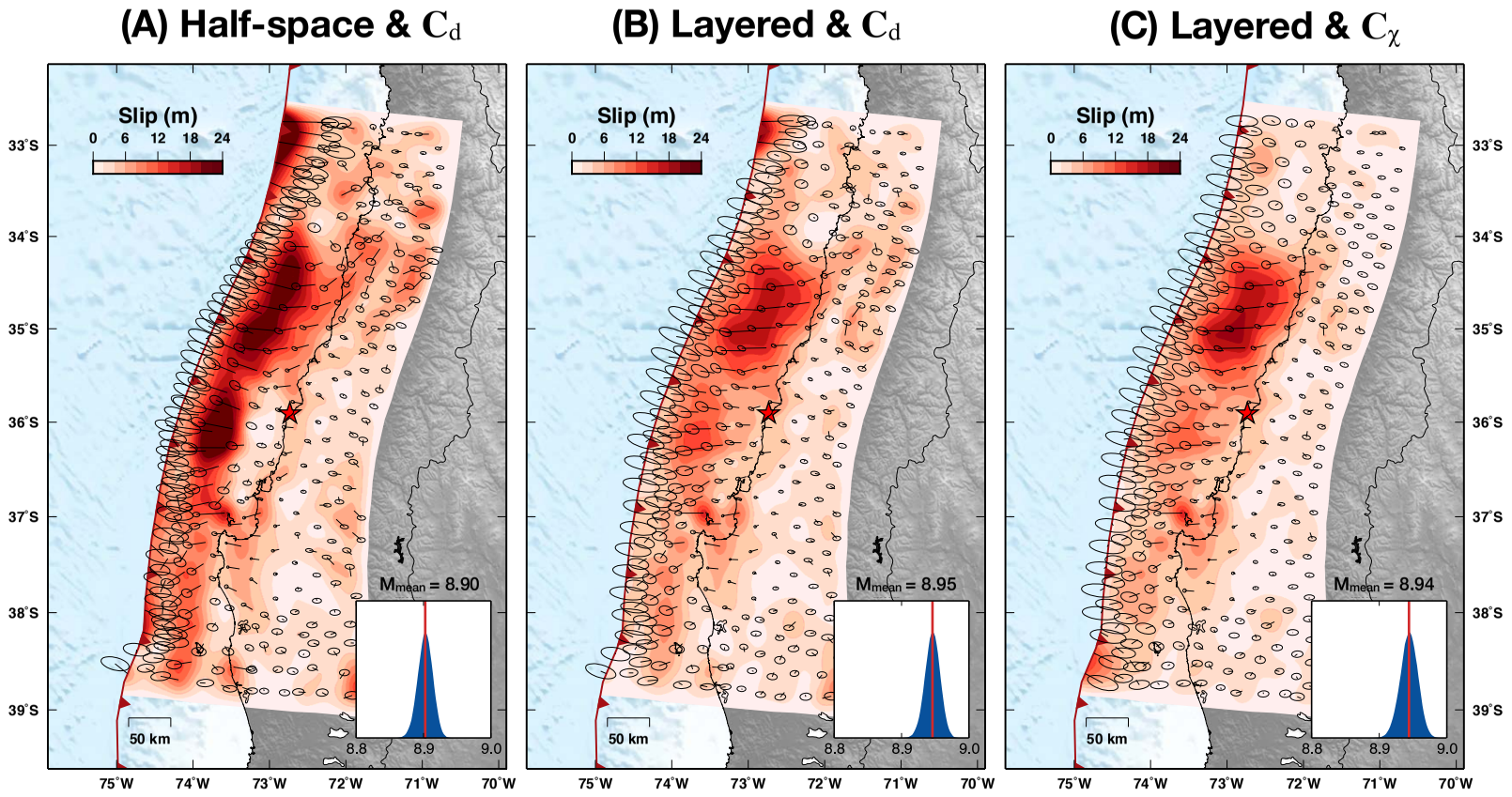


Figure 3.9: *The effect of elastic structure and error models on geodetic inversions.* The combinations of Green's functions in a homogeneous half-space or a 1D layered structure, with $\mathbf{C}_d$ or $\mathbf{C}_\chi$, are used in the inversions. All plotting conventions follow Fig. 3.4.

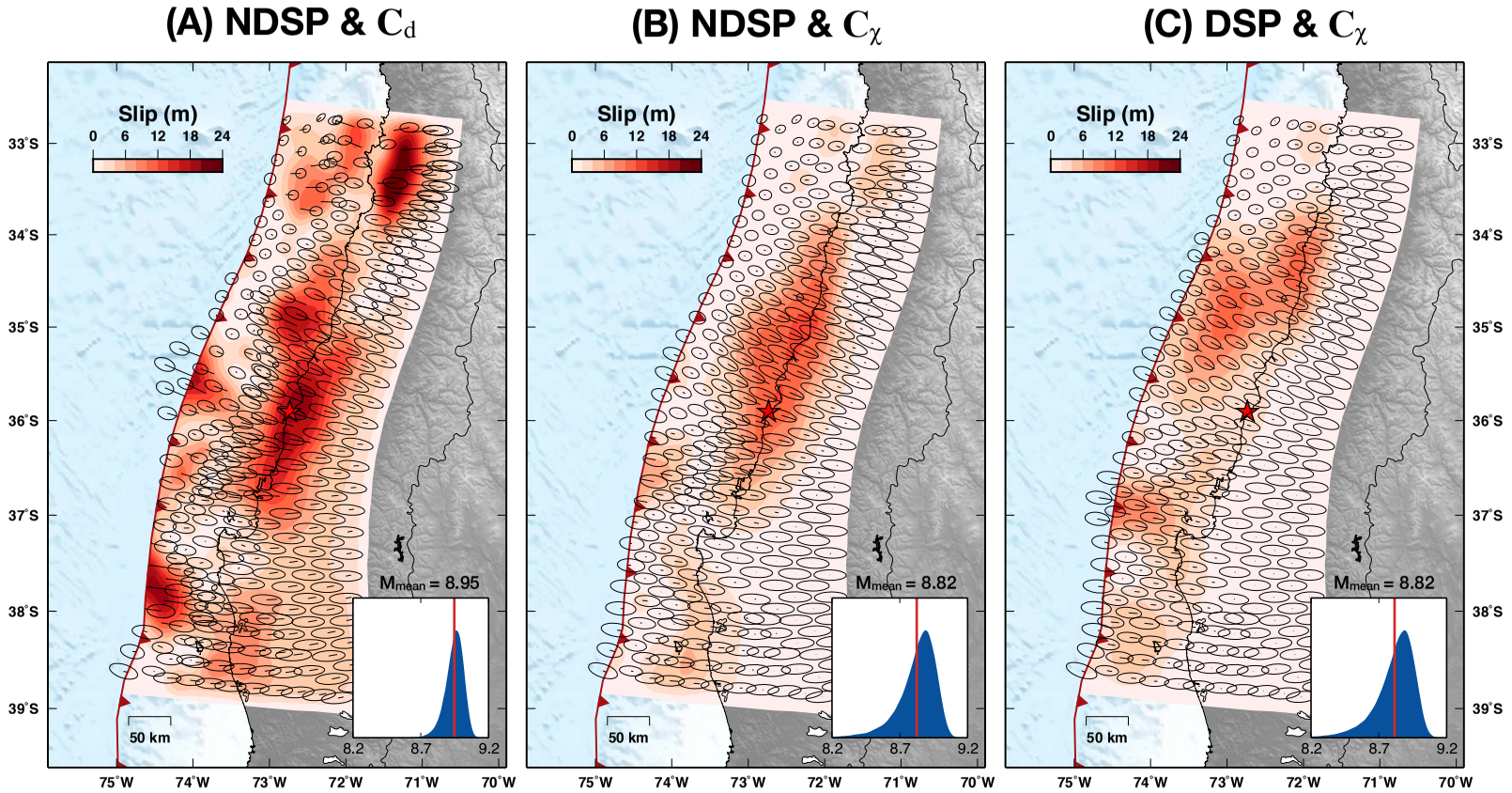


Figure 3.10: *The effect of dispersion and error models on tsunami inversion.* The combinations of non-dispersive (NDSP) or dispersive (DSP) tsunami GFs, and $\mathbf{C}_\mathrm{d}$ or $\mathbf{C}_\chi$, are used in the inversions. The seafloor deformation is computed using the same layered structure as in Fig. 3.4(A). All plotting conventions follow Fig. 3.4.

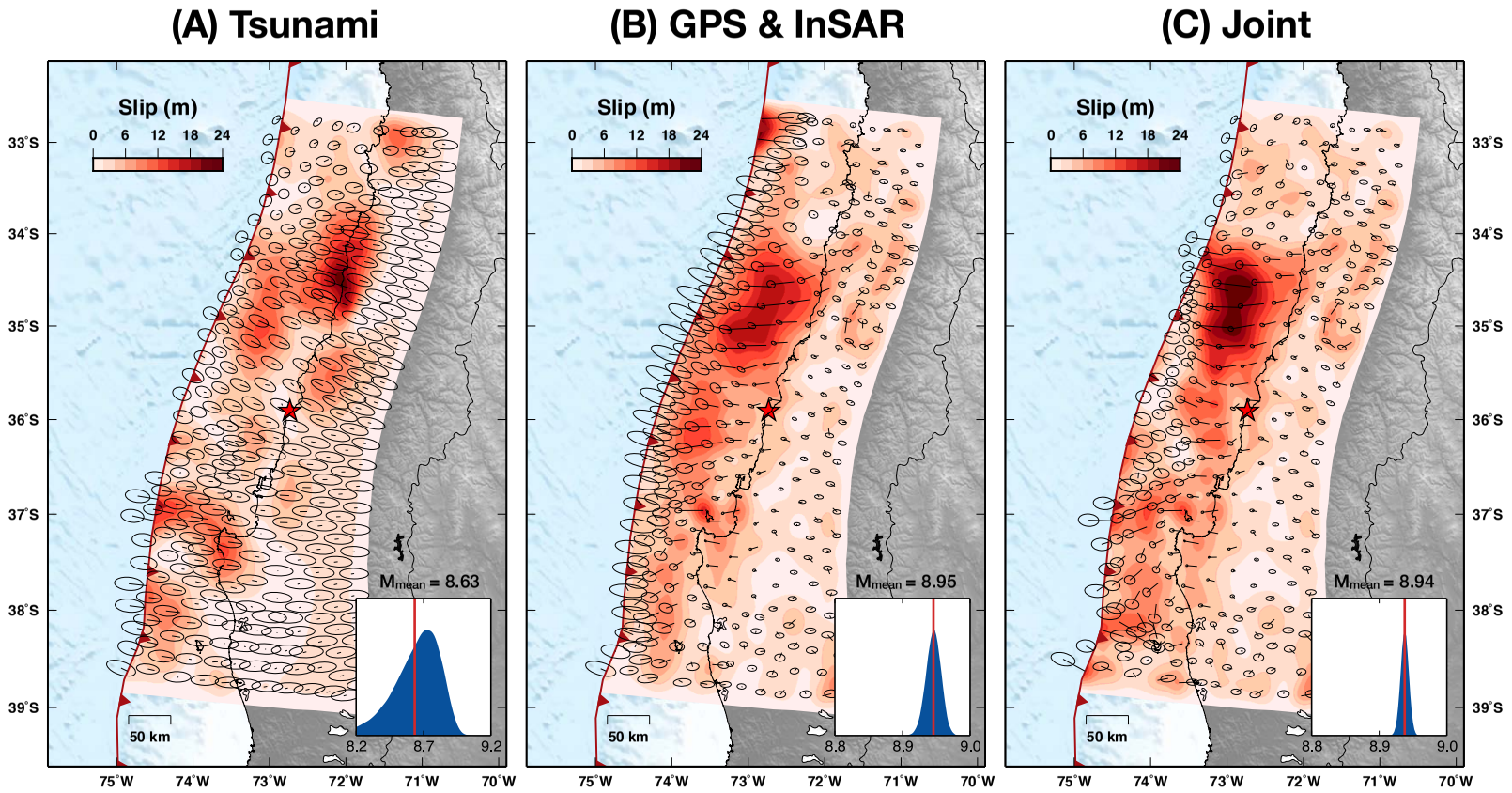


Figure 3.11: *Coseismic fault slip models from tsunami, geodetic, and joint inversions with* $\mathbf{C}_d$. Tsunami dispersion is considered for (A) and (C). A 1D elastic layered structure is used in computing the seafloor and/or land deformation for (A-C). All plotting conventions follow Fig. 3.4.

### 3.3.3 Updip and downdip resolution of fault slip

Our favored mean model from the joint inversion (Fig. 3.4C) has a peak slip of about 21 m, larger than the approximate 15 m in some geodetic-based studies (e.g., *Vigny et al.*, 2011; *Lin et al.*, 2013) and similar to other joint models which include tsunami data (*Lorito et al.*, 2011; *Yue et al.*, 2014). The relatively concentrated slip in our model is partially due to the fact that we do not have *a priori* smoothing and the posterior averaging operator only favors solutions with characteristic length scales larger than the spatial range of our tent functions. The downdip limit of fault slip in the model matches the coastline closely, which is similar to most models with geodetic constraints (*Delouis et al.*, 2010; *Tong et al.*, 2010; *Lorito et al.*, 2011).

In Fig. 3.12, we show the cross-sectional profile of the predicted surface displacement through the region of maximum slip and normal to the trench. The peak seafloor uplift of 4 m occurs about 50 km landward from the trench, and decreases to about 1 m or less at the trench axis, corresponding to the small coseismic slip near the trench as seen in the mean models. The seismic potency integrated along the strike (Fig. 3.13) also suggests that the maximum potency release approximately coincides with the maximum seafloor uplift, and a small fraction of the total potency release occurs at the trench. The transition from seafloor uplift to subsidence coincides with the coastline, with coseismic vertical motion anti-correlated with the topography. This anti-correlation suggests that the topography may represent some inelastic fraction of the long-term interseismic deformation (e.g., *Song and Simons*, 2003).

Geodetically constrained models (e.g., *Tong et al.*, 2010; *Vigny et al.*, 2011; *Lorito et al.*, 2011; *Lin et al.*, 2013) are generally similar in their along-strike locations of peak slip and the slip to the south of the hypocenter. However, their solutions differ greatly in the updip

direction, which could be due to different elastic structures, approximation of fault geometry near the trench, different approaches to the inverse problem and regularization schemes, or the impact of tsunami observations used in some studies.

It is worth noting the largest variability between the three studies that include the tsunami data: a kinematic model based on teleseismic, geodetic, and tsunami data from *Yue et al.* (2014), a static model based on geodetic and tsunami observations from *Lorito et al.* (2011), and a static tsunami-only model from *Fujii and Satake* (2012). The difference between the large slip (about 20 m) near the trench in *Yue et al.* (2014) and no shallow slip in *Lorito et al.* (2011) can be partly due to that the former study includes tsunami dispersion. The model of *Fujii and Satake* (2012) places maximum slip directly below the coast, unlike the other two. Such discrepancy is likely due to that a large null space exists for the tsunami-only inversion in this case (Fig. 3.10), with the resultant best-fitting model highly dependent on the assumed regularization and error models.

The use of a layered structure tends to produce models with slip closer to the coast, compared to the case with a half space, as demonstrated in Fig. 3.9. This is approximately the opposite effect of incorporating tsunami dispersion, which tends to prefer more near-trench slip. Therefore, ignoring either or both effects could lead to a large variability in the final solutions, which might explain much of the discrepancies between different source models, in addition to different inversion schemes.

In Fig. 3.14, we show the comparison between our favored mean slip model with a published model of the accumulated postseismic slip between the $1^{st}$ and $487^{th}$ days after the earthquake (*Lin et al.*, 2013), as well as the aftershocks for the corresponding time period (*Rietbrock et al.*, 2012). The postseismic model is built on similar plate interface geometry as our coseismic model, but is derived with a different inversion approach (*Kositsky and*

*Avouac*, 2010). In general, these two models show a more complementary spatial pattern than those shown in *Lin et al.* (2013), with limited spatial overlap, particularly to the north where slip is better constrained. Most aftershocks occur near the boundaries of co- and post-seismic slip, with clusters of concentrated seismicity to the north, potentially suggesting their responses to stress perturbations and the afterslip right next to the ruptured region (e.g., *Hsu et al.*, 2006).

## 3.4 Conclusion

We develop a semi-analytical Bayesian approach to derive the posterior solutions of coseismic finite-fault slip models for the 2010 $M_{\mathrm{w}}$ 8.8 Maule, Chile earthquake, using both tsunami and geodetic observations. Our computationally efficient method for the linearized problem allows for closed-form expressions for the posterior models and uncertainty estimates. Using uninformative priors, we are able to explore the inherent resolution of each dataset and their respective roles in the joint inversions. These understandings are fundamental for the success of more complicated joint inversions in the Bayesian framework (such as the AlTar we introduced in Chapter 2), which can further incorporate seismic waveforms into a kinematic problem, and adopt stronger prior constraints based on well-justified physics.

We demonstrate how the combinations of assumed error models and approximations in GFs, including the effects of tsunami dispersion and layered structure, can affect fault slip models based on inversions of tsunami, geodetic, or joint datasets. Our favored joint models that incorporate improved GFs for tsunami and geodetic data, as well as realistic model prediction uncertainty, are characterized by a maximum slip of 21 m offshore to the north of the hypocenter, which is generally consistent with most previous studies. Coseismic slip of about 5 m reaches the trench, contradicting previous findings which suggest either

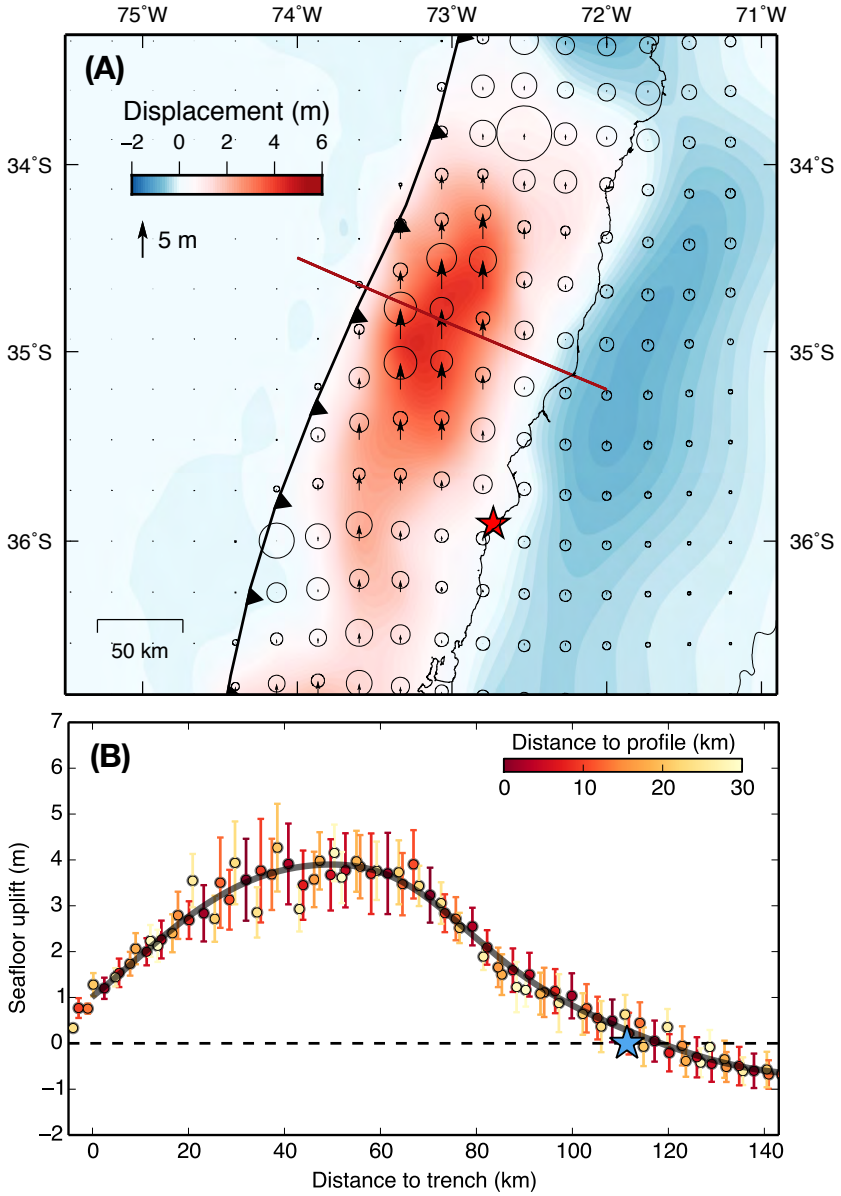


Figure 3.12: *The trench-normal profile of surface displacements predicted from the favored joint models.* (A) Map view of the surface displacement field (in color) and the location of a trench-normal cross section across the region of peak uplift (red line). (B) The profile of surface displacement along the cross section indicated in (A). Blue star represents the hypocenter location projected onto the profile. Predicted displacement on the surface grid within 30 km to the profile are plotted as circles with their uncertainties represented by the error bars and their distances to the profile in color.

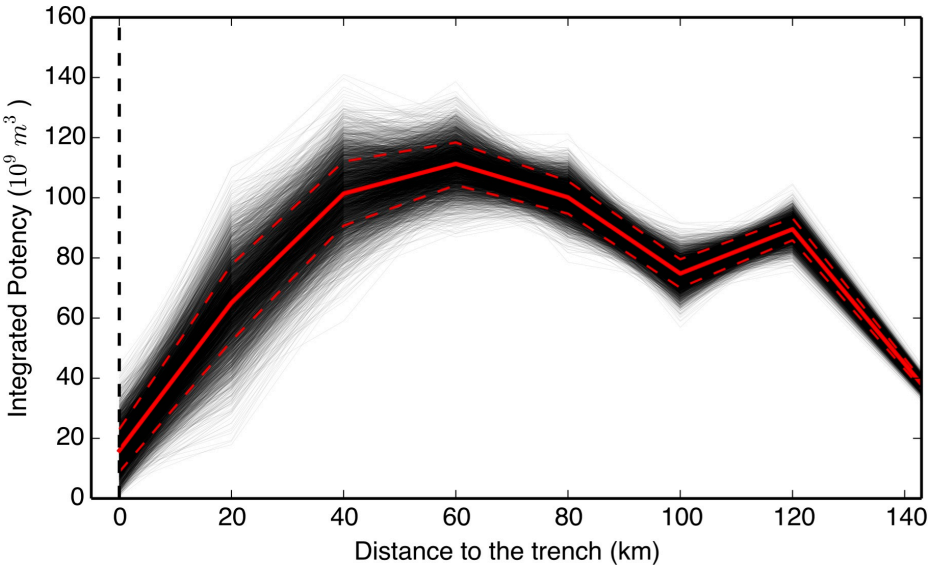


Figure 3.13: *Along-strike integrated seismic potency.* The seismic potency calculated from our favored posterior solutions is shown as a function of the distance to the trench. The mean values and $1\sigma$ error bound are shown as the solid and dashed red lines, respectively. The bump at 120 km to the trench is due to the along-strike variations of fault dip in the 3D geometry.

large near-peak slip or no slip there at all. The corresponding seafloor displacement field has a maximum uplift of 4 m, about 50 km landward from the trench at the edge of the accretionary wedge, and decreases to less than 1 m or less at the trench axis. Such an uplift profile bears resemblance to the seafloor uplift we have derived for the 2011 $M_{\rm w}$ 9.0 Tohoku-Oki earthquake in Chapter 2, with smaller amplitudes of peak uplift and near-trench uplift, which is expected for the smaller-sized Maule earthquake. Although the two earthquakes occur under different tectonic settings, with difference in the trench-to-coast distances and the locations of the hinge-line relative to the coast, such similar near-trench uplift patterns might suggest potentially common failure mechanisms of shallow subduction zones during large megathrust earthquakes.

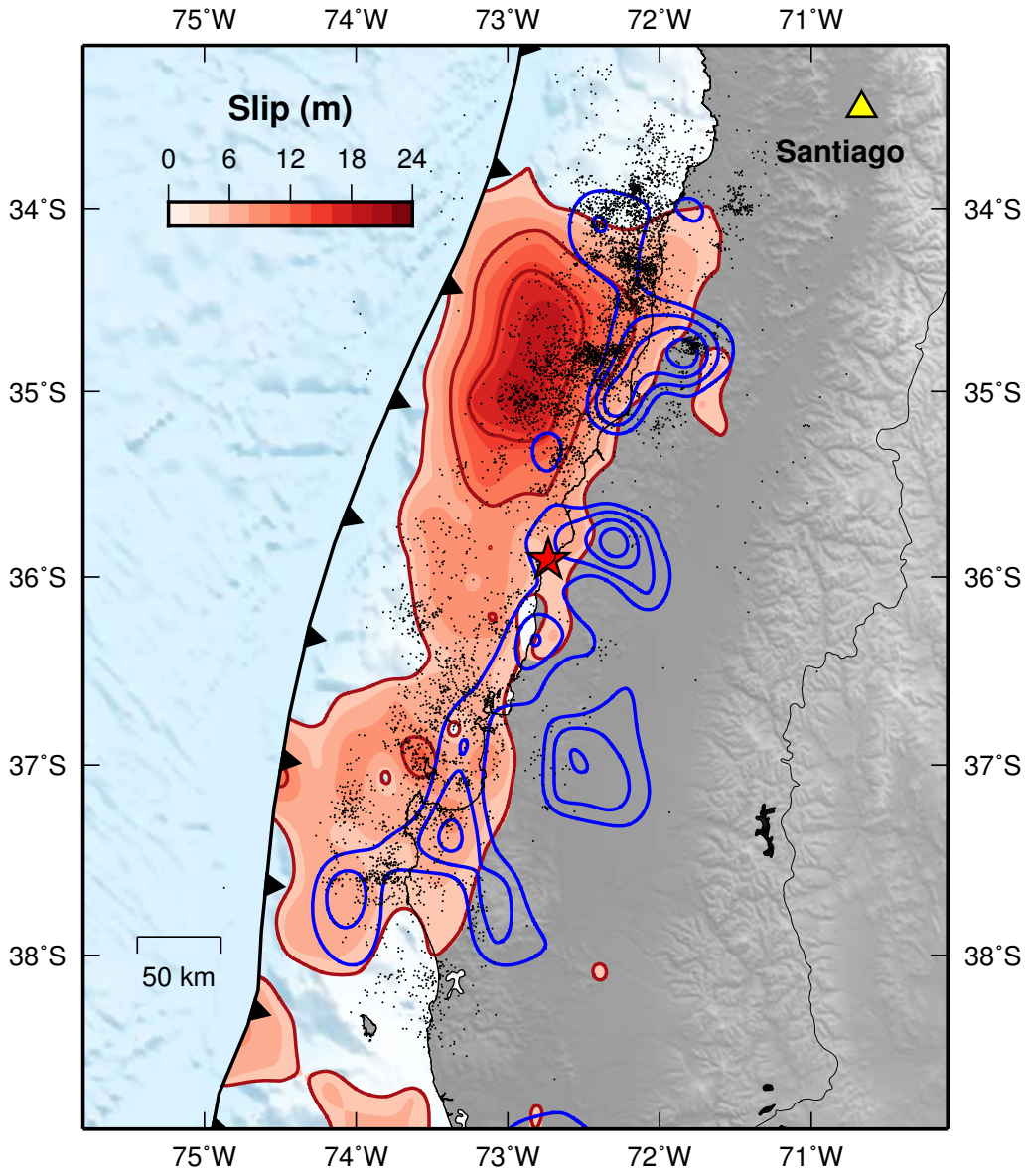


Figure 3.14: *Comparisons between co- and post-seismic fault slip models and aftershocks.* Our favored coseismic slip model is shown in color with a cut-off at 5 m and slip contours of 5 m. Slip contours for the postseismic model (*Lin et al.*, 2013) are shown in blue with intervals of 0.3 m starting at 0.3 m. Aftershocks for the same postseismic period (*Rietbrock et al.*, 2012) are shown as black dots.

# Chapter 4

# Deeper Penetration of Large Earthquake Ruptures on Seismically Quiescent Faults

# Abstract

Why some major strike-slip faults known to have had large earthquakes are silent in the interseismic period is a long-standing enigma. At the very least, microseismicity should occur at the bottom of the seismogenic zone, where loading is concentrated due to deeper aseismic deformation. We suggest that absence of such concentrated microseismicity is an indicator for deeper rupture extent in prior large earthquakes. This conclusion is supported by our numerical simulations of fault behavior as well as observations of recent significant strike-slip events. For the Carrizo segment of the San Andreas Fault in Southern California, we infer that the 1857 Fort Tejon earthquake would have penetrated below the seismogenic zone by at least 3-5 km based on our models. These findings suggest that such deeper ruptures may occur on other seismically quiescent fault segments.

## 4.1 Main Text

It is widely accepted that the style of faulting in the Earth's crust is depth-dependent, with an upper layer that supports microseismicity and large earthquakes and a lower layer that predominantly deforms stably (*Scholz*, 2002). The upper layer is commonly referred to as the "seismogenic zone" and the boundary between the two estimated geodetically is commonly called the "locking depth." This transition with depth is dominated by temperature and occurs both due to bulk properties transitioning from purely elastic to inelastic and due to quasi-static fault friction properties transitioning from velocity-weakening to velocity-strengthening (Fig. 4.1). Major strike slip faults feature extreme localization of slip at seismogenic depths (*Chester and Chester*, 1998) as well as continuing localization of the deformation even below the seismogenic layer, based on studies of deep tectonic tremor (*Shelly*, 2010), postseismic deformation (*Bruhat et al.*, 2011), and exhumed faults (*Cole et al.*, 2007); we will refer to this deeper localization as "deeper creeping fault extensions."

These deeper creeping fault extensions should load the adjacent locked fault areas, inducing microseismicity there. This is indeed observed on some fault segments, most notably the Parkfield segment of the San Andreas Fault (*Waldhauser et al.*, 2004; *Hauksson et al.*, 2012, Fig. 4.2); such pronounced microseismicity streaks that persist both in the interseismic and postseismic periods should be the norm. Yet several stretches of the San Andreas Fault, including Cholame, Carrizo, and Coachella segments, are seismically quiescent (*Hauksson et al.*, 2012, Fig. 4.3). The quiescence over most of the seismogenic zone for such mature faults can be due to their low stress in comparison to their static strength. However, the fault areas right next to the deeper creeping fault extensions should be well-stressed.

Here we show that the absence of concentrated microseismicity at the bottom of the

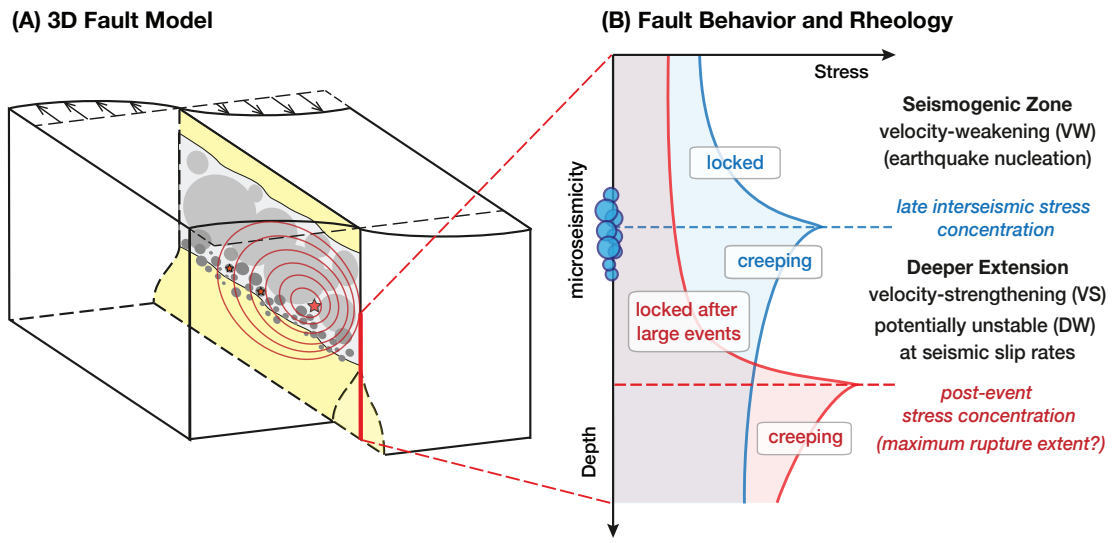


Figure 4.1: *Schematic illustration of our fault model and the locked-creeping transition.* (A) A strike-slip fault model with the seismogenic zone (SZ) (gray), creeping regions (yellow) and fault heterogeneity represented by gray circles. Initiation locations of earthquakes are indicated by red stars. Rupture fronts of a large event are illustrated by red contours. (B) As observed in the (late) interseismic period (blue curve), the locked SZ and creeping regions below are typically interpreted as having velocity-weakening (VW) and velocity-strengthening (VS) rate-and-state frictional properties, respectively. The concentrated stressing induced at the locked-creeping transition promotes microseismicity at the bottom of the SZ. However, during large earthquake rupture, the deeper creeping regions may sustain seismic slip, due to enhanced dynamic weakening (DW) at high slip rates, leading to deeper coseismic rupture extent. The locked-creeping transition after a large seismic event (red curve) is deeper than the VW/VS boundary.

seismogenic zone on mature fault segments can be due to deeper penetration of (previous) large earthquakes. We have conjectured this relation based on the following rather general mechanical consideration. If the locked-creeping transition, and the associated stress concentration, are at the boundary of, or within, the seismogenic zone capable of nucleating seismic events, then one would expect the concentrated loading to cause microseismicity (e.g., *Lapusta and Rice*, 2003). However, if dynamic earthquake rupture penetrates below the seismogenic zone, it would drop stress in the creeping areas, making them effectively locked and putting the locked-creeping transition at a depth below the seismogenic zone,

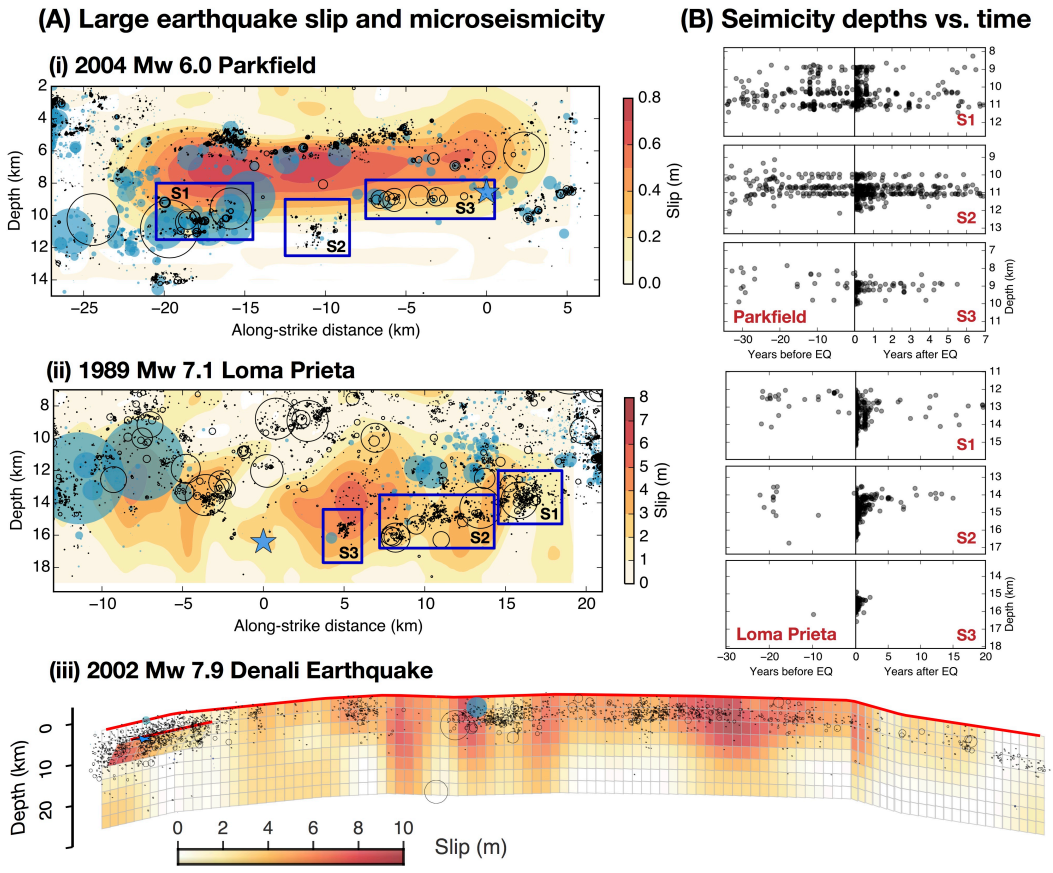


Figure 4.2: *Observations of large earthquakes and microseismicity patterns on major strike-slip faults.* (A) Spatial relations of the inferred coseismic slip during large earthquakes (in color, hypocenters as blue stars) and microseismicity before (blue patches) and after (black circles) the mainshock over time periods $T_b$ and $T_a$, respectively. Smaller earthquakes are plotted using a circular crack model with assumed stress drop of 3 MPa: (i) 2004 $M_w$ 6.0 Parkfield earthquake (*Barbot et al.*, 2012; *Waldhauser et al.*, 2004) ($T_b$ = 35 yr., $T_a$ = 7 yr.), (ii) 1989 $M_w$ 7.1 Loma Prieta earthquake (*Beroza*, 1991) ($T_b$ = 30 yr., $T_a$ = 20 yr.), and (iii) 2002 $M_w$ 7.9 Denali earthquake (*Elliott et al.*, 2007) ($T_b$ = 12 yr., $T_a$ = 10 yr.). (B) Time dependence of seismicity depth before and after the mainshock within local fault regions (outlined in blue) shown in (A).

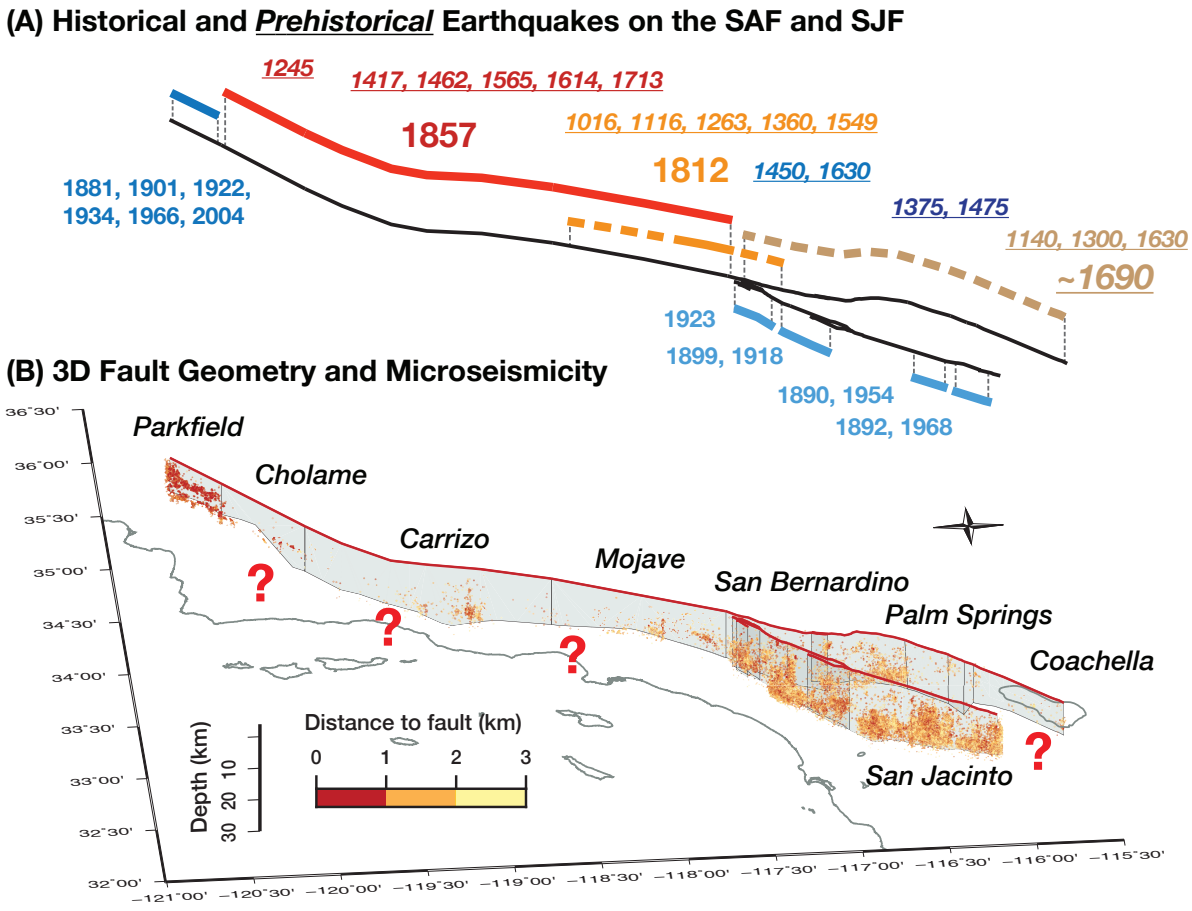


Figure 4.3: *Microseismicity and the potential for deeper ruptures on the San Andreas Fault (SAF) and the San Jacinto Fault (SJF) in Southern California.* (A) Historical and prehistorical earthquakes on the SAF and SJF with approximate rupture extents for major events (solid and dashed lines for well-documented and uncertain cases, respectively) (see Section 4.A.3). Approximate dates for prehistorical events are only shown for the SAF in underlined italics. (B) Seismicity (1981-2011) within 3 km from either the SAF or the SJF (*Waldhauser et al.*, 2004; *Hauksson et al.*, 2012). Active seismicity at great depths is observed on the Parkfield and San Bernardino segments of the SAF and on the SJF. The Cholame, Carrizo, Mojave and Coachella segments of the SAF have been seismically quiet for decades. The 1857 and ∼1690 events likely penetrated below the SZ, and similar behavior can occur in future events.

where the associated stress concentration is unlikely to initiate seismic events. Hence fault segments with deeper slip in large events would lack microseismicity at the bottom of the seismogenic zone, at least until the locked-creeping transition, which would become shallower with time due to reloading by deeper creep, reaches the seismogenic zone. Note that this argument holds regardless of whether the deeper creeping fault extensions are governed by frictional slip (as explored in this work) or inelastic (e.g., viscoelastic or plastic) flow; as long as the extensions are sufficiently localized, as supported by multiple lines of evidence (*Cole et al.*, 2007; *Shelly*, 2010; *Bruhat et al.*, 2011), the loading they impose on the seismogenic zone and its consequences should be the same.

This insight can shed light on the depth extent of past large earthquakes, and hence the potential depth extent of future earthquakes. Note that the depth extent of large earthquakes is fundamental for understanding deep crustal faulting and critically affects earthquake scaling relations and fault segment interactions, which are important ingredients in the assessment of seismic hazard (*Field et al.*, 2014). Geophysical observations of recent large strike-slip earthquakes usually do not provide reliable constraints on the depth of coseismic slip, due to the lack of depth resolution in inverting for fault-slip distribution (*Mai and Thingbaijam*, 2014, Supplementary Materials). Moreover, observations for fault segments with high seismic hazard, such as the San Andreas Fault (SAF) in Southern California, are often limited to the late interseismic periods of large events (*Fialko*, 2006). Meanwhile, a growing number of studies challenge the notion that dynamic slip during earthquakes is always confined within the seismogenic zone. Geological field studies report the overprinting of natural pseudotachylytes on mylonitic deformation, attributed to repeated seismic slip overlapping with aseismic creep below the seismogenic zone (*Lin et al.*, 2005), in accordance with the transitional regimes with brittle and semi-brittle defor-

mation mechanisms in conceptual fault models (*Scholz*, 2002; *Shimamoto*, 1989). Deeper penetration of larger earthquakes can also explain the observed slip-length scaling of large earthquakes (*Shaw and Wesnousky*, 2008).

How can dynamic rupture propagate into the deeper creeping zones that are thought to be aseismic? Current laboratory-based understanding of fault friction includes the following two aspects that have been gaining acceptance and validation through laboratory experiments and comparison of earthquake models with observations. At low slip rates of $10^{-9}$-$10^{-3}$ m/s, consistent with plate motion and processes of earthquake nucleation, friction has been successfully described by logarithmic rate-and-state friction laws (*Dieterich*, 2007, Supplementary Materials). Such laws allow to interpret the seismogenic zones (SZ) as areas of velocity-weakening (VW) properties that allow for earthquake nucleation, and the other fault areas as having velocity-strengthening (VS) properties that promote stable creep (Fig. 4.1). Models with the rate-and-state friction reproduce a wide range of fault behaviors including earthquake sequences and aseismic slip (*Barbot et al.*, 2012). However, at slip rates of $\sim 10^{-1}$ m/s and higher, enhanced dynamic weakening (DW) of fault friction, amply documented in high-velocity laboratory experiments (*Di Toro et al.*, 2011) and supported by theoretical studies (*Rice*, 2006), could dominate earthquake rupture propagation. When an earthquake reaches deeper fault extensions, increased strain rate and shear heating could lead to strain localization and dynamic weakening (*Platt et al.*, 2014), effectively turning the creeping fault regions into seismic ones (*Noda and Lapusta*, 2013).

We confirm the hypothesized relation between the depth of coseismic slip in large earthquakes and microseismicity patterns by numerical simulations of earthquake sequences in two fault models with the laboratory-derived friction laws, without and with deeper penetration of large events (Fig. 4.4). In model M1, dynamic weakening is restricted to occur

within the seismogenic (VW) region, resulting in earthquake rupture confined within the seismogenic zone, whereas model M2 has dynamic weakening extended deeper into the VS areas below the seismogenic zone, allowing deeper earthquake rupture. We use the shear-heating-induced thermal pressurization of pore fluids (*Sibson*, 1973; *Rice*, 2006) as the dynamic weakening mechanism, since fluids can be present at deeper fault extensions; however, the qualitative results of the models should be similar for other potential dynamic weakening mechanisms. The depth extent of efficient dynamic weakening due to thermal pressurization of pore fluids may be different on different faults as it is influenced by a number of factors, including the depth dependence of the shearing zone width and permeability, the extent of the inelastic dilatancy (*Segall and Bradley*, 2012), and the effectiveness of pore pressure in reducing the effective normal stress (*Hirth and Beeler*, 2015). In both models, fault heterogeneity that could generate microseismicity is represented by circular VW patches with smaller nucleation sizes than the overall, much larger VW region that represents the seismogenic zone (Supplementary Materials). While the fault heterogeneity is likely to be more complex, we use the patches and put them only around the VW/VS transition for numerical efficiency. This is because our simulations are quite challenging, as they reproduce all stages of earthquake sequences, including spontaneous earthquake nucleation, dynamic rupture propagation with full inclusion of wave-mediated stress effects, and aseismic slip (*Barbot et al.*, 2012; *Noda and Lapusta*, 2013). The model parameters are given in the Supplementary Materials.

The two models indeed demonstrate the conjectured relation between the depth of coseismic slip in large earthquakes, microseismicity patterns, and the locked-creeping transition (Fig. 4.4B-D). The transition is defined here as the fault depth with slip rates of 10% of $V_{\max}$, the maximum slip rate over the fault at the time; this definition is different from

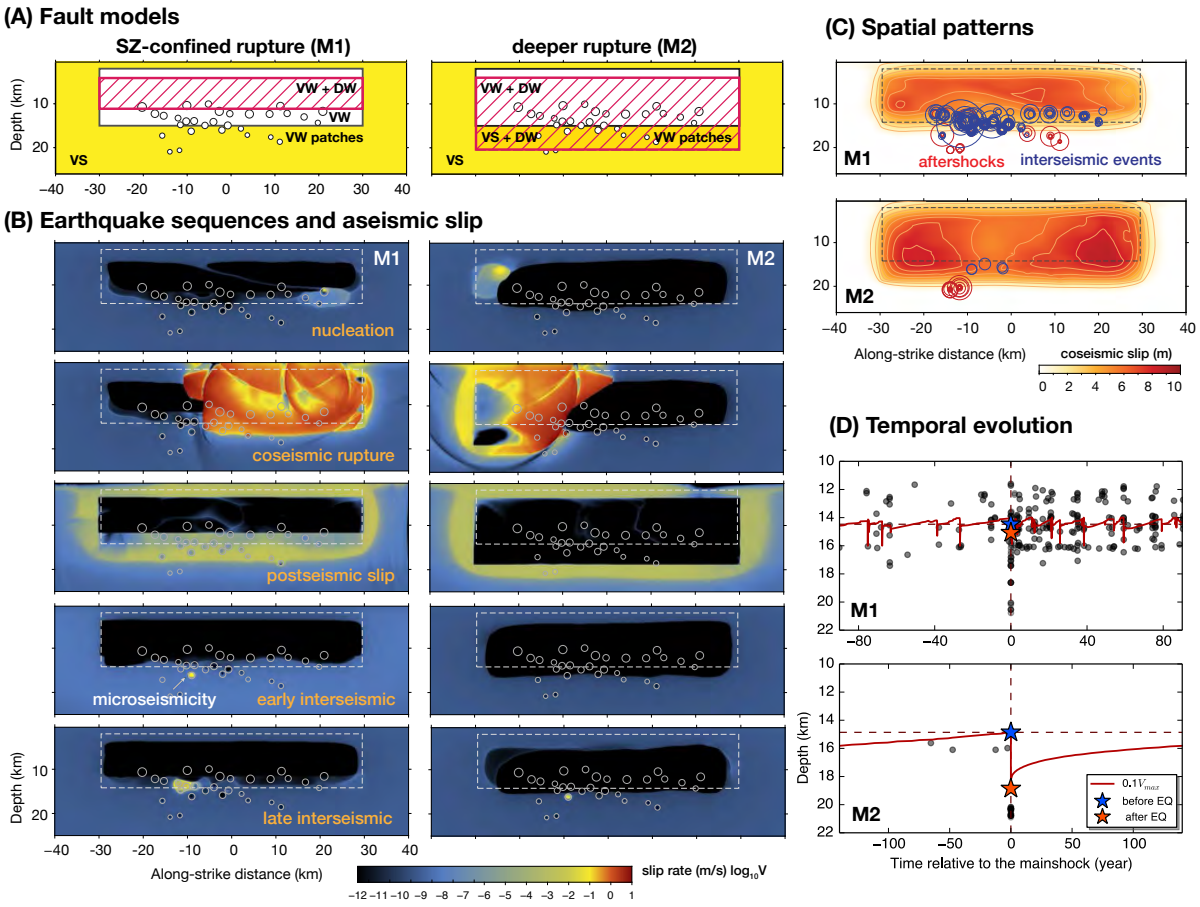


Figure 4.4: *The relation between the depth extent of large earthquakes and microseismicity in simulated earthquake sequences.* (A) Model M1 has DW (red hashed region) within the VW region (white), with ruptures confined to the SZ. Model M2 has DW extending into the VS region (yellow), potentially allowing for deeper ruptures. VW circular patches of smaller nucleation sizes represent fault heterogeneity at the transitional depths. (B) Different stages in the long-term fault behavior illustrated by snapshots of fault slip rate on a logarithmic scale. The two models differ in the coseismic rupture extent, the location of the locked-creeping transition with respect to the VW/VS boundary (white dashed outlines), and hence microseismicity activity. (C) Spatial patterns of microseismicity in the post- and interseismic periods of a typical large event (with coseismic slip in color). Smaller earthquakes are plotted using the same method as in Fig. 4.2. Note the microseismicity streaks in M1 and their near-absence in M2. (D) Time evolution of the locked-creeping transition (LCT) (red line) and seismicity depths (black dots). The blue and red stars represent the depth of LCT before and after the mainshock, respectively. The time windows equal the recurrence times (180 and 280 yr., respectively)

the locking depth inverted from geodetic observations, which interprets the actual depth distribution of slip rates in terms of a simplified locked/fully creeping model. Coseismic slip of large events penetrates into the deeper fault extensions in model M2 but it is largely confined within the seismogenic zone in model M1, as intended. Correspondingly, in M1, the locked-creeping transition is at the bottom of the seismogenic zone from the beginning of the interseismic period, causing abundant microseismicity throughout the interseismic period. In M2, however, the locked-creeping transition is below the seismogenic zone throughout the interseismic period, leading to a small number of seismic events, mostly at the end of the interseismic period and on the VW patches positioned below the large-scale VW/VS transition. The locked/creeping transition migrates up dip over time, and the migration can be approximately predicted based on the earthquake stress drop , product of the VS frictional properties and effective normal stress, fault recurrence time, and long-term fault slip rate (Supplementary Materials).

Observed microseismicity patterns before and after significant earthquakes on tectonic faults further support our hypothesis (Fig. 4.2, Supplementary Materials). On some fault segments, streaks of microseismicity persist at what appears to be rheological boundaries, with increased activity following a significant event, e.g., the 2004 $M_{\mathrm{w}}$ 6.0 Parkfield (Fig. 4.3A) and 1979 $M_{\mathrm{w}}$ 6.4 Imperial Valley (Supplementary Materials) earthquakes. In such cases, the slip in the significant event likely occurs above the deeper concentrated microseismicity. For larger events, such as the 1989 $M_{\mathrm{w}}$ 7.1 Loma Prieta earthquake (Fig. 4.3B), occurrence of microseismicity at depth prior to the mainshock and increased activity following the event are also observed, with some variability in local fault areas. In sharp contrast with these smaller events, microseismicity at depth is largely absent before or after all recent major ($M_{\mathrm{w}} > 7.5$) strike-slip earthquakes that we have considered (Supplementary Mate-

rials), including the 2002 $M_w$ 7.9 Denali (Fig. 4.2C) and 1999 $M_w$ 7.6 Izmit earthquakes. According to our models, this means that these earthquakes extended into the creeping fault extensions, which is more likely for larger events which have larger slip.

The relation between the microseismicity and depth of slip in large earthquakes can help us understand historical events and evaluate potential future earthquake scenarios on mature strike-slip fault segments. The 1857 $M_w$ 7.9 Fort Tejon earthquake is the last major event on the San Andreas/San Jacinto fault system in Southern California (*Hauksson et al.*, 2012, Fig. 4.3) which ruptured the Cholame and Carrizo segments, possibly extending further south (*Sieh*, 1978a; *Zielke et al.*, 2010). The last major earthquake on the Coachella segment occurred in ∼1690 (*Fialko*, 2006). Both events, if repeated, pose severe seismic risks for Southern California. Virtually no microseismicity is currently observed on all three segments (Fig. 4.3). In the light of our modeling, this observation implies that, $\sim 150$ to $\sim 300$ years after the previous major seismic events, the locked-creeping transition on those segments is still below the bottom of the seismogenic zone. To achieve that, dynamic rupture on those segments should have penetrated an additional depth below the seismogenic zone, at least 3-5 km based on our physical model (Supplementary Materials). Interseismic geodetic observations indeed suggest that the Carrizo and Coachella segments are accumulating more potency deficit than other fault segments, which they are expected to release in future events (*Smith-Konter et al.*, 2011).

In summary, we find that the absence of microseismicity at the bottom of seismogenic zones points to deeper rupture extent in recent major earthquakes, likely guided by co-seismic weakening of otherwise stable deeper regions. Furthermore, the deeper penetration may be quite common for large events on mature strike-slip faults. We have demonstrated this phenomenon in a friction-based fault model, but the overall dynamics of the process

should be similar for visco-plastic deeper fault extensions, which may localize and dynamically weaken due to shear-heating and strain-rate effects during large earthquakes (*Platt et al.*, 2014) and maintain their localization through the interseismic period due to the resulting structural differences in terms of their grain size and heterogeneity (*Kelemen and Hirth*, 2007). Our study have focused on major strike-slip faults, but it has important implications for megathrust earthquakes in subduction zones, e.g., Cascadia and Sumatra, given the significant effect of down-dip rupture limit on coastal shaking.

# Appendix

## 4.A Materials and Methods

### 4.A.1 Earthquake catalogues and coseismic slip models

To explore the source processes of major continental strike-slip earthquakes, we study seismicity patterns and coseismic slip distribution associated with events selected based on the following criteria (with some examples presented in Fig. 4.3).

Criteria for selecting smaller events:

- Major earthquakes ($6.0 \leq M_{\mathrm{w}} \leq 7.5$) on the San Andreas Fault (SAF), San Jacinto Fault (SJF), Calaveras Fault and Imperial Valley Fault (IVF);
- Events after 1970s (for the reason of good-quality instrumentation);
- Events with published finite-fault slip models.

Criteria for selecting larger events:

- Large earthquakes ($M_{\mathrm{w}} \geq 7.5$) on mature (large cumulative displacement) continental strike-slip faults;
- Events after 1950s;
- Events in well-instrumented regions;
- Plus two recent historic largest events on the SAF (1857 and 1906 earthquakes).

Sources of models and catalogues for these events are listed in Table 4.1. We study

the near-fault seismicity using highest-resolution earthquake catalogues available in each region, e.g., catalogues of *Waldhauser and Schaff* (2008) and *Hauksson et al.* (2012) in Northern and Southern California, respectively, and relocated catalogues recorded in temporary and/or permanent networks in Alaska and Turkey. We use finite-fault coseismic slip models from published studies, some of which are obtained from the SRCMOD database (*Mai and Thingbaijam*, 2014, `http://equake-rc.info/SRCMOD/`). Note that inversions of coseismic slip distributions for large earthquakes from different studies usually produce solutions with large variability due to the under-determined nature of the inverse problem and choices of regularization schemes (*Mai and Thingbaijam*, 2014). Uncertainty estimation on model parameters is usually not conducted. Major features of the source, such as the along-strike location of the highest slip area, are sometimes similar among different studies and therefore appear to be well constrained. The depth extent of the coseismic slip is more difficult to constrain due to the decreasing resolution with depth, and it could be biased by strong regularization of solutions or the imposed depth limit of the fault geometry. In some cases, where joint datasets are available and testing of data sensitivity with depth is explicitly conducted, a certain depth range or lower bounds could be inferred for the coseismic slip. We consider the space-time evolution of microseismicity patterns for events of different sizes and, where possible, compare them with these more reliable features in finite-fault slip inversions.

### 4.A.2 Microseismicity vs. depth extent of earthquakes from slip models

For mainshocks of smaller sizes ($M_{\mathrm{w}} \sim 6$), spatial persistence of near-horizontal microseismicity streaks before and after the event can be observed, e.g., for the 2004 $M_{\mathrm{w}}$ 6.0 Parkfield earthquake on the SAF (Fig. 4.5A) and the 1979 $M_{\mathrm{w}}$ 6.4 Imperial Valley earthquake. It is

| Event | $M_w$ | Fault | Slip Model | Earthquake Catalogue |
|---|---|---|---|---|
| 2004 Parkfield | 6.0 | SAF | *Barbot et al.* (2012)<br>*Dreger et al.* (2005) | NCSN catalogue[1]<br>*Waldhauser and Schaff* (2008) |
| 1984 Morgan Hill | 6.2 | CF | *Beroza and Spudich* (1988)<br>*Hartzell and Heaton* (1986) | NCSN catalogue<br>*Waldhauser and Schaff* (2008) |
| 1979 Imperial Valley | 6.4 | IVF | *Zeng and Anderson* (2000)<br>*Hartzell and Heaton* (1983) | SCSN catalogue[2]<br>*Hauksson et al.* (2012) |
| 1987 Superstition Hills | 6.6 | SJF | *Larsen et al.* (1992)<br>*Wald et al.* (1990) | SCSN catalogue<br>*Hauksson et al.* (2012) |
| 1989 Loma Prieta | 7.1 | SAF | *Emolo and Zollo* (2005)<br>*Beroza* (1991) | NCSN catalogue<br>*Waldhauser and Schaff* (2008) |
| 1999 Izmit | 7.6 | NAF | *Çakir et al.* (2003)<br>*Reilinger et al.* (2000) | Kandilli catalogue[3]<br>*Bouchon and Karabulut* (2008) |
| 2002 Denali | 7.9 | Denali | *Oglesby et al.* (2004)<br>*Elliott et al.* (2007) | AEIC catalogue[4]<br>*Ratchkovski et al.* (2003) |
| 2001 Kokoxili | 7.9 | Kunlun | *Lasserre et al.* (2005)<br>*Robinson et al.* (2006) | ANSS [5] |
| 1906 San Francisco† | 7.8 | SAF | *Song et al.* (2008a)<br>*Wald et al.* (1993) | *Waldhauser and Schaff* (2008) |
| 1857 Fort Tejon† | 7.9 | SAF | N/A | *Hauksson et al.* (2012) |

[1] NCSN catalogue (http://www.ncedc.org/ncedc/)

[2] SCSN catalogue (http://service.scedc.caltech.edu/eq-catalogs/)

[3] Kandilli catalogue (http://www.koeri.boun.edu.tr)

[4] AEIC catalogue (http://www.aeic.alaska.edu/)

[5] ANSS catalogue (http://quake.geo.berkeley.edu/anss/)

†only seismicity in the recent late interseismic period

SAF: San Andreas Fault; CF: Calaveras Fault; IVF: Imperial Valley Fault;

SJF: San Jacinto Fault.; NAF: North Anatolian Fault

Table 4.1: Coseismic slip models and catalogues for events that satisfy our selection criteria.

reasonable to assume that these streaks represent rheological boundaries on the fault and that seismic slip in the associated large events should occur largely between those streaks. When this consideration is added to the inversion, one can indeed obtain co-seismic slip distribution with those properties. For example, for the 2004 Parkfield earthquake, this was illustrated by *Barbot et al.* (2009) for geodetic data inversion (*Barbot et al.*, 2009, Fig. 4.5, panel A1, top) as well as by *Ma et al.* (2008) for a dynamic model that matched the seismic and geodetic data. However, even for this well-recorded and well-studied earthquake, kinematic source inversions with no such geometric constraints produce slip distributions that are not as clearly bound by microseismicity (*Custódio et al.*, 2005; *Barbot et al.*, 2009, Fig. 4.5, panel A1, bottom). This variability in finite-source slip inversions precludes a detailed study of the relation between seismic slip in large events and microseismicity at the bottom of the seismogenic zone. That is why we focus only on the general features.

Spatial persistence of microseismicity is also observed before and after the 1984 $M_{\mathrm{w}}$ 6.2 Morgan Hill earthquake on the Calaveras fault (Fig. 4.5B, cluster S1 and S2), although the seismicity occurs more in isolated clusters than in streaks. In this case, it is possible that the seismic slip penetrates deeper in some places on the fault, eliminating the bottom-of-the seismogenic-fault microseismicity there, but not in others.

It is sometimes observed that the apparent depth of aftershocks becomes shallower in local clusters in addition to their increased postseismic activity, suggesting that deeper aftershocks are more short-lived than shallower ones (Fig. 4.6 and 4.7). For example, persistent seismicity occurred near the largest coseismic slip for the 1984 $M_{\mathrm{w}}$ 6.3 Morgan Hill earthquake (Fig. 4.5B, *Schaff et al.*, 2002) and 1989 $M_{\mathrm{w}}$ 7.1 Loma Prieta earthquake (Fig. 4.7), with postseismic events getting shallower with time. The change in aftershock depths have been observed during the 1979 $M_{\mathrm{w}}$ 6.4 Imperial Valley earthquake on the fault plane (*Doser*

*and Kanamori*, 1986) and the 1992 $M_w$ 7.3 Landers earthquake (*Rolandone et al.*, 2004). This phenomena resembles what we observe for the deeper VW patches in both end-member models M1 and M2.

Finally, the microseismicity is persistent before and after the 1987 $M_w$ 6.7 Superstition Hills earthquake on the San Jacinto Fault (Fig. 4.6B), but it forms a cloud, with most events shallower than the deeper streaks for the Parkfield and Imperial Valley cases. The finite fault slip models for this event also substantially differ, making it impossible to ascertain the relative position of microseismicity and seismic slip.

The largest strike-slip earthquakes we considered – 1999 $M_w$ 7.6 Izmit, 2001 $M_w$ 7.9 Denali, 2001 $M_w$ 7.9 Kokoxili, and 1906 $M_w$ 7.9 San Francisco – show much diminished activity or even near absence of microseismicity at depth before and after the events, contrary to smaller events above, especially close to the areas of largest slip which are best constrained in inversions.

**1999 $M_w$ 7.6 Izmit.** Coseismic fault slip models based on field offset and InSAR measurements (*Çakir et al.*, 2003) and GPS alone (*Reilinger et al.*, 2000) are shown in Fig. 4.8. Common features of these two and other models based on seismic waveforms (*Yagi and Kikuchi*, 2000; *Sekiguchi and Iwata*, 2002) include an area with the largest slip to the west of the hypocenter, though the depth of maximum slip varies from 6 to 16 km in different studies. This segment with the largest slip is where the earthquake potentially ruptures to the deepest extent, and the same segment has less seismicity in both the pre- and post-mainshock periods compared with regions east of the hypocenter with shallower and smaller slip. On the fault segment with the inferred supershear transition during the earthquake, which is east of the hypocenter, most seismicity is off the fault, as pointed out in *Bouchon and Karabulut* (2008).

**2001 $M_w$ 7.9 Denali.** In Fig. 4.9, coseismic fault slip models based on GPS and seismic data (*Oglesby et al.*, 2004), and joint use of field offsets, GPS and InSAR data (*Elliott et al.*, 2007) show coseismic slip extending to the depth of 15-20 km at some locations. The largest slip occurs at the segment of inferred supershear transition right before jumping to the Totschunda segment. Microseismicity at depth is not seen for nearly all segments in both pre- and post-mainshock periods (relocated AEIC catalogue, $M_c = 2.3$) (*Ratchkovski et al.*, 2003).

**2001 $M_w$ 7.9 Kokoxili.** In Fig. 4.10, coseismic fault slip models constrained by InSAR (*Lasserre et al.*, 2005) has most slip within the upper 10 km, and significant slip occurring below 10 km at rupture end. Synthetic tests show that no slip could be resolved if it is deeper than 20 km. The model based on teleseismic waveforms (*Robinson et al.*, 2006) provided similar constraints: fault slip reaches 10 km in most places and about 20 km in the region of the highest slip. However, for the Tibetan crust, *Mechie et al.* (2004) showed that the 700 °C isotherm is likely to be at a depth of 18 km in this region. Considering that the brittle-semibrittle-plastic transitions for a typical quartzofeldspathic crust is at 350 - 450 °C (*Scholz*, 2002), the coseismic slip during Kokoxili is likely to go beyond the transitional depth ($\sim$ 9-12 km) at locations of high slip. *Bouchon and Karabulut* (2008) reported a lack of large aftershocks for this earthquake given its magnitude, and showed that all of $M_w > 5$ earthquakes appear to occur off the main fault plane (Fig. 4.10).

**1906 $M_w$ 7.9 San Francisco.** As the most recent major event on the SAF, the 1906 San Francisco earthquake is highly relevant to understanding seismic hazard on the Southern SAF where similarly large events are expected. Inversions of geodetic triangulation data found that the best fitting model exhibits right-lateral slip to depths of 15 to 20 km, with about 6 m of surface slip (*Matthews and Segall*, 1993). A slip model that used joint seismic

and geodetic data provides constraints on the along-strike fault slip distribution (*Song et al.*, 2008a) (Fig. 4.11). Present-day seismicity (*Waldhauser and Schaff*, 2008) is nearly absent on the Shelter Cove part of the northern San Andreas Fault where coseismic slip is inferred to be the largest. Based on the analysis of catalogues and reports of felt aftershocks, it was concluded that there was no large aftershocks on the rupture plane (*Meltzner and Wald*, 1999).

**1857 $M_w$ 7.9 Fort Tejon** Paleoseismic trenching provides the only constraint on the slip amplitude and spatial extent of this historical event on the Carrizo segment of the SAF, suggesting a displacement of about 10 m (*Sieh*, 1978a,b) or less at some locations (*Ludwig et al.*, 2010; *Zielke et al.*, 2010). There was no large aftershock close to the segment and lower-than-average aftershock rates, in addition to the segment having low background seismicity rate even before this earthquake (*Meltzner and Wald*, 2003).

Note that *Bouchon and Karabulut* (2008) observed that supershear earthquake ruptures are correlated with the lack of on-fault aftershocks and the onset of off-fault ones, as shown in Fig. 4.8, 4.9, 4.10. They interpret this observation to be due to the ground motion features induced by the Mach front of the supershear ruptures. At the same time, the correlation between large depth extent of coseismic slip, and the lack of deep microseismicity is also a robust feature observed in these cases. Although in some cases (e.g., Kokoxili and Denali), the segment with the largest slip coincides with supershear rupture, that is not the case for the Izmit earthquake. Therefore, it is likely that supershear propagation and deeper penetration of earthquake rupture influence the behavior of microseismicity (including aftershocks) through different physical mechanisms. Both phenomena could be accompanying features of large events due to their prominent dynamic effects. Their physical relation and interactions should be further studied.

### 4.A.3 Paleoseismic Records for the San Andreas and San Jacinto Faults

In Fig. 4.3A, we show the calendar years of major historical and prehistorical earthquakes on the SAF and SJF in southern California, with approximate rupture extents for major events based on most recent literature. For the Parkfield segment, repeating M ∼6 events have been recorded to occur at similar locations (*Bakun et al.*, 2005; *Barbot et al.*, 2012). Further to the south, the 1857 $M_{\mathrm{w}}$ 7.9 Fort Tejon earthquake is well-documented to have ruptured the Cholame, Carrizo, and Mojave segments based on paleoseismic data and historical surveys (*Sieh*, 1978a; *Grant and Donnellan*, 1994; *Runnerstrom et al.*, 2002). Prior to 1857, major historical events on the southern SAF are the two earthquakes that occurred adjacent to each other in Dec. 1812, which we illustrate with a single year and rupture length. The surface rupture of the 1812 event(s) is only confirmed at Wrightwood on the Mojave segment (Jacoby, 1988), and possibly recorded at sites to the north and to the south. Recent studies based on analysis of precariously balanced rocks (*Grant Ludwig et al.*, 2015) and dynamic earthquake modeling (*Lozos*, 2016) suggest that 1812 event could involve the San Jacinto Fault. For simplicity, we illustrate the rupture extent of 1812 only on SAF with the uncertain parts as dashed lines. On the SJF, several M 5-6 events have occurred, as is summarized in *Smith and Sandwell* (2006). For prehistorical earthquakes, we compile the approximate years for events (after A.D 1000) on segments based on paleoseismic studies at representative sites. We summarize the calendar years and references in Table 4.2. Among all these events, the ∼1690 earthquake is likely the penultimate event which could rupture the San Bernardino, Palm Springs, and Coachella segments based on the correlation of paleoseismic data at different trenching sites (*Yule and Sieh*, 2001; *McGill et al.*, 2002; *Philibosian et al.*, 2011), so we illustrate the rupture extent of this event with dashed lines over all three segments.

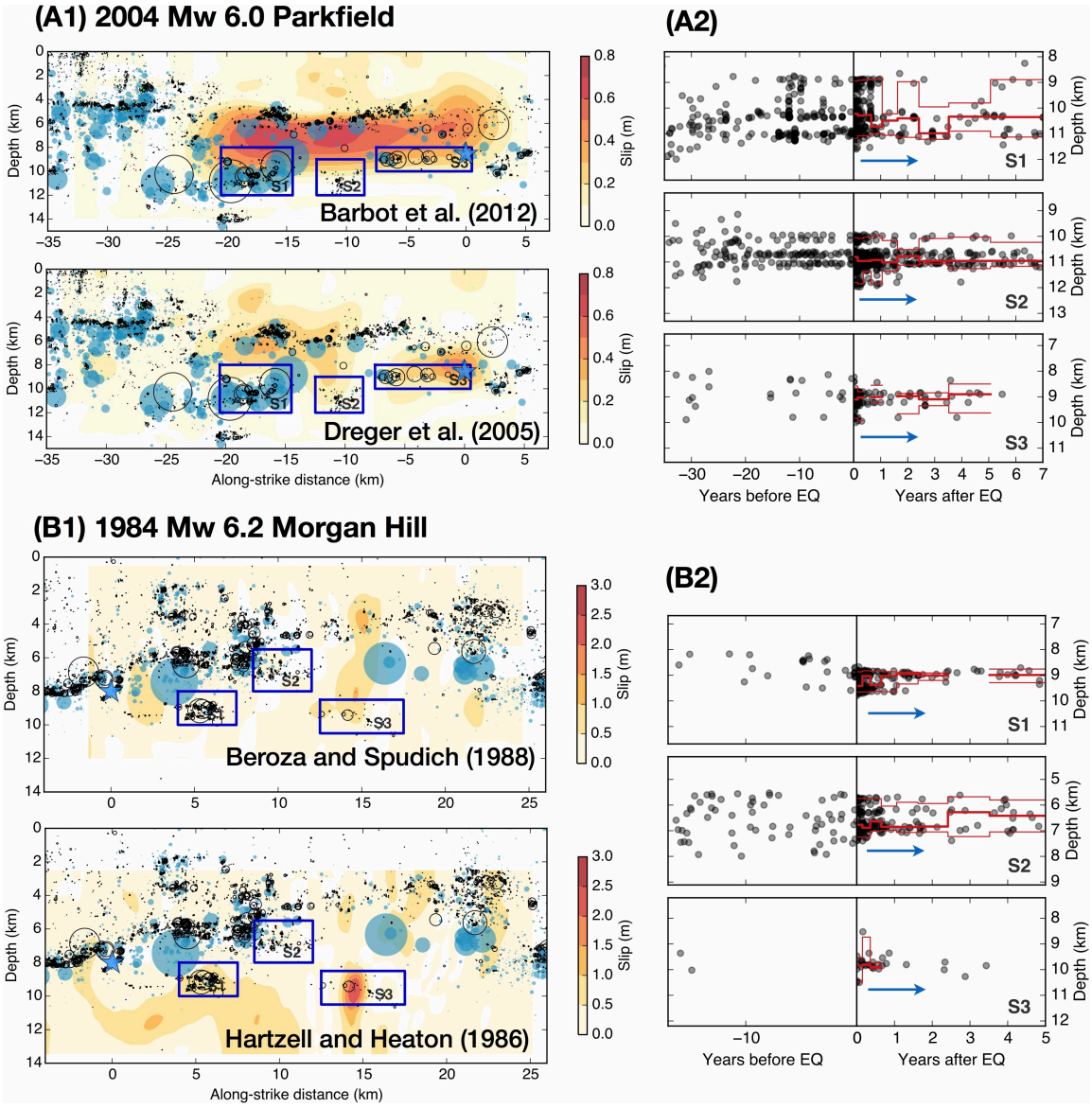


Figure 4.5: *2004 $M_w$ 6.0 Parkfield and 1984 $M_w$ 6.3 Morgan Hill earthquakes.* (Left) Coseismic slip models and seismicity from sources listed in Table 4.1. Blue circular patches show seismicity prior to the mainshock and black circles show aftershocks in the postseismic period, within 2 km of the fault plane. The length of the pre-mainshock and postseismic periods are the same as shown in the figures on the right. (Right) Time evolution of the seismicity depth in clusters highlighted by blue boxes on the left, both in the pre-mainshock and postseismic time windows. Red thick lines indicate the median depths of the aftershocks within each cluster and red thin lines indicate their standard deviation. The completeness magnitude of the catalogue is 2.5 for years after 1980.

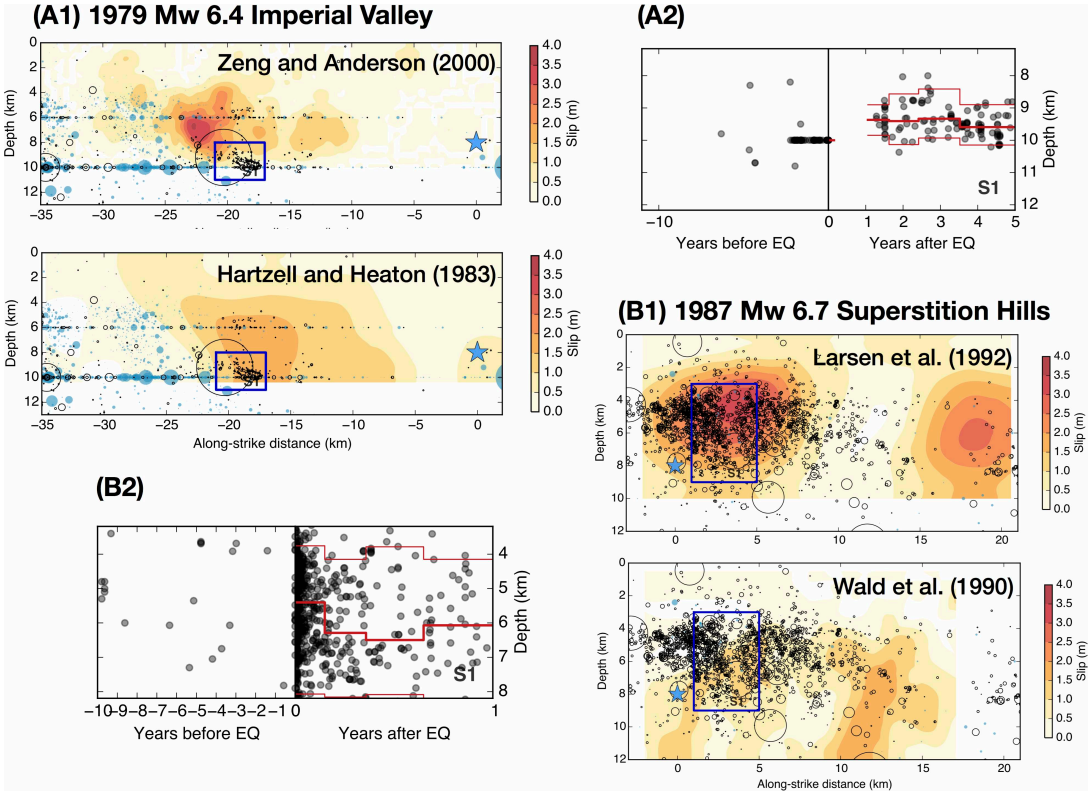


Figure 4.6: *1979 $M_w$ 6.4 Imperial Valley and 1987 $M_w$ 6.7 Superstition Hills earthquakes.* All the plotting conventions are the same as in Fig. 4.5.

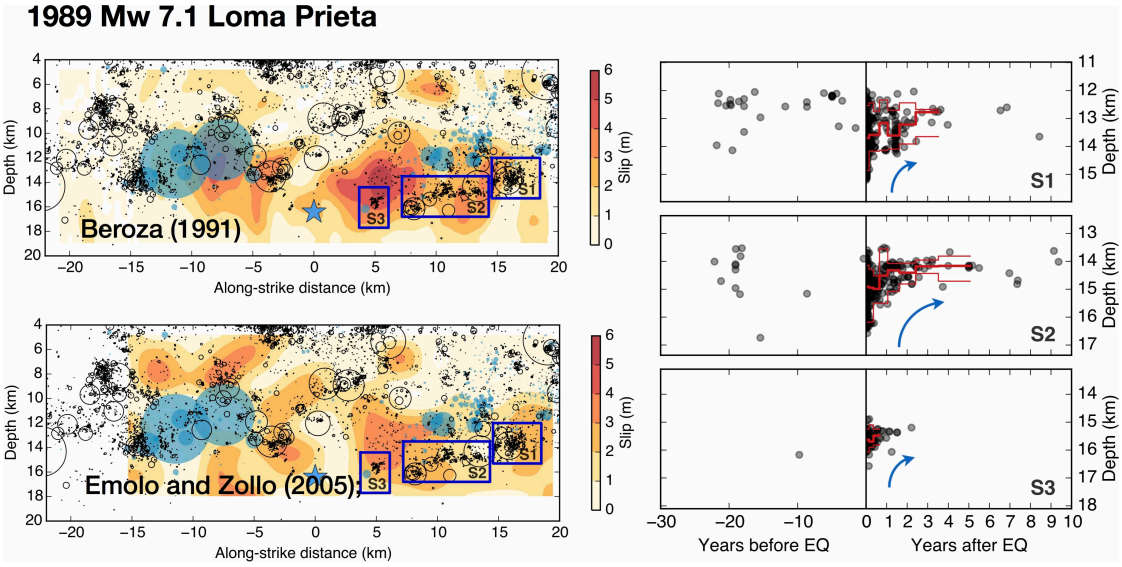


Figure 4.7: *1989 $M_w$ 7.1 Loma Prieta earthquake.* All the plotting conventions are the same as in Fig. 4.5.

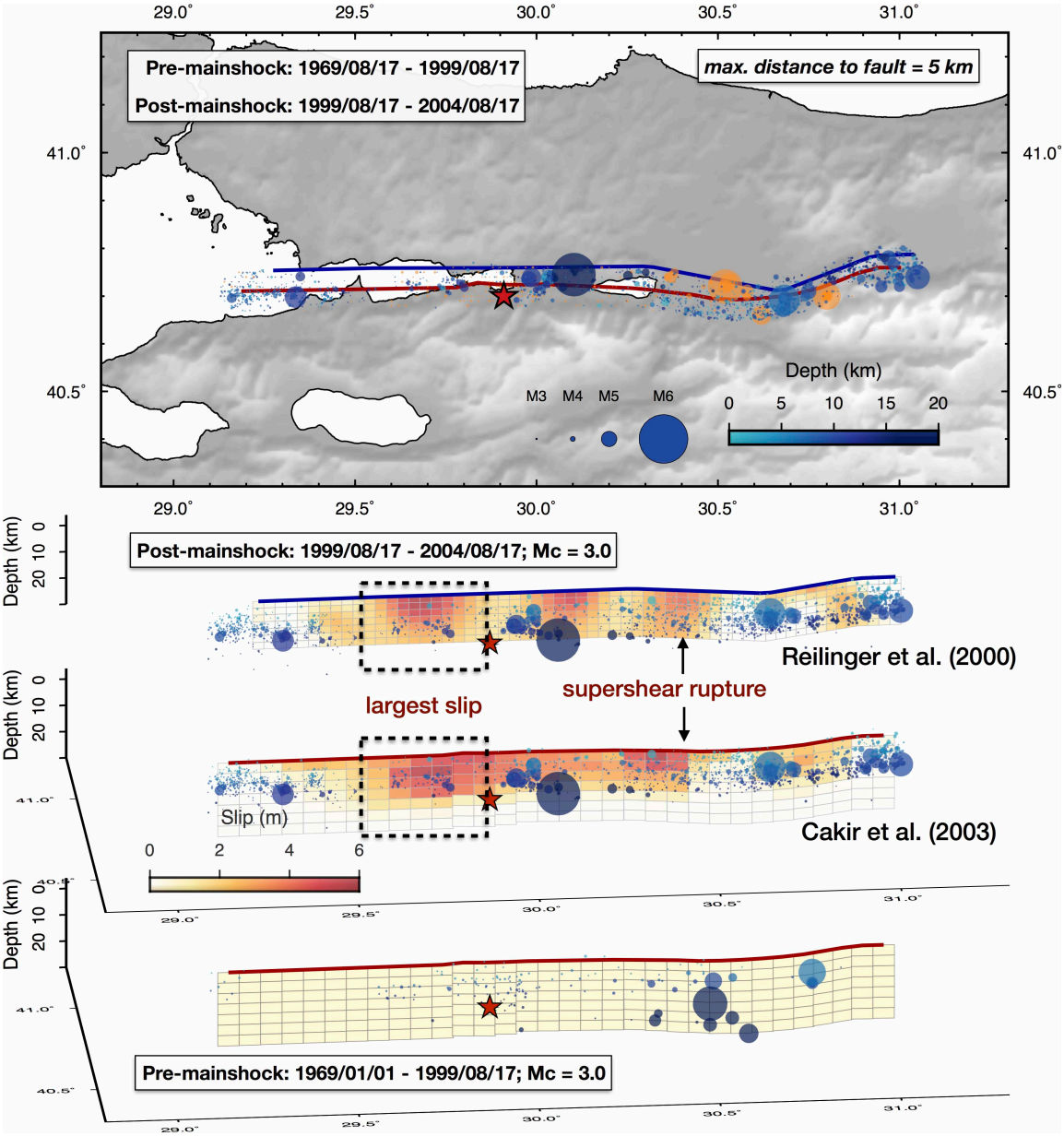


Figure 4.8: *1999 $M_w$ 7.6 Izmit earthquake.* (Top) Map view of seismicity and fault geometry. Fault traces in blue and red correspond to fault models from different studies. Seismicity prior to the mainshock are shown in orange; seismicity after mainshock are colored by their depths (cyan-blue colormap); hypocenter of the mainshock is represented by a red star. (Middle) Coseismic slip models with aftershocks plotted in 3D. (Bottom) Fault geometry and pre-mainshock seismicity colored by their depths. All earthquakes are plotted as circular patches with radii based on circular crack models assuming stress drop of 3 MPa. The completeness magnitude of the catalogue is 3.0. The seismicity is within 5 km of the fault plane.

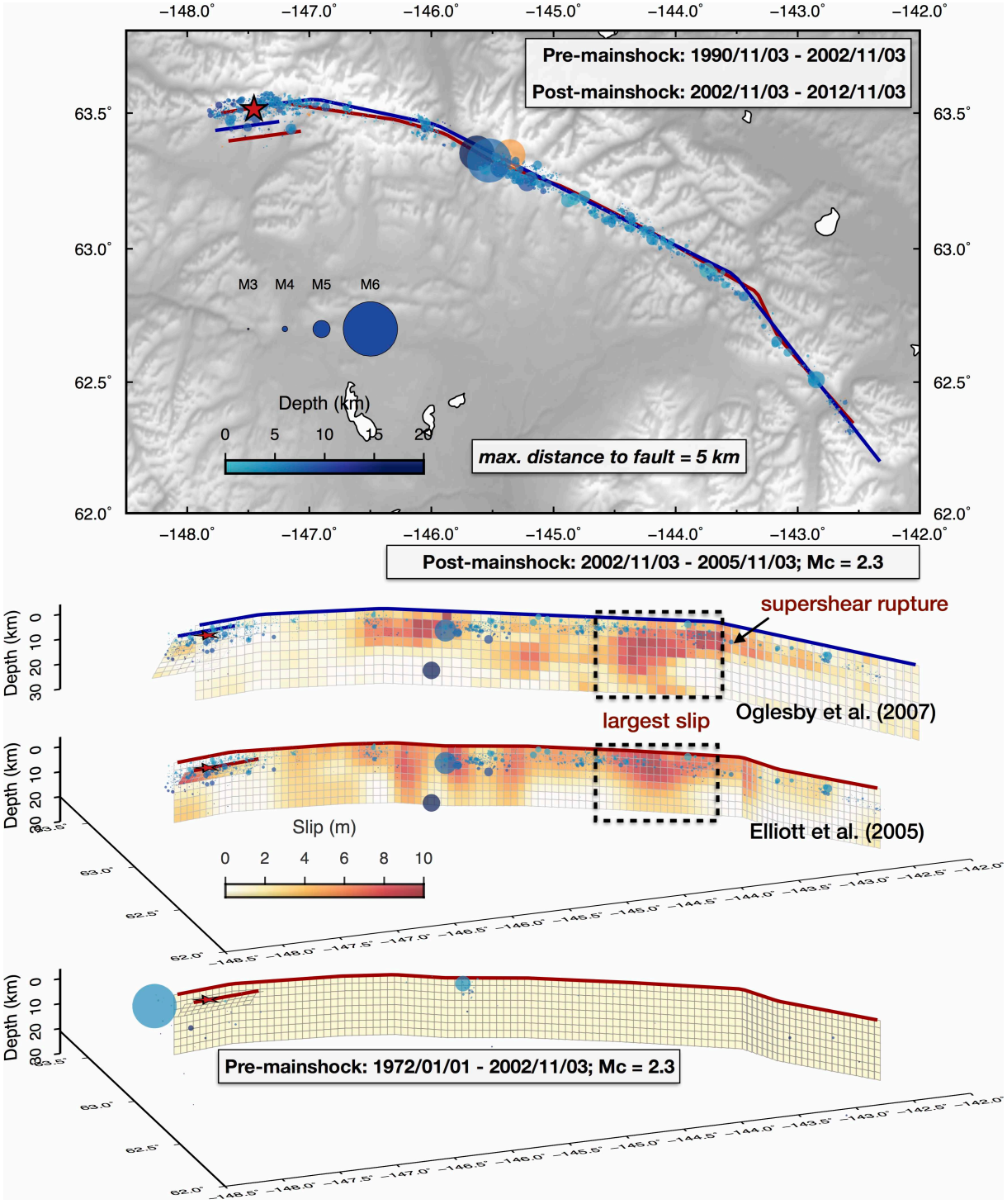


Figure 4.9: *2002 $M_w$ 7.9 Denali earthquake.* (Top) Map view of seismicity and fault geometry. (Middle) Coseismic slip models with aftershocks. (Bottom) Fault geometry and pre-mainshock seismicity. The completeness magnitude of the aftershock catalogue is 2.3. All other plotting conventions are the same as in Fig. 4.8.

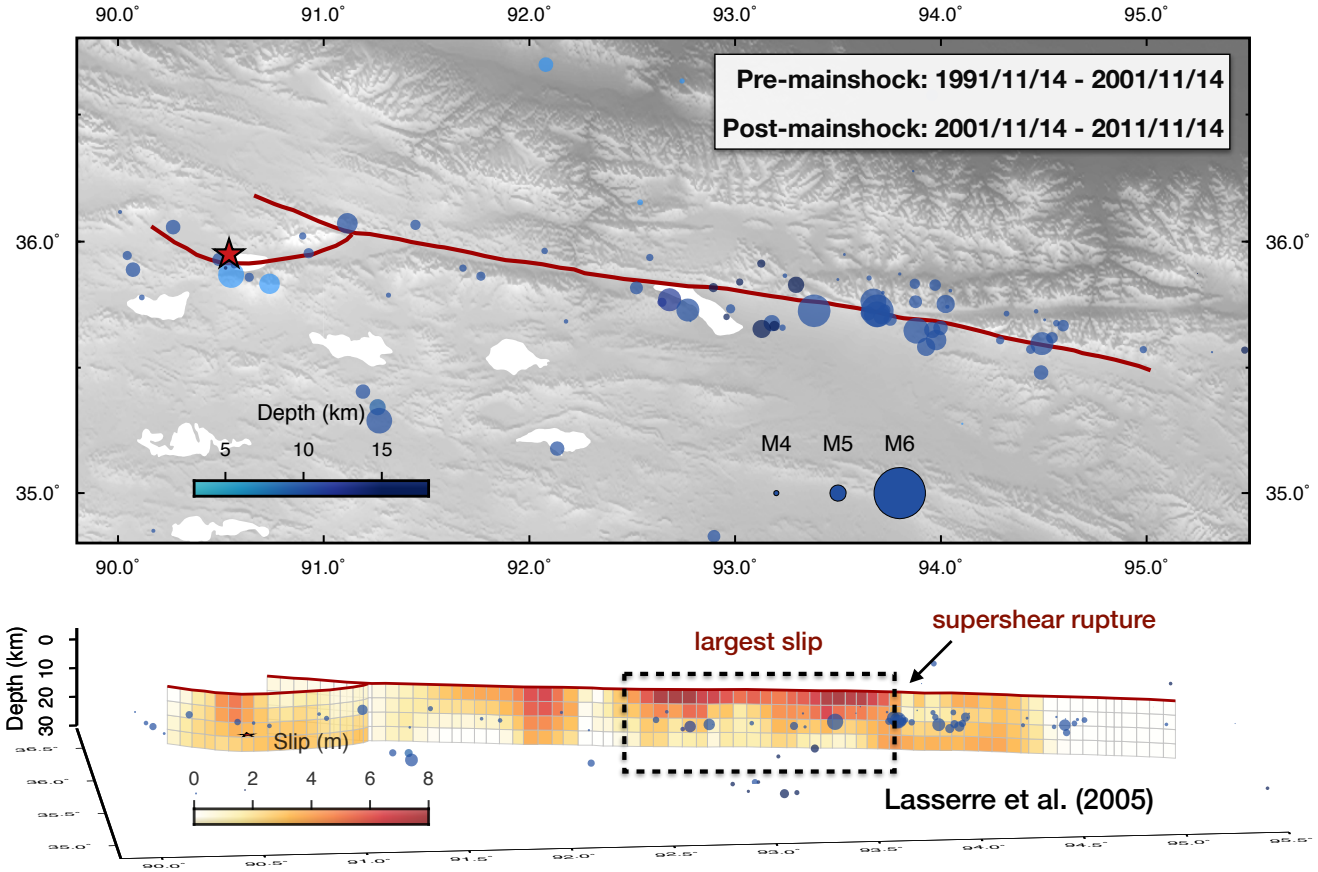


Figure 4.10: *2001 $M_w$ 7.9 Kokoxili earthquake.* (Top) Map view of seismicity and fault geometry. (Bottom) Coseismic slip models and seismicity. All seismicity in the region is shown. Other plotting conventions are the same as in Fig. 4.8.

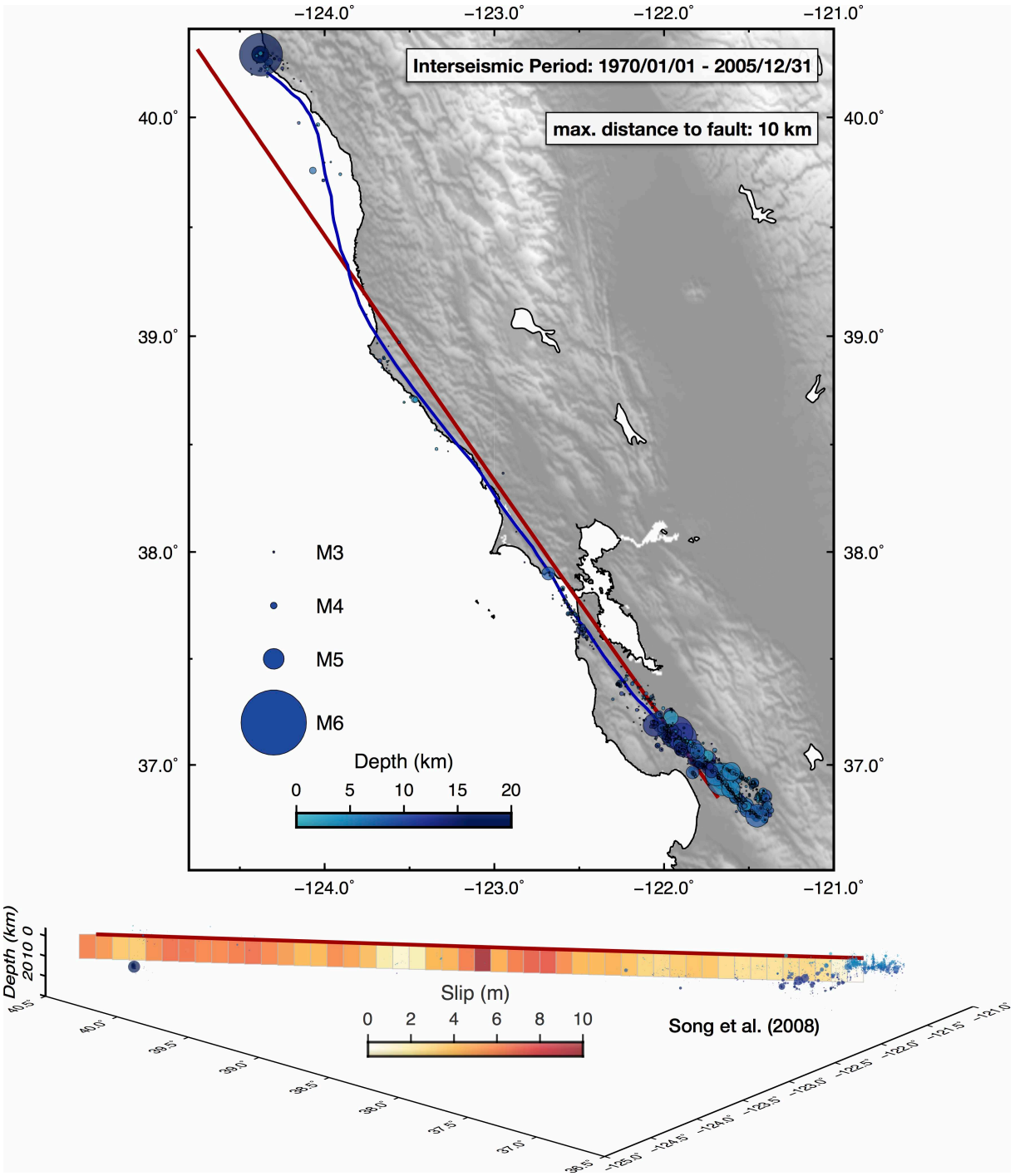


Figure 4.11: *1906 $M_w$ 7.9 San Francisco earthquake.* (Top) Map view of seismicity and fault geometry. The red fault trace is used in the study of coseismic slip model shown below and the blue trace is from the SCEC CFM (Community Fault Model). (Bottom) Coseismic slip models and seismicity. The completeness magnitude of the catalogue is $> 2.5$. Distance threshold for selecting near-fault seismicity is 10 km. All other plotting conventions are the same as in Fig. 4.8.

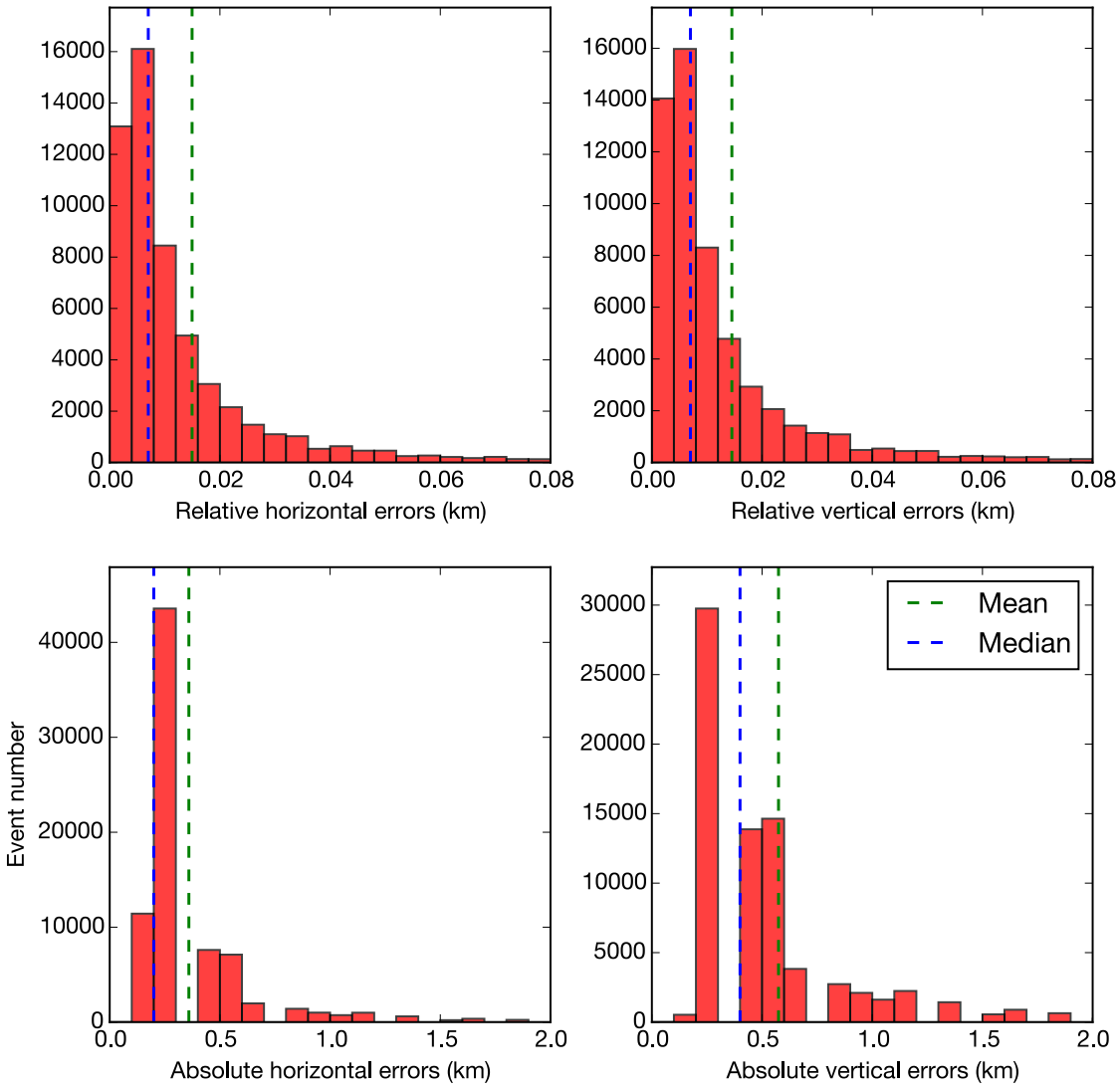


Figure 4.12: *Uncertainty of earthquake locations.* Absolute/relative horizontal/vertical location errors for the seismicity shown in Fig.4.4 extracted from the catalogue of *Hauksson et al.* (2012). With the mean/median location errors below 0.6 km, the locations of seismicity relative to the SAF and SJF are relatively well constrained.

| Fault Segment (Trench Site) | Studies | Earthquake Calendar Years |
|---|---|---|
| Cholame (Las Yeguas*) | *Young et al.* (2002) | 1030-1460 (1245†), 1857 |
| Carrizo (Bidart Fan) | *Ludwig et al.* (2010); *Akçiz et al.* (2010) | 1360-1452 (1417), 1450-1475 (1462), 1510-1612 (1565), 1580-1640 (1614), 1631-1823 (1713), 1857 |
| Mojave (Wrightwood) | *Fumal et al.* (2002); *Biasi et al.* (2002) | 957-1056 (1016), 1047-1181 (1116), 1191-1305 (1263), 1448-1518 (1487), 1508-1569 (1536), 1647-1717 (1685), 1812, 1857 |
| San Bernardino (Plunge Creek) | *McGill et al.* (2002) | 1293-1708 (1450), 1513-1729 (1630) |
| Palm Springs (Burro Flats) | *Yule and Sieh* (2001) | 1300-1450 (1375), 1400-1550 (1475), 1500-1850 (1690?) |
| Coachella (Coachella) | *Philibosian et al.* (2011) | 1090-1152 (1140), 1275-1347 (1300), 1320-1489 (1420‡), 1588-1662 (1630), 1657-1713 (1690) |
| Northern SJF (Mystic Lake) | *Onderdonk et al.* (2013) | 1273-1419 (1342), 1403-1445 (1428), 1521-1616 (1574), 1665-1820 (1698), 1744-1853 (1837), 1850-1940 (1895) |
| Southern SJF (Hog Lake) | *Rockwell et al.* (2014) | 1028-1144 (1080), 1118-1267 (1193), 1267-1315 (1289), 1280-1362 (1311), 1303-1389 (1357), 1535-1627 (1577), 1723-1797 (1761), 1918 |

* Representative trench sites for the dating of paleoseismic events.

† Median or mean value of the earthquake calendar age.

‡ Possible event not shown in Fig. 4.3.

Table 4.2: Calendar years for historical and prehistorical earthquakes (after A.D. 1000) on the SAF and SJF.

### 4.A.4 Numerical methods and model setup

For numerical simulations of long-term fault behavior including earthquake sequences and aseismic slip, we use the spectral boundary integral approach to solve the problem of elastodynamic equations of fault motion coupled with the friction boundary conditions that include evolutions of pore fluid pressure and shear zone temperature through effective normal stress (*Lapusta et al.*, 2000; *Lapusta and Liu*, 2009; *Noda and Lapusta*, 2010, 2013). At each time step, slip rates and shear tractions are determined for each cell of the discretized fault by equating fault shear stress to fault friction (strength). These conditions for different fault cells are coupled, because the shear stress is affected not only by loading but also slipping of the other fault cells through wave-mediated static and dynamic stress transfers. Meanwhile, frictional resistance depends on prior history of slip. The adaptive time stepping in our methodology allows us to resolve slow tectonic loading, earthquake nucleation, fully dynamic earthquake propagation and the postseismic afterslip that follows the mainshock.

In our study, we use the Dieterich-Ruina rate-and-state friction, supplemented by thermally induced evolution of pore pressure (*Dieterich*, 1979, 1981; *Ruina*, 1983; *Rice*, 2006; *Noda and Lapusta*, 2010):

$$\tau = \bar{\sigma} f = (\sigma - p) \left( f^* + a \ln \frac{V}{V^*} + b \ln \frac{V^* \theta}{L} \right) , \tag{4.1}$$

$$\frac{\mathrm{d}\theta}{\mathrm{d}t} = 1 - \frac{V\theta}{L} , \tag{4.2}$$

where $\bar{\sigma}$ is the effective normal stress, $f$ is the friction coefficient, $\sigma$ is the normal stress on the fault (positive in compression), $p$ is the pore pressure, $f^*$ is the reference friction

coefficient at the reference slip rate $V^*$, $\theta$ is the state variable, and $L$ the characteristic evolution distance. The solution methodology uses the form of these expressions regularized near $V = 0$ (*Noda and Lapusta*, 2010).

Our fault models incorporate depth-dependent rate-and-state frictional properties used in *Tse and Rice* (1986) and *Lapusta et al.* (2000), based on experimental results (*Blanpied et al.*, 1995)(Fig. 4.13). The effective compressive normal stress in the interseismic period, when the shear heating effects on pore pressure are negligible, is 3 MPa near the surface, increases to 50 MPa at 3 km depth, and stays constant over the deeper regions; this distribution of $\bar{\sigma}$ is appropriate for an over-pressurized crust at depth (*Suppe*, 2014). Circular VW patches at the transitional depth are used to illuminate the effect of the larger-scale model behavior on microseismicity. The patches are generated randomly, with their radii distributed between 0.3 and 1.0 km and their depths between 10 and 20 km. The generation process favors patches of smaller radii with the increase of depth. This is a simplified representation of rheological boundaries with fault heterogeneity.

Slip is able to develop into earthquake rupture only if the steady state velocity-weakening region of the fault exceeds the nucleation size $h_*$ (*Rice and Ruina*, 1983; *Rice*, 1993; *Ampuero and Rubin*, 2008). For 2D problems, two theoretical estimates of the earthquake nucleation size are from *Rice and Ruina* (1983) and *Ampuero and Rubin* (2008):

$$h^*_{\mathrm{RR}} = \frac{\pi}{4}\frac{\mu^* L}{(\sigma - p)(b - a)} \; ; h^*_{\mathrm{RA}} = \frac{2}{\pi}\frac{\mu^* L b}{(\sigma - p)(b - a)^2}, \tag{4.3}$$

where $\mu^* = \mu$ for mode III and $\mu^* = \mu/(1 - \mu)$ for mode II. In 3D problems, the nucleation size is given by *Ampuero and Rubin* (2008) and *Chen and Lapusta* (2009):

$$h^* = (\pi^2/4) h^*_{\mathrm{RA}}. \tag{4.4}$$

The theoretically estimated nucleation size in our models is about 5 km for the seismogenic region outside the VW patches and about 1.5 km inside the VW patches, based on Eq. 4.4. That makes some of the VW patches slightly larger than their nucleation size at the transitional depth and smaller than their nucleation size at even greater depth of the fault extension.

The fault areas with dynamic weakening experience thermal pressurization of pore fluids due to shear heating, with off-fault diffusion of fluids and heat following the methodology of *Noda and Lapusta* (2010). The corresponding equations are solved throughout the frictional fault interface, but the thermal pressurization is effectively disabled outside of the DW zones (Fig. 4.4) by choosing unfavorable thermo-poro-elastic properties.

Table 4.3 summarizes parameters used in the model. The chosen values of $L$ are larger than those obtained in laboratory, $L$ = 1-100 μm, but facilitate our numerical computation (*Lapusta and Liu*, 2009).

Spatial discretization in the simulations, cell size $\Delta x$, should be small enough to resolve the evolution of stress and slip rate. Two important physical scales in the problem are nucleation size $h^*$ and cohesive zone size $\Lambda$. The nucleation size is a crucial length scale during interseismic periods (*Rice*, 1993; *Ben-Zion and Rice*, 1997; *Lapusta et al.*, 2000) and $h^*/\Delta x$ is an important criterion to assess spatial resolution. The cohesive zone size is important in dynamic rupture and hence $\Lambda/\Delta x$ is another resolution criterion (*Palmer and Rice*, 1973; *Day et al.*, 2005, and references therein). *Day et al.* (2005) established that $\Lambda_0/\Delta x$ of 3 to 5 is required to resolve dynamic rupture. For rate-and-state friction law, $\Lambda_0$, the size of $\Lambda$ at rupture speed of $0^+$, is given as

$$\Lambda_0 = C_1 \frac{\mu^* L}{b\sigma} \tag{4.5}$$

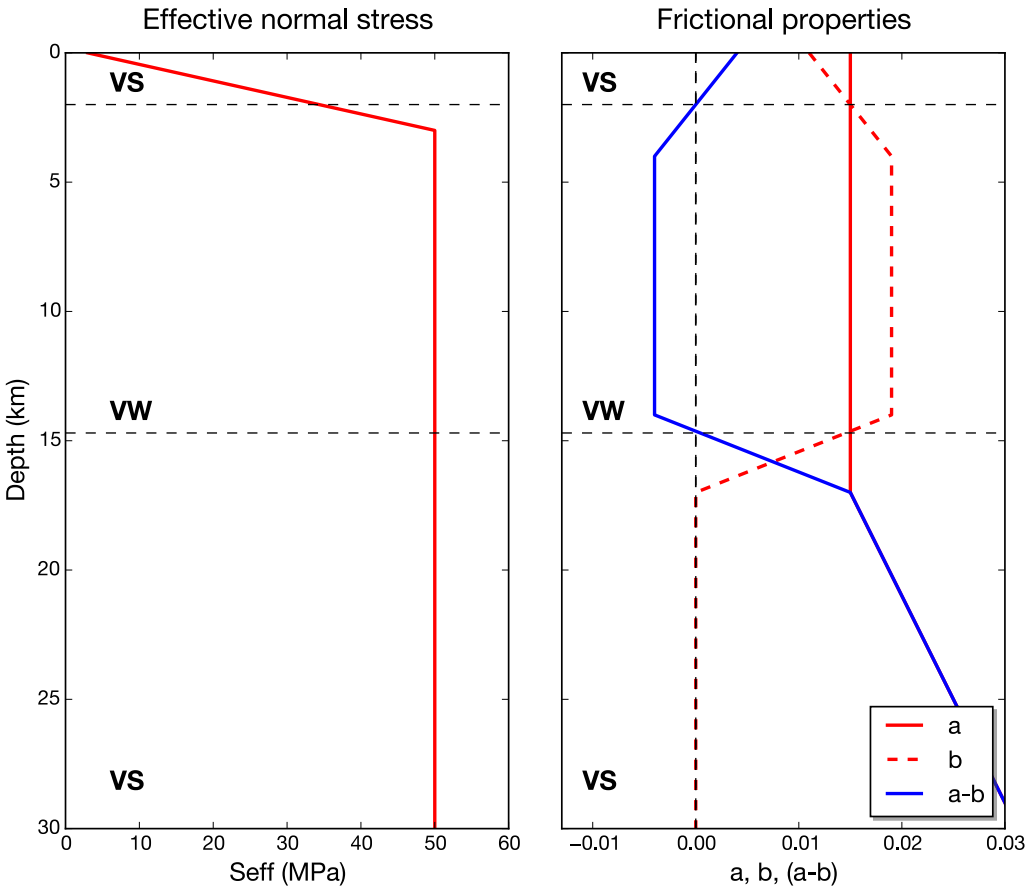


Figure 4.13: *Depth dependence rate-and-state frictional properties and normal stress.* The properties are used in Models M1 and M2 presented in the main text.

The ratio of nucleation size and cohesive zone size is given by $\Lambda_0/h^* \sim (b-a)^2/b^2$. With the chosen values of $a$ and $b$, this ratio is about 0.05. Therefore, resolving the cohesive zone is the more stringent numerical criterion here. In our models, we choose the cell size small enough to resolve the cohesive zone with at least 3 cells, hence resolving the nucleation zones with more than 60 cells. It is also important to resolve the pore pressure effects, with the effective normal stress decreasing behind the rupture front. For the parameters used in our simulations, we find that resolving the rate-and-state weakening, by resolving the cohesive zone size as already discussed, is a more stringent criterion.

| Parameter | Symbol | Value |
|---|---|---|
| Along-strike fault length | $\lambda_x$ | 100 km |
| Along-dip fault length | $\lambda_z$ | 40 km |
| Rate-and-state VW region length | $L_{\text{seis}}$ | 60 km |
| Rate-and-state VW region width | $W_{\text{seis}}$ | 12 km |
| Cell size | $\Delta x$ | 40 m |
| Plate loading rate | $V_{\text{pl}}$ | 32 mm/yr |
| P wave speed | $V_{\text{p}}$ | 5.2 km/s |
| S wave speed | $V_{\text{s}}$ | 3.0 km/s |
| Shear modulus | $\mu$ | 30 GPa |
| Poisson′s ratio | $\nu$ | 0.25 |
| Normal stress for depth over 3 km | $\sigma_0$ | 50 MPa |
| Reference coefficient of friction | $f^*$ | 0.6 |
| Reference slip velocity | $V^*$ | $10^{-6}$ m/s |
| Rate-and-state properties in main VW regions | $a$ | 0.015 |
| | $b$ | 0.019 |
| | $L$ | 4 mm |
| Rate-and-state properties in VW patches | $a$ | 0.011 |
| | $b$ | 0.018 |
| | $L$ | 3 mm |
| Half width of shear zone | $h_{\text{w}}$ | $10^{-2}$ m |
| Hydraulic diffusivity in DW regions | $\alpha_{\text{hy}}$ | $10^{-4}$ m$^2$/s |
| Thermal diffusivity in DW regions | $\alpha_{\text{th}}$ | $10^{-2}$ m$^2$/s |
| Undrained $\Delta p/\Delta T$ | $\Lambda$ | 0.1 MPa/K |

Table 4.3: Parameters for the fault models

## 4.B Supplementary Text

### 4.B.1 Physical mechanisms favoring or discouraging deeper coseismic slip

Deeper coseismic slip below the seismogenic zone (SZ, defined as the zone where earthquakes can nucleate, hence having VW properties at slow slip rates) requires physical mechanisms which allow coseismic weakening in the otherwise creeping VS regions. In laboratory settings, dynamic weakening processes have been commonly reported in high-velocity rock friction experiments, attributed to a variety of mechanisms such as flash heating, thermal pressurization of pore-fluids, thermal decomposition, and silica gel lubrication (*Di Toro et al.*, 2011; *Tullis*, 2015, and references therein). While these mechanisms for enhanced dynamic weakening would presumably work in highly localized shear zones appropriate for mid-seismogenic depths, their efficiency below the seismogenic zone would be affected by a variety of factors that characterize deeper fault extensions. For example, the efficiency of thermal pressurization depends on the competition between permeability of fault rocks which decreases with depth (*Wibberley and Shimamoto*, 2003; *Tanikawa and Shimamoto*, 2009) and shear-zone width that increases with depth (*Cole et al.*, 2007), and the effectiveness of pore pressure in reducing fault stress (*Hirth and Beeler*, 2015). For flash heating, its onset is more difficult at depth due to the increase of ambient temperature (*Passelègue and Goldsby*, 2014), and increased slip partitioning in the shear zone (*Platt et al.*, 2015), both of which are discouraging effects. However, dynamic shear localization (*Platt et al.*, 2014) and inertial effects (*Shimamoto and Noda*, 2014) can aid deeper penetration of earthquake ruptures. The combination of these factors would ultimately determine the arresting depth of large earthquakes, which can be deeper than the low-velocity VW zone where earthquakes can nucleate. This possibility is supported by geological studies which find occurrence of

seismic slip in the mostly ductile regime (*Sibson*, 1980; *Hobbs et al.*, 1986; *Lin et al.*, 2005; *Altenberger et al.*, 2011; *Moecher and Steltenpohl*, 2011; *Toy et al.*, 2011; *Pittarello et al.*, 2012), and has been conjectured in several synoptic models of the shear zone (*Scholz*, 1988; *Shimamoto*, 1989; *Chester*, 1995). These considerations motivate our model M2.

For some fault segments, e.g., the San Jacinto Fault, structural and geometrical complexities, which are possibly related to lower cumulative fault displacement and fault maturity, lead to larger degrees of fault heterogeneity, potentially hindering the susceptibility of the fault to such weakening mechanisms (*Fang and Dunham*, 2013). These fault segments might tend to produce relatively smaller earthquakes confined to the VW regions (e.g., *Wdowinski*, 2009), as seen in model M1.

### 4.B.2 Long-term fault behavior in numerical simulations

The long-term fault behavior in our models consists of slow slip on time scales of tens and hundreds of years and short bursts of dynamic earthquake ruptures lasting seconds. To supplement the summary of the model behavior in Fig. 4.4, we show the simulated long-term evolution of slip, slip rates and stress at local points and along the depth in Fig. 4.15-4.19, with the locations of the points and depth profiles illustrated in Fig. 4.14.

In Fig. 4.15, the accumulated slip along the depth profile over several large earthquakes reveals the difference in the slip partition between seismic and aseismic slip for the two models. In model M1 with SZ-confined rupture, minor coseismic penetration and interseismic creep overlap around the VW/VS boundary, and most of the VW and VS regions accommodate seismic and aseismic slip, respectively. In model M2 with deeper rupture, overlap of seismic and aseismic slip occurs in the VS regions that experience DW. Any VS region that experiences seismic or postseismic slip creeps at a rate lower than the plate rate

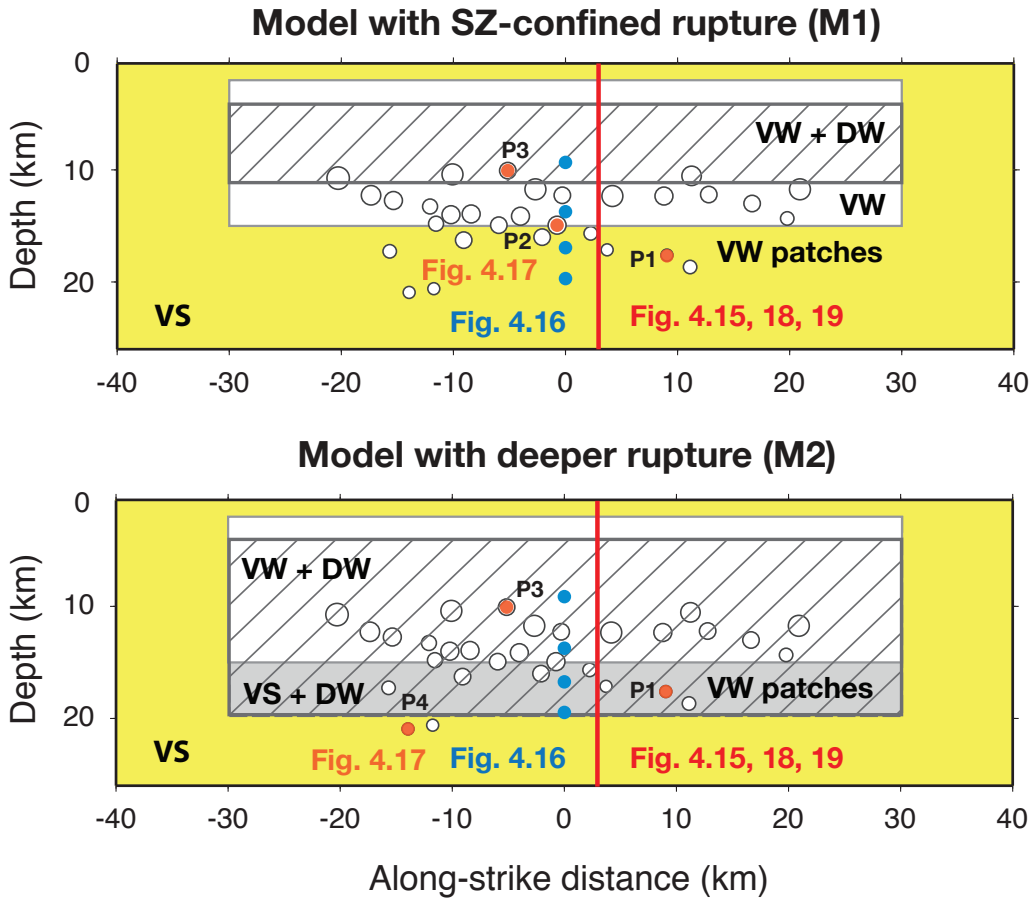


Figure 4.14: *Illustration of the locations of the along-depth profiles and observation points.* The along-depth profiles (red) and observation points (blue and orange) are used for plots in Fig. 4.15-4.19.

in the late interseismic period, since, on average, the slip has to match that implied by the plate rate.

The time evolution of local shear tractions and slip rates is shown for different fault areas in Fig. 4.16, and for points within VW patches which are surrounded by regions of different fault properties in Fig. 4.17. In model M1, the VW region in the mid-seismogenic depth slips during large earthquake rupture. Deeper VW regions experience stress perturbation due to frequent seismicity at the transitional depths. The VS regions experience stress increase (or negative stress drop) after large earthquake rupture, go through postseismic

slip, and return to steady-state stress after the postseismic period. In model M2, VW regions produce unstable slip and VS regions, if with DW, also participate in coseismic slip, with large positive stress drop and recovery of stress later. The VW patches either produce frequent seismicity (point P2), or experience mostly recurring aseismic transients if they are below the nucleation size (P1 and P4), or only participate in the rupture of large events (P3).

In Fig. 4.18 and 4.19, the time evolution of fault shear stress and slip rate from near-locked to near-plate-rate values is shown for the post- and inter-seismic periods following a typical large event. The large variation of slip rates along depth essentially defines the locked-creeping transition, and correponds to a stress concentration front, as expected. We define the locked-creeping transition as the depth of slip rates reaching $0.1V_{\max}$, where $V_{\max}$ is the maximum slip rate over the fault at the time (note that $V_{\max} = V_{\rm pl}$ during most of the interseismic period). In model M1, this transition stays at essentially the same depth throughout post- and inter- seismic periods; in model M2, it changes with time, as discussed in more details in a following section.

### 4.B.3 Estimating the migration of stress concentration front

When earthquake rupture penetrates below the seismogenic zone (VW region), the stress concentration front (SCF) induced at the locked-creeping transition (LCT) is within the VS region, and migrates updip due to gradual resumption of creep in the post- and inter-seismic periods, as shown in Fig. 4.4 and 4.19. Therefore, the depth of the SCF in the interseismic period is connected to the depth extent of (previous) coseismic slip.

As illustrated in Fig. 4.20A, the SCF moves up dip with time, separating locked and creeping regions. The coseismically ruptured region gets loaded while stress decays in the

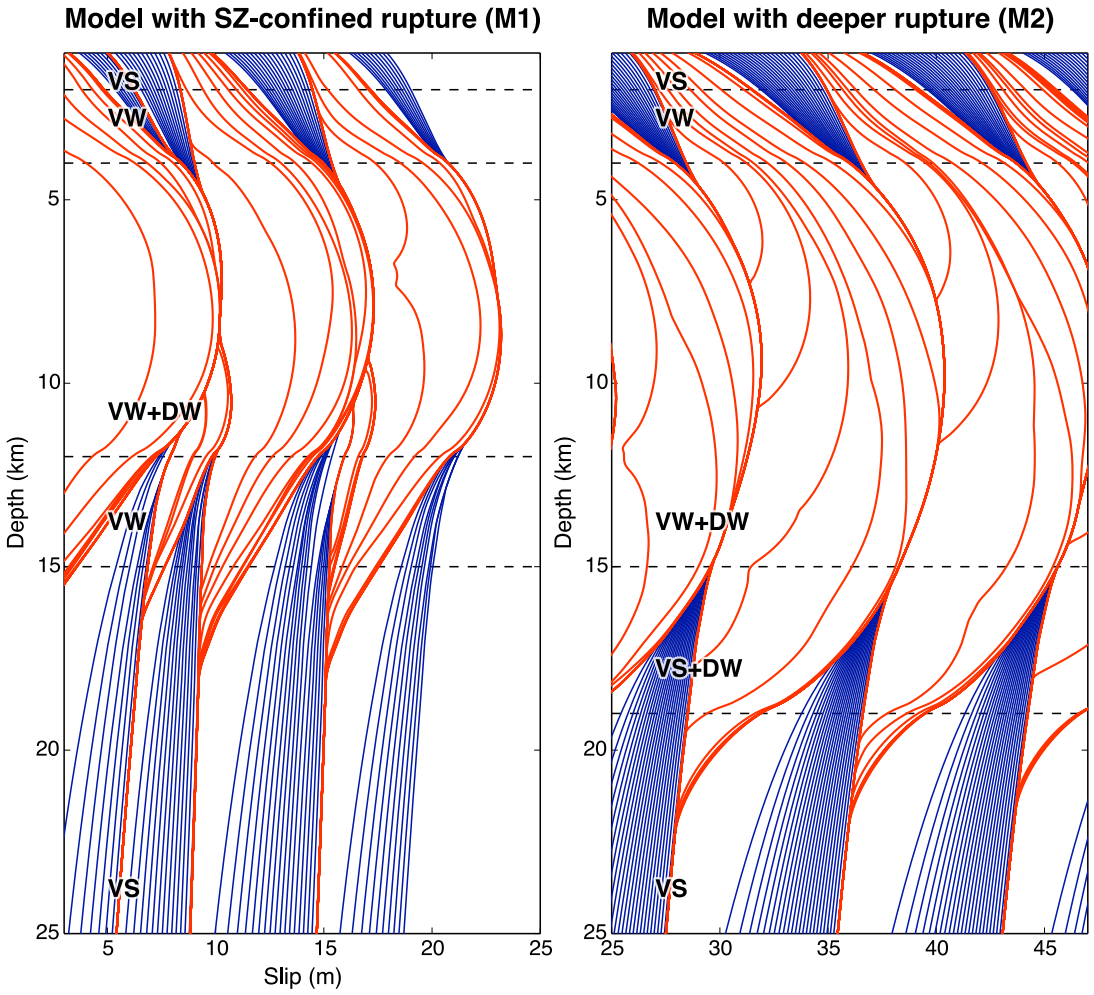


Figure 4.15: *Accumulated fault slip along depth over several large earthquakes.* The coseismic period is illustrated by red lines plotted every second, while blue lines are lotted every 10 years during post- and inter-seismic periods. Note that at the depths where seismic and aseismic slip overlap, slip rate is significantly below the plate rate in the late interseismic periods of both models.

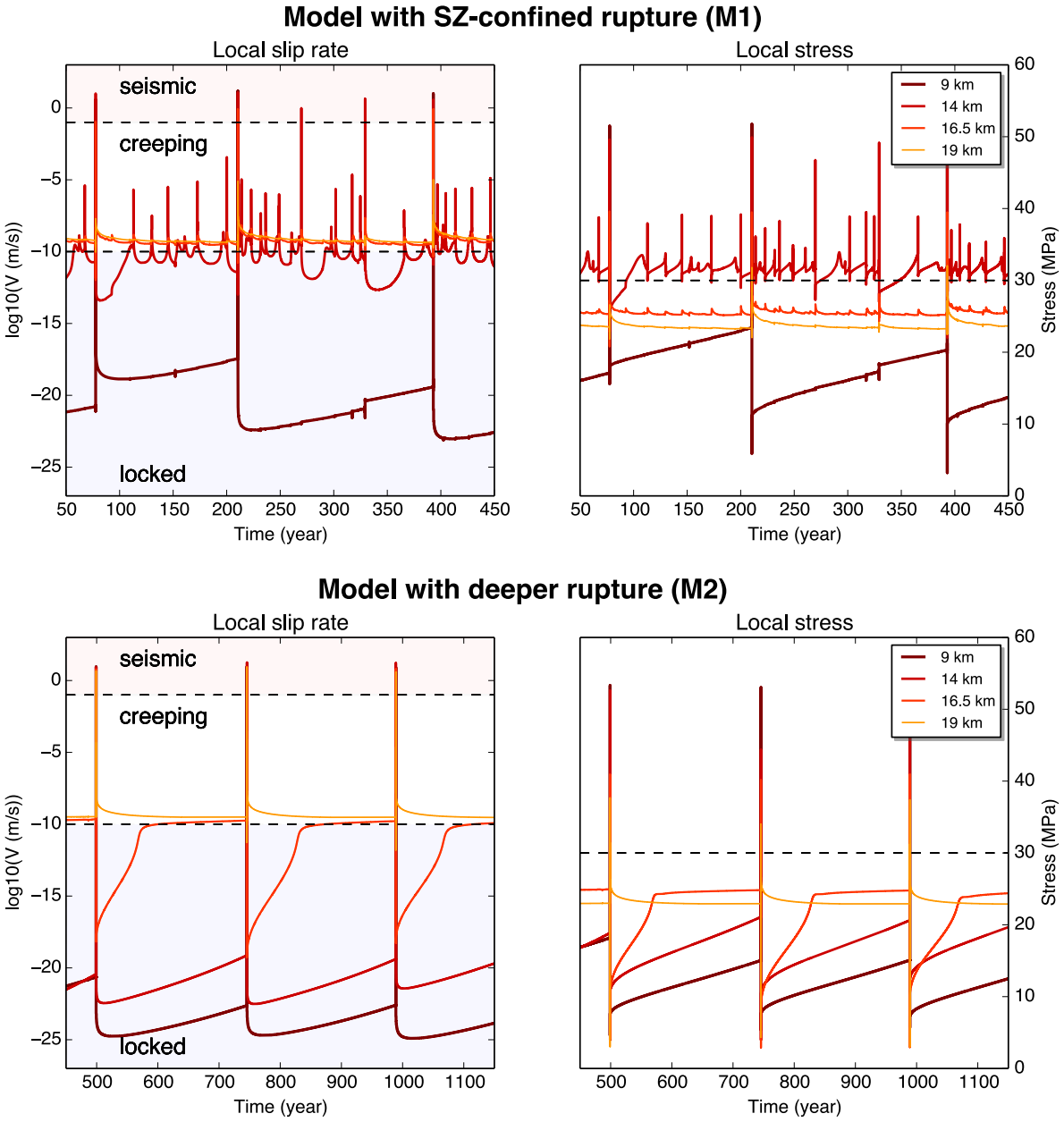


Figure 4.16: *Long-term evolution of stress and slip rate of the points on the fault.* The location of the points are illustrated in Fig. 4.14 in blue. (Top) Model M1 with SZ-confined rupture. (Bottom) Model M2 with deeper rupture. Points at different depths represent regions with different frictional properties, namely 9 km: VW + DW, 14km: VW in M1 and VW+DW in M2, 16.5 km: VS in M1 and VS+DW in M2, and 19 km: VS.

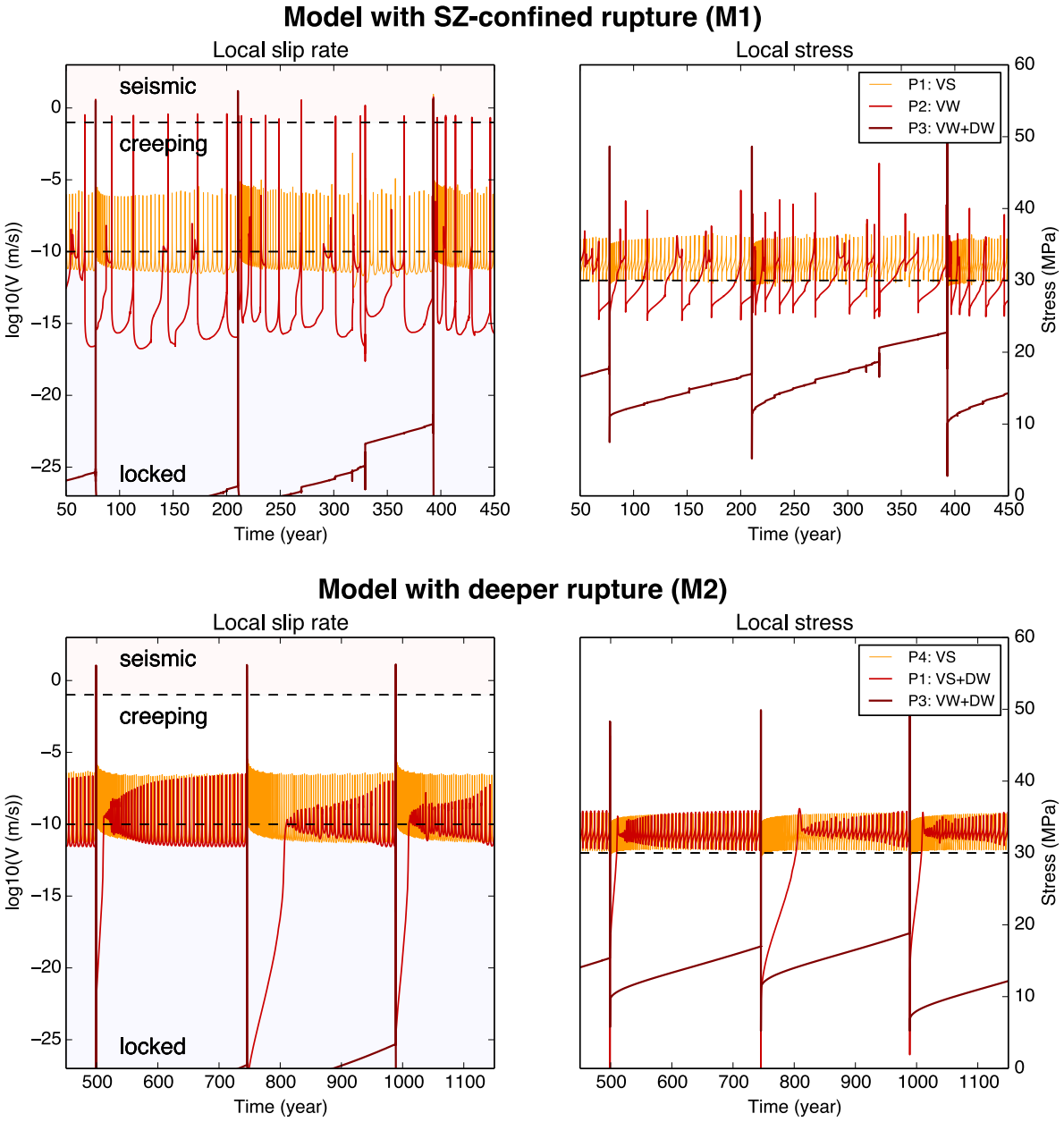


Figure 4.17: *Long-term evolution of stress and slip rate of the points within VW patches.* The locations of the VW patches on the fault are illustrated in Fig. 4.14 in orange. (Top) Model M1 with SZ-confined rupture. (Bottom) Model M2 with deeper rupture. Points (P1, P2, P3 and P4) at different locations are all within VW patches, but surrounded by different frictional properties illustrated in the legends.

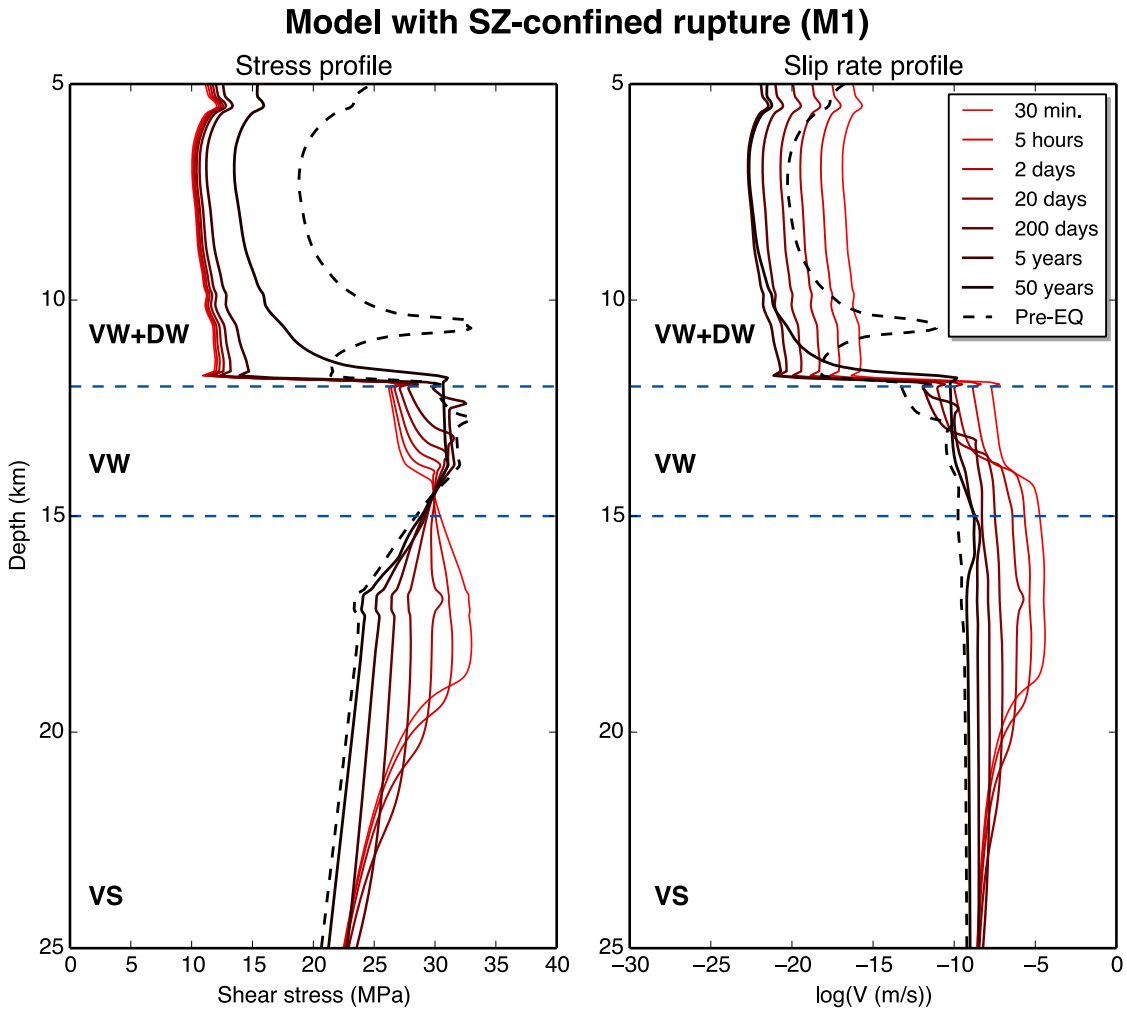


Figure 4.18: *Time evolution of the along-depth shear stress and slip rate profiles in model 1.* Depth profiles of shear stress and slip rate are plotted in the post- and inter- seismic periods of a typical large event. The solid lines (in color and with increasing weights) correspond to times of 30 minutes, 5 hours, 20 days, 200 days, 5 years and 50 years after the event. The dashed line, marked Pre-EQ, gives profiles 2 years before the next major earthquake.

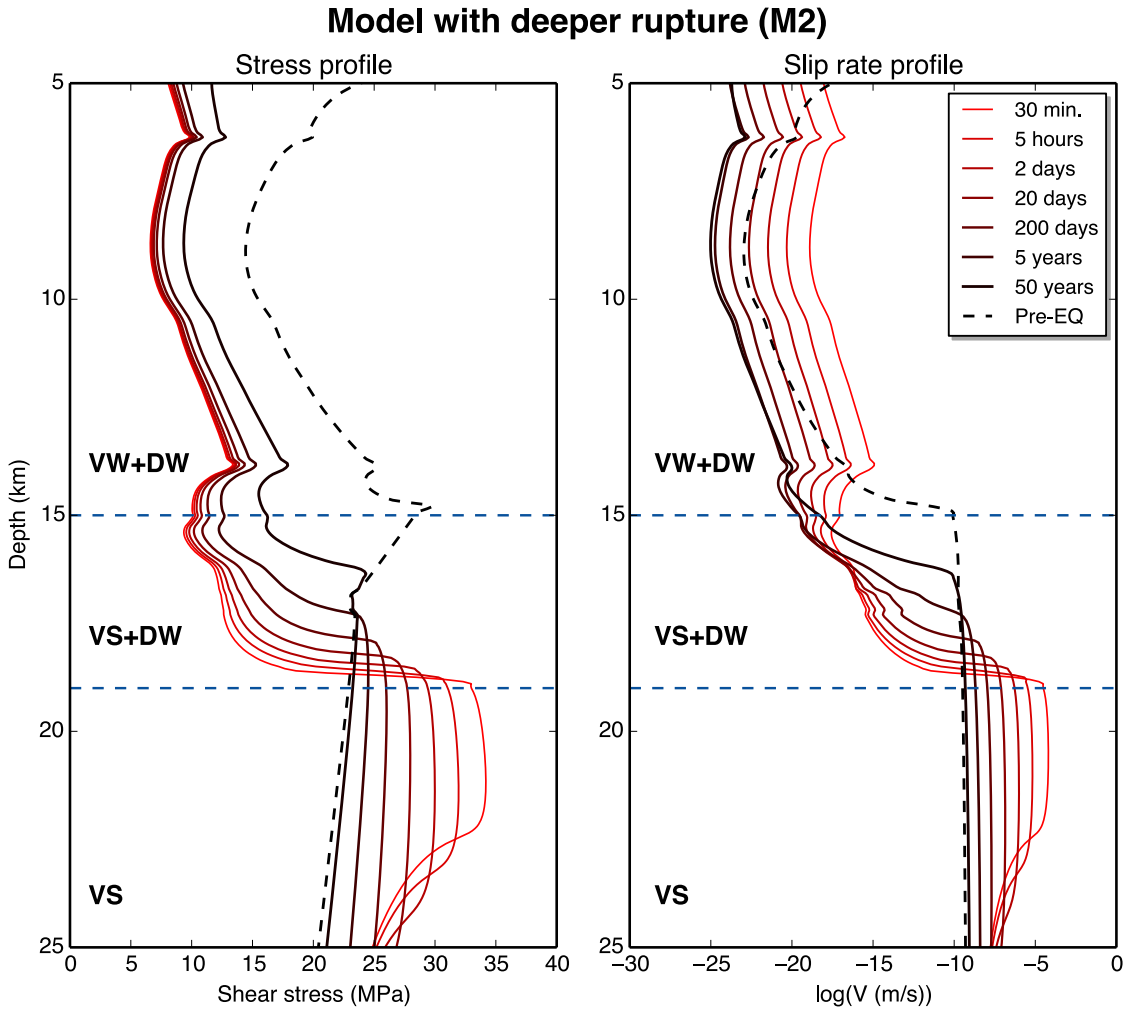


Figure 4.19: *Time evolution of the along-depth shear stress and slip rate profiles in model M2.* The format is the same as Fig. 4.18

unruptured region due to postseismic slip. Let us denote the difference between the stress levels across the SCF by $\Delta\tau_{c-l}$. In Fig. 4.20C-D, the incremental stress and slip over several consecutive time periods indicate that this process is similar to a 2D (Mode III) anti-plane quasi-static crack that slowly advances into the locked region, with time-dependent creeping rates and stress concentration in front of the crack tip. Based on kinematics, the propagation speed of the SCF is equal to the spatial slip gradient (right behind the tip) times maximum slip rate at the SCF. Since slip gradient, as shear strain, is related to stress difference via shear modulus $\mu$, and maximum slip rate at the SCF is just the creeping rate $V_c(t)$, we arrive at the following expression:

$$V_{\text{prop}}(t) = \alpha\,\mu\frac{V_c(t)}{\Delta\tau_{c-l}(t)} \tag{4.6}$$

where $\alpha$ is a coefficient to account for geometrical effects of mapping our results into this approximate model, $\Delta\tau_{c-l}(t)$ is the stress difference across SCF, and $t$ is the time since the previous large earthquake. $\Delta\tau_{c-l}(t)$ is affected by several processes and can be written as:

$$\Delta\tau_{c-l}(t) = \tau_c(t) - \tau_l(t) = \tau_c(t) - [\tau_c(0^-) + \Delta\tau + \Delta\tau_{\text{load}}(t)], \tag{4.7}$$

where $\tau_c(t)$ and $\tau_l(t)$ are the stresses in the creeping and locked regions at time $t$, respectively, $t = 0^-$ is the time right before the earthquake, $\Delta\tau$ is coseismic stress increase, and $\Delta\tau_{\text{load}}$ is the stress increase from loading. $\Delta\tau$ is comparable to the static stress drop during the earthquake $\Delta\tau_{\text{eq}}(< 0)$, so we assume $\Delta\tau = -\Delta\tau_{\text{eq}} > 0$.

To use Eq. 4.6, we need an estimate of $V_c(t)$ and $\tau_c(t)$. In the VS region below the seismogenic zone, postseismic afterslip following large events has been amply documented, (e.g., *Reilinger et al.*, 2000; *Bruhat et al.*, 2011). These observations can be well explained with steady-state VS friction, at least for periods after tens of days since the event, as

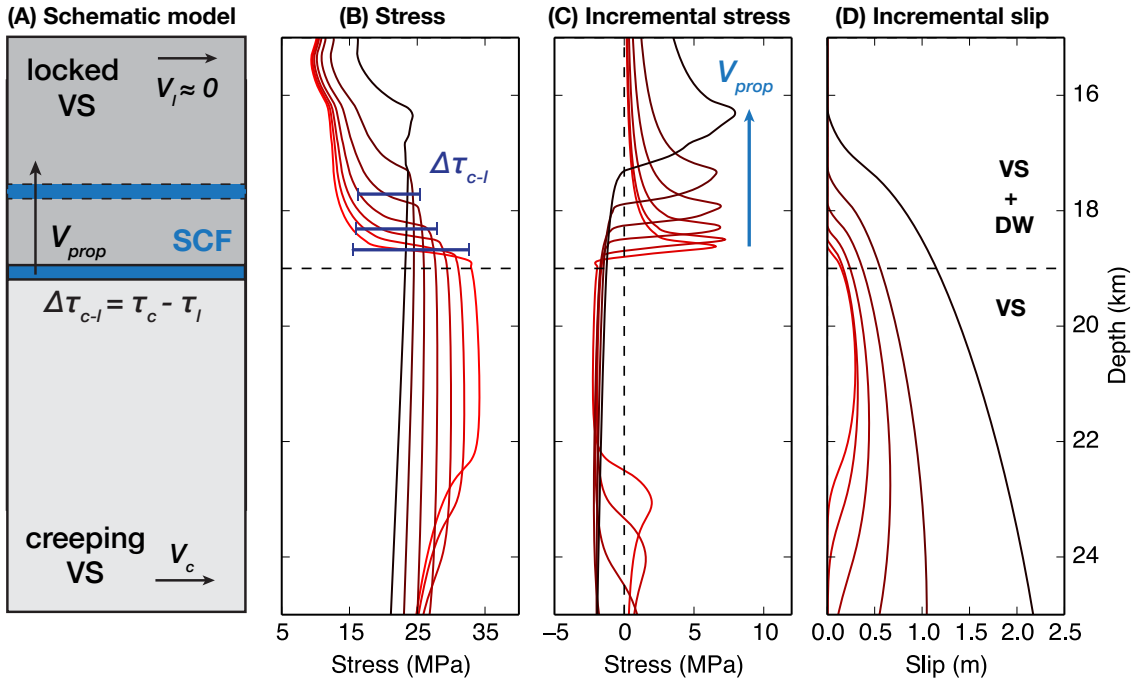


Figure 4.20: *Post- and inter-seismic migration of the SCF after a deeper-penetrating event.* (A) Schematics of the SCF, represented by blue strips with solid and dashed outlines, advancing up-dip with propagation speed $V_{\rm prop}$. The locked and creeping VS regions are associated with slip rate $V_{\rm l}(\approx 0)$, $V_{\rm c}$ and shear stress $\tau_{\rm l}$, $\tau_{\rm c}$, respectively. Stress across SCF is $\Delta\tau_{\rm c-l}$. (B) Depth profile of shear stress during the post- and inter-seismic periods (from red to black: 30 min, 5 hours, 2, 20, 200 days, 5 and 50 years), similar to Fig. 4.19. $\Delta\tau_{\rm c-l}$ for different times are highlighted. (C) Incremental stress and (D) incremental slip during the time intervals shown in (B), indicating a quasi-static, slowly expanding crack. The stress peaks in (C) indicate approximate locations of the SCF. The horizontal black dashed lines indicate the rheological boundaries between VS+DW and VS regions and the vertical dashed line marks the zero-level for stress change.

supported by numerical studies (*Perfettini and Avouac*, 2004; *Perfettini and Ampuero*, 2008). Hence we can write:

$$\tau_{\rm c}(t) = \bar{\sigma}\left[f^* + a\log(V_{\rm c}(t)/V^*)\right] \tag{4.8}$$

Note that we have simplified the notations by using only rate-and-state parameter $a$ since $b = 0$ for the deeper fault extensions in our models. When $b \neq 0$, $a$ is replaced by $(a - b)$ in Eq. 4.8. Formulations for steady-state postseismic fault slip are derived in *Perfettini and*

*Avouac* (2004) with a spring-slider analog. The spring-slider (SS) model ignores the time variation in the size and properties of the afterslip fault zone, but may provide a simplified description of our results. In the context of earthquake sequences, the loading rate $V_0$ and the rate before perturbation $V_i$ in their model coincide with the late-interseismic fault slip rate in our models, therefore $V_i = V_0 = V_c(0^-)$. Recognizing that, we express fault slip rate $V_c(t)$, slip $\delta_c(t)$, and stress $\tau_c(t)$ with formulations modified from *Perfettini and Avouac* (2004) as follows:

$$\delta(t) = V_i\, t_r \log\left[1 + d(\exp(t/t_r) - 1)\right] , \tag{4.9a}$$

$$V_c(t) = V_i \frac{d\exp(t/t_r)}{1 + d(\exp(t/t_r) - 1)} , \tag{4.9b}$$

$$\tau_c(t) = \bar{\sigma} f^* + a \log(V_c(t)/V^*) , \tag{4.9c}$$

with

$$d = \exp(-\Delta\tau_{eq}/a\bar{\sigma}) = V_c(0^+)/V_c(0^-) \quad \text{and} \quad t_r = a\bar{\sigma}/kV_i = a\bar{\sigma}/\dot{\tau} ,$$

where $t_r$ is the characteristic time for the postseismic period, $k$ is the spring stiffness in the spring-slider model, and $\dot{\tau}$ is the shear stressing rate.

To compare the behavior of our models with the simplified formulation above, we take the values of $a\bar{\sigma}$, recurrence time $T_r$ ($\sim$ 250 yr), coseismic stress drop $\Delta\tau_{eq}$ ($\sim$ 10 MPa), and $V_i$ ($0.4 - 0.5V_{pl}$) from the 3D models. Using the constraint for total slip, $T_r V_{pl} = V_i\, t_r \log(1 + d(\exp(T_r/t_r) - 1))$, we solve for the effective $t_r$. In Fig. 4.21, we show the behaviors of VS regions in three models (model M2-L, M2, M2-H) with different frictional properties at depth. The general trend of the postseismic fault response in the VS region of the 3D models is predicted relatively well by Eq. 4.9 for $t > 10^6$ seconds (10 days) after the event. The increasing deviations with larger $a$ suggest a time-variable $t_r$ in the 3D models

due to the expansion of postseismic slipping regions. In the late interseismic period before an event, the VS region slips at a rate below the long-term plate rate, as seen in other studies as an expanding stress-shadowing zone (*Hetland and Simons*, 2010). In the context of our models, such lower rate is needed to balance the afterslip.

Combining Eq. 4.6 and Eq. 4.9, the migration speed of the SCF in the post- and interseismic periods is given as:

$$V_{\rm prop}(t) = \alpha G \, \frac{V_{\rm c}(t)}{\tau_{\rm c}(t) - \left[\tau_{\rm c}(0^-) + \Delta\tau_{\rm eq} + \Delta\tau_{\rm load}(t)\right]} \approx \alpha G \, V_{\rm c}(t) \left[\bar{\sigma} f^* + a\,\bar{\sigma} \log(V_{\rm c}(t)/V^*) - (\tau_{\rm c}(0^-) + \Delta\tau_{\rm eq})\right]^{-1},$$

where the pre-seismic stress level for the creeping regions is $\tau_{\rm c}(0^-) = \bar{\sigma}\,[\mu^* + a \log(V_i/V^*)]$. We ignore the stressing $\Delta\tau_{\rm load}(t)$, since this term is smaller compared to other stress changes, and this simplification leads to a lower-bound estimate on $V_{\rm prop}$. Then we get the following estimate for the migration speed and propagation distance of the SCF:

$$V_{\rm prop}(t) = \frac{\alpha G \, V_{\rm c}(t)}{a\,\sigma \log\left(V_{\rm c}(t)/V_i\right) - \Delta\tau_{\rm eq}}, \tag{4.10}$$

$$D_{\rm prop}(t) = \int_0^t V_{\rm prop}(t')\,{\rm d}t' \quad \text{for} \quad t \le T_{\rm r}. \tag{4.11}$$

Using Eq. 4.11, we find that $\alpha = 0.18$ gives a reasonable match between our 3D fault models and the simplified estimate, with deviations expected for cases with larger $a\bar{\sigma}$ (Fig. 4.22). Nonetheless, the total migration distance in all models is well reproduced. We further estimate the total migration distance of SCF, and hence of the locked-creeping transition, for fault segments with a range of properties, e.g., known $T_{\rm r}$ and $V_{\rm pl}$ and feasible values for $a\bar{\sigma}$ and $\Delta\tau_{\rm eq}$. In Fig. 4.23, we make such an estimation for $a$ = 0.005-0.03, $\sigma$ = 50-200 MPa and $\Delta\tau_{\rm eq}$ = 3-12 MPa, assuming different combinations of parameters

$V_i = 0.4V_{\rm pl}$ or $0.6V_{\rm pl}$ and $T_r = 200$ or 250 yr. We observe that $D_{\rm prop}$ depends strongly on $\Delta\tau_{\rm eq}$ and relatively weakly on $a\bar{\sigma}$. In the cases with small $a\bar{\sigma}$, a significant fraction of the postseismic slip occurs in a short time period ($t < 10$ days) following the event, so the approximate model would under-estimate $D_{\rm prop}$. In the cases with large $a\bar{\sigma}$, the overall small postseismic slip rate over a large characteristic time would lead to a smaller $D_{\rm prop}$. Based on these considerations, for events with larger stress drops ($> 5$ MPa) and reasonable values of $a\bar{\sigma}$, this migration distance could be at least 3-5 km.

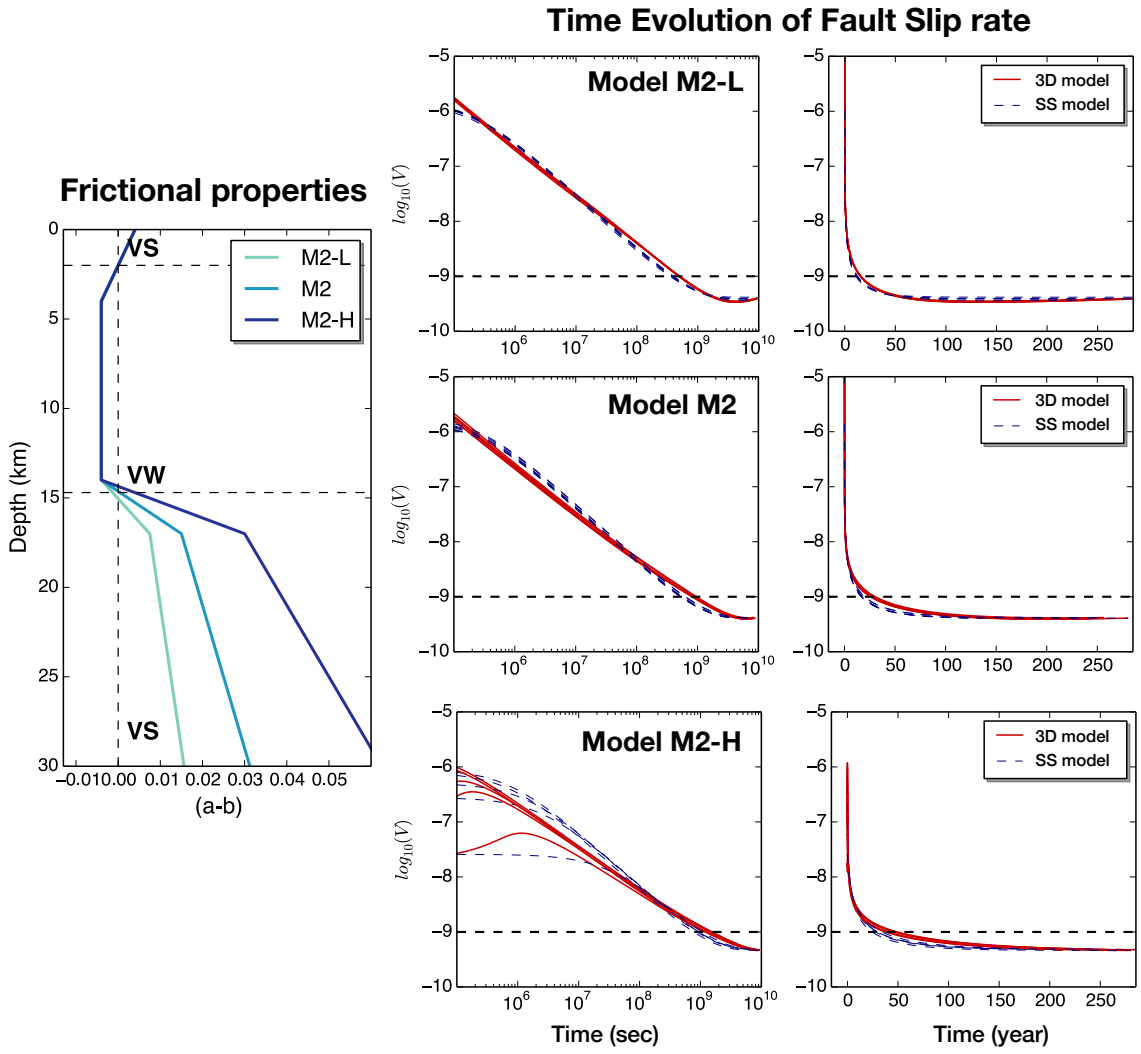


Figure 4.21: *Postseismic response of faults with different frictional properties at depth.* (Left) Depth profiles of frictional properties $(a-b)$ for three models denoted by M2-L, M2 and M2-H. (Right) Postseismic fault slip rate at the depth of 21.5 km ($a-b = 0.01, 0.02, 0.04$ for the three models, respectively), just below the rupture extent of the preceding large event. Red lines give numerical results from our 3D models and blue dashed lines are theoretical predictions based on the spring-slider (SS) model (Eq. 4.9).

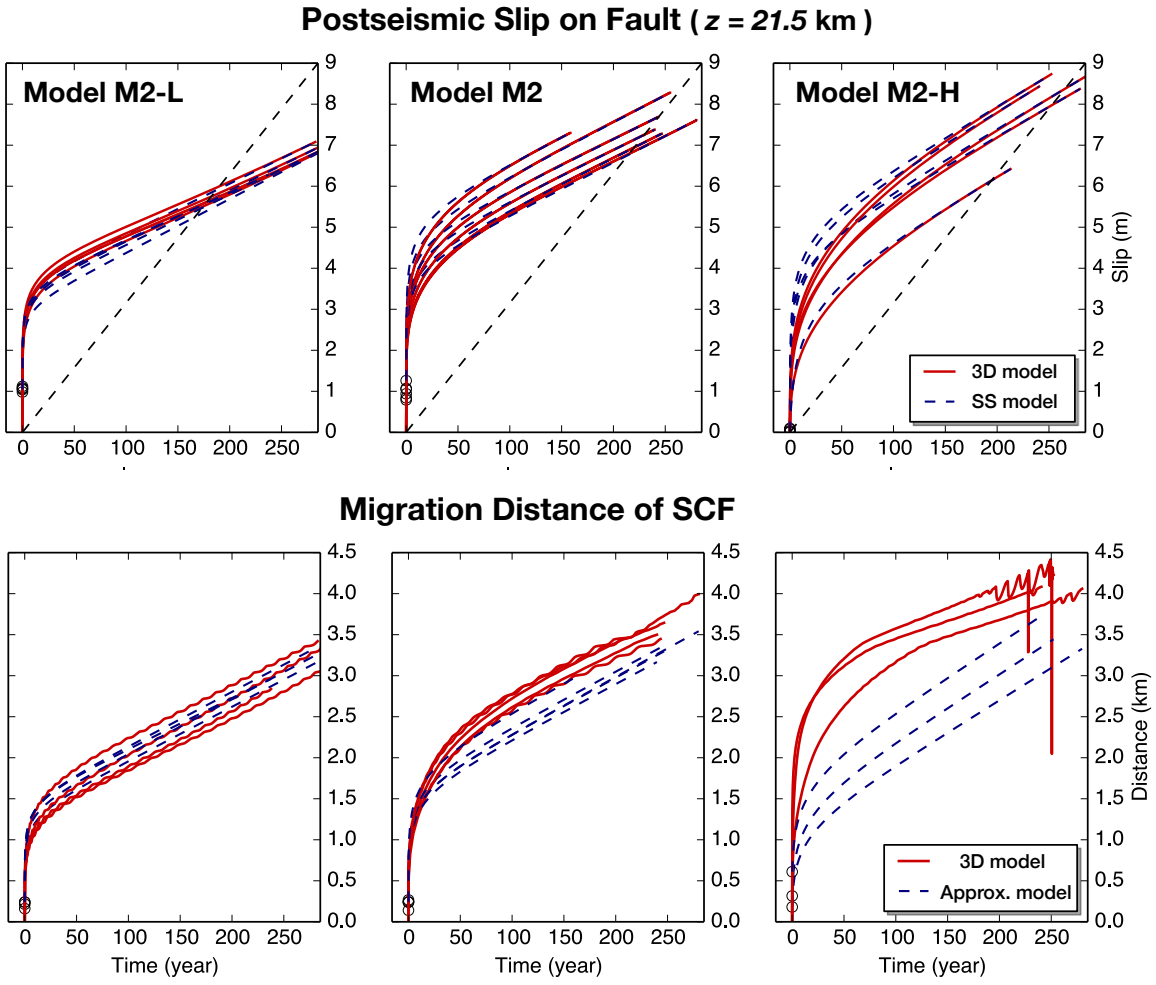


Figure 4.22: *Post- and inter-seismic fault slip and the migration of SCF.* (Top) Postseismic fault slip in the VS region ($z = 21.5$ km) in the 3D models and spring-slider (SS) models. The three 3D models have different frictional properties at depth, as shown in Fig. 4.21. (Bottom) Migration of the stress concentration front (SCF) (defined as the depth with the slip rate of $0.1V_{\max}$, where $V_{\max}$ is the maximum slip rate over the fault at the time) in 3D models and in 3D models and the approximation (Eqs. 4.10-11). Black circles represent the time of $10^5$ s, the start time for the approximate solution.

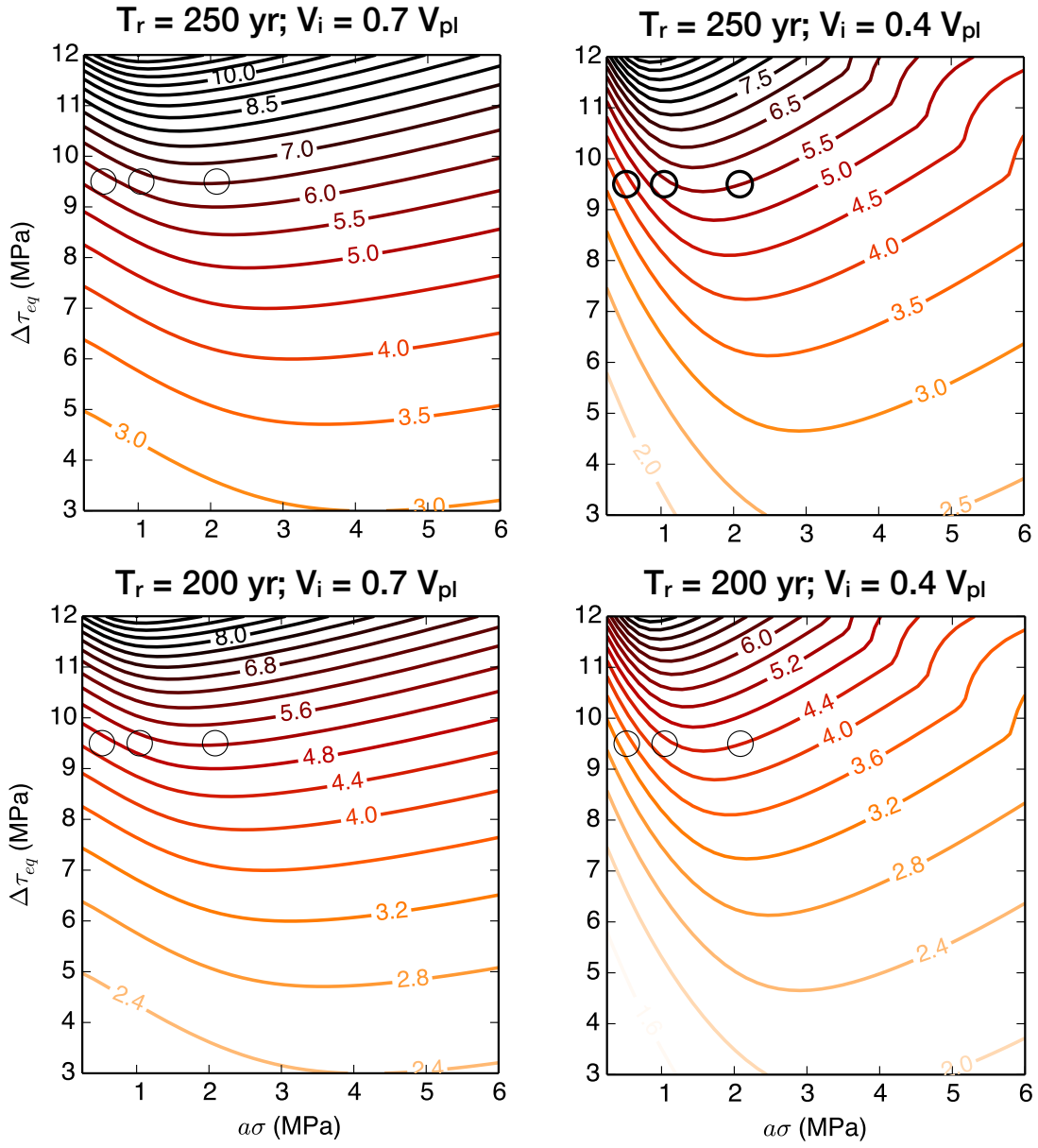


Figure 4.23: *Dependence of migration distance $D_{prop}$ of the SCF on $\Delta\tau_{eq}$ and $a\bar{\sigma}$.* Different combinations of earthquake recurrence time $T_{\rm r} = 200, 250$ yr. and late interseismic fault slip rate $V_i = 0.4V_{\rm pl}$, $0.7V_{\rm pl}$ are used in the calculation. Black circles (thick outlines) represent the approximate locations in the parameter space for the three models M2-L, M2, and M2-H ($T_{\rm r} \approx 250$ yr., $V_i \approx 0.4V_{\rm pl}$) and their corresponding locations (thin outlines) in other plots.

# Chapter 5

# Connecting Seismicity, Fault Locking and Large Earthquake Rupture at Depth

# Abstract

The thickness of the seismogenic zone is commonly determined based on seismicity or fault locking depth inferred from surface geodetic measurements. The physical relation between the seismicity and estimates of fault locking, and their constraints on the locked-creeping (LC) transition on faults have important implications for fault behavior and rheology at depth, but remain poorly understood. We study the behavior of seismicity and the LC transition in fault models governed by rate-and-state friction and enhanced dynamic weakening, with microseismicity resulting in our models due to fault heterogeneity favoring nucleation. We find that the LC transition between the fully locked and fully creeping regions occurs over a broad depth range. The true locking depth ($D_{\mathrm{lock}}$), associated with the stress concentration front (SCF) and microseismicity, is located near the top of the LC transition, while the locking depth estimated geodetically ($D_{\mathrm{geod}}$) depends on the spatial distribution of fault slip rates. Following large earthquakes, $D_{\mathrm{lock}}$ either stays near the bottom of the seismogenic zone or becomes shallower due to the up-dip migration of SCF, while $D_{\mathrm{geod}}$ tends to deepen as the slip deficit region expands. This leads to a divergence of $D_{\mathrm{lock}}$ and $D_{\mathrm{geod}}$ in the late interseismic period, which is most pronounced in the case of deeper penetration of earthquake rupture and/or significant postseismic slip. *A priori* assumption that $D_{\mathrm{geod}}$ equals to the depth of seismicity could lead to an underestimation of fault slip rates and a discrepancy with geological estimates. The discrepancy between seismicity and $D_{\mathrm{geod}}$,

if accurately determined, could indicate conditions of the LC transition, and constrain the spatial extent of co- and post-seismic fault slip. However, for some fault segments, this relation could be complicated by highly heterogeneous fault properties and additional physical mechanisms at the transitional depths.

## 5.1 Introduction

The depth of faulting and its temporal evolution are important for understanding fault rheology and estimating moment release deficit directly relevant for seismic hazard assessments. For well-instrumented major strike-slip fault systems, e.g., the San Andreas and San Jacinto faults in Southern California (Fig. 5.1), cut-off depths of seismicity ($D_{\mathrm{seis}}$), determined with high-resolution earthquake catalogue (*Nazareth and Hauksson*, 2004; *Hauksson*, 2011), and interseismic fault locking depth ($D_{\mathrm{geod}}$), inferred from surface geodetic measurements (*Smith-Konter et al.*, 2011; *Tong et al.*, 2014), give independent estimates on the thickness of the seismogenic zone for different fault segments. As shown in Chapter 4, the transition from the fully locked to creeping regions on the fault occurs over a band, while a geodetically determined $D_{\mathrm{geod}}$ is based on inversions of surface velocity field using a simplified model. Hence it is important to understand the relation between the seismicity and $D_{\mathrm{geod}}$, and whether/how they relate to the depth extent of large earthquake rupture ($D_{\mathrm{rupt}}$).

Conventional earthquake cycle models that focus on deformation over large time scales usually adopt simplistic treatment of these depths. For example, in the elastic dislocation model (Fig. 5.2; *Savage and Burford*, 1973), long-term fault slip is accommodated by uniform coseismic slip within the seismogenic zone (SZ) and interseismic creep below, with $D_{\mathrm{rupt}}$ and $D_{\mathrm{geod}}$ coinciding as the base of the SZ. Kinematic viscoelastic earthquake cycle models (e.g., *Savage and Prescott*, 1978) introduce time-dependence of $D_{\mathrm{geod}}$, yet retain the unrealistic stress singularities at the tip of the dislocation. With stress perturbations from the imposed earthquake, models that incorporate viscoelasticity and rate-and-state friction (e.g., *Li and Rice*, 1987; *Hetland et al.*, 2010; *Takeuchi and Fialko*, 2012) have physically more realistic fault and/or bulk behavior. While these models reproduce the effect of earth-

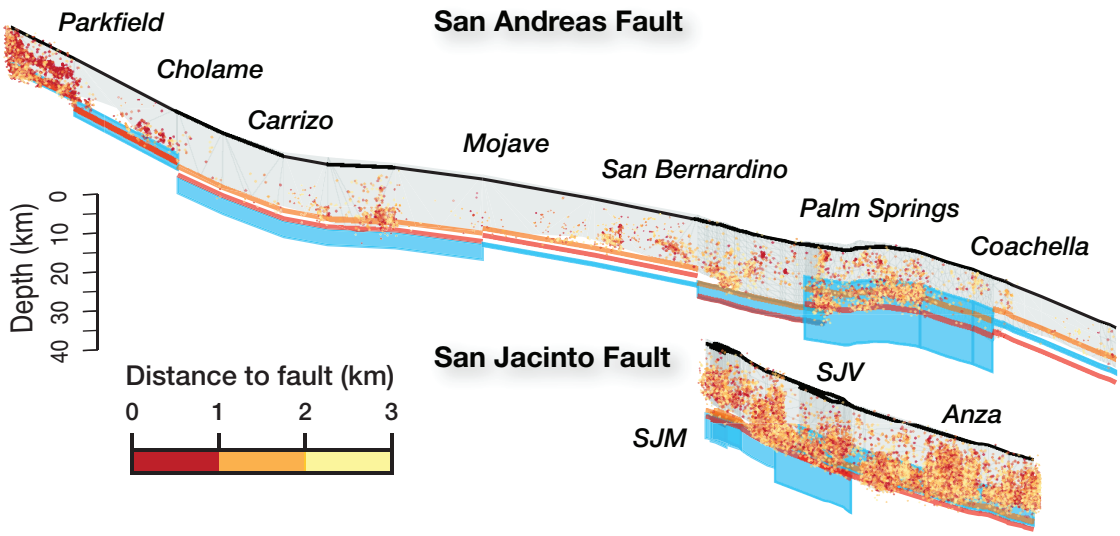


Figure 5.1: *Seismicity and geodetic locking depths on the Southern San Andreas and San Jacinto fault.* Fault geometry is from the Southern California Earthquake Center (SCEC) Community Fault Model (CFM) (*Plesch et al.*, 2007). Blue bands represent the range of fault locking depths within $1\sigma$ uncertainty determined from surface geodetic measurements (*Smith-Konter et al.*, 2011). Orange and red lines represent the 90% and 99% cut-off depths of seismicity (*Nazareth and Hauksson*, 2004; *Lin et al.*, 2007). Seismicity from the catalog of *Hauksson et al.* (2012) is plotted within 3 km of the fault geometry. SJM: San Jacinto Mountain. SJV: San Jacinto Valley.

quakes on post- and inter-seismic crustal deformation, they do not provide insights on how the loading from deeper creeping regions affect the locked zone. Understanding the behavior of seismicity at the transitional depth between the locked and creeping regions is also important, because large earthquakes tend to initiate around this depth (*Das and Scholz*, 1983) and could be related to small earthquakes (*Lapusta and Rice*, 2003). In this study, we explore the behavior of seismicity and geodetic observables in long-term fault models that include microseismicity and large earthquake rupture, to understand their spatial and temporal relations, and the connections between interseismic and coseismic fault behavior.

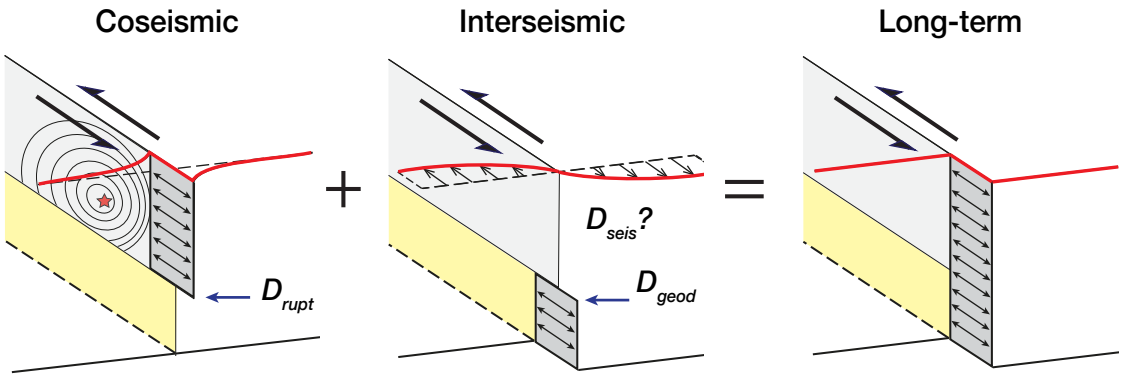


Figure 5.2: *Conventional elastic dislocation model for earthquake cycles.* The long-term fault slip budget comprises uniform coseismic slip in the seismogenic zone and interseismic fault creep below. $D_{\text{rupt}}$ during the earthquakes and $D_{\text{geod}}$ in the interseismic period coincide and define the base of the seismogenic zone. Seismicity is not relevant in such kinematic models, and $D_{\text{seis}}$ is often assumed to delineate the base of the seismogenic zone and therefore should be the same as or close to $D_{\text{lock}}$.

## 5.2 Model setup

Laboratory friction experiments and theoretical studies have documented rate-and-state friction (RSF) at low slip rates relevant for earthquake nucleation (*Dieterich*, 1979, 1981; *Ruina*, 1983), as well as a variety of mechanisms for enhanced dynamic weakening (DW) at high slip rates relevant for the propagation of earthquake rupture (e.g. *Rice*, 2006; *Tullis*, 2015, and references therein). The two physical mechanisms are active at different slip rate regimes, so the transitional depth of RSF properties and the depth extent of DW properties are not necessarily the same.

We consider four scenarios of different frictional properties (RSF and/or DW) at the transitional depth of the fault, as shown in Fig. 5.3. In model M1 (Fig. 5.3A), the fault is only governed by RSF with depth-dependent steady-state velocity-weakening (VW) and velocity-strengthening (VS) properties based on laboratory experiments (*Blanpied et al.*, 1995). The depth-dependence of RSF properties has been used to explain the depth variation of fault slip behavior (*Scholz*, 1998) and successfully applied to 2D models of earthquake

sequence and aseismic slip (*Tse and Rice*, 1986; *Lapusta et al.*, 2000), and 3D modeling of the $M_w$ 6.0 Parkfield sequence (*Barbot et al.*, 2012).

In addition to the RSF properties, models M2-4 (Fig. 5.3B-D) incorporate DW within different depth limits with respect to the VW/VS transition of RSF: shallower DW in model M2 (Fig. 5.3B), DW ending at the VW/VS transition in model M3 (Fig. 5.3C), and deeper DW in model M4 (Fig. 5.3D), thereby allowing coseismic weakening of faults and the rupture and arrest of large earthquakes at different depths. Models M2 and M4 have been considered in Chapter 4 to explain the quiescence of seismicity that results from deeper penetration of earthquake rupture. Building on Chapter 4, here we expand the range of fault models and further explore and characterize the differences between the models in terms of geodetic and seismic observables arising in the long-term fault behavior. In part, we focus on the relation between the gradual creeping-locked transition characteristic for such models and geodetically estimated locking depth $D_{\text{geod}}$.

## 5.3 Seismic and aseismic behavior in long-term fault models

### 5.3.1 Large earthquake rupture and seismicity

The long-term behavior of fault models shown in Fig. 5.3 is characterized by stable fault creep over the time scale of years, punctuated by short bursts of large earthquakes lasting tens of seconds, and postseismic fault slip that follows, as well as the occurrence of microseismicity, the patterns of which patterns vary across models depending on the frictional properties at depth.

We show the spatial relation between the coseismic slip during large earthquakes and microseismicity in Fig. 5.4. The maximum earthquake slip is about 2 m in model M1 and

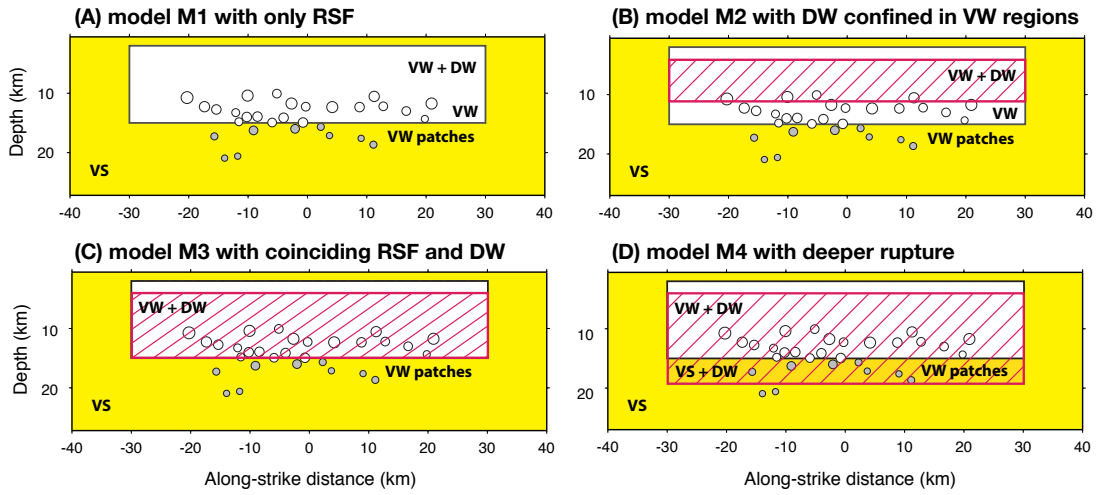


Figure 5.3: *Fault models with different frictional properties at the seismic-aseismic transition.* (A) Model M1 with only rate-and-state friction (RSF), which contains a shallower steady-state velocity-weakening (VW) region (white) and a deeper steady-state velocity-strengthening (VS) region (yellow). (B) Model M2 with dynamic weakening (DW) (red hashed region) confined within the VW region. (C) Model M3 with the depth extent of DW coinciding with the VW/VS transition. (D) Model M4 with deeper extent of DW than the VW/VS transition. VW patches (small circles) that represent fault heterogeneity are imposed near the VW/VS boundary, following the same spatial distribution and frictional properties across the four models; most patches are within the VW region (white circles) but some are in the deeper VS region (gray circles).

reaches about 10 m in the other models, due to more prominent fault weakening and larger coseismic stress drop aided by DW. This is reflected in the difference in recurrence times of large events between M1 (about 40 yr) and the other 3 models M2-4 (approximately 180 yr, 200 yr and 250 yr, respectively). Larger depth extent of DW leads to small increase in average fault slip during the earthquakes, with spatial variations in coseismic slip as a result of complex rupture in the heterogeneous stress field developed over prior fault slip history. The most prominent difference in the fault behavior between models manifest itself in the patterns of microseismicity. Over similar time periods, model M2 produces the most active seismicity at the transitional depth due to the sharp stress gradient between the fully locked region (VW+DW) and higher-stressed region (VW) below. Comparing models M2-M4, we find that the number of events decreases with the increase of the depth extent

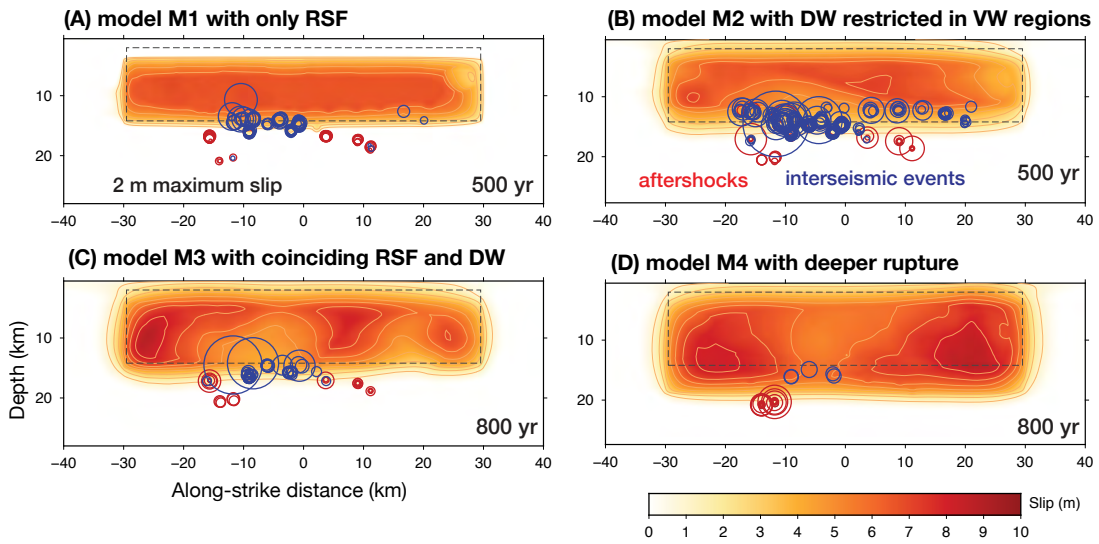


Figure 5.4: *Distribution of large earthquake slip and seismicity in the long-term fault models.* The four scenarios correspond to the four models in Fig. 5.3. Coseismic slip during a typical fault-spanning large earthquake is plotted for each model with contours of 0.4 m for (A) and 1 m for (B)-(D). The "aftershocks" (red) are arbitrarily selected as events that occur within 3 years following the mainshock, and the interseismic events (blue) are seismicity that occur outside this "aftershock period". Seismicity is plotted as circles with size determined from the circular crack model with equivalent seismic moment and assumed stress drop of 3 MPa, over a time period of 500 yr. for (A)-(B) and 800 yr. for (C)-(D).

of earthquake rupture and hence the locked region. In comparison, model M1 has smaller activity of microseismicity since the stress changes on the purely RSF fault is relatively minor. The absence of a seismically active transition region contributes to the delayed occurrence of large events, leading to larger recurrence intervals associated with M3 and M4.

Analysis of the stress state at the transitional depth further illuminates the underlying process that controls the microseismicity. In Fig. 5.5, we show the depth profiles of fault shear stress for different post- and inter-seismic times, as well as the incremental stress and slip for the corresponding time windows (defined as the increase in stress and slip over a time period), which are indicative of stressing on the fault. From comparisons between M1-3, we observe that (1) VW regions with DW (above the red lines in M2 and M3) experience

near-complete stress drop and produce little microseismicity throughout the interseismic period; (2) VW regions without DW (above the blue line in M1) experience minor stress drop and microseismicity start to appear in the later interseismic period when significant creep penetrates into the VW region; (3) The VW regions without DW but next to those with DW (between the red and blue lines in M2) have rapid increase in stress immediately following the earthquake, leading to frequent seismicity throughout the interseismic period. In model M4, microseismicity is nearly absent, with events only occurring on the patches in the VS region in the late interseismic period.

In all four models, the occurrence of microseismicity is related to the stress concentration front (SCF) induced at the updip tip of the creeping crack between the fully locked and downdip creeping regions, and it is still smoothed over some small depth range, as seen in column (ii) of Fig. 5.5. Here we define the true locking depth $D_{\text{lock}}$ as the depth at which fault slip rate just exceeds a relative threshold ($V = 0.1V_{\text{max}}$, where $V_{\text{max}}$ is the maximum slip rate on the fault). $D_{\text{lock}}$ is physically meaningful since it is approximately located at the updip tip of the creeping crack and also the center location of SCF. Since the high stressing rates at $D_{\text{lock}}$ should influence microseismicity, $D_{\text{lock}}$ is expected to be close to the empirically determined cut-off depths of seismicity ($D_{\text{seis}}$) for cases when $D_{\text{lock}}$ lingers in one place, at the bottom of the VW region. This direct association of $D_{\text{lock}}$ and $D_{\text{seis}}$ would then also lead to spatially concentrated microseismicity, like for the Parkfield segment (*Waldhauser et al.*, 2004). The relation between $D_{\text{lock}}$ and $D_{\text{seis}}$ could be more complicated if a significant fraction of microseismicity occurs in isolated fault heterogeneity surrounded by the creeping regions, such as the events (blue) in column (v) of Fig. 5.5 and cases considered in Section 5.5. While $D_{\text{lock}}$ migrates updip with time between the ruptured and creeping VS regions in model M4, as studied in Chapter 4, it usually does not change

significantly in depth in models M1-3, but it is susceptible to constant perturbations from nearby small events.

### 5.3.2 Fault coupling and geodetically-estimated fault locking depth

We use the interseismic fault coupling (ISC, defined as equal to $1 - V/V_{\rm pl}$, where the plate rate $V_{\rm pl} = 10^{-9}$ m/s in our models), a common parameter used in studies of interseismic deformation of subduction zones (e.g., *Konca et al.*, 2008; *Kaneko et al.*, 2010), to compare the conditions and time evolution of interseismic creep in these models and their differences, with the coupling for M2 and M4 shown in Fig. 5.6. Model M2 has earthquake ruptures confined in SZ, with a sharp transition from the fully locked (ISC equal to 1) to fully creeping (ISC equal to 0) regions in the early interseismic periods. Model M4 hosts events that penetrate deeper into the VS regions, thus a larger spatial extent of ruptured region and surrounding postseismic slip. In both models, the regions of slip rate lower than $V_{\rm pl}$ expands in space with time. We call this the slip deficit zone, which is similar to the stress shadowing region discussed in (*Bürgmann*, 2005; *Hetland and Simons*, 2010), but differs in the sense that, in our models, the expansion of the region is directly affected by the amplitude and spatial extent of postseismic fault slip, and to a lesser extent, by the conditions of the locked zone. Besides, another prominent feature observed in both models, in particular M4, is the shrinkage of the fully locked region (ISC equal to 0), due to mechanical erosion from the surrounding creep. The evolution processes of the fully locked zone and slip deficit zone has direct influence on the time dependence and relation between the true locking depth ($D_{\rm lock}$) and the geodetically-determined locking depth ($D_{\rm geod}$).

In Fig. 5.7, we show the depth profiles of fault slip rates for several typical post- and inter-seismic times in model M4. Toward the end of the interseismic periods, the region with

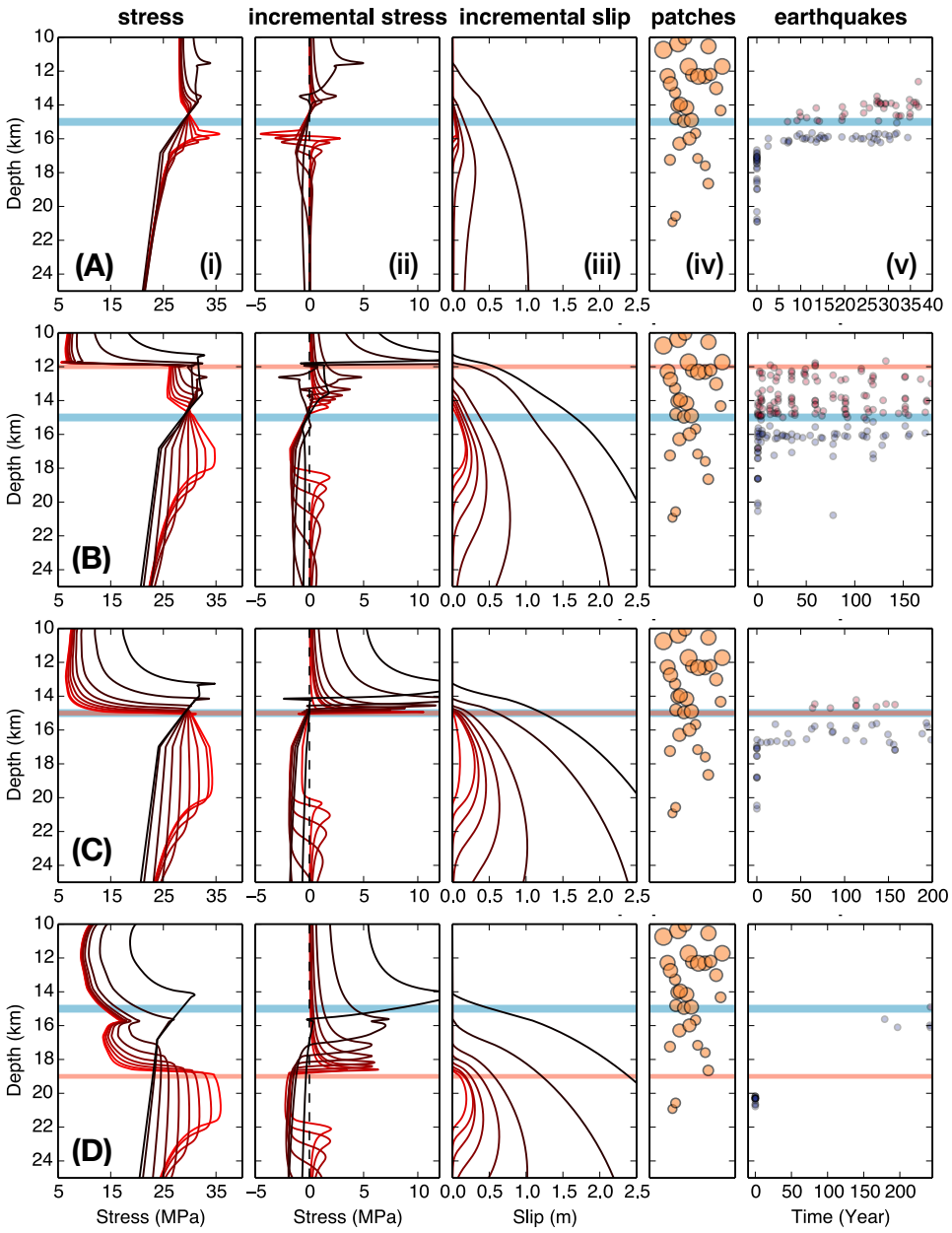


Figure 5.5: *The depth distributions of stress, stressing, fault slip and seismicity.* The four rows (A)-(D) correspond to the four models M1-4 in Fig. 5.3, respectively. The depth distribution of shear stress is plotted in column (i) at different times: 3 min, 30 min, 5 hours, 2 days, 20 days, 200 days, 5 yr, and 50 yr (except for (A)) following the main shock, which are equally spaced on the logarithmic scale of time and change in color from red to black. In column (ii) and (iii), the depth distribution of incremental stress and slip are shown for the time intervals corresponding to the times in (i). In column (iv), an illustrative view of the depth distribution of VW fault patches is displayed with the along-strike dimension compressed in the horizontal axis. In column (v), time evolution of the depths of seismicity in VW region (red) and those in VS region (blue) are plotted in each model. Blue and red horizontal lines correspond to the VW/VS boundary and the depth limit of DW.

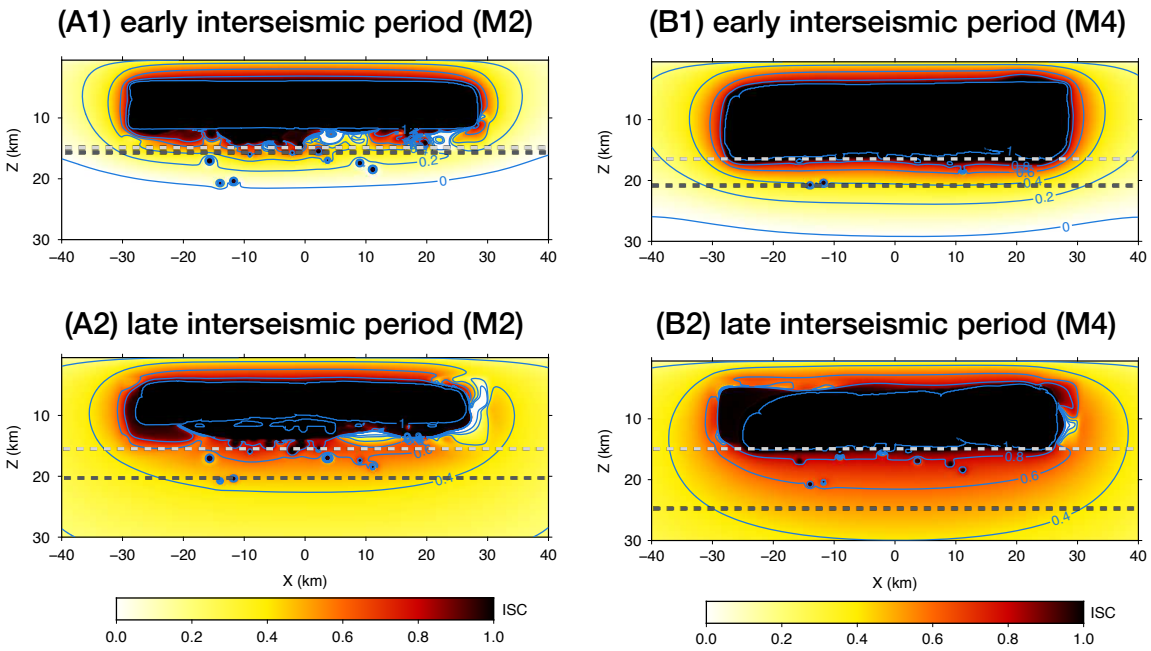


Figure 5.6: *Time evolution of fault coupling in the interseismic periods.* The interseismic fault coupling (ISC, defined as $1 - V/V_{\rm pl}$, where $V$ is the fault slip rate and $V_{\rm pl}$ is the plate rate) is shown in color with contours of 0.2 for the early interseismic (36 yr after the large earthquake for A1 and 50 yr after for B1) and late interseismic (36 yr before the next earthquake for A2, and 50 yr before for B2) periods of fault model M2 (A) and M4 (B), as shown in Fig. 5.3. The recurrence time of large events are approximately 180 yr and 250 yr. for model M2 and M4. The corresponding $D_{\rm lock}$ and $D_{\rm geod}$ are represented by gray and black dashes lines.

slip rate that transitions from fully locked state to near plate rate, occurs over a significantly broad depth range from 15 km to more than 30 km. The corresponding fault-parallel surface velocity profiles, predicted in a homogeneous half-space (*Okada*, 1992), feature high strain rates across the fault and half the plate rate in the far-field velocity field (not shown in the plot).

On one hand, the true locking depth $D_{\rm lock}$ is physically well-defined by the stress concentration front at the tip of the downdip creeping front. We find that this depth could be estimated reasonably well by the depth at which fault slip rate just exceeds a threshold value in the relative sense (e.g., $V = 0.1V_{\rm max}$, where $V_{\rm max}$ is the maximum slip rate on the fault). An alternative could be an absolute threshold (e.g, $V = 0.1V_{\rm pl}$). Both choices pro-

duce similar results for the interseismic period. On the other hand, the determination of the fault locking depth $D_{\text{geod}}$, as commonly inferred from geodetic measurements, is an inverse problem that depends on the assumption of forward models and the choice of formulation. The inversion for the fault locking depth $D_{\text{geod}}$ is usually done together with fault slip rate $V_{\text{cr}}$, based on the dislocation model in a elastic half space or layered viscoelastic model, where $V_{\text{cr}}$ is the uniform creeping rate below $D_{\text{geod}}$ (e.g., *Savage and Burford*, 1973; *Smith-Konter et al.*, 2011). In the elastic dislocation model, the surface velocity profile across the fault $v(x)$ is a simple function of the fault-normal distance $x$, with two parameters, the depth of dislocation $D$, i.e., $D_{\text{geod}}$, and the far-field velocity (plate rate) $V_{\text{cr}}$:

$$v(x) = \frac{V_{\text{cr}}}{\pi} \arctan \frac{x}{D} \tag{5.1}$$

In Fig. 5.8, we demonstrate such procedure using the results from our fault models as physically plausible scenarios. We construct synthetic surface velocity profiles, as in Fig. 5.7B, with station spacing of 2 km and assuming uncorrelated Gaussian errors of 2 mm/yr, based on the depth distribution of fault slip rates from several typical epochs in the interseismic period of a large earthquake. Then we invert for $D_{\text{geod}}$ and $V_{\text{cr}}$ for these epochs within a distance of 100 km from the fault. The inversion is conducted in a Bayesian formulation, in which uncertainty and correlation could be easily studied. In Fig. 5.8A, the joint probability density function (PDF) of $D_{\text{geod}}$ and $V_{\text{cr}}$, shown in the form of $1\sigma$ and $2\sigma$ Bayesian credible regions, indicates the domain of the parameter space that generates reasonable data fit within associated errors, with the peak of PDF indicating the maximum likelihood estimate (MLE). Since we use uninformative uniform prior on $D_{\text{geod}}$ and $V_{\text{cr}}$, the size of the credible region in Fig. 5.8A reflects the inherent resolution of the data and problem,

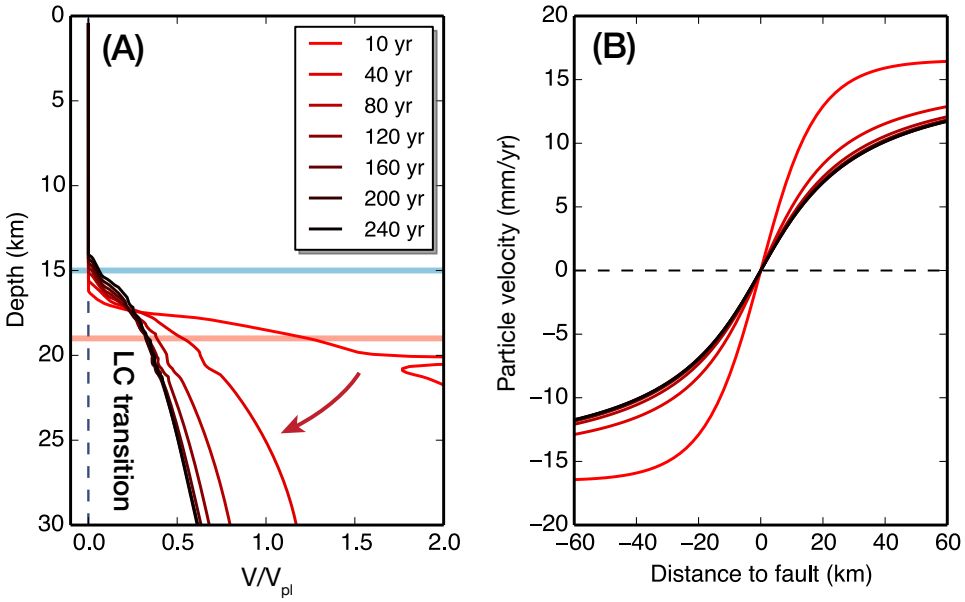


Figure 5.7: *Time-dependent fault slip rates at depth and surface velocity.* (A) Fault slip profiles along the depth (averaged over 5 km along the fault strike) are shown for different times following the large earthquake in model M4. The locked-creeping (LC) transition between the fully locked and fully creeping regions occurs over a broad depth range. Blue and red horizontal lines correspond to the VW/VS boundary and the depth limit of DW. The regions above 10 km are assumed fully locked in the prediction of surface deformation. (B) The fault-parallel surface velocity profile across the fault results from the corresponding fault slip rate profile at depth in (A) and is also time-dependent.

with the marginal and conditional PDF of $D_{\mathrm{geod}}$ corresponding to an unconstrained and perfectly constrained $V_{\mathrm{cr}}$, and thus a upper and lower bound on the uncertainty of $D_{\mathrm{geod}}$, respectively. Alternatively, more reasonable prior constraints could be adopted, e.g., from the geological estimates (*Segall*, 2002), to reduce the uncertainty and change the most likely values. Besides, denser station coverage and smaller observational error could both help reduce the uncertainty on $D_{\mathrm{geod}}$.

### 5.3.3 Spatial relations and temporal evolutions of different depths

In Section 5.3.1, we have identified the true locking depth $D_{\mathrm{lock}}$ as the depth of stress concentration and relevance for promoting microseismicity. In Section 5.3.2, we have developed

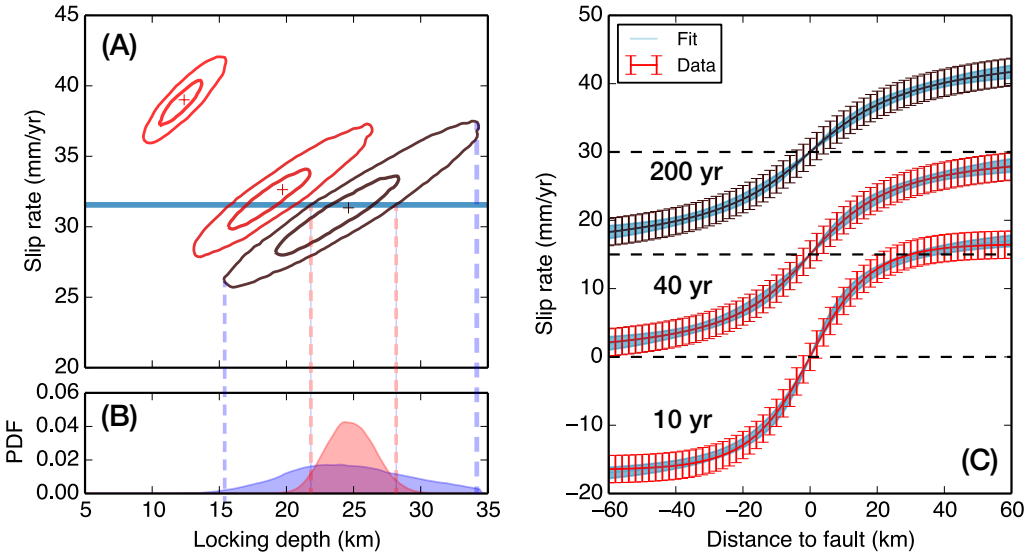


Figure 5.8: *Inversion of the locking depth $D_{geod}$ and fault slip rate $V_{cr}$.* (A) The joint posterior probability density function (PDF) for $D_{\rm geod}$ and $V_{\rm cr}$ is shown for three times in the interseismic period: 10, 40 and 200 yr after the earthquake. The two parameters at each time are inverted from the synthetic surface velocity profile predicted from the along-dip profile of fault slip rates (e.g., Fig. 5.7) based on the dislocation model in a homogeneous half-space, assuming uncorrelated Gaussian errors ($\sigma = 2$ mm/yr.) on the data. The smaller and larger ellipses represent the 68% and 95% Bayesian credible regions for the joint PDF through Gaussian kernel density estimation (KDE). The blue line indicates the true fault slip rate $V_{\rm pl} = 10^{-9}$ m/s = 31.6 mm/yr. (B) The marginal PDF (blue) and the conditional PDF (red) of the locking depth are shown, corresponding to unconstrained and perfectly constrained fault slip rate (at $V_{\rm pl}$). (C) The fit of the synthetic surface velocity profiles (red or black lines with error bars) using the posterior solutions obtained in (A) are shown as blue lines.

the procedure to determine the equivalent $D_{\rm lock}$ and $D_{\rm geod}$ from the depth distribution of slip rates in our physical models. Here we further explore the spatial-temporal relations between the two, and their relation to the boundary of VW/VS regions and the depth extent of large earthquake rupture $D_{\rm rupt}$. In addition, we also consider an empirical measure of the fault locking depth ($D_{0.5\rm C}$), where the fault slip rate equals half the plate rate, which, as we show in the following provides a gross estimate of $D_{\rm geod}$.

We show the depth of $D_{\rm rupt}$, $D_{\rm lock}$, and $D_{0.5\rm C}$ and their time evolutions for the four models in Fig. 5.3(A-C, E). Overall, $D_{\rm lock}$ depends on the gradient of fault slip rates and is

located near the top of the LC transition, while $D_{\mathrm{geod}}$ depends on the depth distribution of fault slip rates. $D_{\mathrm{lock}}$ either stays near VW/VS boundary when the earthquake is confined in SZ, or becomes shallower after deeper penetration of coseismic slip into the VS region, while $D_{\mathrm{geod}}$ tends to deepen in all four models, as the slip deficit region expands in the late interseismic period. Therefore, $D_{\mathrm{lock}}$ and $D_{\mathrm{geod}}$ reflect different aspects of fault behavior and could diverge, especially in the presence of deeper penetration of coseismic slip and significant afterslip.

Let us compare the results for cases with the same deeper $D_{\mathrm{rupt}}$ as M4 but three $(a-b)$ values in the VS regions, 0.01, 0.02 and 0.04, respectively (Fig. 5.9D-F). For the case with the smallest $(a-b)$ (Fig. 5.9F), rapid postseismic fault slip reaches a broader region surrounding the SZ, and decays in amplitude quickly afterwards, leading to a larger slip deficit zone even in the earlier interseismic period (50 yrs after the earthquake), and differences in the inferred $D_{\mathrm{geod}}$ and its time evolution. This further demonstrates that the slip deficit zone is predominantly affected by postseismic slip in our models.

We note that the empirical estimate $D_{0.5\mathrm{C}}$ tracks $D_{\mathrm{geod}}$ closely, in particular for the case with a broader LC transition (Fig. 5.9D-F). As we also show in Fig. 5.6, the equivalent $D_{\mathrm{geod}}$ (black dashed lines) is located close to the 0.5 contour lines of ISC below the SZ. Therefore, the $D_{\mathrm{geod}}$ could be empirically interpreted as the depth where fault slip rate reaches approximately half the plate loading rate.

## 5.4 Inferring the geodetic locking depths on major faults

Inferring the fault locking depth from surface geodetic measurements is challenging and complicated by several factors in practice, including limited coverage and quality of observations, complexity of the source geometry and structure, in addition to the inherent

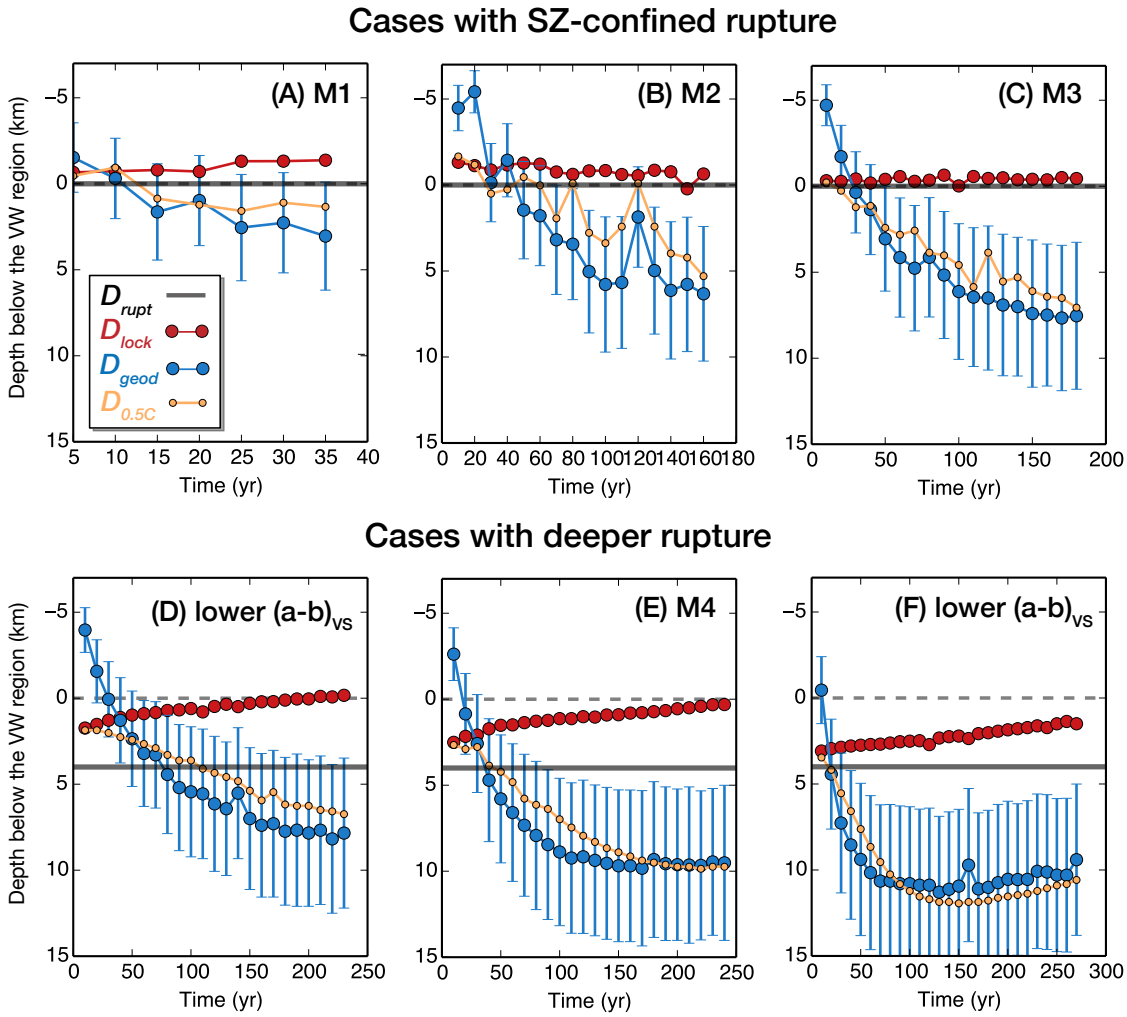


Figure 5.9: *Time dependence of $D_{lock}$, $D_{geod}$ and $D_{0.5C}$ in the interseismic period.* $D_{\rm lock}$, the true locking depth, defined at the depth where fault slip rate reaches $0.1V_{\rm max}$, is shown in red for several time windows in the interseismic period. $D_{\rm geod}$, inferred from surface geodetic measurements, is shown in blue with error bars for the marginal uncertainties. $D_{0.5C}$ represent the depth at which ISC equals 0.5, i.e., $V = 0.5V_{\rm pl}$. $D_{\rm rupt}$ is indicated by the black solid line and the VW/VS boundary as the black dashed line. All depths are considered as the distance below the VW region. The three models on the top row have earthquake ruptures confined in the SZ, while the three on the bottom have deeper earthquake ruptures and different VS properties at deeper fault extensions.

uncertainty of and correlation between $D_{\text{geod}}$ and $V_{\text{cr}}$. Among these factors, a major and common source of uncertainty comes from the elastic structure. In Fig. 5.10, we explore whether the inversion based on the elastic dislocation model would bias the estimate of $D_{\text{geod}}$ when a more realistic LC transition and a typical layered structure (e.g., *Kanamori and Hadley*, 1975, a 1D reference model for Southern California) are present. We consider two slip rate profiles along depth, one from the more realistic LC transition (LCT) in our models and the other from the dislocation model (DSL), with the latter chosen so that both have nearly identical surface expressions. We find that the dislocation-model-based inversions of the synthetic surface profiles generated from the DSL and LCT in layered structure significantly underestimate $D_{\text{lock}}$ by about 5 km. This is because more compliant shallow layer tend to produce more localized surface deformation that would be mapped into shallower locking depth in a homogeneous half-space. Geodetic studies on the San Andreas and San Jacinto faults indeed find that elastic heterogeneity, as well as fault geometry, has a large effect on the inference of fault locking depth and slip rate (*Lindsey and Fialko*, 2013; *Lindsey et al.*, 2013). However, the difference between results of DSL and LCT is smaller (about 1 km) in comparison, suggesting that geodetic inversions will not underestimate the apparent locking depth significantly simply because a more realistic transitional region is present (*Savage*, 2006). Considering that elastic heterogeneity, such as layered structure and damaged fault zone, especially in the shallow layers, (e.g., *Allam and Ben-Zion*, 2012), are characteristic of tectonic faults, the geodetic inversions based on the dislocation model in a homogeneous half-space are likely to provide an underestimate of $D_{\text{geod}}$.

The along-depth slip partition within a seismic cycle, as seen in our models, is illustrated in Fig. 5.11. Earthquake rupture can potentially penetrate deeper below the SZ, with $D_{\text{lock}}$ migrating updip or otherwise stay in depth in the post- and inter-seismic periods.

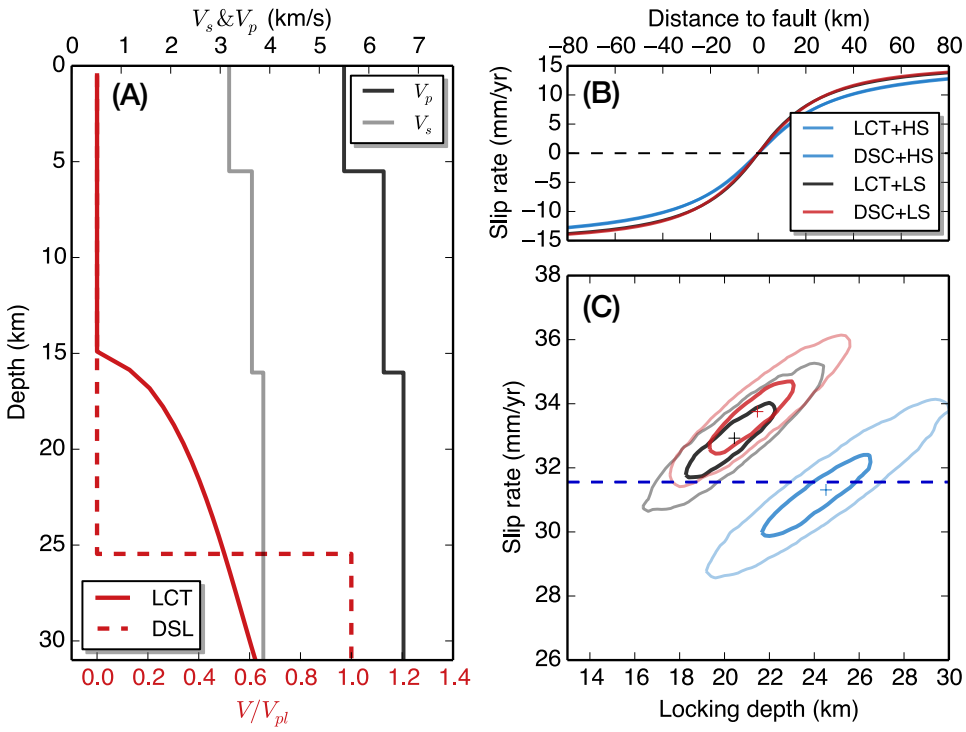


Figure 5.10: *The effect of layered elastic structure on the inference of $D_{geod}$ and $V_{cr}$.* (A) depth distribution of fault slip rates in the dislocation model (DSL) and the model with more realistic locked-creeping transition (LCT) and a representative layered structure (LS) with $V_{\rm p}$ and $V_{\rm s}$ shown (*Kanamori and Hadley*, 1975). The DSL and LCT have the equivalent surface expression in the half space (HS). (B) surface expression for different combination of fault slip rate profiles and elastic structure. (C) Inferred $1\sigma$ (68%) credible region in the parameter space of $D_{\rm geod}$ or $V_{\rm cr}$. Given a certain $V_{\rm cr}$, inversion based on LCT and LS would underestimate $D_{\rm geod}$.

Regardless of the depth of coseismic slip, postseismic slip occurs in the creeping VS region below, expanding in space and yet decaying in amplitude, eventually leading to a slip deficit zone that slips below the plate rate. As a result, the divergence of the shallower $D_{\rm lock}$ and the deeper $D_{\rm geod}$ is anticipated and indeed observed in all our models. Since $D_{\rm geod}$ correlates strongly with $V_{\rm cr}$ in the inversion (Fig. 5.8A), *a priori* assumptions that $D_{\rm geod}$ should be the same as seismicity depth, which is more relevant to $D_{\rm lock}$, could lead to underestimation of $V_{\rm cr}$, which could contribute to the discrepancy between the geodetic and geological estimates of the fault slip rate, among other factors (e.g., *Chuang and Johnson*,

2011). From the other perspective, the difference between $D_{\rm lock}$ and $D_{\rm geod}$, if accurately determined, would be indicative of the extent of deeper penetration of coseismic slip and/or the amplitude and spatial extent of postseismic slip. With the Carrizo segment of the SAF as an example (Fig. 5.1), the current discrepancy of the seismicity-based estimates (13.9, 14.4 and 16.0 km for 90%, 95%, and 99% cut-off depths, predominantly controlled by a local cluster, *Lin et al.*, 2007) and $D_{\rm lock}$ ($18.7 \pm 2$, *Smith-Konter et al.*, 2011) could be even larger, if taking into account the potential bias in the inversions due to ignoring elastic heterogeneity, as illustrated in Fig. 5.10, suggesting that significant postseismic slip should have occurred, in addition to the coseismic deeper penetration as inferred from the paucity of microseismicity (Chapter 4).

Another important issue is the relation between the depths of coseismic rupture $D_{\rm rupt}$ and interseismic fault locking $D_{\rm geod}$. In all our models, $D_{\rm geod}$ is always deeper than $D_{\rm rupt}$, because the slip deficit zone expands to counter-balance the contribution from the co- and post-seismic periods. In the limit where the postseismic slip is negligible, $D_{\rm geod}$ could coincide with $D_{\rm rupt}$, but this limit is probably unrealistic given that postseismic slip is commonly documented for large earthquakes (*Marone et al.*, 1991; *Hearn et al.*, 2002; *Perfettini and Avouac*, 2007). However, this reasoning for the maximum $D_{\rm rupt}$ being constrained by $D_{\rm geod}$ is based on the assumption of the quasi-periodic recurrence of large earthquakes, as is the case in our models. In reality, the relation between $D_{\rm rupt}$ and $D_{\rm geod}$ on the segment may be complicated by the variability of earthquake rupture, resulting in along-strike variations in slip and arresting depths, which might be assessed through paleoseismic trenching studies at different sites on the fault.

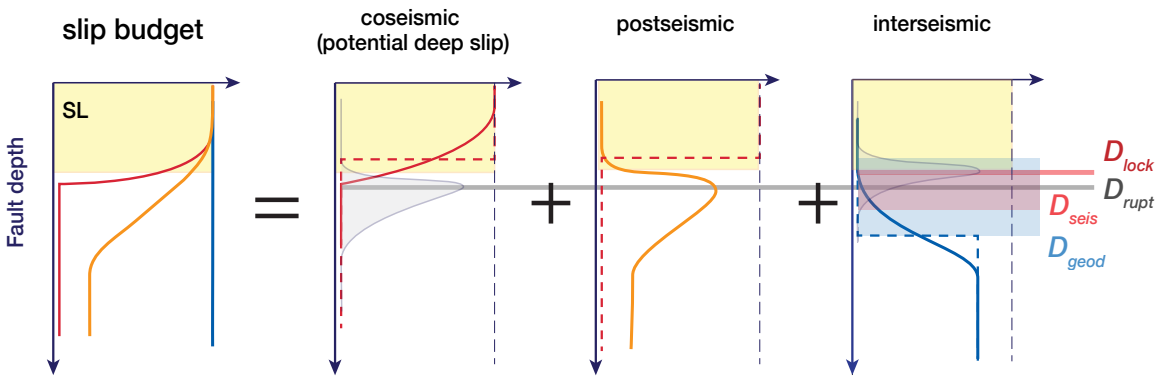


Figure 5.11: *Illustration of slip partition and $D_{geod}$, $D_{seis}$ $D_{lock}$, and $D_{rupt}$ in a seismic cycle.* The slip budget is split between the co-, post- and inter-seismic periods of fault. The gray profile indicates the depth distribution of stressing rates, which determines $D_{\text{lock}}$ (horizontal red line) and corresponds to $D_{\text{rupt}}$ (horizontal black line) right after the earthquake. The red, orange and blue lines represent fault slip during the co-, post- and inter-seismic periods, with the red and blue dashed lines corresponding to the depth of dislocation model with the near-equivalent surface expression. The red and blue band indicate the approximate depth range for $D_{\text{seis}}$ and possible range for $D_{\text{geod}}$.

## 5.5 Seismicity and fault heterogeneity at the transitional depth

While $D_{\text{geod}}$ is some depth-averaged estimate of the broad LC transition, we identify $D_{\text{lock}}$ as the physically meaningful boundary between the locked and creeping regions and more relevant for seismicity and therefore $D_{\text{seis}}$. There are cases where $D_{\text{seis}}$ is sensitive to local clusters and outliers, e.g., Carrizo segment where the only seismicity is observed north of Mojave, and the Coachella segment where 90% and 99% $D_{\text{seis}}$ differs significantly due to overall paucity of events (Fig. 5.1). On fault segments with sufficient and concentrated seismicity, e.g., the Parkfield segment (Fig. 5.1), seismicity is expected to occur predominantly at $D_{\text{lock}}$, where stressing rates are highest.

However, the observations of Anza segment of the San Jacinto fault and the Imperial Valley fault (*Smith-Konter et al.*, 2011) seem to suggest an alternative relation that $D_{\text{lock}}$ could be significantly shallower than seismicity and $D_{\text{seis}}$, even when taking into account the effect of elastic heterogeneity (*Lindsey et al.*, 2013). We offer a possible explanation for such

behavior, as illustrated in Fig. 5.12. More mature faults, characterized by large cumulative displacement and simple geometry, presumably would have more uniform along-strike fault properties and some heterogeneity at the transitional depth, which motivate our models M1-M4 (Fig. 5.12A1). However, it could be speculated that for faults with geometrical, lithological and structural complexity, variation of fault properties along the strike and at the transitional depth would be expected (*Sibson*, 1984, Fig. 5.12B1) .

Motivated by the consideration above, we develop a fault model that features along-strike variations in large VW regions, and VW patches that represent fault heterogeneity, which are not limited to the large VW region, but distributed in the deeper VS region (Fig. 5.12B2). The long-term fault behavior consists of frequent microseismicity ($M_{\mathrm{w}} \sim 4$) in the interseismic periods of occasional larger events ($M_{\mathrm{w}}$ 6-6.5) (Fig. 5.13). The apparent interseismic locking depth for the segment, inverted from stacked profiles of the surface velocity field across the fault based on a dislocation model in a homogeneous half-space (Fig. 5.14), stays with time at around 6-8 km, while most seismicity occur at 12 km and even deeper due to loading from the surrounding creeping regions, suggesting that such a model with deep creep can indeed reproduce the discrepancy of seismicity and $D_{\mathrm{rupt}}$ (*Wdowinski*, 2009). It might be questioned whether a large number of isolated VW patches can exist in VS regions, since they should produce repeating earthquakes predominantly, which is not observed for the San Jacinto Fault (*Lindsey et al.*, 2013). In our model, while most of the isolated VW patches produce repeating earthquakes, nearby patches also interact and produce complicated behavior. Therefore, it might still be possible to have these VW patches with high spatial density, so that they frequently interact and do not simply repeat by themselves.

There remains a possibility that the region below the geodetic locking depth could still be

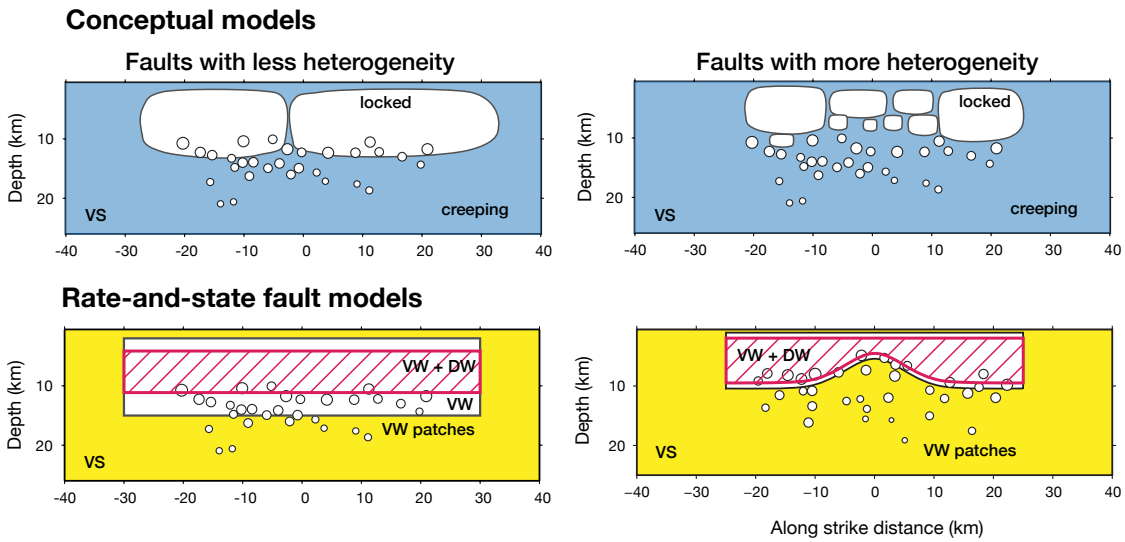


Figure 5.12: *Conceptual and physical models for faults with other heterogeneity.* (Top) Conceptual understanding of fault heterogeneity. More mature faults have along-strike uniform properties, narrower transitional region at depth with less rheological heterogeneities, while less mature faults have structural complexities, potentially characterized by along-strike variations of fault properties and broader transitional region at depth. (Bottom) Rate-and-state fault models motivated by the conceptual models above. Model M2 on the left, together with other models in Fig. 5.3, represent faults with less heterogeneity, while the model (M5) on the right represent faults with more heterogeneity and complexity.

VW, but with a much larger nucleation size, e.g., due to fluid overpressure (*Suppe*, 2014), or inelastic dilatancy (*Segall and Rice*, 1995; *Segall et al.*, 2010). Microseismicity could occur at highly stressed local heterogeneity. Further study is needed to explore whether this model could produce fault locking that is compatible with geodetic observations.

In either case, the occurrence of microseismicity depends more on the surrounding creep rates (just like seismicity indicated by blue circles in Fig. 5.5), than the location of the stress concentration front. Thus perhaps to a great extent $D_{\text{seis}}$ would depend on the combined effects of statistical properties of fault heterogeneity distribution and the fault slip rate profiles in the LC transition, while $D_{\text{lock}}$ only delineate the upper bound of the seismicity band. In all, the relation between $D_{\text{seis}}$ and $D_{\text{lock}}$ would be complicated by other forms of fault heterogeneity or additional physical mechanisms at the transitional depth.

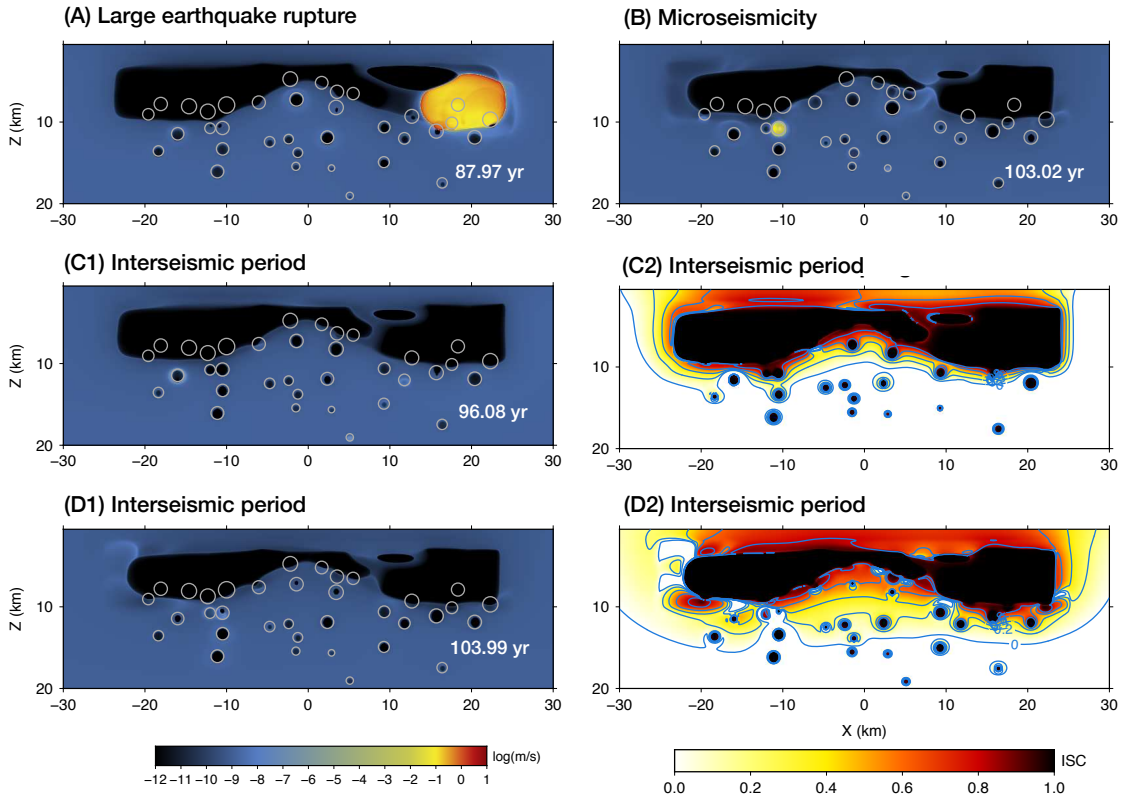


Figure 5.13: *Complex fault behavior and variation of fault coupling in model M5.* Snapshots of a large earthquake rupture (A), microseismicity (B) and interseismic periods (C1,D1) are shown from the long-term behavior of model M5 with logarithmic slip rate in color. The distributions of ISC corresponding to (C1) and (D1) are shown in (C2) and (D2).

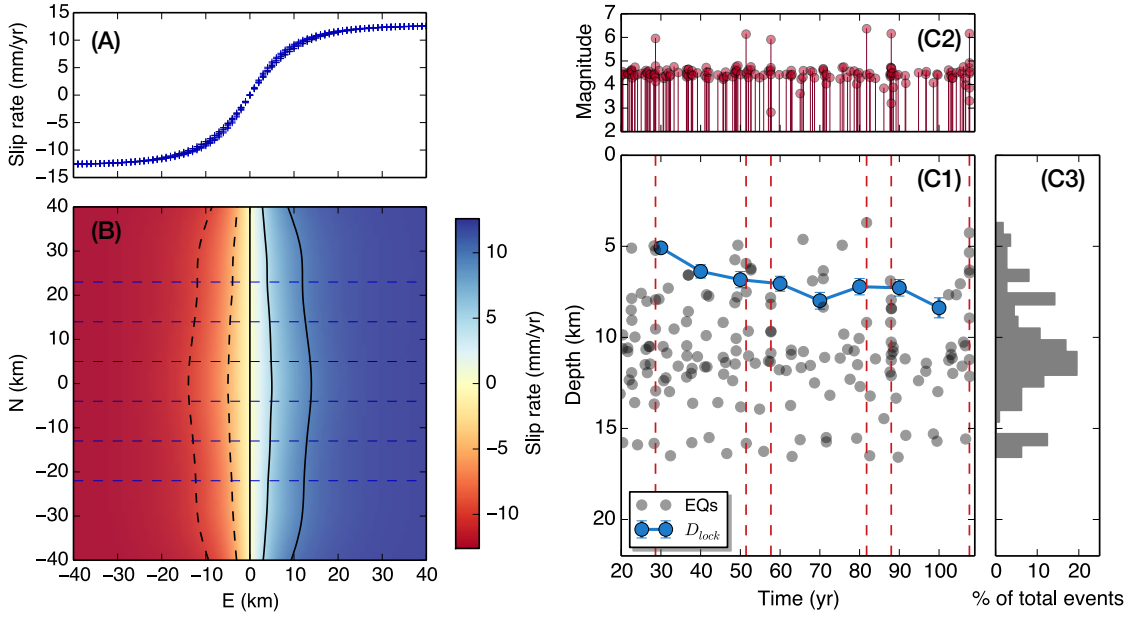


Figure 5.14: *Shallower locking depth and deeper seismicity in model M5.* Stacked profiles of fault-parallel slip rate (A) sampled from the 2D surface velocity field across the fault (B) in the interseismic period of the model M5 are used to invert the apparent $D_{\text{geod}}$ for the segment. The fault is assumed fully locked at depth $< 5$ km. Dashed blue lines are sampling profiles. Time evolution of the apparent geodetic locking depth for this segment and the depth of seismicity is shown in (C1), with the magnitudes and overall depth distribution of seismicity in (C2) and (C3), respectively, suggesting that $D_{\text{seis}}$ is deeper than $D_{\text{geod}}$ in this model.

## 5.6 Conclusion

The depth of faulting is commonly estimated by methods based on the depth distribution of seismicity, or the fault locking depth inferred from surface geodetic measurements. To understand the physical relation between these estimates, we study the behavior of seismicity and the locked-creeping transition on faults using long-term fault models governed by rate-and-state friction laws and enhanced dynamic weakening mechanisms, in which microseismicity occur due to fault heterogeneity favoring nucleation. The locked-creeping transition between the fully locked and fully creeping regions occurs a broad depth range, with the true locking depth ($D_{\text{lock}}$), which relates to the stress concentration front, near the top of the LC transition and the geodetically estimated locking depth ($D_{\text{geod}}$) at the

depth with approximately half of the far-field plate rate. The divergence of the two depths toward the late interseismic period is anticipated, accompanied by the shrinkage of fully locked zone (ISC equal to 0) and the expansion of the slip deficit zone (ISC smaller than 1), as an indicator of the extent of deeper coseismic rupture and/or postseismic slip. This relation is generally consistent with the observations of the Carrizo and Coachella segments on the San Andreas Fault, which hosted major earthquakes in the past, and the discrepancy may be more significant considering the common underestimation of $D_{\mathrm{geod}}$ due to ignoring elastic heterogeneity. While these considerations are expected to apply to mature faults with simple geometry and minor fault heterogeneity, the relation between seismicity and $D_{\mathrm{lock}}$ is complicated by other forms of heterogeneity and additional physical mechanisms on faults segments such as the Anza segment of the San Jacinto fault.

# Chapter 6

# Conclusion and Perspective

We have explored earthquake source processes from two different perspectives: inverse Bayesian modeling for two major megathrust events, the 2011 $M_{\mathrm{w}}$ 9.0 Tohoku-Oki and the 2010 $M_{\mathrm{w}}$ 8.8 Maule earthquakes in Chapters 1 and 2, and forward elastodynamic modeling of the interactions between seismic and aseismic processes at the base of the seismogenic zone on continental strike-slip faults, with the San Andreas Fault in California as our motivating example, in Chapters 3 and 4. Though different in terms of the earthquake locations and our approaches, the two parts do share similarity – both the shallow subduction zones and deeper fault extensions are regions in the earth which are almost inaccessible and remote from monitoring, thus making it crucially important to improve our ability to extract information from limited observations and to draw physical constraints from integrative modeling.

The Bayesian formulation provides an explicit and internally consistent framework that objectively assimilates the data and the prior knowledge into the inference of models. This is particularly relevant for geophysical problems, since we often rely on the physical intuitions and additional constraints to make up for the limitations in observations. In Chapters 1 and 2, we have taken advantage of the Bayesian framework in a seemingly unconventional way – we purposefully opt for minimal *a priori* assumptions, namely uninformative Gaus-

sian priors, in deriving the posterior solutions for the seafloor displacement and fault slip models. In doing so, our Bayesian approaches enjoy the computational advantages of the semi-analytical formulation. Another major motivation is that, by using minimal *a priori* assumptions on model roughness and positivity, we are allowed to explore the inherent resolutions of tsunami data, as in Chapter 1, and the complementarity of tsunami and geodetic data and their respective roles in joint inversions, as in Chapter 2. The understanding of these problems would be difficult to achieve by conventional optimization approaches that reply on regularization terms which are often chosen arbitrarily. With our methodology, we have been able to image the seafloor displacement field during the 2011 Tohoku-Oki earthquake using only tsunami waveforms, and also provide constraints on the seafloor uplift near the trench for the 2010 Maule earthquake. With these improved models, an important next step for increasing the resolution of our source models is to incorporate other datasets, e.g., seismic waveforms, and to make use of stronger *a priori* constraints, e.g., positivity of slip or other forms that are physically justifiable. In such efforts, the analytical approaches would have to give way to computationally expensive sampling algorithms, as we have explored in Chapter 1 for our kinematic seafloor models using the CATMIP algorithm (*Minson et al.*, 2013) and the AlTar computational framework that we have developed over the years at Caltech. The piecewise linear parameterization of source models and the Eikonal solver for advancing rupture front on unstructured grids that we developed in Chapter 1 could be easily incorporated into more complex forward models, e.g., with 3D Green's functions for the land and seafloor displacement computed from finite-element methods (e.g., *Aagaard et al.*, 2013), and/or kinematic earthquake scenarios on nonplanar faults.

The characteristic seafloor uplift patterns we found in both Tohoku and Maule earthquakes have important implications for the coseismic failure and tsunamigenic mechanisms

of the shallow subduction zones. The deformation near the trench, especially for the 2011 Tohoku-Oki earthquake, has been greatly debated with conflicting conclusions largely as a result of inadequate understanding of the resolution of tsunami data, uncertainties of near-field seafloor measurements, and the difficulty in comparing different source inversion studies. Our methodology with relatively simple formulations and minimal assumptions reveals that the peak uplift coincides with the edge of the accretionary wedge and decays toward the trench, suggesting either stronger velocity-strengthening properties near the trench, or decreased efficiency in fault weakening, or inelastic deformation. The two events occur in tectonic environments with large differences in trench-to-coast distances and hinge-line locations relative to the coast, but the similarity in the observed uplift could suggest potentially common mechanisms that demand further study. In any case, it remains an open question as to whether larger fault slip and seafloor uplift could occur at the trench in future earthquakes, such as the large event expected at the Cascadia subduction zone. If it is indeed possible to have larger or even peak slip at the trench, then there would be strong implications for even larger tsunami hazard than we have encountered in the 2011 Tohoku-Oki earthquake. To shed light on this puzzle, more observational studies are needed for tsunamigenic megathrust earthquakes, as well as tsunami earthquakes, in a more systematic and consistent manner. Physical modeling that considers more realistic geometry, bulk and fault properties, and dynamic processes would also be needed to identify underlying physical mechanisms and explore model parameters that could match observations.

Starting in Chapter 3, we have switched our focus to major continental strike-slip faults, such as the San Andreas Fault in Southern California. Our study offers an explanation for the long-standing enigma of seismic quiescence on mature fault segments that are known to have hosted large events: the deeper penetration of large earthquake ruptures below the

seismogenic zone. Our simulations of rate-and-state fault models that incorporate enhanced dynamic weakening at the deeper fault extension indeed reproduce the hypothesized relation between microseismicity and depth extent of large events. Observations of recent large strike-slip earthquakes, including the 2001 $M_{\mathrm{w}}$ 7.9 Kokoxili and 2002 $M_{\mathrm{w}}$ 7.9 Denali, support our theory. In this study, we have largely focused on the observational connections in the problem, and therefore we choose to impose the depth limit for enhanced dynamic weakening in our fault models. The depth of large earthquake ruptures are hence determined by this imposed depth. Physically speaking, why would larger earthquakes penetrate deeper? What kind of fault properties and physical processes affect or determine the depth extent of earthquake ruptures? We have briefly discussed the important physical considerations in Section 4.B.1. Understanding the aforementioned questions in physically more realistic fault models is one of our ongoing efforts. In Fig. 6.1, we show a demonstrative example to provide some physical intuitions and insights on this problem. In this example, we adopt depth-dependent permeability based on laboratory measurements (*Mizoguchi et al.*, 2008), and shear-zone width motivated by geological studies (*Cole et al.*, 2007), in our rate-and-state fault model with DW, including two most common mechanisms – flash heating in the seismogenic zone and thermal pressurization of pore fluids potentially active throughout the fault zone (*Rice*, 2006). As a result, the simulated earthquake sequence in the models is characterized by variability in arresting depths during each single event, as dynamic rupture develops along the strike and interacts with shear-heating mechanisms, forming a positive feedback loop between the dynamic process and fault weakening (Fig. 6.1A). The complexity of single events leads to the spatial-temporal complexity throughout the sequence, even though the frictional properties are uniform along the strike (Fig. 6.1B). With these physical models, we could explore how the earthquake rupture and arrest processes at

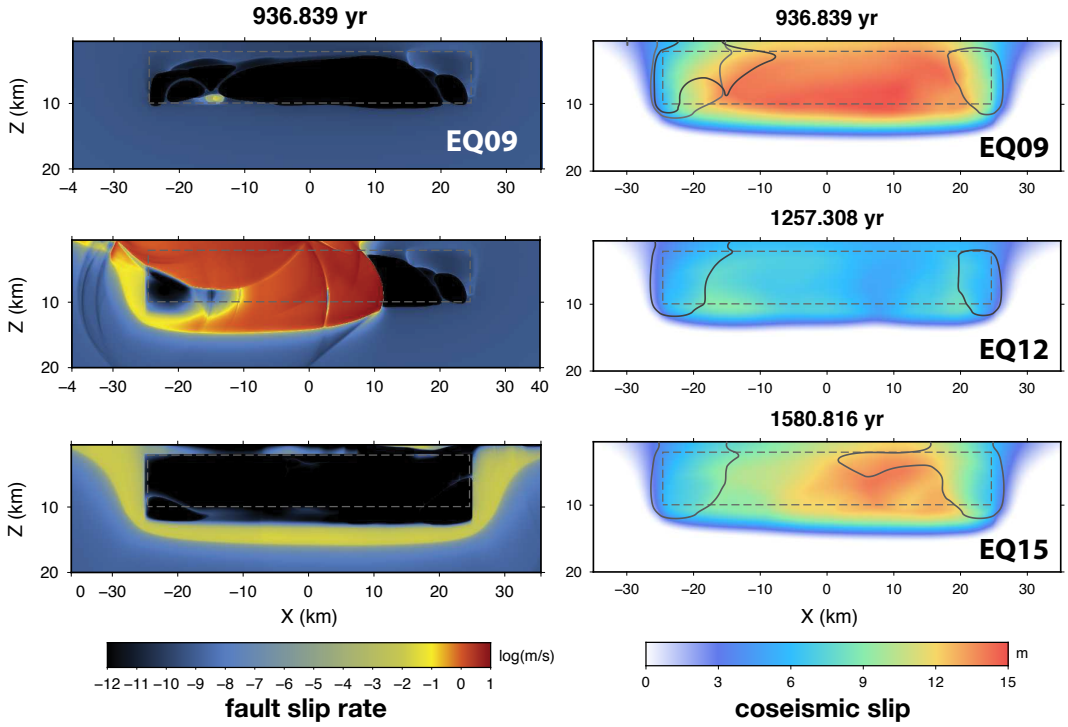


Figure 6.1: *Variability in earthquake slip and arresting depths in models with depth-dependent permeability and shear-zone width.* (Left) Snapshots of a large earthquake rupture with the slip rate in color on the logarithmic scale. (Right) Spatial distributions of coseismic slip are shown for three consecutive earthquakes. The spatial extent of smaller earthquakes that occur between the larger events are indicated by black lines. The fault properties are the same throughout the simulation.

depth would affect the along-strike variability of fault slip and their interactions with the presence of frictional heterogeneity.

In Chapter 4, we study the relation between the geodetic observables of fault locking and the behavior of seismicity in our models. We find the divergence between the effective geodetic locking depth and the true locking depth toward the late interseismic period in all our models, due to either deeper penetration of large earthquake ruptures, or significant postseismic slip on the fault, or both. Our studies suggest that with the combination of seismicity and geodetic estimates, we would be able to better understand the locked-creeping transitions on faults and the connection between interseismic and coseismic fault behavior. Our friction-based fault models used in Chapter 3 and 4 do not yet include viscoelastic

or plastic behavior of the deeper ductile crust, although localized fault roots are expected for at least mature faults. It remains a future work to assess how the incorporation of the inelastic properties and flow laws (e.g., *Takeuchi and Fialko*, 2012; *Shimamoto and Noda*, 2014) would change the fault behavior at the transitional depths, and the relation between different depth estimates.

Although we have focused on continental strike-slip faults, the proposed relation between seismicity, fault locking, and large earthquake slip should be qualitatively applicable to the deeper portion of the subduction zone megathrust. Some major faults such as the Main Himalayan Thrust indeed feature concentrated seismicity band near the downdip limit of the present-day locked zone (*Ader et al.*, 2012), while the Cascadia subduction zone has been seismically quiescent for long and a deeper downdip rupture has been speculated (*McCrory et al.*, 2014). The typical source dimension, geometry and depth distribution of frictional properties in subduction zones would need to be considered to establish a quantitative relation between the depth of potential large earthquake slip and the observed fault coupling for these regions.

Moving forward, observation-based inverse modeling and idealized physical modeling could play more synergistic roles in elucidating the complexity of earthquake source processes. On one hand, the resolution of inverted source models could be enhanced by not only using multiple datasets and complementary observations, but also incorporating physically-justifiable prior constraints on the model. For example, energy-based criteria could be considered in the inversion of deep earthquake slip (*Matthews and Segall*, 1993) and could lead to better constrained and more informative results, which are relevant to our interpretations and hypothesis testing in Chapter 3 & 4. On the other hand, improved geophysical forward modeling which is used in the inverse problem would presumably reduce the model

prediction (epistemic) errors and lead to better results. For example, 3D elastic structure and more sophisticated hydrodynamics could be used for predicting surface deformation due to fault slip and simulating tsunami waveforms, respectively. The Bayesian formulation provides an internally consistent and straightforward framework for incorporating physically-motivated prior constraints, and also an objective and quantitative method for comparing different model classes based on their overall performance and model complexity (*Beck*, 2010), and therefore such formulation is ideal for the integration of observations and physical models.

# Bibliography

Aagaard, B. T., M. G. Knepley, and C. A. Williams (2013), A domain decomposition approach to implementing fault slip in finite-element models of quasi-static and dynamic crustal deformation, *J. Geophys. Res. Solid Earth*, *118*(6), 3059–3079, doi:10.1002/jgrb.50217.

Ader, T. J., J.-P. Avouac, J. Liu-Zeng, H. Lyon-Caen, L. Bollinger, J. Galetzka, J. Genrich, M. Y. Thomas, K. Chanard, S. N. Sapkota, S. Rajaure, P. Shrestha, L. Ding, and M. Flouzat (2012), Convergence rate across the Nepal Himalaya and interseismic coupling on the Main Himalayan Thrust: Implications for seismic hazard, *J. Geophys. Res.*, *117*(B4), B04,403, doi:10.1029/2011JB009071.

Akçiz, S. O., L. G. Ludwig, J. R. Arrowsmith, and O. Zielke (2010), Century-long average time intervals between earthquake ruptures of the San Andreas fault in the Carrizo Plain, California, *Geology*, *38*(9), 787–790, doi:10.1130/G30995.1.

Allam, A. A., and Y. Ben-Zion (2012), Seismic velocity structures in the southern California plate-boundary environment from double-difference tomography, *Geophys. J. Int.*, *190*(2), 1181–1196, doi:10.1111/j.1365-246X.2012.05544.x.

Allgeyer, S., and P. Cummins (2014), Numerical tsunami simulation including elastic loading and seawater density stratification, *Geophys. Res. Lett.*, *41*(7), 2368–2375.

Altenberger, U., G. Prosser, M. Ruggiero, and C. Gunter (2011), Microstructure and petrology of a Calabrian garnet-bearing pseudotachylyte - a link to lower-crustal seismicity, *Geol. Soc. London Spec. Publ.*, *359*(1), 153–168, doi:10.1144/SP359.9.

Amante, C., and B. Eakins (2009), ETOPO1 1 arc-minute global relief model: procedures, data sources and analysis, *Tech. rep.*, NOAA Technical Memorandum NESDIS NGDC-24. National Geophysical Data Center, NOAA. doi:10.7289/V5C8276M.

Ammon, C. J., T. Lay, H. Kanamori, and M. Cleveland (2011), A rupture model of the 2011 off the Pacific coast of Tohoku Earthquake, *Earth Planets Space*, *63*(7), 693–696, doi:10.5047/eps.2011.05.015.

Ampuero, J.-P., and A. M. Rubin (2008), Earthquake nucleation on rate and state faults–Aging and slip laws, *J. Geophys. Res. Solid Earth*, *113*(B1).

Aster, R. C., B. Borchers, and C. H. Thurber (2013), *Parameter Estimation and Inverse Problems*, Academic Press.

Bakun, W. H., B. T. Aagaard, B. Dost, W. L. Ellsworth, J. L. Hardebeck, R. A. Harris, C. Ji, M. J. S. Johnston, J. Langbein, J. J. Lienkaemper, A. J. Michael, J. R. Murray, R. M. Nadeau, P. A. Reasenberg, M. S. Reichle, E. A. Roeloffs, A. Shakal, R. W. Simpson, and F. Waldhauser (2005), Implications for prediction and hazard assessment from the 2004 Parkfield earthquake, *Nature*, *437*(7061), 969–974, doi:10.1038/nature04067.

Barbot, S., Y. Fialko, and Y. Bock (2009), Postseismic deformation due to the Mw 6.0 2004 Parkfield earthquake: Stress-driven creep on a fault with spatially variable rate-and-state friction parameters, *J. Geophys. Res. Solid Earth*, *114*(B7), n/a–n/a, doi:10.1029/2008JB005748, b07405.

Barbot, S., N. Lapusta, and J.-P. Avouac (2012), Under the hood of the earthquake machine: Toward predictive modeling of the seismic cycle, *Science*, *336*(6082), 707–710, doi:10.1126/science.1218796.

Bayes, M., and M. Price (1763), An essay towards solving a problem in the doctrine of chances. by the late rev. Mr. Bayes, F. R. S. communicated by Mr. Price, in a letter to John Canton, A. M. F. R. S., *Philosophical Transactions*, *53*, 370–418, doi:10.1098/rstl.1763.0053.

Beck, J. L. (2010), Bayesian system identification based on probability logic, *Struct. Contr. Health. Monit.*, *17*(7), 825–847.

Ben-Zion, Y., and J. R. Rice (1997), Dynamic simulations of slip on a smooth fault in an elastic solid, *J. Geophys. Res.*, *102*(17,771).

Beroza, G. C. (1991), Near-source modeling of the Loma Prieta earthquake: Evidence for heterogeneous slip and implications for earthquake hazard, *Bull. Seismol. Soc. Am.*, *81*(5), 1603–1621.

Beroza, G. C., and P. Spudich (1988), Linearized inversion for fault rupture behavior - Application to the 1984 Morgan-Hill, California, earthquake, *J. Geophys. Res.*, *93*(B6), 6275–6296.

Biasi, G. P., R. J. Weldon, T. E. Fumal, and G. G. Seitz (2002), Paleoseismic event dating and the conditional probability of large earthquakes on the southern San Andreas fault, California, *Bull. Seismol. Soc. Am.*, *92*(7), 2761–2781, doi:10.1785/0120000605.

Blanpied, M. L., D. A. Lockner, and J. D. Byerlee (1995), Frictional slip of granite at hydrothermal conditions, *J. Geophys. Res. Solid Earth*, *100*(B7), 13,045–13,064.

Bletery, Q., A. Sladen, B. Delouis, M. Vallée, J.-M. Nocquet, L. Rolland, and J. Jiang (2014), A detailed source model for the Mw 9.0 Tohoku-Oki earthquake reconciling geodesy, seismology, and tsunami records, *J. Geophys. Res. Solid Earth*, *119*(10), 7636–7653, doi: 10.1002/2014JB011261.

Bouchon, M., and H. Karabulut (2008), The aftershock signature of supershear earthquakes, *Science*, *320*(5881), 1323–1325, doi:10.1126/science.1155030.

Bruhat, L., S. Barbot, and J.-P. Avouac (2011), Evidence for postseismic deformation of the lower crust following the 2004 Mw 6.0 Parkfield earthquake, *J. Geophys. Res.*, *116*(B8), doi:10.1029/2010JB008073.

Bürgmann, R. (2005), Interseismic coupling and asperity distribution along the Kamchatka subduction zone, *J. Geophys. Res.*, *110*(B7), B07,405–17, doi:10.1029/2005JB003648.

Çakir, Z., J.-B. de Chabalier, R. Armijo, B. Meyer, A. Barka, and G. Peltzer (2003), Coseismic and early post-seismic slip associated with the 1999 Izmit earthquake (Turkey), from SAR interferometry and tectonic field observations, *Geophys. J. Int.*, *155*(1), 93–110, doi:10.1046/j.1365-246X.2003.02001.x.

Chen, T., and N. Lapusta (2009), Scaling of small repeating earthquakes explained by interaction of seismic and aseismic slip in a rate and state fault model, *J. Geophys. Res. Solid Earth*, *114*, B01,311, doi:10.1029/2008JB005749.

Chester, F. M. (1995), A rheologic model for wet crust applied to strike-slip faults, *J. Geophys. Res. Solid Earth*, *100*(B7), 13,033–13,044.

Chester, F. M., and J. S. Chester (1998), Ultracataclasite structure and friction processes of the Punchbowl fault, San Andreas system, California, *Tectonophysics*, *295*(1-2), 199–221.

Chu, R., S. Wei, D. V. Helmberger, Z. Zhan, L. Zhu, and H. Kanamori (2011), Initiation of the great Mw 9.0 Tohoku–Oki earthquake, *Earth Planet. Sci. Lett.*, *308*(3-4), 277–283, doi:10.1016/j.epsl.2011.06.031.

Chuang, R. Y., and K. M. Johnson (2011), Reconciling geologic and geodetic model fault slip-rate discrepancies in Southern California: Consideration of nonsteady mantle flow and lower crustal fault creep, *Geology*, *39*(7), 627–630, doi:10.1130/G32120.1.

Cole, J., B. R. Hacker, L. Ratschbacher, J. F. Dolan, G. Seward, C. Frohlich, and W. Frank (2007), Localized ductile shear below the seismogenic zone: Structural analysis of an exhumed strike-slip fault, Austrian Alps, *J. Geophys. Res. Solid Earth*, *112*(B12), doi: 10.1029/2007JB004975.

Comte, D., J. Battaglia, C. Thurber, H. Zhang, L. Dorbath, and B. Glass (2004), High-resolution subducting slab structure beneath northern Chile using the double-difference tomography method, *AGU Fall Meeting Abstracts*, p. B200.

Cubas, N., N. Lapusta, J.-P. Avouac, and H. Perfettini (2015), Numerical modeling of long-term earthquake sequences on the NE Japan megathrust: Comparison with observations and implications for fault friction, *Earth Planet. Sci. Lett.*, *419*, 1–12, doi:10.1016/j.epsl. 2015.03.002.

Custódio, S., P. Liu, and R. J. Archuleta (2005), The 2004 Mw 6.0 Parkfield, California, earthquake: Inversion of near-source ground motion using multiple data sets, *Geophysical Research Letters*, *32*(23), doi:10.1029/2005GL024417, l23312.

Das, S., and C. H. Scholz (1983), Why large earthquakes do not nucleate at shallow depths, *Nature*, *141*(3), 183–206, doi:10.1016/j.pepi.2003.11.002.

Day, S. M., L. A. Dalguer, and N. Lapusta (2005), Comparison of finite difference and boundary integral solutions to three-dimensional spontaneous rupture, *J. Geophys. Res.*, *110*(B12307), 1–23.

Delouis, B., J.-M. Nocquet, and M. Vallée (2010), Slip distribution of the February 27, 2010 Mw = 8.8 Maule Earthquake, central Chile, from static and high-rate GPS, InSAR, and broadband teleseismic data, *Geophys. Res. Lett.*, *37*(17), L17,305, doi: 10.1029/2010GL043899.

Di Toro, G., R. Han, T. Hirose, N. De Paola, S. Nielsen, K. Mizoguchi, F. Ferri, M. Cocco, and T. Shimamoto (2011), Fault lubrication during earthquakes, *Nature*, *471*(7339), 494–498, doi:10.1038/nature09838.

Dieterich, J. (2007), Applications of rate- and state-Dependent friction to models of fault-slip and earthquake occurrence, in *Treatise on Geophysics (Second Edition)*, edited by G. Schubert, second edition ed., pp. 93 – 110, Elsevier, Oxford, doi:http://dx.doi.org/10.1016/B978-0-444-53802-4.00075-0.

Dieterich, J. H. (1979), Modeling of rock friction .1. Experimental results and constitutive equations, *J. Geophys. Res.*, *84*(NB5), 2161–2168, doi:10.1029/JB084iB05p02161.

Dieterich, J. H. (1981), Potential for geophysical experiments in large scale tests, *Geophys. Res. Lett.*, *8*(7), 653–656, doi:10.1029/GL008i007p00653/pdf.

Doser, D. I., and H. Kanamori (1986), Depth of seismicity in the Imperial Valley region (1977-1983) and its relationship to heat flow, crustal structure, and the October 15, 1979, earthquake, *J. Geophys. Res.*, *91*, 675–688.

Dreger, D. S., L. Gee, P. Lombard, M. H. Murray, and B. Romanowicz (2005), Rapid finite-

source analysis and near-fault strong ground motions: Application to the 2003 Mw 6.5 San Simeon and 2004 Mw 6.0 Parkfield earthquakes, *Seismol. Res. Lett.*, *76*(1), 40–48, doi:10.1785/gssrl.76.1.40.

Duputel, Z., P. S. Agram, M. Simons, S. E. Minson, and J. L. Beck (2014), Accounting for prediction uncertainty when inferring subsurface fault slip, *Geophys. J. Int.*, *197*(1), 464–482, doi:10.1093/gji/ggt517.

Duputel, Z., J. Jiang, R. Jolivet, M. Simons, L. Rivera, J.-P. Ampuero, B. Riel, S. E. Owen, A. W. Moore, S. V. Samsonov, F. Ortega Culaciati, and S. E. Minson (2015), The Iquique earthquake sequence of April 2014: Bayesian modeling accounting for prediction uncertainty, *Geophys. Res. Lett.*, *42*(19), 7949–7957, doi:10.1002/2015GL065402, 2015GL065402.

Elliott, J. L., J. T. Freymueller, and B. Rabus (2007), Coseismic deformation of the 2002 Denali fault earthquake: Contributions from synthetic aperture radar range offsets, *J. Geophys. Res.*, *112*(B6), B06,421, doi:10.1029/2006JB004428.

Emolo, A., and A. Zollo (2005), Kinematic source parameters for the 1989 Loma Prieta earthquake from the nonlinear inversion of accelerograms, *Bull. Seismol. Soc. Am.*, *95*(3), 981–994, doi:10.1785/0120030193.

Engdahl, E. R., and A. Villaseñor (2002), 41 global seismicity: 1900–1999, *Int. Geophys.*, *81*, 665–XVI.

Engdahl, E. R., R. van der Hilst, and R. Buland (1998), Global teleseismic earthquake relocation with improved travel times and procedures for depth determination, *Bull. Seismol. Soc. Am.*, *88*(3), 722–743.

Fang, Z., and E. M. Dunham (2013), Additional shear resistance from fault roughness and stress levels on geometrically complex faults, *J. Geophys. Res. Solid Earth*, *118*(7), 3642–3654, doi:10.1002/jgrb.50262.

Fialko, Y. (2006), Interseismic strain accumulation and the earthquake potential on the southern San Andreas fault system, *Nature*, *441*(7096), 968–971, doi:10.1038/nature04797.

Field, E. H., R. J. Arrowsmith, G. P. Biasi, and P. Bird (2014), Uniform California Earthquake Rupture Forecast, version 3 (UCERF3)—The time-independent model, *Bull. Seismol. Soc. Am.*, *104*(3), 1122–1180, doi:10.1785/0120130164.

Fu, Z., W.-K. Jeong, Y. Pan, R. M. Kirby, and R. T. Whitaker (2011), A fast iterative method for solving the Eikonal equation on triangulated surfaces, *SIAM J. Sci. Comput.*, *33*(5), 2468–2488, doi:10.1137/100788951.

Fujii, Y., and K. Satake (2012), Slip distribution and seismic moment of the 2010 and 1960 Chilean earthquakes inferred from tsunami waveforms and coastal geodetic data, *Pure. Appl. Geophys.*, *170*(9-10), 1493–1509, doi:10.1007/s00024-012-0524-2.

Fujiwara, T., S. Kodaira, T. No, Y. Kaiho, N. Takahashi, and Y. Kaneda (2011), The 2011 Tohoku-Oki earthquake: Displacement reaching the trench axis, *Science*, *334*(6060), 1240, doi:10.1126/science.1211554.

Fumal, T. E., M. J. Rymer, and G. G. Seitz (2002), Timing of large earthquakes since A.D. 800 on the Mission Creek strand of the San Andreas fault zone at Thousand Palms Oasis, near Palm Springs, California, *Bull. Seismol. Soc. Am.*, *92*(7), 2841–2860, doi:10.1785/0120000609.

Geist, E., and R. Dmowska (1999), Local tsunamis and distributed slip at the source, *Pure. Appl. Geophys.*, *154*(3), 485–512.

Grant, L. B., and A. Donnellan (1994), 1855 and 1991 surveys of the San Andreas fault: Implications for fault mechanics, *Bull. Seismol. Soc. Am.*, *84*(2), 241–246.

Grant Ludwig, L., J. N. Brune, A. Anooshehpoor, M. D. Purvance, R. J. Brune, and J. C. Lozos (2015), Reconciling precariously balanced rocks (PBRs) with large earthquakes on the San Andreas fault system, *Seismol. Res. Lett.*, doi:10.1785/0220140239.

Haberland, C., A. Rietbrock, D. Lange, K. Bataille, and T. Dahm (2009), Structure of the seismogenic zone of the southcentral Chilean margin revealed by local earthquake traveltime tomography, *J. Geophys. Res. Solid Earth*, *114*(B1), doi:10.1029/2008JB005802, b01317.

Hampel, A., N. Kukowski, J. Bialas, C. Huebscher, and R. Heinbockel (2004), Ridge subduction at an erosive margin: The collision zone of the Nazca Ridge in southern Peru, *J. Geophys. Res. Solid Earth*, *109*(B2), n/a–n/a, doi:10.1029/2003JB002593, b02101.

Hartzell, S. H., and T. H. Heaton (1983), Inversion of strong ground motion and teleseismic waveform data for the fault rupture history of the 1979 Imperial Valley, California, earthquake, *Bull. Seismol. Soc. Am.*, *73*(6A), 1553.

Hartzell, S. H., and T. H. Heaton (1986), Rupture history of the 1984 Morgan Hill, California, earthquake from the inversion of strong motion records, *Bull. Seismol. Soc. Am.*, *76*(3), 649–674.

Hauksson, E. (2011), Crustal geophysics and seismicity in Southern California, *Geophys. J. Int.*, *186*(1), 82–98, doi:10.1111/j.1365-246X.2011.05042.x.

Hauksson, E., W. Yang, and P. M. Shearer (2012), Waveform relocated earthquake catalog for Southern California (1981 to June 2011), *Bull. Seismol. Soc. Am.*, *102*(5), 2239–2244, doi:10.1785/0120120010.

Hayes, G. P. (2011), Rapid source characterization of the 2011 Mw 9.0 off the Pacific coast of Tohoku Earthquake, *Earth Planets Space*, *63*(7), 529–534, doi:10.5047/eps.2011.05.012.

Hearn, E. H., R. Bürgmann, and R. E. Reilinger (2002), Dynamics of İzmit earthquake postseismic deformation and loading of the Düzce earthquake hypocenter, *Bull. Seismol. Soc. Am.*, *92*(1), 172–193, doi:10.1785/0120000832.

Hetland, E. A., and M. Simons (2010), Post-seismic and interseismic fault creep II: transient creep and interseismic stress shadows on megathrusts, *Geophys. J. Int.*, *181*(1), 99–112, doi:10.1111/j.1365-246X.2009.04482.x.

Hetland, E. A., M. Simons, and E. M. Dunham (2010), Post-seismic and interseismic fault creep I: model description, *Geophys. J. Int.*, *181*(1), 81–98, doi:10.1111/j.1365-246X.2010.04522.x.

Hirth, G., and N. M. Beeler (2015), The role of fluid pressure on frictional behavior at the base of the seismogenic zone, *Geology*, *43*(3), 223–226, doi:10.1130/G36361.1.

Hobbs, B. E., A. Ord, and C. Teyssier (1986), Earthquakes in the ductile regime?, *Pure. Appl. Geophys.*, *124*(1-2), 309–336, doi:10.1007/BF00875730.

Hossen, M. J., P. R. Cummins, and J. Dettmer (2015), Tsunami waveform inversion for sea surface displacement following the 2011 Tohoku earthquake: Importance of dispersion and source kinematics, *J. Geophys. Res. Solid Earth*, *120*, doi:10.1002/(ISSN)2169-9356.

Hsu, Y.-J., M. Simons, J.-P. Avouac, J. Galetzka, K. Sieh, M. Chlieh, D. Natawidjaja, L. Prawirodirdjo, and Y. Bock (2006), Frictional afterslip following the 2005 Nias-Simeulue earthquake, Sumatra, *Science*, *312*(5782), 1921–1926, doi:10.1126/science.1126960.

Hsu, Y. J., M. Simons, and C. Williams (2011), Three-dimensional FEM derived elastic Green's functions for the coseismic deformation of the 2005 Mw 8.7 Nias-Simeulue, Sumatra earthquake, *Geochem. Geophys. Geosyst.*, doi:10.1029/2011GC003553.

Hubbard, J., S. Barbot, E. M. Hill, and P. Tapponnier (2015), Coseismic slip on shallow décollement megathrusts: implications for seismic and tsunami hazard, *Earth-Sci. Rev.*, *141*(C), 1–11.

Ide, S., A. Baltay, and G. C. Beroza (2011), Shallow dynamic overshoot and energetic deep rupture in the 2011 Mw 9.0 Tohoku-Oki earthquake, *Science*, *332*(6036), 1426–1429, doi:10.1126/science.1207020.

Iinuma, T., M. Ohzono, Y. Ohta, and S. Miura (2011), Coseismic slip distribution of the 2011 off the Pacific coast of Tohoku Earthquake (M 9.0) estimated based on GPS data—Was the asperity in Miyagi-oki ruptured?, *Earth Planets Space*, *63*(7), 643–648.

Iinuma, T., R. Hino, M. Kido, D. Inazu, Y. Osada, Y. Ito, M. Ohzono, H. Tsushima, S. Suzuki, H. Fujimoto, and S. Miura (2012), Coseismic slip distribution of the 2011 off the Pacific coast of Tohoku earthquake (M9.0) refined by means of seafloor geodetic data, *J. Geophys. Res.*, *117*(B7), B07,409, doi:10.1029/2012JB009186.

Ito, Y., T. Tsuji, Y. Osada, M. Kido, D. Inazu, Y. Hayashi, H. Tsushima, R. Hino, and

H. Fujimoto (2011), Frontal wedge deformation near the source region of the 2011 Tohoku-Oki earthquake, *Geophys. Res. Lett.*, *38*(15), doi:10.1029/2011GL048355.

Jaynes, E. T. (2003), *Probability Theory: The Logic of Science*, Cambridge University Press, UK.

Jolivet, R., M. Simons, P. S. Agram, Z. Duputel, and Z.-K. Shen (2015), Aseismic slip and seismogenic coupling along the central San Andreas Fault, *Geophys. Res. Lett.*, *42*(2), 297–306, doi:10.1002/2014GL062222.

Kajiura, K. (1981), Tsunami energy in relation to parameters of the earthquake fault model, *Tokyo Univ. Earthquake Research Inst. Bull.*, *56*, 415–440.

Kanamori, H., and D. Hadley (1975), Crustal structure and temporal velocity change in Southern California, *Pure. Appl. Geophys.*, *113*(1), 257–280, doi:10.1007/BF01592916.

Kaneko, Y., J.-P. Avouac, and N. Lapusta (2010), Towards inferring earthquake patterns from geodetic observations of interseismic coupling, *Nat. Geosci.*, *3*(5), 363–369, doi:10.1038/ngeo843.

Kelemen, P. B., and G. Hirth (2007), A periodic shear-heating mechanism for intermediate-depth earthquakes in the mantle, *Nature*, *446*(7137), 787–790, doi:10.1038/nature05717.

Kido, M., Y. Osada, H. Fujimoto, R. Hino, and Y. Ito (2011), Trench-normal variation in observed seafloor displacements associated with the 2011 Tohoku-Oki earthquake, *Geophys. Res. Lett.*, *38*(24), n/a–n/a, doi:10.1029/2011GL050057, l24303.

Kodaira, S., T. No, Y. Nakamura, T. Fujiwara, Y. Kaiho, S. Miura, N. Takahashi, Y. Kaneda, and A. Taira (2012), Coseismic fault rupture at the trench axis during the 2011 Tohoku-oki earthquake, *Nat. Geosci.*, *5*(9), 646–650, doi:10.1038/ngeo1547.

Koketsu, K., Y. Yokota, N. Nishimura, Y. Yagi, S. Miyazaki, K. Satake, Y. Fujii, H. Miyake, S. Sakai, and Y. Yamanaka (2011), A unified source model for the 2011 Tohoku earthquake, *Earth Planet. Sci. Lett.*, *310*(3), 480–487, doi:10.1016/j.epsl.2011.09.009.

Konca, A. O., J.-P. Avouac, A. Sladen, A. J. Meltzner, K. E. Sieh, P. Fang, Z. Li, J. Galetzka, J. Genrich, and M. Chlieh (2008), Partial rupture of a locked patch of the Sumatra megathrust during the 2007 earthquake sequence, *Nature*, *456*(7222), 631–635.

Kositsky, A., and J. P. Avouac (2010), Inverting geodetic time series with a principal component analysis-based inversion method, *J. Geophys. Res.*, *115*(B3), B03,401, doi:10.1029/2009JB006535.

Kozdon, J. E., and E. M. Dunham (2013), Rupture to the trench: Dynamic rupture simulations of the 11 March 2011 Tohoku earthquake, *Bull. Seismol. Soc. Am.*, *103*(2B), 1275–1289, doi:10.1785/0120120136.

Krabbenhöft, A., J. Bialas, H. Kopp, N. Kukowski, and C. Hübscher (2004), Crustal structure of the Peruvian continental margin from wide-angle seismic studies, *Geophys. J. Int.*, *159*(2), 749–764, doi:10.1111/j.1365-246X.2004.02425.x.

Kundu, P., I. Cohen, and D. Dowling (2012), Fluid Mechanics, 920 pp.

Lapusta, N., and Y. Liu (2009), Three-dimensional boundary integral modeling of spontaneous earthquake sequences and aseismic slip, *J. Geophys. Res. Solid Earth*, *114*(B9), doi:10.1029/2008JB005934.

Lapusta, N., and J. R. Rice (2003), Nucleation and early seismic propagation of small and large events in a crustal earthquake model, *J. Geophys. Res. Solid Earth*, *108*(B4), 2205, doi:10.1029/2001JB000793.

Lapusta, N., J. R. Rice, Y. Ben-Zion, and G. T. Zheng (2000), Elastodynamic analysis for slow tectonic loading with spontaneous rupture episodes on faults with rate- and state-dependent friction, *J. Geophys. Res. Solid Earth*, *105*(B10), 23,765–23,789, doi: 10.1029/2000JB900250.

Larsen, S., R. Reilinger, H. Neugebauer, and W. Strange (1992), Global positioning system measurements of deformations associated with the 1987 Superstition Hills Earthquake: Evidence for conjugate faulting, *J. Geophys. Res. Solid Earth*, *97*(B4), 4885–4902, doi: 10.1029/92JB00128.

Lasserre, C., G. Peltzer, F. Crampé, Y. Klinger, J. van der Woerd, and P. Tapponnier (2005), Coseismic deformation of the 2001 Mw= 7.8 Kokoxili earthquake in Tibet, measured by synthetic aperture radar interferometry, *J. Geophys. Res.*, *110*(B12), B12,408, doi: 10.1029/2004JB003500.

Lay, T. (2011), Possible large near-trench slip during the 2011 Mw9.0 off the Pacific coast of Tohoku Earthquake, *Earth Planets Space*, *63*(7), 687–692, doi:10.5047/eps.2011.05.033.

Lay, T., C. J. Ammon, H. Kanamori, K. D. Koper, O. Sufri, and A. R. Hutko (2010), Teleseismic inversion for rupture process of the 27 February 2010 Chile (Mw 8.8) earthquake, *Geophys. Res. Lett.*, *37*(13), doi:10.1029/2010GL043379, l13301.

Lévěque, J. J., and L. A. Rivera (1993), On the use of the checker-board test to assess the resolution of tomographic inversions, *Geophys. J. Int.*, doi:10.1111/j.1365-246X.1993.tb05605.x.

Li, V. C., and J. R. Rice (1987), Crustal deformation in great California earthquake cycles, *J. Geophys. Res.*, *92*(B11), 11,533–11,551.

Lin, A., T. Maruyama, S. Aaron, K. Michibayashi, A. Camacho, and K. Kano (2005), Propagation of seismic slip from brittle to ductile crust: Evidence from pseudotachylyte of the Woodroffe thrust, central Australia, *Tectonophysics*, *402*(1-4), 21–35, doi:10.1016/j.tecto.2004.10.016.

Lin, G., P. M. Shearer, and E. Hauksson (2007), Applying a three-dimensional velocity model, waveform cross correlation, and cluster analysis to locate Southern California seismicity from 1981 to 2005, *J. Geophys. Res.*, *112*(B12), B12,309, doi:10.1029/2007JB004986.

Lin, Y. N., A. Sladen, F. Ortega-Culaciati, M. Simons, J.-P. Avouac, E. J. Fielding, B. A. Brooks, M. G. Bevis, J. Genrich, A. Rietbrock, C. Vigny, R. Smalley, and A. Socquet (2013), Coseismic and postseismic slip associated with the 2010 Maule Earthquake, Chile: Characterizing the Arauco Peninsula barrier effect, *J. Geophys. Res. Solid Earth*, *118*(6), 3142–3159, doi:10.1002/jgrb.50207.

Lindsey, E. O., and Y. Fialko (2013), Geodetic slip rates in the southern San Andreas Fault System: Effects of elastic heterogeneity and fault geometry, *J. Geophys. Res. Solid Earth*, *118*(2), 689–697, doi:10.1029/2012JB009358.

Lindsey, E. O., V. J. Sahakian, Y. Fialko, Y. Bock, S. Barbot, and T. K. Rockwell (2013), Interseismic Strain Localization in the San Jacinto Fault Zone, *Pure. Appl. Geophys.*, doi:10.1007/s00024-013-0753-z.

Liu, P. L.-F., Y.-S. Cho, S. Yoon, and S. Seo (1995), Numerical simulations of the 1960 Chilean tsunami propagation and inundation at Hilo, Hawaii, in *Tsunami: Progress in Prediction, Disaster Prevention and Warning*, pp. 99–115, Springer.

Lorito, S., A. Piatanesi, V. Cannelli, F. Romano, and D. Melini (2010), Kinematics and source zone properties of the 2004 Sumatra-Andaman earthquake and tsunami: Nonlinear joint inversion of tide gauge, satellite altimetry, and GPS data, *J. Geophys. Res.*, *115*(B2), B02,304–20, doi:10.1029/2008JB005974.

Lorito, S., F. Romano, S. Atzori, X. Tong, A. Avallone, J. Mccloskey, M. Cocco, E. Boschi, and A. Piatanesi (2011), Limited overlap between the seismic gap and coseismic slip of the great 2010 Chile earthquake, *Nat. Geosci.*, *3*(1), 1–5, doi:10.1038/ngeo1073.

Lozos, J. C. (2016), A case for historic joint rupture of the San Andreas and San Jacinto faults, *Sci. Adv.*, *2*(3), doi:10.1126/sciadv.1500621.

Ludwig, L. G., S. O. Akciz, G. R. Noriega, O. Zielke, and J. R. Arrowsmith (2010), Climate-modulated channel incision and rupture history of the San Andreas fault in the Carrizo Plain, *Science*, *327*(5969), 1117–1119, doi:10.1126/science.1182837.

Ma, S. (2012), A self-consistent mechanism for slow dynamic deformation and tsunami generation for earthquakes in the shallow subduction zone, *Geophys. Res. Lett.*, *39*(11).

Ma, S., S. Custódio, R. J. Archuleta, and P. Liu (2008), Dynamic modeling of the 2004 Mw 6.0 Parkfield, California, earthquake, *J. Geophys. Res. Solid Earth*, *113*(B2), doi:10.1029/2007JB005216, b02301.

Maeda, T., T. Furumura, S. Sakai, and M. Shinohara (2011), Significant tsunami observed at ocean-bottom pressure gauges during the 2011 off the Pacific coast of Tohoku Earthquake, *Earth Planets Space*, *63*(7), 803–808, doi:10.5047/eps.2011.06.005.

Mai, P. M., and K. K. S. Thingbaijam (2014), SRCMOD: An online database of finite-fault rupture models, *Seismol. Res. Lett.*, *85*(6), 1348–1357, doi:10.1785/0220140077.

Marone, C. J., C. H. Scholz, and R. Bilham (1991), On the mechanics of earthquake afterslip, *J. Geophys. Res. Solid Earth*, *96*(B5), 8441–8452, doi:10.1029/91JB00275.

Masterlark, T. (2003), Finite element model predictions of static deformation from dislocation sources in a subduction zone: Sensitivities to homogeneous, isotropic, poisson-solid, and half-space assumptions, *J. Geophys. Res. Solid Earth*, *108*(B11), n/a–n/a, doi:10.1029/2002JB002296, 2540.

Masterlark, T., C. DeMets, H. F. Wang, O. Sánchez, and J. Stock (2001), Homogeneous vs heterogeneous subduction zone models: Coseismic and postseismic deformation, *Geophys. Res. Lett.*, *28*(21), 4047–4050, doi:10.1029/2001GL013612.

Matthews, M. V., and P. Segall (1993), Estimation of depth-dependent fault slip from measured surface deformation with application to the 1906 San Francisco earthquake, *J. Geophys. Res.*, *98*(B7), 12,153, doi:10.1029/93JB00440.

McCrory, P. A., R. D. Hyndman, and J. L. Blair (2014), Relationship between the Cascadia fore-arc mantle wedge, nonvolcanic tremor, and the downdip limit of seismogenic rupture, *Geochem. Geophys. Geosyst.*, *15*(4), 1071–1095, doi:10.1002/2013GC005144.

McGill, S., S. Dergham, K. Barton, T. Berney-Ficklin, D. Grant, C. Hartling, K. Hobart, R. Minnich, M. Rodriguez, E. Runnerstrom, J. Russell, K. Schmoker, M. Stumfall, J. Townsend, and J. Williams (2002), Paleoseismology of the San Andreas fault at Plunge Creek, near San Bernardino, Southern California, *Bull. Seismol. Soc. Am.*, *92*(7), 2803–2840, doi:10.1785/0120000607.

Mechie, J., S. V. Sobolev, L. Ratschbacher, A. Y. Babeyko, G. Bock, A. G. Jones, K. D. Nelson, K. D. Solon, L. D. Brown, and W. Zhao (2004), Precise temperature estimation

in the Tibetan crust from seismic detection of the $\alpha$-$\beta$ quartz transition, *Geology*, *32*(7), 601, doi:10.1130/G20367.1.

Melgar, D., and Y. Bock (2013), Near-field tsunami models with rapid earthquake source inversions from land- and ocean-based observations: The potential for forecast and warning, *J. Geophys. Res. Solid Earth*, *118*(11), 5939–5955, doi:10.1002/2013JB010506, 2013JB010506.

Meltzner, A. J., and D. J. Wald (1999), Foreshocks and aftershocks of the great 1857 California earthquake, *Bull. Seismol. Soc. Am.*, *89*(4), 1109–1120.

Meltzner, A. J., and D. J. Wald (2003), Aftershocks and triggered events of the great 1906 California earthquake, *Bull. Seismol. Soc. Am.*, *93*(5), 2160–2186, doi:10.1029/2003RG000119.

Meltzner, A. J., K. Sieh, M. Abrams, D. C. Agnew, K. W. Hudnut, J.-P. Avouac, and D. H. Natawidjaja (2006), Uplift and subsidence associated with the great Aceh-Andaman earthquake of 2004, *J. Geophys. Res.*, *111*(B2), B02,407–8, doi:10.1029/2005JB003891.

Miller, M. D., M. Simons, J. F. Adkins, and S. E. Minson (2015), The information content of pore fluid 18O and [Cl], *J. Phys. Oceanogr.*, *45*(8), 2070–2094, doi:10.1175/jpo-d-14-0203.1.

Minson, S. E., M. Simons, and J. L. Beck (2013), Bayesian inversion for finite fault earthquake source models I—theory and algorithm, *Geophys. J. Int.*, *194*(3), 1701–1726, doi:10.1093/gji/ggt180.

Minson, S. E., M. Simons, J. L. Beck, F. Ortega, J. Jiang, S. E. Owen, A. W. Moore, A. Inbal, and A. Sladen (2014), Bayesian inversion for finite fault earthquake source

models – II: the 2011 great Tohoku-oki, Japan earthquake, *Geophys. J. Int.*, *198*(2), 922–940, doi:10.1093/gji/ggu170.

Miyazaki, S. (2011), Seismic and aseismic fault slip before and during the 2011 off the Pacific coast of Tohoku earthquake, *Earth Planets Space*, *63*(7), 637–642, doi:10.5047/eps.2011.07.001.

Mizoguchi, K., T. Hirose, T. Shimamoto, and E. Fukuyama (2008), Internal structure and permeability of the Nojima fault, southwest Japan, *J. Struct. Geol.*, *30*(4), 513–524.

Moecher, D. P., and M. G. Steltenpohl (2011), Petrological evidence for co-seismic slip in extending middle-lower continental crust: Heier's zone of pseudotachylyte, north Norway, *Geol. Soc. London Spec. Publ.*, *359*(1), 169–186, doi:10.1144/SP359.10.

Moreno, M., D. Melnick, M. Rosenau, J. C. Baez, J. Klotz, O. Oncken, A. Tassara, J. Chen, K. Bataille, M. G. Bevis, A. Socquet, J. Bolte, C. Vigny, B. A. Brooks, I. Ryder, V. Grund, B. Smalley, D. Carrizo, M. Bartsch, and H. Hase (2012), Toward understanding tectonic control on the Mw 8.8 2010 Maule Chile earthquake, *Earth Planet. Sci. Lett.*, *321-322*, 152–165, doi:10.1016/j.epsl.2012.01.006.

Nazareth, J. J., and E. Hauksson (2004), The seismogenic thickness of the Southern California crust, *Bull. Seismol. Soc. Am.*, *94*(3), 940–960.

Noda, H., and N. Lapusta (2010), Three-dimensional earthquake sequence simulations with evolving temperature and pore pressure due to shear heating: Effect of heterogeneous hydraulic diffusivity, *J. Geophys. Res.*, *115*(B12), doi:10.1029/2010JB007780.

Noda, H., and N. Lapusta (2013), Stable creeping fault segments can become destructive as a result of dynamic weakening, *Nature*, *493*(7433), 518–521, doi:10.1038/nature11703.

Oglesby, D. D., D. S. Dreger, R. A. Harris, N. Ratchkovski, and R. Hansen (2004), Inverse kinematic and forward dynamic models of the 2002 Denali fault earthquake, Alaska, *Bull. Seismol. Soc. Am.*, *94*(6), S214–S233, doi:10.1785/0120040620.

Okada, Y. (1992), Internal deformation due to shear and tensile faults in a half-space, *Bull. Seismol. Soc. Am.*, *82*(2), 1018–1040.

Oncken, O., E. Luschen, J. Mechie, S. Sobolev, A. Schulze, C. Gaedicke, S. Grunewald, J. Bribach, G. Asch, P. Giese, et al. (1999), Seismic reflection image revealing offset of Andean subduction-zone earthquake locations into oceanic mantle, *Nature*, *397*(6717), 341–344.

Onderdonk, N. W., T. K. Rockwell, S. F. McGill, and G. I. Marliyani (2013), Evidence for seven surface ruptures in the past 1600 years on the Claremont fault at Mystic Lake, northern San Jacinto fault zone, California, *Bull. Seismol. Soc. Am.*, *103*(1), 519–541, doi:10.1785/0120120060.

Ortega Culaciati, F. H. (2013), Aseismic deformation in subduction megathrusts: Central Andes and north-east Japan, Ph.D. thesis, Dissertation (Ph.D.), California Institute of Technology.

Ozawa, S., T. Nishimura, H. Suito, T. Kobayashi, M. Tobita, and T. Imakiire (2011), Coseismic and postseismic slip of the 2011 magnitude-9 Tohoku-Oki earthquake, *Nature*, *475*(7356), 373–376, doi:10.1038/nature10227.

Palmer, A., and J. R. Rice (1973), The growth of slip surfaces in the progressive failure of over-consolidated clay, *Proc. R. Soc. London, Ser. B Mathematical and Physical Sciences*, *332*(1591), 527–548.

Passelègue, F. X., and D. L. Goldsby (2014), The influence of ambient fault temperature on flash-heating phenomena, *Geophys. Res. Lett.*, *41*, 828–835, doi:10.1002/(ISSN)1944-8007.

Peregrine, D. H. (1967), Long waves on a beach, *J. Fluid Mech.*, *27*, 815–827.

Perfettini, H., and J.-P. Ampuero (2008), Dynamics of a velocity strengthening fault region: Implications for slow earthquakes and postseismic slip, *J. Geophys. Res. Solid Earth*, *113*(B9), B09,411, doi:10.1029/2007JB005398.

Perfettini, H., and J. P. Avouac (2004), Postseismic relaxation driven by brittle creep: A possible mechanism to reconcile geodetic measurements and the decay rate of aftershocks, application to the Chi-Chi earthquake, Taiwan, *J. Geophys. Res. Solid Earth*, *109*(B2), B02,304, doi:10.1029/2003JB002488.

Perfettini, H., and J. P. Avouac (2007), Modeling afterslip and aftershocks following the 1992 Landers earthquake, *J. Geophys. Res.*, *112*(B7), B07,409, doi:10.1029/2006JB004399.

Philibosian, B., T. E. Fumal, and R. Weldon (2011), San Andreas fault earthquake chronology and Lake Cahuilla history at Coachella, California, *Bull. Seismol. Soc. Am.*, *101*(1), 13–38, doi:10.1785/0120100050.

Pittarello, L., G. Pennacchioni, and G. D. Toro (2012), Amphibolite-facies pseudotachylytes in Premosello metagabbro and felsic mylonites (Ivrea Zone, Italy), *Tectonophysics*, *580*, 43 – 57, doi:http://dx.doi.org/10.1016/j.tecto.2012.08.001.

Plafker, G., and M. Rubin (1978), Uplift history and earthquake recurrence as deduced from marine terraces on Middleton Island, Alaska, *Tech. Rep. 687-721*, U.S. Geological Survey Open-File Report 78-943.

Platt, J., B. Proctor, T. Mitchell, G. Hirth, D. Goldsby, G. Di Toro, N. Beeler, and T. Tullis (2015), The role of gouge and temperature on flash heating and its hysteresis, *EGU General Assembly Conference Abstracts*, *17*, 7787.

Platt, J. D., J. W. Rudnicki, and J. R. Rice (2014), Stability and localization of rapid shear in fluid-saturated fault gouge: 2. Localized zone width and strength evolution, *J. Geophys. Res. Solid Earth*, *119*(5), 4334–4359, doi:10.1002/2013JB010711.

Plesch, A., J. Shaw, C. Benson, W. A. Bryant, S. Carena, M. Cooke, J. F. Dolan, G. Fuis, E. Gath, L. Grant, E. Hauksson, T. H. Jordan, M. Kamerling, M. Legg, S. Lindvall, H. Magistrale, C. Nicholson, N. Niemi, M. E. Oskin, S. Perry, G. Planansky, T. Rockwell, P. M. Shearer, C. Sorlien, M. P. Suss, J. Suppe, J. Treiman, and R. Yeats (2007), Community Fault Model (CFM) for Southern California, *Bull. Seismol. Soc. Am.*, *97*(6), 1793–1802, doi:10.1785/0120050211.

Ratchkovski, N. A., R. A. Hansen, J. C. Stachnik, T. Cox, O. Fox, L. Rao, E. Clark, M. Lafevers, S. Estes, and J. B. MacCormack (2003), Aftershock sequence of the Mw 7.9 Denali fault, Alaska, earthquake of 3 November 2002 from regional seismic network data, *Seismol. Res. Lett.*, *74*(6), 743–752.

Reilinger, R. E., S. Ergintav, R. Burgmann, and S. McClusky (2000), Coseismic and postseismic fault slip for the 17 August 1999, M= 7.5, Izmit, Turkey earthquake, *Science*, *289*(5484), 1519–1524, doi:10.1126/science.289.5484.1519.

Rice, J. R. (1993), Spatio-temporal complexity of slip on a fault, *J. Geophys. Res.*, *98*(B6), 9885–9907.

Rice, J. R. (2006), Heating and weakening of faults during earthquake slip, *J. Geophys. Res.*, *111*(B5), doi:10.1029/2005JB004006.

Rice, J. R., and A. L. Ruina (1983), Stability of Steady Frictional Slipping, *J. Appl. Mech.-T. ASME*, *50*(2), 343–349.

Rietbrock, A., I. Ryder, G. Hayes, C. Haberland, D. Comte, S. Roecker, and H. Lyon-Caen (2012), Aftershock seismicity of the 2010 Maule Mw=8.8, Chile, earthquake: Correlation between co-seismic slip models and aftershock distribution?, *Geophys. Res. Lett.*, *39*(8), doi:10.1029/2012GL051308, l08310.

Robinson, D. P., C. Brough, and S. Das (2006), The Mw 7.8, 2001 Kunlunshan earthquake: Extreme rupture speed variability and effect of fault geometry, *J. Geophys. Res.*, *111*(B8), B08,303, doi:10.1029/2005JB004137.

Rockwell, T. K., T. E. Dawson, J. Young Ben-Horin, and G. Seitz (2014), A 21-event, 4,000-year history of surface ruptures in the Anza seismic gap, San Jacinto fault, and implications for long-term earthquake production on a major plate boundary fault, *Pure. Appl. Geophys.*, *172*(5), 1143–1165, doi:10.1007/s00024-014-0955-z.

Rolandone, F., R. Bürgmann, and R. M. Nadeau (2004), The evolution of the seismic-aseismic transition during the earthquake cycle: Constraints from the time-dependent depth distribution of aftershocks, *Geophys. Res. Lett.*, *31*(23), L23,610, doi:10.1029/2004GL021379.

Romano, F., A. Piatanesi, S. Lorito, N. D'Agostino, K. Hirata, S. Atzori, Y. Yamazaki, and M. Cocco (2012), Clues from joint inversion of tsunami and geodetic data of the 2011 Tohoku-oki earthquake, *Sci. Rep*, *2*, doi:10.1038/srep00385.

Romano, F., E. Trasatti, S. Lorito, C. Piromallo, A. Piatanesi, Y. Ito, D. Zhao, K. Hirata, P. Lanucara, and M. Cocco (2014), Structural control on the Tohoku earthquake rupture process investigated by 3D FEM, tsunami and geodetic data, *Sci. Rep*, *4*, doi:10.1038/srep05631.

Ruina, A. (1983), Slip instability and state variable friction laws, *J. Geophys. Res. Solid Earth*, *88*(B12), 10,359–10,370, doi:10.1029/JB088iB12p10359.

Runnerstrom, E. E., L. B. Grant, J. R. Arrowsmith, D. D. Rhodes, and E. M. Stone (2002), Displacement across the Cholame segment of the San Andreas fault between 1855 and 1893 from cadastral surveys, *Bull. Seismol. Soc. Am.*, *92*(7), 2659–2669, doi:10.1785/0120000603.

Saito, T., Y. Ito, D. Inazu, and R. Hino (2011), Tsunami source of the 2011 Tohoku-Oki earthquake, Japan: Inversion analysis based on dispersive tsunami simulations, *Geophys. Res. Lett.*, *38*, doi:10.1029/2011GL049089.

Satake, K. (1988), Effects of bathymetry on tsunami propagation: Application of ray tracing to tsunamis, *Pure. Appl. Geophys.*, *126*(1), 27–36, doi:10.1007/BF00876912.

Satake, K., and Y. Tanioka (1999), Sources of tsunami and tsunamigenic earthquakes in subduction zones, *Pure. Appl. Geophys.*, *154*(3), 467–483.

Satake, K., Y. Fujii, T. Harada, and Y. Namegaya (2013), Time and space distribution of coseismic slip of the 2011 Tohoku earthquake as inferred from tsunami waveform data, *Bull. Seismol. Soc. Am.*, *103*(2B), 1473–1492, doi:10.1785/0120120122.

Sato, M., T. Ishikawa, N. Ujihara, S. Yoshida, M. Fujita, M. Mochizuki, and A. Asada

(2011), Displacement above the hypocenter of the 2011 Tohoku-Oki earthquake, *Science*, *332*(6036), 1395–1395, doi:10.1126/science.1207401.

Savage, J., and W. Prescott (1978), Asthenosphere readjustment and the earthquake cycle, *J. Geophys. Res. Solid Earth*, *83*(B7), 3369–3376.

Savage, J. C. (2006), Dislocation pileup as a representation of strain accumulation on a strike-slip fault, *J. Geophys. Res.*, *111*(B4), B04,405–14, doi:10.1029/2005JB004021.

Savage, J. C., and R. O. Burford (1973), Geodetic determination of relative plate motion in central California, *J. Geophys. Res.*, *78*(5), 832–845, doi:10.1029/JB078i005p00832/pdf.

Schaff, D. P., G. Bokelmann, G. C. Beroza, F. Waldhauser, and W. L. Ellsworth (2002), High-resolution image of Calaveras Fault seismicity, *J. Geophys. Res. Solid Earth*, *107*(B9), –ESE 5–16, doi:10.1029/2001JB000633.

Scholz, C. H. (1988), The brittle-plastic transition and the depth of seismic faulting, *Geol. Rundsch.*, *77*(1), 319–328.

Scholz, C. H. (1998), Earthquakes and friction laws, *Nature*, *391*(6662), 37–42.

Scholz, C. H. (2002), *The Mechanics of Earthquakes and Faulting, 2nd ed.*, Cambridge University Press.

Scholz, C. H. (2014), The rupture mode of the shallow largeslip surge of the Tohokuoki earthquake, *Bull. Seismol. Soc. Am.*, *104*(5), 2627–2631, doi:10.1785/0120140130.

Segall, P. (2002), Integrating geologic and geodetic estimates of slip rate on the San Andreas fault system, *Int. Geol. Rev.*, *44*(1), 62–82, doi:10.2747/0020-6814.44.1.62.

Segall, P. (2010), *Earthquake and Volcano Deformation*, Princeton University Press, doi: 10.2307/j.ctt7sg19.

Segall, P., and A. M. Bradley (2012), The role of thermal pressurization and dilatancy in controlling the rate of fault slip, *J. Appl. Mech.*, *79*(3), 031,013, doi:10.1115/1.4005896.

Segall, P., and J. R. Rice (1995), Dilatancy, compaction, and slip instability of a fluid-Infiltrated fault, *J. Geophys. Res. Solid Earth*, *100*(B11), 22,155–22,171.

Segall, P., A. M. Rubin, A. M. Bradley, and J. R. Rice (2010), Dilatant strengthening as a mechanism for slow slip events, *J. Geophys. Res.*, *115*(B12), B12,305, doi:10.1029/ 2010JB007449.

Sekiguchi, H., and T. Iwata (2002), Rupture process of the 1999 Kocaeli, Turkey, earthquake estimated from strong-motion waveforms, *Bull. Seismol. Soc. Am.*, *92*(1), 300–311.

Shao, G., C. Ji, and D. Zhao (2011), Rupture process of the 9 March, 2011 Mw 7.4 Sanriku-Oki, Japan earthquake constrained by jointly inverting teleseismic waveforms, strong motion data and GPS observations, *Geophys. Res. Lett.*, *38*, doi:10.1029/2011GL049164.

Shaw, B. E., and S. G. Wesnousky (2008), Slip-length scaling in large earthquakes: The role of deep-penetrating slip below the seismogenic layer, *Bull. Seismol. Soc. Am.*, *98*(4), 1633–1641, doi:10.1785/0120070191.

Shelly, D. R. (2010), Migrating tremors illuminate complex deformation beneath the seismogenic San Andreas fault, *Nature*, *463*(7281), 648–U75, doi:10.1038/nature08755.

Shimamoto, T. (1989), The origin of S-C Mylonites and a new fault-zone model, *J. Struct. Geol.*, *11*(1-2), 51–64, doi:10.1016/0191-8141(89)90035-7.

Shimamoto, T., and H. Noda (2014), A friction to flow constitutive law and its application to a 2-D modeling of earthquakes, *J. Geophys. Res. Solid Earth*, *119*(11), 8089–8106, doi:10.1002/2014JB011170.

Sibson, R. H. (1973), Interactions between temperature and pore-fluid pressure during earthquake faulting and a mechanism for partial or total stress relief, *Nature*, *243*(126), 66–68.

Sibson, R. H. (1980), Transient discontinuities in ductile shear zones, *J. Struct. Geol.*, *2*(1-2), 165–171, doi:10.1016/0191-8141(80)90047-4.

Sibson, R. H. (1984), Roughness at the base of the seismogenic zone: contributing factors, *J. Geophys. Res.*, *89*(B7), 5791–5799.

Sieh, K. E. (1978a), Slip along the San Andreas fault associated with the great 1857 earthquake, *Bull. Seismol. Soc. Am.*, *68*(5), 1421–1448.

Sieh, K. E. (1978b), Central California foreshocks of the great 1857 earthquake, *Bull. Seismol. Soc. Am.*, *68*(6), 1731–1749.

Simons, M., S. E. Minson, A. Sladen, F. Ortega, J. Jiang, S. Owen, L. Meng, J.-P. Ampuero, S. Wei, R. Chu, D. V. Helmberger, H. Kanamori, E. A. Hetland, A. W. Moore, and F. H. Webb (2011), The 2011 magnitude 9.0 Tohoku-oki earthquake: Mosaicking the megathrust from seconds to centuries, *Science*, *332*(6036), 1421–1425.

Smith, B. R., and D. T. Sandwell (2006), A model of the earthquake cycle along the San Andreas Fault System for the past 1000 years, *J. Geophys. Res.*, *111*(B1), B01,405, doi: 10.1029/2005JB003703.

Smith-Konter, B. R., D. T. Sandwell, and P. M. Shearer (2011), Locking depths estimated from geodesy and seismology along the San Andreas Fault System: Implications for seismic moment release, *J. Geophys. Res.*, *116*(B6), B06,401, doi:10.1029/2010JB008117.

Song, S. G., G. C. Beroza, and P. Segall (2008a), A unified source model for the 1906 San Francisco earthquake, *Bull. Seismol. Soc. Am.*, *98*(2), 823–831, doi:10.1785/0120060402.

Song, T.-R. A., and M. Simons (2003), Large trench-parallel gravity variations predict seismogenic behavior in subduction zones, *Science*, *301*(5633), 630–633, doi:10.1126/science.1085557.

Song, Y., L. Fu, V. Zlotnicki, C. Ji, V. Hjorleifsdottir, C. Shum, and Y. Yi (2008b), The role of horizontal impulses of the faulting continental slope in generating the 26 December 2004 tsunami, *Ocean Model.*, *20*(4), 362–379.

Suppe, J. (2014), Fluid overpressures and strength of the sedimentary upper crust, *J. Struct. Geol.*, *69*, 481–492, doi:10.1016/j.jsg.2014.07.009.

Takeuchi, C. S., and Y. Fialko (2012), Dynamic models of interseismic deformation and stress transfer from plate motion to continental transform faults, *J. Geophys. Res.*, *117*(B5), doi:10.1029/2011JB009056.

Tanikawa, W., and T. Shimamoto (2009), Frictional and transport properties of the Chelungpu fault from shallow borehole data and their correlation with seismic behavior during the 1999 Chi-Chi earthquake, *J. Geophys. Res.*, *114*(B1), doi:10.1029/2008JB005750.

Tanioka, Y., and K. Satake (1996), Tsunami generation by horizontal displacement of ocean bottom, *Geophys. Res. Lett.*, *23*(8), 861–864.

Tappin, D. R., S. T. Grilli, J. C. Harris, R. J. Geller, T. Masterlark, J. T. Kirby, F. Shi, G. Ma, K. K. S. Thingbaijam, and P. M. Mai (2014), Did a submarine landslide contribute to the 2011 Tohoku tsunami?, *Mar. Geol.*, *357*(C), 344–361, doi:10.1016/j.margeo.2014.09.043.

Tarantola, A. (2005), *Inverse Problem Theory and Methods for Model Parameter Estimation*, SIAM.

Tassara, A., H.-J. Götze, S. Schmidt, and R. Hackney (2006), Three-dimensional density model of the Nazca plate and the Andean continental margin, *J. Geophys. Res. Solid Earth*, *111*(B9), n/a–n/a, doi:10.1029/2005JB003976, b09404.

Tong, X., D. T. Sandwell, K. Luttrell, B. Brooks, M. G. Bevis, M. Shimada, J. Foster, R. Smalley Jr., H. Parra, J. C. Baez Soto, M. Blanco, E. Kendrick, J. Genrich, and D. J. Caccamise II (2010), The 2010 Maule, Chile earthquake: Downdip rupture limit revealed by space geodesy, *Geophys. Res. Lett.*, *37*(24), n/a–n/a, doi:10.1029/2010GL045805.

Tong, X., B. R. Smith-Konter, and D. T. Sandwell (2014), Is there a discrepancy between geological and geodetic slip rates along the San Andreas Fault System?, *J. Geophys. Res. Solid Earth*, *119*(3), 2518–2538, doi:10.1002/2013JB010765.

Toy, V. G., S. Ritchie, and R. H. Sibson (2011), Diverse habitats of pseudotachylytes in the Alpine Fault Zone and relationships to current seismicity, *Geol. Soc. London Spec. Publ.*, *359*(1), 115–133, doi:10.1144/SP359.7.

Tsai, V. C., J.-P. Ampuero, H. Kanamori, and D. J. Stevenson (2013), Estimating the effect of earth elasticity and variable water density on tsunami speeds, *Geophys. Res. Lett.*, *40*(3), 492–496, doi:10.1002/grl.50147.

Tse, S. T., and J. R. Rice (1986), Crustal earthquake instability in relation to the depth variation of frictional slip properties, *J. Geophys. Res.*, *91*(B9), 9452–9472, doi:10.1029/JB091iB09p09452/full.

Tullis, T. (2015), Mechanisms for friction of rock at earthquake slip rates, in *Treatise on Geophysics (Second Edition)*, edited by G. Schubert, second edition ed., pp. 139 – 159, Elsevier, Oxford, doi:http://dx.doi.org/10.1016/B978-0-444-53802-4.00073-7.

Ujiie, K., H. Tanaka, T. Saito, A. Tsutsumi, J. J. Mori, J. Kameda, E. E. Brodsky, F. M. Chester, N. Eguchi, S. Toczko, and Expedition 343 and 343T Scientists (2013), Low coseismic shear stress on the Tohoku-oki megathrust determined from laboratory experiments, *Science*, *342*(6163), 1211–1214, doi:10.1126/science.1243485.

Vigny, C., A. Socquet, S. Peyrat, J. C. Ruegg, M. Metois, E. Fukuyama, and K. B. Olsen (2011), The 2010 Mw 8.8 Maule megathrust earthquake of Central Chile, monitored by GPS, *Science*, doi:10.1126/science.1204132.

Wald, D. J., D. V. Helmberger, and S. H. Hartzell (1990), Rupture process of the 1987 Superstition Hills earthquake from the inversion of strong-motion data, *Bull. Seismol. Soc. Am.*, *80*(5), 1079–1098.

Wald, D. J., H. Kanamori, D. V. Helmberger, and T. H. Heaton (1993), Source study of the 1906 San-Francisco earthquake, *Bull. Seismol. Soc. Am.*, *83*(4), 981–1019.

Waldhauser, F., and D. P. Schaff (2008), Large-scale relocation of two decades of Northern California seismicity using cross-correlation and double-difference methods, *J. Geophys. Res.*, *113*(B8), B08,311, doi:10.1029/2007JB005479.

Waldhauser, F., W. L. Ellsworth, D. P. Schaff, and A. Cole (2004), Streaks, multiplets, and

holes: High-resolution spatio-temporal behavior of Parkfield seismicity, *Geophys. Res. Lett.*, *31*(18), doi:10.1029/2004GL020649.

Wang, K., and J. He (2008), Effects of frictional behavior and geometry of subduction fault on coseismic seafloor deformation, *Bull. Seis. Soc. Amer.*, *98*(2), 571–579.

Wang, K., and Y. Hu (2006), Accretionary prisms in subduction earthquake cycles: The theory of dynamic coulomb wedge, *J. Geophys. Res. Solid Earth*, *111*(B6), n/a–n/a, doi:10.1029/2005JB004094, b06410.

Wang, K., T. Sun, T. Fujiwara, S. Kodaira, and J. He (2015), How large is the fault slip at trench in the M=9 Tohoku-oki earthquake?, in *EGU General Assembly Conference Abstracts*, vol. 17, p. 7855.

Watada, S. (2013), Tsunami speed variations in density-stratified compressible global oceans, *Geophys. Res. Lett.*, *40*(15), 4001–4006, doi:10.1002/grl.50785.

Watada, S., S. Kusumoto, and K. Satake (2014), Traveltime delay and initial phase reversal of distant tsunamis coupled with the self-gravitating elastic earth, *J. Geophys. Res. Solid Earth*, *119*(5), 4287–4310, doi:10.1002/2013JB010841, 2013JB010841.

Wdowinski, S. (2009), Deep creep as a cause for the excess seismicity along the San Jacinto fault, *Nat. Geosci.*, *2*(12), 882–885, doi:10.1038/ngeo684.

Wei, S., R. W. Graves, D. V. Helmberger, J.-P. Avouac, and J. Jiang (2012), Sources of shaking and flooding during the Tohoku-Oki earthquake A mixture of rupture styles, *Earth Planet. Sci. Lett.*, *333-334*(C), 91–100, doi:10.1016/j.epsl.2012.04.006.

WGCEP (1995), Working group on california earthquake probabilities, seismic hazards in

southern california: Probable earthquakes, 1994 to 2024, *Bull. Seismol. Soc. Am.*, *85*(2), 379–439.

Wibberley, C., and T. Shimamoto (2003), Internal structure and permeability of major strike-slip fault zones: the Median Tectonic Line in Mie Prefecture, Southwest Japan, *J. Struct. Geol.*, *25*(1), 59–78, doi:10.1016/S0191-8141(02)00014-7.

Yagi, Y., and M. Kikuchi (2000), Source rupture process of the Kocaeli, Turkey, earthquake of August 17, 1999, obtained by joint inversion of near-field data and teleseismic data, *Geophys. Res. Lett.*, *27*(13), 1969–1972, doi:10.1029/1999GL011208.

Yamazaki, Y., Z. Kowalik, and K. F. Cheung (2009), Depth-integrated, non-hydrostatic model for wave breaking and run-up, *Int. J. Numer. Meth. Fluids*, *61*(5), 473–497.

Yamazaki, Y., K. F. Cheung, and Z. Kowalik (2011), Depth-integrated, non-hydrostatic model with grid nesting for tsunami generation, propagation, and run-up, *Int. J. Numer. Meth. Fluids*, *67*(12), 2081–2107, doi:10.1002/fld.2485.

Yokota, Y., K. Koketsu, Y. Fujii, K. Satake, S. Sakai, M. Shinohara, and T. Kanazawa (2011), Joint inversion of strong motion, teleseismic, geodetic, and tsunami datasets for the rupture process of the 2011 Tohoku earthquake, *Geophys. Res. Lett.*, *38*(7), n/a–n/a, doi:10.1029/2011GL050098.

Yoshida, Y., H. Ueno, D. Muto, and S. Aoki (2011), Source process of the 2011 off the pacific coast of tohoku earthquake with the combination of teleseismic and strong motion data, *Earth Planets Space*, *63*(7), 565–569, doi:10.5047/eps.2011.05.011.

Young, J. J., J. R. Arrowsmith, L. Colini, L. B. Grant, and B. Gootee (2002), Three-

dimensional excavation and eecent rupture history along the Cholame segment of the San Andreas fault, *Bull. Seismol. Soc. Am.*, *92*(7), 2670–2688, doi:10.1785/0120000604.

Yue, H., and T. Lay (2013), Source rupture models for the Mw 9.0 2011 Tohoku earthquake from joint inversions of high-rate geodetic and seismic data, *Bull. Seismol. Soc. Am.*, *103*(2B), 1242–1255, doi:10.1785/0120120119.

Yue, H., T. Lay, L. A. Rivera, C. An, C. Vigny, X. Tong, and J. C. Baez Soto (2014), Localized fault slip to the trench in the 2010 Maule, Chile Mw=8.8 earthquake from joint inversion of high-rate GPS, teleseismic body waves, InSAR, campaign GPS, and tsunami observations, *J. Geophys. Res. Solid Earth*, *119*(10), 7786–7804, doi:10.1002/2014JB011340.

Yule, D., and K. Sieh (2001), The paleoseismic record at Burro Flats: Evidence for a 300-year average recurrence for large earthquakes on the San Andreas fault in San Gorgonio Pass, southern California, in *Geol. Soc. Am. Abstr.*, vol. 33, p. 31.

Zeng, Y., and J. Anderson (2000), Evaluation of numerical procedures for simulating near-fault long-period ground motions using Zeng method, *Tech. rep.*, Report 2000/01 to the PEER Utilities Program.

Zhao, H. (2005), A fast sweeping method for eikonal equations, *Math. Comp.*, *74*(250), 603–627.

Zielke, O., J. R. Arrowsmith, L. G. Ludwig, and S. O. Akciz (2010), Slip in the 1857 and earlier large earthquakes along the Carrizo Plain, San Andreas fault, *Science*, *327*(5969), 1119–1122, doi:10.1126/science.1182781.